

# The HUNGARIAN JOURNAL OF INDUSTRY AND CHEMISTRY (HJIC)

formerly (until 2012) the Hungarian Journal of Industrial Chemistry

The HJIC is an international periodicals that focuses on results of fundamental and applied research in the field of

- Biotechnology
- Chemical Engineering Science
- Chemical Processes
- Energetics
- Environmental Chemistry
- Environmental Engineering & Technology
- Industrial Management
- Material Science
- Mechanical Engineering
- Mechatronics
- Process & System Engineering
- Recycling

in the form of original papers, reviews, short communications, and conference proceedings written in English.

## EDITORIAL BOARD

*Editor-in-chief:* RÓBERT K. SZILÁGYI  
Department of Chemistry and Biochemistry,  
Montana State University, Bozeman, MT, U.S.A.

*Honorary Senior Editor:* GÉZA HORVÁTH  
Department of Chemical Engineering Science,  
University of Pannonia, Veszprém, Hungary

### Associate Editors:

JÁNOS ABONYI  
Department of Process Engineering,  
University of Pannonia, Veszprém, Hungary

NORBERT MISKOLCZI  
MOL Department of Hydrocarbon and Coal Processing,  
University of Pannonia, Veszprém, Hungary

DEZSŐ BODA  
Department of Physical Chemistry,  
University of Pannonia, Veszprém, Hungary

DÓRA RIPPEL PETHŐ  
Department of Chemical Engineering Science,  
University of Pannonia, Veszprém, Hungary

### Editors:

LÁSZLÓ BARTHA  
MOL Department of Hydrocarbon and Coal Processing,  
University of Pannonia, Veszprém, Hungary

ZOLTÁN KOVÁCS  
Department of Management,  
University of Pannonia, Veszprém, Hungary

KATALIN BÉLAFI-BAKÓ  
Research Institute of Bioengineering,  
Membrane Technology and Energetics,  
University of Pannonia, Veszprém, Hungary

JÁNOS KRISTÓF  
Department of Analytical Chemistry,  
University of Pannonia, Veszprém, Hungary

PETER CZERMAK  
Institute of Bioprocess Engineering and  
Pharmaceutical Technology, Mittelhessen University of  
Applied Sciences, Giessen, Germany

ISTVÁN SZALAI  
Institute of Physics and Mechatronics,  
University of Pannonia, Veszprém, Hungary

DÉNES FODOR  
Institute of Mechanical Engineering,  
University of Pannonia, Veszprém, Hungary

FERENC SZEIFERT  
Department of Process Engineering,  
University of Pannonia, Veszprém, Hungary

MARIA GAVRILESCU  
Department of Environmental Engineering  
and Management,  
Gheorghe Asachi Technical University of Iasi, Romania

JÁNOS SZÉPVÖLGYI  
Research Centre for Natural Sciences,  
University of Pannonia, Veszprém, Hungary

LÁSZLÓ GUBICZA  
Research Institute of Bioengineering, Membrane  
Technology and Energetics,  
University of Pannonia, Veszprém, Hungary

IMRE TÍMÁR  
Institute of Mechanical Engineering,  
University of Pannonia, Veszprém, Hungary

JENŐ HANCSÓK  
MOL Department of Hydrocarbon and Coal Processing,  
University of Pannonia, Veszprém, Hungary

GYULA VATAI  
Department of Food Engineering,  
Corvinus University of Budapest, Hungary

JIRÍ KLEMEŠ  
Centre for Process Integration and Intensification,  
University of Pannonia, Veszprém, Hungary

GÁBOR VERESS  
Federation of Technical and Scientific Societies –  
MTESZ Budapest, Hungary

IBOLYA ZSOLDOS  
Department of Material Science and Technology,  
Széchenyi István University, Győr, Hungary

---

EDITORIAL OFFICE: UNIVERSITY OF PANNONIA, P.O. BOX 158, VESZPRÉM, 8201 (HUNGARY)

Tel.: +36 (88) 624-746, e-mail: [hjic@almos.uni-pannon.hu](mailto:hjic@almos.uni-pannon.hu); web: [hjic.mk.uni-pannon.hu](http://hjic.mk.uni-pannon.hu)

Felelős szerkesztő: Szilágyi Róbert Károly Nyelvi lektor: Matthew Chen

Kiadja: Pannon Egyetem, 8200 Veszprém, Egyetem u. 10.

Levél cím: H-8201 Veszprém, Postafiók 158, Tel.: (88) 624-000

Felelős kiadó: a Pannon Egyetem, Mérnöki Kar dékánja

## EDITORIAL PREFACE

The Editorial Board of HJIC dedicates this Issue to the National Scientific Students' Associations (Tudományos Diákkör, in Hungarian, abbreviated as TDK) that is a real Hungaricum with a 62 years old tradition. This Association includes all the Universities and Colleges of Hungary, where scientific research of any kind is being conducted. The members of the Association are the faculty members, scientific advisors, and their B.Sc. or M.Sc. students.

Participation in the work of TDK is completely voluntary. Students spend some of their free time with a faculty mentor, choose a research topic, learn the basics of the field, do the measurements or the calculations under the supervision of the chosen teacher/researcher in addition to their regular academic duties. At the end, they write a dissertation based on their results. These dissertations are peer reviewed and then presented at yearly institutional TDK-Conferences, where the students receive suggestions from a panel of scientists and professors, receive a score for their written documents and oral presentations. Based on these scores, they may win legitimacy to present their results at the National TDK-Conference. TDK is a remarkable organization in Hungary that was kept alive by people who do their work from pure enthusiasm for the love of their profession. It is not an exaggeration to say that the TDK-students form the elite of all the University students. They are the ones who proceed to M.Sc. level, become PhD students, and, at the end, ideally become colleagues of their former faculty advisors.

During their work as part of TDK, students learn systematic problem-solving, formulating good questions, critical thinking, composing their thoughts into concise, well-formulated sentences, preparing meaningful figures, elaborating the literature of the field, and presenting their result in front of a scientific panel and an audience. Even those students who do not continue their life in the academia tend to remember their time spend on TDK activities as useful and memorable. Often, the skills acquired while being involved in a TDK project are not part of the regular education at a given University. TDK gives them something extra.

This issue contains selected articles from students and their supervisors about their results presented at the TDK conferences during 2013-2014. With this issue, the Editorial Board wishes to honour the effort of all TDK students and their advisors for keeping this unique tradition alive with their devoted work.

DEZSŐ BODA AND TIBOR DULAI

University of Pannonia, Veszprém, HUNGARY

Guest Editors

**Table of Contents**

<b>Comparative Assessment of the Mussel Micronucleus Test versus Bacterial Bioassays for Genotoxicity Testing of Benzo[A]Pyrene</b> BETTINA ECK-VARANKA, ESZTER HORVÁTH, ÁRPÁD FERINCZ, GÁBOR PAULOVITS, NÓRA KOVÁTS .....	1-5
<b>Improving the Interfacial Properties of Glass Fibre Reinforced and Unreinforced Waste Sourced Low Density Polyethylene/Acrylonitrile Butadiene Styrene/Polystyrene Composites</b> JÁNOS SÓJA, VLADIMIR SEDLARIK, PAVEL KUCHARCZYK, NORBERT MISKOLCZI .....	7-12
<b>Application of Online and Laboratory Methods for the Investigation of Surface Water</b> JANKA BOBEK, ZSÓFIA KOVÁCS, ZOLTÁN ZSILÁK .....	13-18
<b>Adsorption and Intercalation of Small Molecules on Kaolinite from Molecular Modelling Studies</b> ATTILA TÁBOROSI, RÓBERT KURDI, RÓBERT K. SZILÁGYI .....	19-23
<b>Impact of Size Heterogeneity of Core-Shell Packing Materials on Chromatographic Separation of Large Biomolecules</b> DIÁNA LUKÁCS, KRISZTIÁN HORVÁTH .....	25-29
<b>Effects of Washing of Raw Material on Properties of Carbon Nanotube Containing Poly(Ethylene-Terephthalate) Composites</b> TÍMEA MOLNÁR, CSILLA VARGA, LÁSZLÓ BARTHA .....	31-37
<b>Investigation the Properties of Y-Ba-Cu-Oxide Superconductors Prepared by Hydraulic Pressing and Moulding</b> ANNA MALOVECZKY, MARGIT ENISZ-BÓDOGH, TAMÁS KULCSÁR .....	39-42
<b>Effects of Ultrasonic Disintegration, Hot-Compressed Liquid Water Pre-treatment and Steam Explosion on Solvolysis and Digestibility of Grain Sorghum Stover</b> DÁNIEL CAPÁRI, ANDRÁS DALLOS .....	43-50
<b>Development of a Reaction Structure Identification Tool</b> JÁNOS KONTOS, LÁSZLÓ RICHÁRD TÓTH, TAMÁS VARGA .....	51-56

## EDITORIAL PREFACE

*Systems and control theory* is a constantly evolving scientific area and the dominant driving force in key industries and engineering fields e.g. process engineering, automotive engineering, bioengineering, and the energy industry. The aim of the current issue (Volume 42, Number 2) is to provide an overview of research topics pursued by selected PhD students.

The papers presented here were selected from contributions at the 13<sup>th</sup> International PhD Workshop on Systems and Control Conference held on August 25, 2014 ([virt.uni-pannon.hu/phdws2014](http://virt.uni-pannon.hu/phdws2014)). The objective of the conference was to establish an international forum for young researchers. The meeting provided opportunities for the participants to present and discuss the latest results and up-to-date applications in systems and control.

This issue represents the entire spectrum of systems and control engineering as follows:

- process modelling and analysis
- control (traditional, intelligent, adaptive, etc.)
- process monitoring and supervision
- system identification and signal processing
- bioengineering
- traffic control
- reaction kinetic networks
- modelling of complex systems (classical, hierarchical, Bayesian, fuzzy, networks)
- image processing and pattern recognition
- artificial intelligence
- soft computing (neural, genetic, fuzzy algorithms, etc.)
- software (parallel computing, distributed and network computing, data visualization)
- decision making (decision support, data mining)
- applications of systems and control theory

The organizers are grateful for the contributions of the authors.

The tradition of the International PhD Workshop continues.

You are invited to participate at the 14<sup>th</sup> International PhD Workshop in Veszprém in 2015!

ATTILA MAGYAR

University of Pannonia, Veszprém, HUNGARY

Guest Editor

**Table of Contents**

<b>A Comparison of Advanced Non-Linear State Estimation Techniques for Ground Vehicles</b> GYÖRGY MAX, BÉLA LANTOS .....	57-64
<b>Telemedical Heart Rate Measurement for Lifestyle Counselling</b> MARIO SALAI, GERGELY TUBOLY, ISTVÁN VASSÁNYI, ISTVÁN KÓSA .....	65-70
<b>The Application of Unknown Input Estimators to Damp Load Oscillations of Overhead Cranes</b> BÁLINT PATARTICS, BÁLINT KISS .....	71-77
<b>Challenges of Enterprise Policy Compliance with Smartphone Enablement or an Alternative Solution Based on Behaviour-Based User Identification</b> SÁNDOR DOBOS, ATTILA KOVÁCS .....	79-84
<b>Measurement-Based Modelling and Simulation of a Hydrogen-Generating Dry Cell for Complex Domestic Renewable Energy Systems</b> ATTILA GÖLLEI, PÉTER GÖRBE, ATTILA MAGYAR, LÁSZLÓ NEUKIRCHNER .....	85-89
<b>Quasi-Polynomial Representation-Based Control of Mechanical Systems</b> LÁSZLÓ NEUKIRCHNER, ATTILA MAGYAR .....	91-95
<b>A Network Model for Simulating the Dynamic Behaviour of an Energy Distribution Network</b> LEVENTE BÁLINT, TIBOR DULAI, ÁGNES STARK-WERNER, GERGELY APOSTOL, ÁDÁM TOMPOS .....	97-101
<b>On the Parametric Uncertainty of Weakly Reversible Realizations of Kinetic Systems</b> GYÖRGY LIPTÁK, GÁBOR SZEDERKÉNYI, KATALIN M. HANGOS .....	103-107
<b>Stability and Parameter Sensitivity Analyses of an Induction Motor</b> ATTILA FODOR, ROLAND BÁLINT, ATTILA MAGYAR, GÁBOR SZEDERKÉNYI .....	109-113

## COMPARATIVE ASSESSMENT OF THE MUSSEL MICRONUCLEUS TEST VERSUS BACTERIAL BIOASSAYS FOR GENOTOXICITY TESTING OF BENZO[A]PYRENE

BETTINA ECK-VARANKA,<sup>✉</sup> ESZTER HORVÁTH,<sup>1</sup> ÁRPÁD FERINCZ,<sup>1</sup> GÁBOR PAULOVITS,<sup>2</sup> AND NÓRA KOVÁTS<sup>1</sup>

<sup>1</sup> Department of Limnology, University of Pannonia, Egyetem str. 10, Veszprém, H-8200, HUNGARY

<sup>2</sup> Centre for Ecological Research, Hungarian Academy of Sciences, Balaton Limnological Institute,  
Klebelsberg K. str. 3., Tihany, H-8237, HUNGARY

<sup>✉</sup>E-mail: kovats@almos.vein.hu

Polycyclic aromatic hydrocarbons are hazardous compounds to the environment and human health, thus their detection is an important task. In this study the genotoxic effect of benzo[a]pyrene (B[a]P) was examined on a freshwater mussel *Unio pictorum* and results were compared to bacterial tests, such as the Ames test and SOS chromotest. The aim of the study was to calibrate the sensitivity of the mussel micronucleus test to that of the two bacterial tests using B[a]P as a reference chemical. The Ames and the micronucleus tests gave similar response both in sensitivity and in concentration-response pattern. These two tests are proposed to be applied in a battery for genotoxicity testing.

**Keywords:** micronucleus test, Ames fluctuation test, SOS chromotest, PAH

### Introduction

Polycyclic aromatic hydrocarbons (PAHs) are ubiquitous widespread contaminants. The US Environmental Protection Agency (EPA) created a list of priority pollutants that have the greatest concern due to potential exposure and adverse health effects on humans. There are 16 PAHs on this list, of which the most hazardous are acenaphthene, fluoranthene, naphthalene, benzo[a]anthracene and benzo[a]pyrene [1]. These compounds have proven to have carcinogenic and mutagenic effects on animals and humans, hence their regulation is very important [2].

Major sources of PAHs are internal combustion engines, residential heating, incineration, and coke production. There are also natural sources, such as forest fires or volcanoes. PAHs are present in the atmosphere as gas and/or particulate phases and might be transported to other environmental compartments such as soil, sediment, and water *via* dry or wet deposition. Heavier PAHs, such as benzo[a]pyrene (B[a]P), are almost totally adsorbed onto particles. Their further environmental fate in solid compartments is mostly influenced by their low water solubility. However, once taken up by the organism, the detoxification mechanism converts these compounds into more soluble molecules. It was shown that the seawater bivalve, *Mytilus sp.* can activate B[a]P to mutagenic compounds and produce reactive oxygen species (ROS) [3]. For assessing environmental exposure, benzo[a]pyrene seems to be a good indicator,

due to the strong correlation between B[a]P and other PAHs [4]. In IARC Monograph Volume 3 it was concluded that benzo[a]pyrene produced tumours in a wide range of animals tested, following exposure by many different routes (oral, dermal, inhalation, intratracheal, intrabronchial, subcutaneous, intraperitoneal, intravenous). It had both a local and a systemic carcinogenic effect [5].

There are various reasons why the genotoxicity of PAHs as well as of other mutagenic compounds is tested on mussels. First of all, bivalves are sedentary creatures, being exposed to both water and sediment contamination. Secondly, their ability to bioaccumulate contaminants is well known and widely used in biomonitoring studies. Actually, the fact that they can not only bioaccumulate waterborne mutagens, but also metabolise them into active forms, on one hand increase their usefulness in these studies but on the other hand may enhance the potential risk to consumers [6].

Of genotoxicity markers, the micronucleus test (MN) is the most widely established, relatively easy-to-perform test. Micronuclei formation indicates chromosomal DNA damage occurring as a result of either chromosome breakage or chromosome mis-segregation during mitosis [7].

BANNI *et al.* used digestive gland cells of the marine mussel *Mytilus galloprovincialis* in an acute test. In this assay, mussels were exposed to 75 nM B[a]P for different exposure time. Micronucleus frequency started to show significant response after 24 hours exposure, reaching the maximum after 72 hours [8]. WOZNICKI *et al.* also tested B[a]P genotoxicity using the MN test, but

on another species, the freshwater *Sinanodonta woodiana* (referred to *Anodonta woodiana* in the original article) [9] in which the time-dependency of ecological effect was demonstrated. Maximum micronucleus formation was experienced after 4 days of exposure, but after it started to decrease, most possibly due to adaptive mechanisms.

The mussel micronucleus (MN) test has also been used in real-world environments, especially for detecting contamination from oil spills. BOLOGNESI *et al.* demonstrated that even 10 years after the wreck of the tanker Haven at the Ligurian coast of Italy, micronucleus frequency in caged oysters was a reliable way to detect the release of genotoxic compounds [10]. MARTINS *et al.* assessed genotoxicity of sediment containing PAHs and metals after dredging operations. The sediment previously was classified as 'trace contaminated', but dredging modified the mobility of pollutants, which was clearly visible in the mussel MN test [11]. In addition to the MN test for eukaryotic organisms, which results in chromosomal damage, several bacterial tests are also available for screening purposes due to their rapid response and short exposure time.

The SOS chromotest is a short-term, enzymatic colorimetric assay for the detection of the presence of genotoxic compounds using *Escherichia coli* PQ 37 strain as described by QUILLARDET *et al.* [12]. The SOS system is a complex, DNA-damage activated response under the regulation of the SOS promoter. In *E. coli* PQ 37 the only functioning  $\beta$ -galactosidase gene (*lacZ*) is fused to the bacterial *sfiA* SOS operon. Thus, SOS response initiates *lacZ* transcription, and  $\beta$ -galactosidase activity is detected spectrophotometrically by the addition of X-gal (5-bromo-4-chloro-3-indolyl- $\beta$ -D-galactopyranoside) [13, 14].

The Ames bacterial reverse mutation assay applies genetically engineered strains of *Salmonella typhimurium*. The method is based on the chemical triggered reversion of histidine producing ability of the strains, enabling them to grow on histidine free medium. Several different methods have been developed, including the plate incorporation assay, the pre-incubation method, and the fluctuation test [15–17].

The Ames fluctuation test is a microplate adapted version of the Salmonella reverse mutation assay with a pH change indicated colorimetric endpoint. This method is suitable for the screening of large numbers of samples, and because of its sensitivity it is ideal for water sample testing [18].

The ability of both the SOS chromotest and the Ames test to detect genotoxicity of B[a]P has been long established [19, 20]. B[a]P was also used as a reference chemical for calibrating the newt micronucleus test or Jaylet test [21].

The correlation between the genotoxic substances and the number of micronuclei in an organism has been used in water toxicological tests since the 1980's [22]. The micronuclei are small bodies containing DNA parts that appear near the nucleus as a result of chromosome breakage or mitotic spindle dysfunction. This process can occur without external factors as well, but the effect

of genotoxic substances made a far greater number of micronuclei than normal. Therefore the micronuclei frequency may characterise the extent of genetic damage that accumulate over the life of the individual [23]. The MN test, performed on freshwater mussel species, is widely distributed for assessing genotoxic effects triggered by environmental pollutants [24, 25].

Still, the micronucleus test has gained relatively low attention in Hungary, therefore a native freshwater mussel, *Unio pictorum* was introduced as test organism. Main aim of the study was to calibrate this test also using B[a]P as reference chemical, by comparing its sensitivity to that of the bacterial assays.

## Materials and Methods

### *Test organisms*

*Unio pictorum* specimens were collected from Lake Balaton and were kept in a flow-through aquarium. Water source was Lake Balaton water, therefore not only proper oxygenation was ensured, but a constant food supply as well. Animals were acclimatized for 4 weeks prior to testing.

### *Test conditions and treatment*

The assay was performed based on the protocol described by WOZNICZKI *et al.* with some modifications. A B[a]P stock solution was prepared in acetonitrile in 1 mg cm<sup>-3</sup> concentration for the following series: 70  $\mu\text{g dm}^{-3}$ , 175  $\mu\text{g dm}^{-3}$ , 350  $\mu\text{g dm}^{-3}$  and 700  $\mu\text{g dm}^{-3}$ . For solvent control 0.07% acetonitrile was used, and solvent quantity was adjusted to 0.07% in each treatment. *U. pictorum* specimens with length of 5–8 cm were used. Treatments were performed in triplicates. For each concentration and for the controls, the volumes of the aquaria were 3 l. They were aerated during the experiment and temperature was set at 22 °C. Exposure time was 4 days.

### *Micronucleus test*

After 4 days, haemolymph was taken from the posterior adductor using the non-lethal technique described by GUSTAFSON *et al.* [26]. A 1 ml aliquot of haemolymph was mixed with 0.3 ml, 10% acetic acid in methanol as a fixative and centrifuged at 1000 rpm for 5 minutes. The supernatant was discarded and the rest was fixed in 1 ml 80 % ethanol. In this way the sample can be kept refrigerated for several weeks. For processing the samples, refrigerated samples were centrifuged again at 1000 rpm for 5 minutes. The supernatant was discarded and the pellet containing the cells was smeared onto a microscope slide and allowed to dry. After that the slides were fixed in 80 % methanol, dried and stained with 5 % Giemsa in distilled water for 20 minutes.

Photos were taken by a Zeiss AxioScope A1 microscope with an AxioCam ICC1 camera and Zen 2011 program at 400x magnification. Micronuclei were

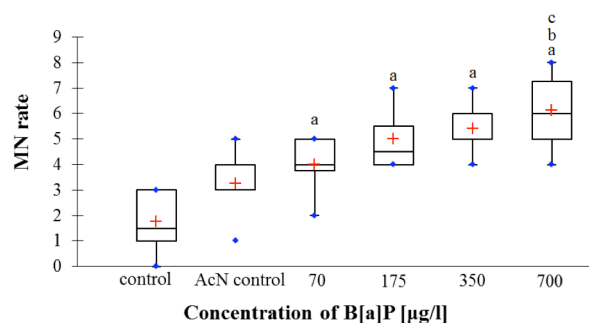


Figure 1: Result of the MN test with B[a]P showing significant difference compared to control (a), to AcN control (b) and to 70  $\mu\text{g dm}^{-3}$  B[a]P (c)

identified according to FENECH [27]. For each animal 250 cells were counted. One-way ANOVA with Tukey post hoc test was used to compare the mean MN numbers between the treatments.

For SOS chromotest the SOS chromotest TM kit (EBPI – Environmental Bio-detection Products Inc.) was used according to the manufacturer's instructions, and in compliance with the OECD guidelines No 471:1977 [28]. B[a]P concentrations were 1400  $\mu\text{g dm}^{-3}$ , 700  $\mu\text{g dm}^{-3}$ , 350  $\mu\text{g dm}^{-3}$ , 175  $\mu\text{g dm}^{-3}$ , 87.5  $\mu\text{g dm}^{-3}$ , 43.75  $\mu\text{g dm}^{-3}$ , 21.88  $\mu\text{g dm}^{-3}$ , 10.9  $\mu\text{g dm}^{-3}$ , 0  $\mu\text{g dm}^{-3}$ . Acetonitrile concentration was adjusted to 0.07% in each sample, and an additional DMSO solvent control was also used. The absorbance of samples was detected on 615 and 405 nm with DiareaderELx800 ELISA device. The SOS repair system induction was measured by the calculation of induction factor (IF) and induction potential (SOSIP) according to KRIFATON [29]. Samples with 1.5 or higher IF were considered genotoxic.

#### Ames test

The fluctuation Ames test was performed according to HUBBARD with slight modification. In short, *Salmonella typhimurium* TA100 cells were pre-cultured overnight in nutrient broth (Oxoid) on 37 °C. Cells were washed twice in Davis minimal medium (67.4 mM  $\text{PO}_4^{3-}$ , 8.38 mM  $\text{SO}_4^{2-}$ , 15.1 mM  $\text{NH}_4^+$ , 5.1 mM  $\text{Na}^+$ , 98.1 mM  $\text{K}^+$ , 0.83 mM  $\text{Mg}^{2+}$ , 1.7 mM citrate, 139  $\mu\text{M}$  glucose 10  $\mu\text{g cm}^{-3}$  histidine, 0.1 mg  $\text{cm}^{-3}$  D-biotin) and cell number was adjusted to  $10^6$  cells  $\text{cm}^{-3}$ . B[a]P was added to the samples in 700  $\mu\text{g dm}^{-3}$ , 350  $\mu\text{g dm}^{-3}$ , 175  $\mu\text{g dm}^{-3}$ , 70  $\mu\text{g dm}^{-3}$  and 0  $\mu\text{g dm}^{-3}$  and acetonitrile concentration was adjusted to 0.07%. Samples were distributed in 200  $\mu\text{l}$  volumes to 96 well microplates. Cell free control, a solvent free negative control, and a positive control with 0.5  $\mu\text{g cm}^{-3}$  concentration  $\text{NaN}_3$  were also applied. Plates were incubated in humid chamber for 72 hours in 37 °C. On the day of evaluation 20  $\mu\text{l}$  of 2 mg  $\text{cm}^{-3}$  aqueous solution of bromocresolpurple was added to each sample. Purple colour signified negative, yellow positive (cell growth) result. Intermediate shades were regarded positive. The experiment was also performed with S9 activation, in which case 10 ml suspension contained 2.5 ml S9 mix (EBPI) assembled according to the producer's guide (S9 activation

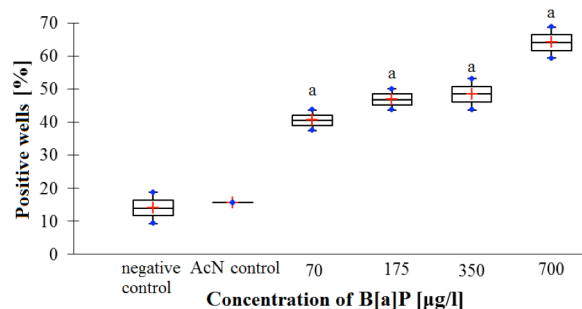


Figure 2: Result of the S9 supplemented fluctuation Ames test with B[a]P (significant difference compared to control (a))

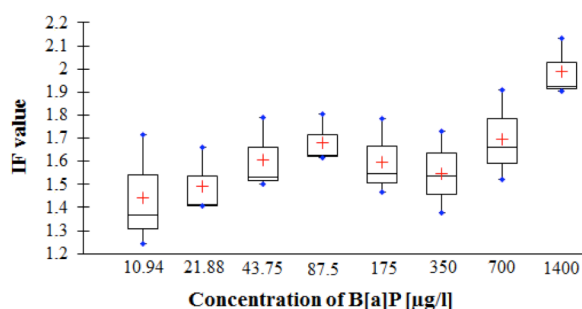


Figure 3: Result of the S9 supplemented SOS chromotest with B[a]P

simulates metabolic processes in the liver of higher organisms). For positive control 2-amino-antracene was used in 100  $\mu\text{g cm}^{-3}$  concentration. For the evaluation of mutagenic effect the  $\chi^2$ -test was applied with 95% confidence level [30].

## Results and Discussions

Genotoxic response is expressed as number of micronuclei/250 cells in case of the mussel micronucleus test, percentage of positive wells in case of the Ames test and IF value in case of the SOS chromotest. Significant difference between the control and all treatments was observed in case of micronucleus numbers (ANOVA:  $F = 12.015$ ;  $df = 5$ ;  $P < 0.00001$ , Tukey post hoc:  $P < 0.002$ ); however, only the highest concentration treatment differed from the AcN-control (Tukey post hoc  $P = 0.02$ ). The difference between the lowest (70  $\mu\text{g dm}^{-3}$ ) and highest (700  $\mu\text{g dm}^{-3}$ ) concentrations was also indicated (Fig. 1).

$\chi^2$ -square tests indicated significant differences between the control and all treatments in case of ratios of Ames fluctuations test ( $P < 0.0017$ ) (Fig. 2). The results of SOS chromotest are shown in Fig. 3.

To date no assessment has been published for comparing the sensitivity of the mussel micronucleus test and bacterial genotoxicity assays. There are a few comparative works; however, those are based on amphibian micronucleus tests. One protocol uses *Xenopus laevis* embryos and the end-point of the test is number of micronucleated erythrocytes per thousand. The test is standardised, international and some national

test protocols apply, e.g. the AFNOR NFT 90-325 procedure [31]. MOUCHET *et al.* tested genotoxicity of PAH-contaminated soil leachates on the amphibian MN test and two bacterial tests (Ames and Mutatox) [30]. The latter test developed by the Microbics Company (now Azur Environmental) uses dark mutants of the luminescent bacterium *Vibrio fischeri*. In the presence of mutagenic compounds, these mutants can revert and recover their luminescence, which is easily measurable by a luminometer. It was found that the MN test was able to detect genotoxicity, while the Ames test was not. Sensitivity of the Mutatox test was intermediate. It should be noted that chemical analysis of both soil and leachate samples revealed much lower individual PAH concentration in leachates than in the soil samples.

LE CURIEUX *et al.* used the SOS chromotest, the Ames fluctuation test and another amphibian, the newt *Pleurodeles waltl* for a comparative assessment of 7 chemicals, including B[a]P. In their study, the newt micronucleus test was the most sensitive, the fluctuation test and the SOS chromotest gave practically similar but lower response [33].

In our study all three tests gave positive response, but analysis of the concentration-response graphs shows somewhat different patterns. Bacterial tests gave positive response only with S9 activation. Ideal concentration-response graphs were found for the MN test and the S9 supplemented Ames test. Ideal concentration-response curve is observed when the response steadily increases for each higher effluent concentration [34]. Main difference is the response given in the AcN control, which elucidated micronucleus formation but the Ames test gave practically the same response for both controls. Notably, WOZNICZKI *et al.* did not find concentration-response relationship when tested B[a]P on *Sinanodonta woodiana*.

In the SOS chromotest after S9 activation, positive response was given for the lowest concentration, but no clear concentration-response relationship could be established. In general, sensitivity of the SOS chromotest is considered lower than that of the Ames test. For example, there are mutagenic compounds that do not induce the SOS response, such as benzidine, cyclophosphamide, acridines, and ethidiumbromide [13].

### Conclusions

The very similar response of the Ames test and the micronucleus test (considering both sensitivity and concentration-response pattern) indicate that B[a]P elucidates both chromosomal aberrations and point mutation, and is genotoxic for prokaryotes and eukaryotes as well; however, this is not necessarily the case for all potentially genotoxic chemicals. As such, for testing genotoxicity of either individual compounds or environmental samples, application of both tests can be advised, defining the minimum necessary battery as the MN and Ames tests.

### Acknowledgements

This work was supported by the TÁMOP-4.2.2.A-11/1/KONV-2012-0064 research program. This project is supported by the European Union and co-financed by the European Social Fund.

### REFERENCES

- [1] USEPA: Priority Pollutants List (Appendix A to 40 CFR Part 423). U.S. Environmental Protection Agency, Office of Water, 2000
- [2] GASPARI L., CHANG S.S., SANTELLA R.M., GARTE S., PEDOTTI P., TAIOLI E.: Polycyclic aromatic hydrocarbon-DNA adducts in human sperm as marker of DNA damage and infertility, *Mutation Res.*, 2003, 535, 155–160
- [3] LIVINGSTONE D.R., GARCIA MARTINEZ P., MICHEL X., NARBONNE J.F., O'HARA S., RIBERA D., WINSTONE G.W.: Oxyl radical generation as a pollution-mediated mechanism of toxicity in the common mussels, *Mytilus edulis L.*, and other mollusks, *Func. Ecol.*, 1990, 4, 415–424
- [4] RUBAILO I., OBERENKO A.V.: Polycyclic Aromatic Hydrocarbons as Priority Pollutants, *J. Siberian Fed. Uni. – Chem.* 2008, 4(1), 344–354
- [5] IARC: Certain polycyclic aromatic hydrocarbons and heterocyclic compounds. IARC Monographs of the Evaluation of the Carcinogenic Risk of Chemicals to Humans, 1973, 3, 1–271
- [6] FERGUSON L.R., GREGORY T.J., PEARSON A.E., HAY J.E., LEWIS G.D.: Mutagenicity tests as a monitoring tool for potential mutagens and carcinogens in shellfish gathering areas of New Zealand, *New Zealand J. Marine Freshwater Res.*, 1996, 30(4), 413–421
- [7] BOLOGNESI C., FENECH M.: Mussel micronucleus cytome assay, *Nature Protocols*, 2012, 7(6), 1125–1137
- [8] BANNI M., NEGRI A., DAGNINO A., JEBALI J., AMEUR S., BOUSSETTA H.: Acute effects of benzo[a]pyrene on digestive gland enzymatic biomarkers and DNA damage on mussel *Mytilus galloprovincialis*, *Ecotoxicology Environ. Safety*, 2010, 73, 842–848
- [9] WOZNICZKI P., LEWANDOWSKA R., BRUZAN P., ZIOMEK E., BARDEGA R.: The level of DNA damage and the frequency of micronuclei in haemolymph of freshwater mussels *Anodonta woodiana* exposed to benzo[a]pyrene, *Acta Toxicologia*, 2004, 12(1), 41–45
- [10] BOLOGNESI C., PERRONE E., ROGGIERI P., SCIUTTO A.: Bioindicators in monitoring long term genotoxic impact of oil spill: Haven case study, *Marine Environ. Res.*, 2006, 62, 287–291
- [11] MARTINS M., COSTA P.M., RAIMUNDO J., VALE C., FERREIRA A.M., COSTA M.H.: Impact of remobilized contaminants in *Mytilus edulis* during dredging operations in a harbour area: Bioaccumulation and biomarker responses, *Ecotoxicology Environ. Safety*, 2012, 85, 96–103

- [12] QUILLARDET P., HOFNUNG M.: The SOS Chromotest, a colorimetric bacterial assay for genotoxins: procedures, *Mutation Res.*, 1985, 147, 65–78
- [13] QUILLARDET P., HOFNUNG M.: The SOS chromotest: A review, *Mutation Res.*, 1993, 297(3), 235–279
- [14] HOFNUNG M., QUILLARDET P., GOERLICH O., TOUATI E.: SOS chromotest and the use of bacteria for the detection and diagnosis of genotoxic agents, *Trends in Genetic Risk Assessment Academic Press, London*, 1989, pp. 125–136
- [15] AMES B.N., LEE F.D., DURSTON W.E.: An Improved Bacterial Test System for the Detection and Classification of Mutagens and Carcinogens, *PNAS USA*, 1973, 70(3), 782–786
- [16] MORTELMANS K., ZEIGER E.: The Ames Salmonella/microsome mutagenicity assay, *Mutation Res.*, 2000, 455(1–2), 29–60
- [17] JOMINI S., LABILLE J., BAUDA P., PAGNOUT C.: Modifications of the bacterial reverse mutation test reveals mutagenicity of TiO<sub>2</sub> nanoparticles and byproducts from a sunscreen TiO<sub>2</sub>-based nanocomposite, *Toxicology Lett.*, 2012, 215, 54–61
- [18] LE CURIEUX F., GILLER S., GAUTHIER L., ERB F., MARZIN D.: Study of the genotoxic activity of six halogenated acetonitriles, using the SOS chromotest, the Ames-fluctuation test and the newt micronucleus test, *Mutation Res.*, 1995, 341, 289–302
- [19] QUILLARDET P., DE BELLECOMBE C., HOFNUNG M.: The SOS Chromotest, a colorimetric bacterial assay for genotoxins: validation study with 83 compounds, *Mutation Res.*, 1985, 147, 79–95
- [20] BRAMS A., BUCHET J.P., CRUTZEN-FAYT M.C., DE MEESTER C., LAUWERYS R., LÉONARD A.: A comparative study, with 40 chemicals, of the efficiency of the Salmonella assay and the SOS Chromotest (kit procedure), *Toxicology Lett.*, 1987, 38, 123–133
- [21] ZOLL-MOREUX C.: Consequences of the contamination of the aquatic environment by mercury, benzo(a)pyrene, and organochlorine pesticides for two amphibians *Pleurodeles waltl* and *Xenopus laevis*, PhD Thesis, Paul Sabatier University Toulouse, 1991, Toulouse, 1991 (in French)
- [22] DAS R.K., NANDA N.K.: Induction of micronuclei in peripheral erythrocytes of fish *Heteropneustes fossilis* by mitomycin C and paper mill effluent, *Mutation Researches*, 1986, 175, 67–71
- [23] BOLOGNESI C., BUSCHINI A., BRANCHI E., CARBONI P., FURLINI M., MARTINO A., MONTEVERDE M., POLI P., ROSSI C.: Comet and micronucleus assays in zebra mussel cells for genotoxicity assessment of surface drinking water treated with three different disinfectants, *Sci Total Environ.*, 2004, 333(1–3), 127–136
- [24] SCARPATO R., MIGLIORE L., BARALE R.: The micronucleus assay in *Anodonta cygnea* for the detection of drinking water mutagenicity, *Mutation Res.*, 1990, 245, 231–237
- [25] DOPP E., BARKER C.M., SCHIFFMANN D., REINISCH C.L.: Detection of micronuclei in hemocytes of *Mya arenaria*: association with leukemia and induction with an alkylating agent, *Aquatic Toxicology*, 1996, 34, 31–45
- [26] GUSTAFSON L.L., STOSKOPF M.K., BOGAN A.E., SHOWERS W., KWAK T.J., HANLON S., LEVINE J.F.: Evaluation of a nonlethal technique for hemolymph collection in *Elliptio complanata*, a freshwater bivalve (Mollusca: Unionidae), *Diseases of Aquatic Organisms 2005*, 65, 159–165
- [27] FENECH M., NEVILLE S.: Conversion of excision-repairable DNA lesions to micronuclei within one cell cycle in human lymphocytes, *Environ. Mol. Mutagenesis*, 1992, 19(1), 27–36
- [28] OECD Guidelines No. 471: Bacterial Reverse Mutation Test, 1977
- [29] KRIFATON CS.: Development of biomonitoring systems for detecting aflatoxin-B1 and zearalenon. PhD Thesis, Szent István University, Gödöllő, 2012 (in Hungarian)
- [30] HUBBARD S.A., GREEN M.H.L., GATEHOUSE D., BRIDGES J.W.: The fluctuation test in bacteria, *Handbook of Mutagenicity Test Procedures*, 1984, pp. 141–160
- [31] Association française de normalisation (AFNOR) Standard NFT90-325. Water quality. Evaluation of genotoxicity using amphibian larvae (*Xenopus laevis*, *Pleurodeles waltl*), 2000 (in French)
- [32] MOUCHET F., GAUTHIER T.L., MAILHES C., JOURDAIN M.J., FERRIER V., TRIFFAULT G., DEVAUXE A.: Biomonitoring of the genotoxic potential of aqueous extracts of soils and bottom ash resulting from municipal solid waste incineration, using the comet and micronucleus tests on amphibian (*Xenopus laevis*) larvae and bacterial assays (Mutatox<sup>®</sup> and Ames tests), *Sci. Total Environ.*, 2006, 355, 232–246
- [33] LE CURIEUX F., MARZIN D., FRANÇOISE E.: Comparison of three short-term assays: results on seven chemicals. Potential contribution to the control of water genotoxicity, *Mutation Res.*, 1993, 319, 223–236
- [34] USEPA: Method Guidance and Recommendations for Whole Effluent Toxicity (WET) Testing (40 CFR Part 136). EPA 821-B-00-004, U.S. Environmental Protection Agency, Office of Water, 2000



HUNGARIAN JOURNAL OF INDUSTRY AND CHEMISTRY

HJIC

Advertise upcoming meetings,  
conferences and workshops;  
make public announcements;  
introduce your research laboratory;  
a new product or a service

on the pages of the

**Hungarian Journal of Industry and Chemistry**

Please contact us if interested!

---

EDITORIAL OFFICE: UNIVERSITY OF PANNONIA  
P.O. BOX 158, VESZPRÉM H-8201 (HUNGARY)  
Tel.: +36 (88) 624-746, E-mail: [hjic@almos.uni-pannon.hu](mailto:hjic@almos.uni-pannon.hu);  
web: [hjic.mk.uni-pannon.hu](http://hjic.mk.uni-pannon.hu)  
Felelős szerkesztő: Szilágyi Róbert, PhD  
Kiadja: Pannon Egyetem, 8200 Veszprém, Egyetem u. 10.  
Levélcím: H-8201 Veszprém, Postafiók 158, Tel.: (88) 624-000

## IMPROVING THE INTERFACIAL PROPERTIES OF GLASS FIBRE REINFORCED AND UNREINFORCED WASTE SOURCED LOW DENSITY POLYETHYLENE/ACRYLONITRILE BUTADIENE STYRENE/POLYSTYRENE COMPOSITES

JÁNOS SÓJA,<sup>1</sup> VLADIMIR SEDLARIK,<sup>2</sup> PAVEL KUCHARCZYK,<sup>2</sup> AND NORBERT MISKOLCZI<sup>1</sup>✉

<sup>1</sup> MOL Department of Hydrocarbon & Coal Processing, Institute of Chemical Engineering and Process Engineering,  
Faculty of Engineering, University of Pannonia, Egyetem u. 10, Veszprém, H-8200, HUNGARY

<sup>2</sup> Centre of Polymer Systems, University Institute, Tomas Bata University in Zlín, Nad Ovcimou 3685, Zlín, 76001,  
CZECH REPUBLIC

✉E-mail: mnorbert@almos.uni-pannon.hu

This work is focused on compatibilization of immiscible waste sourced low density polyethylene (LDPE), acrylonitrile butadiene styrene (ABS), and polystyrene (PS) blends by different surface modifying routes. To reach better mechanical properties of the given reused waste blends 20% glass fibre was used. The ratio of waste LDPE/ABS/PS was 3.6/2.0/1.0 both in the presence and absence of glass fibre, while the applied concentration of the surface modifying routes was 1% in each case. Blends of raw materials had been manufactured by two roll mill, and specimens were obtained by the press moulded plates. The properties of samples were studied by mechanical testing. Results show that blending of the three kinds of waste polymers without compatibilizers resulted immiscible blends with poor mechanical properties. This could be significantly improved by the application of the commercial and synthetic surface treatment additives. Generally, favourable properties were found in the presence of 20% glass fibre. Especially AD-1 and AD-2 experimental and commercial  $\gamma$ -aminopropylsilane additives showed the best results.

**Keywords:** immiscible, compatibilizer, waste mechanical recycling, tensile strength

### Introduction

Owing to the increasing application of polymers, the utilization of wastes plastics causes serious challenges. According to reports the energetic utilization of polymer wastes were mainly investigated, such as incineration, chemical recycling, and/or mechanical recycling [1–7]. It is also well known that the industrially used plastics are not exchangeable with other constructional materials (glass, metals, etc.). Excess energy use and/or more greenhouse gas emissions would be incurred upon replacement of plastics with other materials. Therefore most of the key industrial segments, such as transportation, aviation, packaging, civil engineering, cannot function without polymers. From the 50s' the plastic industry went through a significant development, which is a reason for their wide-spread and diverse applications often for highly specific purposes. In the case of plastic composites, they provide alternative solutions to problems of increasing strength, maintaining compatibility and malleability [2, 4, 6–14].

The mechanical recycling of polymers is a reshaping process using waste polymeric materials or even the mixtures of unused and waste polymers. Basically the

waste polymer can be originated from two sources. In “closed-loop” recycling, the same product is manufactured from the same recycled components. For instance, the material of bottles (in some cases) can be recycled. In contrast, there is a recycling route, when the repeated remanufactured products are becoming less valuable [10–12, 15, 16]. A major challenge in mechanical recycling of polymers is immiscibility that leads to phase separation causing significant reductions in mechanical properties of the polymer mixtures. There are specific kinds of polymers that are immiscible with each other, such as polyolefin-PA, polyolefin-ABS, polyolefin-PET. Therefore, polymer blends may contain two phases, such as disperse and continuous.

Generally, the difference in chemical and physical properties of phases are the source of the above mentioned immiscibility problem. Therefore, coupling agents with special chemical structure can be used to create adequate chemical/physical interaction between the constituents of polymer mixtures. For this purpose grafted-MA or silane based compounds are widely used. These compatibilizers are able to increase the interfacial tension in boundary layer of polymer blends, which results in better chemical/physical interactions [17, 18].

Table 1: The main properties of waste polymers

	LDPE	ABS	PS
tensile strength, MPa	15.8±1.4	34.4±2.5	25.6±1.9
tensile modulus, MPa	420±33	1750±88	1720±95
elongation, %	351.5±35.5	4.7±0.3	189.6±10.2
flexural strength, MPa	-	29.0±2.2	21.0±1.7
flexural modulus, MPa	-	1820±79	1140±73
CHARPY strength, kJ mm <sup>-2</sup>	3.8±0.4	10.5±1.1	5.9±0.4

Table 3: Sample compositions without glass fibre in weight %

Sample No.	1	2	3	4	5	6	7	8
LDPE	55	54	54	54	54	54	54	54
ABS	30	30	30	30	30	30	30	30
PS	15	15	15	15	15	15	15	15
C-1	-	1	-	-	-	-	-	-
C-2	-	-	1	-	-	-	-	-
AD-1	-	-	-	1	-	-	-	-
AD-2	-	-	-	-	1	-	-	-
AD-3	-	-	-	-	-	1	-	-
AD-4	-	-	-	-	-	-	1	-
Peroxide	-	-	-	-	-	-	-	1

In this work, the feasibility of mechanical recycling of automotive industry waste mixtures of low-density polyethylene (LDPE), acrylonitrile butadiene styrene (ABS), and polystyrene (PS) were studied. The effects of various compatibilization techniques on mechanical properties of the prepared ternary ABS/LSPE/PS systems were studied.

## Materials and Methods

### Raw Materials

Waste polymers used as raw materials in our experimental work were selectively collected directly from automotive industry. The main properties of the plastic wastes are summarized in Table 1. The LDPE has the lowest tensile strength (15.8 MPa), which is followed by the polystyrene (25.6 MPa), and the ABS (34.4 MPa). Tensile modulus showed similar order as well. Due to the chemical structure of plastics, the LDPE had the highest elongation (351.5%), while ABS the lowest (4.7%). The average particle size for each tested plastic wastes were in the range of 4–5 mm, with moisture content of 0.7–0.8 %. Moreover, significant differences were noticed in the CHARPY impact strength of samples; because the maximum value was measured in the case of ABS (10.5 kJ mm<sup>-2</sup>), while the smallest regarding LDPE (3.8 kJ mm<sup>-2</sup>).

Table 2: The main of experimental coupling agents

	AD-1	AD-2	AD-3	AD-4
appearance	solid	dense liquid	solid	solid
side chain	C <sub>16</sub> -C <sub>18</sub>	polyisobutylene	styrene	C <sub>20</sub> -C <sub>22</sub>

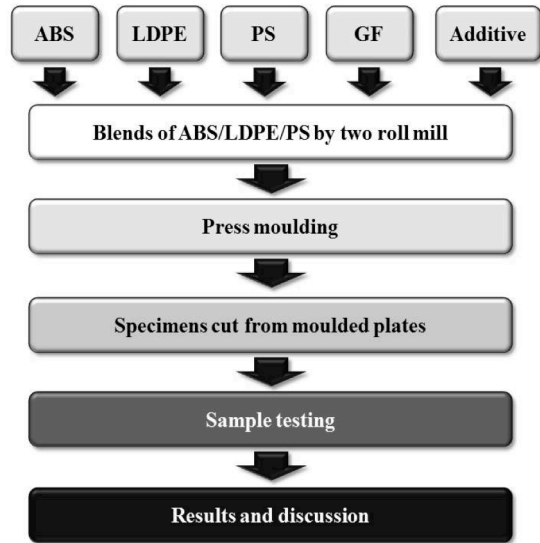


Figure 1: Sample preparation and testing

As known, blends of ABS and LDPE are immiscible phases in the most cases. Therefore, the mechanical properties of ABS and LDPE blend are significantly worse than that of the constituents, either ABS or LDPE. In order to enhance their properties, the interfacial forces must be improved between the constituents. In our work, different commercial and synthetic compatibilizers were used for improving the interfacial properties and decrease the interfacial tension of composites. Two commercially available compounds of  $\gamma$ -aminopropyl silane (C-1) (Aldrich Chemistry), and polyethylene grafted with maleic anhydride (C-2) (Viba Spa) were used as compatibilizer agents. The synthetic agents were maleic anhydride intermediates made from different olefins at the Department of MOL Hydrocarbon and Coal Processing, University of Pannonia with significantly different physical and chemical properties. The main properties of the four additives are summarized in Table 2.

### Sample Preparation

Blends of waste LDPE/ABS/PS were prepared by two roll mill. Then sample plates were manufactured by press moulding. Fig.1 demonstrates the flow of the experimental work.

For composite manufacturing a Labtech two roll mill (Labtech Ltd, Thailand) was used. The temperatures of the rolls were 170 °C and 190 °C with friction ratio of 0.5. The compositions of samples are summarized in Tables 3 and 4.

In selected cases E-type unsized glass fibre with 4–5 cm average length was also added to the composites in its 20%. The E-type GF was produced by Ovens

Table 4: Sample compositions with glass fibre in weight %

Sample No.	10	11	12	13	14	15	16
LDPE	43	43	43	43	43	43	43
ABS	24	24	24	24	24	24	24
PS	12	12	12	12	12	12	12
GF	20	20	20	20	20	20	20
C-1	1	-	-	-	-	-	-
C-2	-	1	-	-	-	-	-
AD-1	-	-	1	-	-	-	-
AD-2	-	-	-	1	-	-	-
AD-3	-	-	-	-	1	-	-
AD-4	-	-	-	-	-	1	-
Peroxide	-	-	-	-	-	-	1

Corning and it contained mainly SiO<sub>2</sub>, CaO and Al<sub>2</sub>O<sub>3</sub>. The ratio of waste LDPE/ABS/PS was 3.6/2/1 both in the presence and absence of glass fibre, while the applied concentration of the additives was 1% in each case. The additives were directly added to the molten polymer during the sample sheet manufacturing. In two cases organic peroxide (di-*tercier*-butyl-peroxide) was used to modify the interfacial surface of composites.

The sample blending composites were press moulded at 180 °C using 6.8 ton loading and then specimens with dimension of 1 mm x 10 mm x 100 mm were cut from the composite plates.

#### Determination of Tensile Strength

The tensile properties of the composites were determined by Instron 3345 universal tensile machine using 90 mm/min crosshead displacement rate. During the tests, the ambient temperature was 23 °C, and the relative humidity was 35 % in all cases. Preloading was not applied.

#### Determination of Flexural Strength

The three point flexural tests were performed by also the before mentioned Instron 3345 universal tensile tester. The crosshead displacement rate was 20 mm min<sup>-1</sup> in all cases.

#### Determination of Charpy Impact Properties

A CEAST Resil IMPACTOR was used for determination of Charpy impact strength. The machine was equipped with a 4J hammer, while the specimens were cut.

## Results and discussion

### Tensile properties

Fig.2 compares the tensile strength of samples. It can be seen that the tensile strength has changed in the range of

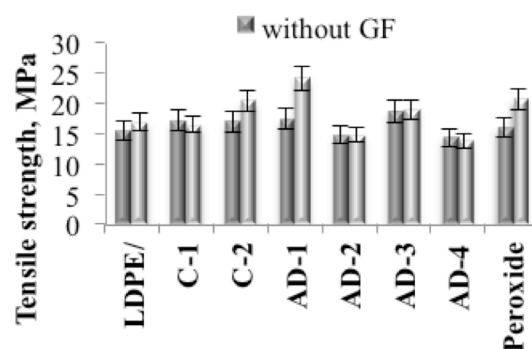


Figure 2: Tensile strength of samples 13.8 and 24.1 MPa. However, the reinforced composites

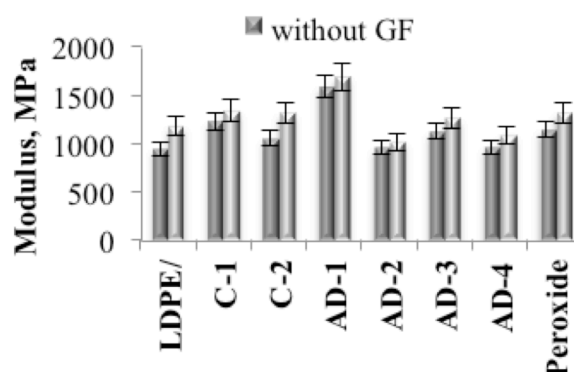


Figure 3: Tensile modulus of LDPE/ABS/PS samples

have significantly better resistance against constant tensile loading (13.8–24.1 MPa), than that of unreinforced (14.2–18.5 MPa). According to data the highest values were obtained in the case sample containing A-1 surface modifier agent in the presence of GF (24.1 MPa), while that was the highest in using AD-3 additive without GF (18.5 MPa).

From Table 1, the raw materials had 34.4 MPa (ABS), 25.6 MPa (PS) and 15.8 MPa (LDPE) tensile strength. On the contrary, the untreated LDPE/ABS/PS composites have tensile strength of 15.3 MPa without fibres, and 16.8 MPa in the presence of 20% glass fibre. It means that presumably owing to the immiscible phases the LDPE/ABS/PS composites without surface modifying additive has lower strength than its constituents. In three samples (C-1, AD-2, and AD-4) the tensile strength of glass fibre free, but treated composites was lower than that of untreated. This is probably due to the reason of the additive has been disadvantageously altered in surface characteristics of the plastic mixture. The largest increase in the tensile strength occurred for AD-1 (+12%) and AD-3 (+21%) additives without GF, while the peroxide (+23%), and AD-1 (43%) samples have resulted the best properties using 20% glass fibre, as well.

The Young's modulus, as the measure of the elastic property of sample, changed in the range between 1015 and 1685 MPa in the presence of glass fibre, while the values were between 937 and 1579 MPa without GF reinforcing (Fig.3). The maximum value of tensile modulus was found by the using AD-1 surface treating agent both presence and absence of GF (1579 MPa and

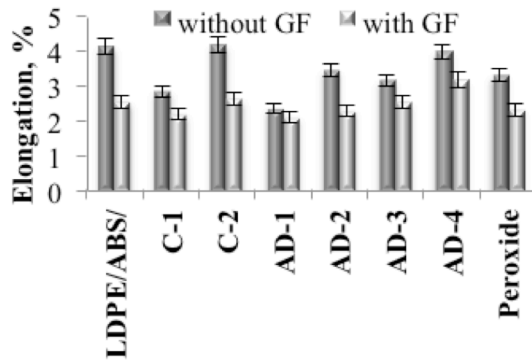


Figure 4: Elongation of samples measured at tensile test

1685 MPa). On the basis of data in Table 1, the tensile modulus of LDPE, ABS and PS raw materials were 420, 1750 and 1720 MPa, respectively. The untreated LDPE/ABS/PS samples had significantly lower tensile moduli with 937 MPa and 1173 MPa in the presence and absence of GF, respectively. Presumably it was the consequence of the phase separation occurring the immiscible polymers. The compatibility of immiscible polymer blends could be significantly improved by the above mentioned additives, because not only the tensile strength, but also the tensile modulus was significantly increased e.g. by the application of AD-1 additive (+44% with GF and +69% without GF). In general, the tensile modulus was higher in the presence of glass fibre than without that.

The relative elongation refers to the change in sample length during the tensile tests. Rigid materials (polyamide, ABS, etc.) have low value of elongation, while that of significantly higher in case of soft or rubber like elastic polymers (polyethylene, PP, PS, rubber, etc.).

The relative elongation (Fig.4) follows the opposite trends than tensile strength or modulus. It is changed in the range of 2.33 and 4.29% without GF, or 2.09 and 3.16% with GF. It means that the glass fibre presence resulted lower values of relative elongation. The surface treating agents have only slight effect to the elongation apart from AD-1 sample, because the difference between the treated and untreated samples was 63% in case of AD-1. In any other cases this value was less than 20%.

#### Flexural Properties

Results from flexural tests are summarized in Figs.5 and 6. The flexural strength was in the range of 17.3 and 22.6 MPa in case of GF reinforced LDPE/ABS/PS composites and between 13.7 and 19.9 MPa in case of unreinforced specimens. The best result was found when the interfacial surface of LDPE/ABS/PS composite and/or the glass fibre surface were modified by AD-3 additive (22.6 MPa). In the presence of AD-3 additive the unreinforced LDPE/ABS/PS blend had 19.9 MPa flexural strength value. Generally, the tensile properties were favourable in case of reinforced, than that of unreinforced samples. According to Table 1, the waste ABS and PS raw materials had flexural strength

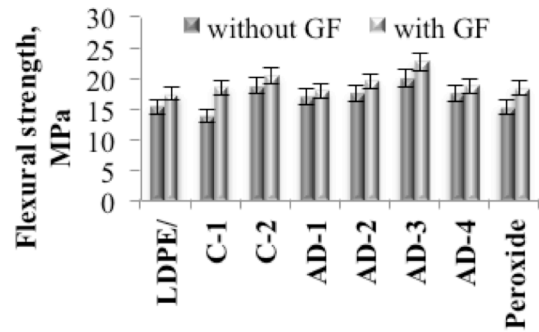


Figure 5: Flexural strength of LDPE/ABS/PS samples

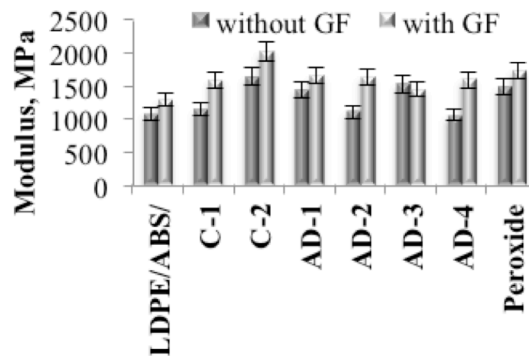


Figure 6: Flexural modulus of ABS/LDPE/PS samples

of 29.0 MPa and 21.0 MPa, respectively. On the other hand, the flexural strength of unreinforced LDPE/ABS/PS was 15.3 MPa, which can be increased to 17.3 MPa in the presence of GF. It means that the flexural strength was below the lowest value of constituent (PS, 21.0 MPa) even in the presence of GF. Comparing tensile and flexural strength, it can be concluded that the effect of the surface modifying agents were more significant to the tensile than to the flexural properties. The negative effect of surface modifying agents was observed in some cases. For instance, flexural strength was reduced in case of C-1 and peroxide additives. Regarding the flexural strength the largest increase occurred in the presence of AD-3 (+30%) and C-2 (+22%) additives without glass fibre reinforcements. The increasing in flexural strength was 30% (without GF) and 31% (with GF) in case of AD-3 additive, while that of was 22% (without GF) and 17% (with GF).

Regarding flexural modulus, similar results were obtained as discussed above. ABS and PS raw materials have 1820 and 1140 MPa flexural modulus, respectively. According to Fig.6, the flexural modulus was 1080 MPa and 1285 MPa in case of unreinforced and reinforced LDPE/ABS/PS composite without surface treating agents. The flexural modulus indicates the rigidity. Higher modulus means greater rigidity. Results demonstrate that the flexural modulus changes in the range 1285 and 2015 MPa in the presence of GF, whereas values were between 1040 and 1637 MPa in case of the non-reinforced composites. The maximum value of flexural modulus was given specimens

containing C-2 surface treating additives both with and without glass fibres.

### CHARPY Impact Strength

The CHARPY impact test determines the amount of energy absorbed by a material during fracture. Fig.7 summarizes the CHARPY impact strength of samples as a function of surface treatment additives. The impact strength of the samples ranged from 4.7 to 9.1 kJ mm<sup>-2</sup>, in which reinforced composite materials was between the higher range of 5.9 and 9.1 kJ mm<sup>-2</sup>. The highest value was in a sample including AD-1 surface modification agent, and glass fibre (9.1 kJ mm<sup>-2</sup>). In case of the same additive without reinforced fibre the impact strength was 7.1 kJ mm<sup>-2</sup>.

Results show that the impact strength could be increased in each case due to surface treatment. The impact strength of LDPE/ABS/PS composite was 4.7 kJ mm<sup>-2</sup> without reinforced and 6.8 kJ mm<sup>-2</sup> in reinforced by glass fibres. The largest growth was observed in the case of the sample containing C-2 (+53%) and AD-1 (+51%) additives for samples without glass fibres. Contrary, the least growth was observed in the case of the sample containing AD-2 (+4%) additives. Regarding the GF reinforced samples, the largest growth was observed when the AD-1 (+34%) and C-2 (+29%) additive were used. Only the AD-2 additive resulted in lower impact strength, than ABS/LDPE/PS excluding any additive (-13%).

### Conclusion

In this paper the efficiency of different compatibilizers in waste sourced LDPE/ABS/PS composite were investigated both in absence and presence of 20% E-type glass fibre. It was found that both the tensile and flexural properties of samples could be significantly improved by both synthetic and commercial coupling agent. The tensile strength and elastic modulus were the best when AD-1, a C<sub>16</sub>-C<sub>18</sub> olefin containing polyakanyl polymaleic anhydride compatibilizers and 20% GF were applied. Thus, compared to the LDPE/ABS/PS composite without glass fibre and surface modifying additives, the tensile strength showed 58 %, and the elastic modulus showed an 80 % increase. Regarding flexural properties similar result were observed, but not with AD-1, rather than AD-3, a polyakanyl polymaleic anhydride additive that resulted in the best properties, such as increase of 22.6 MPa in flexural strength. CHARPY impact strength increase was the largest (9.1 kJ mm<sup>-2</sup>) in a sample containing AD-1 agent in the presence of glass fibres, which converts to about 90% increase relative the LDPE/ABS/PS blend without GF and compatibilizing additives. Synergistic effect of glass fibres and some of the compatibilizers can lead to increase of CHARPY impact strength by 94% in comparison to unmodified LDPE/ABS/PS sample.

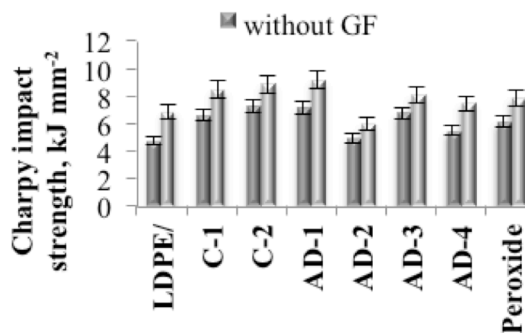


Figure 7: Charpy impact strength of LDPE/ABS/PS samples

### Acknowledgements

V.S. and P.K are thankful for support from the project of Operational Programme Research and Development for Innovations co-funded by the European Regional Development Fund (project CZ.1.05/2.1.00/03.0111).

### REFERENCES

- [1] LAI S.-M., LI H.-C., LIAO Y.-C.: Properties and preparation of compatibilized nylon 6 nanocomposites/ABS blends: Part II – Physical and thermal properties, *Eu. Polymer J.*, 2007, 43(5), 1660–1671
- [2] MAJUMDAR B., KESKKULA H., PAUL D.R.: Morphology of nylon 6/ABS blends compatibilized by a styrene/maleic anhydride copolymer, *Polymer*, 1994, 35(15), 3164–3172
- [3] HALE W., KESKKULA H., PAUL D.R.: Compatibilization of PBT/ABS blends by methyl methacrylate-glycidyl methacrylate-ethyl acrylate terpolymers, *Polymer*, 1999, 40(2), 365–377
- [4] KUDVA R.A., KESKKULA H., PAUL D.R.: Properties of compatibilized nylon 6/ABS blends: Part II. Effects of compatibilizer type and processing history, *Polymer*, 2000, 41(1), 239–258
- [5] HUSSEIN I.A., HAMEED T., SHARKH B.F.A., MEZGHANI K.: Miscibility of hexene-LLDPE and LDPE blends: influence of branch content and composition distribution, *Polymer*, 2003, 44(16), 4665–4672
- [6] ZAINAL Z., ISMAIL H.: The Effects of Short Glass Fibre (SGF) Loading and a Silane Coupling Agent on Properties of Polypropylene/Waste Tyre Dust/Short Glass Fibre (PP/WTD/SGF) Composites, *Polymer-Plastics Techn. Engng.*, 2011, 50(3), 297–305
- [7] LI Y., SHIMIZU H.: Improvement in toughness of poly(l-lactide) (PLLA) through reactive blending with acrylonitrile–butadiene–styrene copolymer (ABS): Morphology and properties, *Eu. Polymer J.*, 2009, 45(3), 738–746

- [8] LIM J.C., CHO K.Y., PARK J.-K.: Weld line characteristics of PC/ABS blend. II. Effect of reactive compatibilizer, *J Appl. Polymer Sci.*, 2008, 108(6), 3632–3643
- [9] SUN S., TAN Z., ZHOU C., ZHANG M., ZHANG H.: Effect of ABS grafting degree and compatibilization on the properties of PBT/ABS blends, *Polymer Composites*, 2007, 28(4), 484–492
- [10] SUPRI A.G., ISMAIL H.: Effect of Vinyl Alcohol-Phthalic Anhydride on Properties of Low Density Polyethylene (LDPE)/Tyre Dust (TD) Composites, 2012, 51(6), 549–555
- [11] SUPRI A.G., ISMAIL H.: The Effect of Isophorone Diisocyanate-Polyhydroxyl Groups Modified Water Hyacinth Fibers (*Eichhornia Crassiper*) on Properties of Low Density Polyethylene/Acrylonitrile Butadiene Styrene (LDPE/ABS) Composites, *Polymer-Plastics Techn. Engng.*, 2011, 50(2), 113–120
- [12] GHANI S.A., TAN S.J., YENG T.S.: Properties of Chicken Feather Fiber-Filled Low-Density Polyethylene Composites: The Effect of Polyethylene Grafted Maleic Anhydride, *Polymer-Plastics Techn. Engng.*, 2013, 52(5), 495–500
- [13] VILAPLANA F., KARLSSON S.: Quality Concepts for the Improved Use of Recycled Polymeric Materials: A Review, *Macromol. Mater. Engng.*, 2008, 293(4), 274–297
- [14] ZURALE M.M., BHADE S.J.: Properties of fillers and reinforcing fibers, *Mech. Composite Mater.*, 1998, 34(5), 463–472
- [15] PÉREZ R., ROJO E., FERNÁNDEZ M., LEAL V., LAFUENTE P., SANTAMARÍA A.: Basic and applied rheology of m-LLDPE/LDPE blends: Miscibility and processing features, *Polymer*, 2005, 46(19), 8045–8053
- [16] SHIEH Y.-T., LIU C.-M.: Silane grafting reactions of LDPE, HDPE, and LLDPE, *J. App. Polymer Sci.*, 1999, 74(14), 3404–3411
- [17] TRIACCA V.J., ZIAEE S., BARLOW J.W., KESKKULA H., PAUL D.R.: Reactive compatibilization of blends of nylon 6 and ABS materials, *Polymer*, 1991, 32(8), 1401–1413
- [18] ARAÚJO E.M., HAGE E. JR., CARVALHO A.J.F.: Thermal properties of nylon6/ABS polymer blends: Compatibilizer effect, *J. Mat. Sci.*, 2004, 39(4), 1173–1178

## APPLICATION OF ONLINE AND LABORATORY METHODS FOR THE INVESTIGATION OF SURFACE WATERS

JANKA BOBEK,<sup>1✉</sup> ZSÓFIA KOVÁCS,<sup>1</sup> AND ZOLTÁN ZSILÁK<sup>2</sup>

<sup>1</sup> Institute of Environmental Engineering, University of Pannonia, Egyetem Str. 10, Veszprém H-8200, HUNGARY

<sup>2</sup> Department of General and Inorganic Chemistry, University of Pannonia, Egyetem Str. 10, Veszprém H-8200, HUNGARY

✉E-mail: bobek.janka@gmail.com

Pollutions in surface waters run down quickly, so the pollution waves cannot be detected by traditional point sampling. Remote controlled online monitoring methods can make the tracking of pollutants possible. These solutions ensure that we can immediately access up-to-date information. The goal of our paper was to compare online monitoring and laboratory measurement techniques. During our work, we investigated the chemical and physical properties of the Séd creek in Veszprém with two different online monitoring systems. Furthermore, we made parallel laboratory measurements of samples taken weekly to evaluate the measurement results of online methods. We discuss the difficulties of installation and operation of online systems and problems arising during emergencies caused by weather.

**Keywords:** Séd creek, on-line monitoring systems, comparing measurement techniques

### Introduction

The 2000/60/EC EU Water Framework Directive (WFD) prescribes that by 2015 all surface water bodies have to reach a good ecological and chemical status. To ensure this, we need to have information about the status of water quality. A desirable feature would be the possibility of continuously track the status of our water bodies with a cost effective monitoring system.

The goal of our work was to introduce online monitoring systems and laboratory methods used to measure the physical-chemical parameters of the Séd creek in Veszprém. In order to continuously monitor water quality, two online monitoring systems were installed, which operate on different principles. The majority of our work was to test the Mobile Monitoring Station (No. 1), which was developed at the Environmental Engineering Institute of the University of Pannonia. In addition, we had the opportunity to follow up the operation of a more complex Mobile Monitoring Station (No. 2), which was manufactured by Combit IT Ltd. The two monitoring stations were placed strategically that the effect of the town of Veszprém on the stream could be measured. With the help of measurements made online and control measurements made in the laboratory, we mapped the loads effecting the Séd creek and to detect pollutant waves travelling down the stream.

### Materials and Methods

The investigated water body is the middle section of Séd creek. The water body belongs to the Danube catchment and in it to the Northern-Mezőföld and Eastern-Bakony subunit. The Séd originates in the Bakony, then flows through the city of Veszprém, and joins Nádor Canal at Ósi. The total length of Séd-Sárvíz-mill canal is 71.82 km. Point pollutions are caused on the territory by communal and industrial wastewater inlets. Intensive agriculture and husbandry are characteristic. Because of the side-point sources, we also have to focus on the investigation of diffuse pollutions [4].

#### *Description of Installed Online Monitoring Stations*

Two online water quality Mobile Monitoring Stations were installed on the middle section of Séd creek. The evaluated period of continuous measurement was between the August 4, 2013 and October 11, 2013. The two stations were different with respect of place of installation, power source, size, security, sampling, measured physical-chemical parameters, as summarized in *Table 1*. Mobile Monitoring Station 1 (*Fig.1*) was located at the section of Séd creek, where it enters Veszprém, while Mobile Monitoring Station 2 is at the exit point from the city (*Fig.1*).

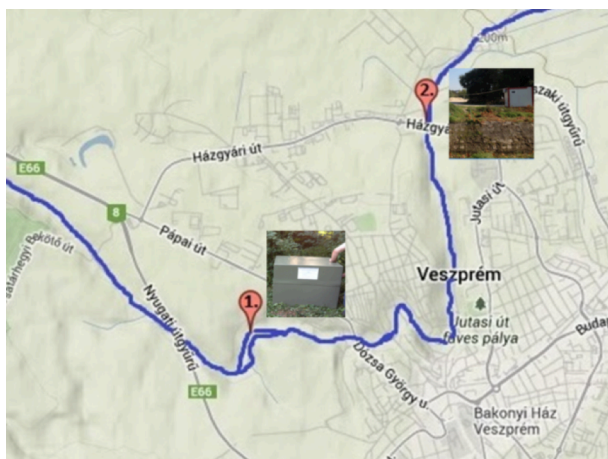


Figure 1: Location of installed Mobile Monitoring Stations

## Results and Discussion

### Online Measurements

During the period of August 4, 2013 and October 11, 2013, a tendency was observed for every measured parameter. In Fig.3, the pH measured at the examined section of Séd was between 7.3–8.0. The average value of conductivity is  $720 \mu\text{S cm}^{-1}$ , the value of turbidity is 30 NTU. Differences and jumps compared to the baseline indicate pollution, heavy rain or malfunction.

Owing to the placing of the Mobile Monitoring Stations changes could be detected in the pH values between the two sampling points. At Mobile Monitoring Station 1 pH value was in average 0.4–0.5 points higher (7.85) than at Mobile Monitoring Station 2 (7.45) (Fig.4). There are numerous karst water inflows into the Séd as it flows through the city, which causes the lowering of pH. Possible acidic pollutants from roadways, rainwater inlets and industrial areas can also add to the mild acidification of the water body.

In the case of measured ionic concentrations (Fig.5) it was observed that all components have a background

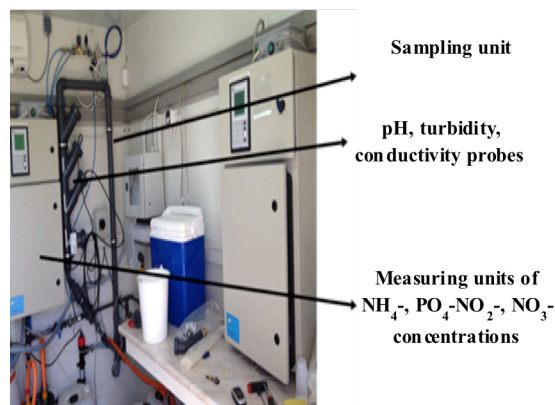
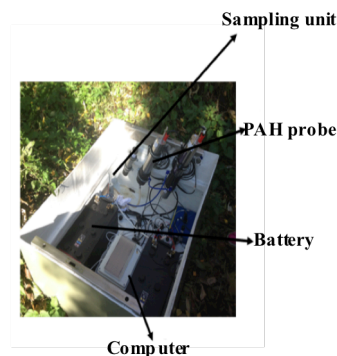


Figure 2: Structure of Mobile Monitoring Station 1 and 2

baseline with a well-defined average concentration. The differences from the baseline appear as peaks that can indicate pollutants or rainy weather. The baseline concentrations are 0.09, 0.03, 0.02, and  $4.5 \text{ mg dm}^{-3}$  for  $\text{PO}_4^{3-}\text{-P}$ ,  $\text{NH}_4^+\text{-N}$ ,  $\text{NO}_2^-\text{-N}$ , and  $\text{NO}_3^-\text{-N}$ , respectively from their average values.

When evaluating the timecourse of all chemical parameters, salient values can be identified and associated with some kind of an event. If we compare Figs.3 and 5 carefully, we can see that peaks appear at the same time for all components. During the evaluation of data, we identified pollutants, which were washed into the creek due to precipitation.

Table 1: Properties of Mobile Monitoring Stations

	Monitoring Station No.1	Monitoring Station No.2
location of installation	entry point into Veszprém in inner defense area of the waterworks	exit point from Veszprém on an industrial area
size	85×85×85 cm outer size monitoring station made of hardened plastic	2.4×2.4 m base area, 2.5 m height monitoring station
transportation	car	truck with crane
power source	2 pcs of 12 volt lead battery	line power (220V)
measured parameters	pH [11]	pH [12]
	turbidity [9]	turbidity [3]
	conductivity [8]	conductivity [2]
	water temperature [11]	$\text{NH}_4^+\text{-N}$ concentration [13]
	dissolved oxygen concentration [10]	$\text{PO}_4^{3-}\text{-P}$ concentration [16]
sampling	every 15 minutes weekly battery replacement cleaning of the probes	$\text{NO}_3^-\text{-N}$ concentration [14]
		$\text{NO}_2^-\text{-N}$ concentration [15]
maintenance		every hour
		changing reagents and blind reagent calibration (biweekly)
		supplying distilled water (biweekly) cleaning of sample dispenser vessel sampling tubes

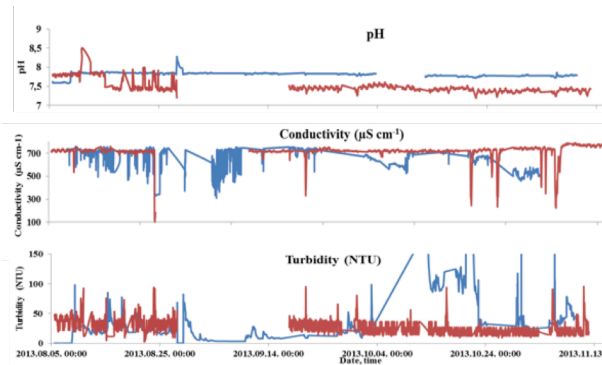


Figure 3: Results of physical parameters measured (blue: Station 1, red: Station 2)

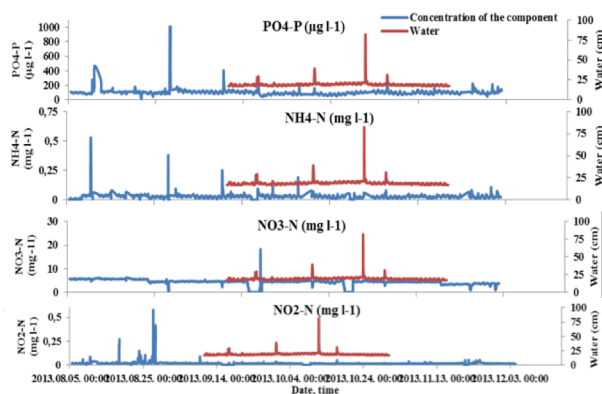


Figure 5: Change of concentration of measured ions

In addition, we detected pollution waves in two occasions. As can be expected, point sampling cannot give detailed information about the status of a water body. The advantage of online methods is clear due to their continuous monitoring, even if they are only operated for a short period of time. Thus, we will get a more holistic picture about the status of a water body toward implementing efficient measures for water quality protection.

#### Pollutant Leaching from Precipitation

To identify events, we used data from Measurement Station 2. In addition, water level data were downloaded from the water management web page of the Ministry of Interior, Hungary. The water level of Séd is at an average of 20 cm. From the time points in Figs. 3–5, we select an event occurred on September 30, 2013.

Around the time of the event, the water level started rising, the concentrations of physical-chemical parameters have also started to change. The pollutant downwash was detected between 04:00 and 06:00 according to the results; the concentration peak appeared at 05:00. Viewing physical parameters (Fig. 6) the value of turbidity has risen, and after reaching the positive peak (14.6 NTU) it started to decrease. Other physical parameters were seen as negative troughs. In the falloff phase all parameters moved back to the average value. Looking at the chemical components (Fig. 6) as an effect of the rising water level,  $\text{NH}_4^+\text{-N}$ ,  $\text{PO}_4^{3-}\text{-P}$  and  $\text{NO}_2^-\text{-N}$  concentrations have risen, while  $\text{NO}_3^-\text{-N}$  concentration appeared as a negative trough. Outstanding physical-chemical parameters (e.g.  $\text{PO}_4^{3-}\text{-P}$

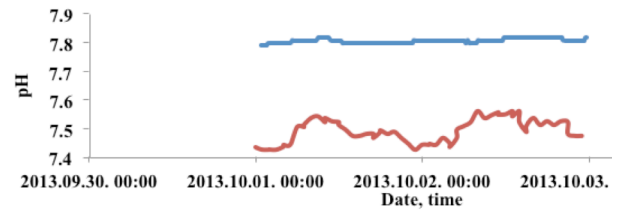


Figure 4: Variation of pH value as a result of discharge from the city (blue: Station 1, red: Station 2)

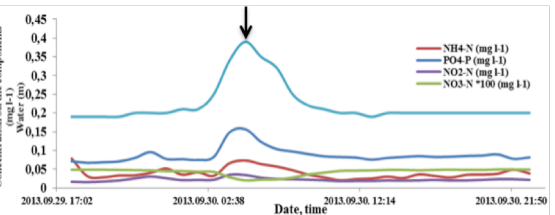
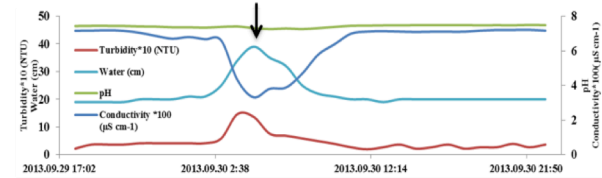


Figure 6: Effect of precipitation on the physico-chemical components

at  $0.15 \text{ mg dm}^{-3}$  level) measured as an effect of pollutants washed in during precipitation. Afterwards, the  $\text{PO}_4^{3-}\text{-P}$  level moved back to its near average range of  $50 \mu\text{g dm}^{-3}$ .

#### Detecting Pollutants

Pollutant waves were identified as events, when water level rise did not support the deviations of data points from their expected average values. Alternatively, as a result of precipitation, water level of Séd doubled relative to its average value without the presence of in pollutant waves.

As an example, we analyze here the effect of a pollution wave appeared on September 26, 2013. The pollution was detected between 17:00 and 19:00 with reaching its peak at 18:00. Looking at physical parameters (Fig. 7) turbidity values doubled relative to the average of 60 NTU. Conductivity decreased significantly from  $700 \mu\text{S cm}^{-1}$  to  $640 \mu\text{S cm}^{-1}$ . The pH decreased by 0.1 unit to 7.3. When we look at ion concentrations in Fig. 7,  $\text{NH}_4^+\text{-N}$  concentration rose fourfold compared to the baseline ( $0.19 \text{ mg dm}^{-3}$ ).  $\text{PO}_4^{3-}\text{-P}$  and  $\text{NO}_2^-\text{-N}$  concentrations also showed significant rise ( $30\text{--}180 \mu\text{g dm}^{-3}$ ).  $\text{NO}_3^-\text{-N}$  displayed a negative trough at  $40 \mu\text{g dm}^{-3}$ , but this component was the least sensitive to the change.

#### Measurement of Polyaromatic Hydrocarbons

Based on the data points taken every 15 minutes by the polyaromatic hydrocarbon (PAH) probe (TRIOS) at Measuring Station 1 (Fig. 8) a PAH pollutant wave was not detected during the investigated period. The baseline of PAH compounds was measured to be  $6\text{--}7 \mu\text{g dm}^{-3}$  and  $13\text{--}15 \mu\text{g dm}^{-3}$ . Values significantly differing from

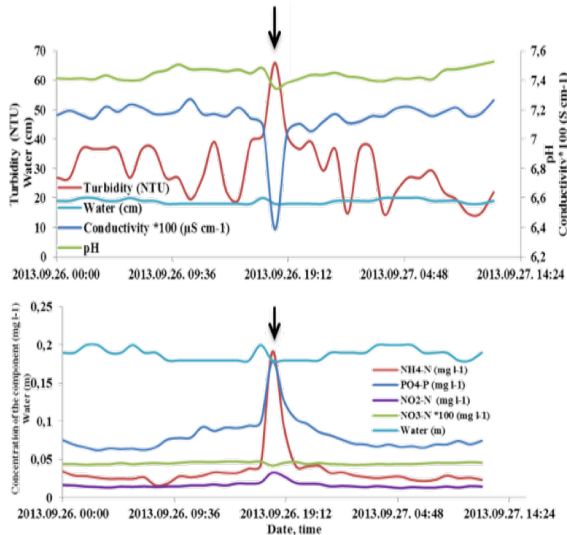


Figure 7: Effects of a pollutant wave on the physical-chemical parameters components

the baseline ( $35 \mu\text{g dm}^{-3}$ ) can be counted as measurement errors.

*Evaluation of Laboratory Measurement Results*

In the duration of the investigation, we have taken point samples at the two measurement sites 13 times. The samples were always taken according to standard MSZ ISO 5667-1:2007 [6] in the same time when the monitoring stations recorded data. The samples were transported in a cooler according to standard MSZ EN ISO 5667-3:2004 [7], and were analyzed on the day of sampling. Table 2 summarized the type of instruments used for measurements.

We compared the data obtained at Measurement Station 2 with the results of laboratory measurements (Fig.9). Correlation can be found for the outliers measured at the monitoring station ( $250 \mu\text{g dm}^{-3} \text{PO}_4^{3-}\text{-P}$ ) and in the laboratory ( $310 \mu\text{g dm}^{-3} \text{PO}_4^{3-}\text{-P}$ ). However, difference was found in the  $\text{NO}_3^{-}\text{-N}$  concentrations between the laboratory and measurement station results showing around half values for the laboratory measurements than those from the measurement stations. Based on these observations we proposed that the analyzer at the Mobile Monitoring Station measures higher concentration than the real concentration.

*The Effect of the City of Veszprém on Séd*

Using laboratory measurements, the effect of the city of Veszprém on the creek’s water quality was measured. The results obtained for averages of 13 samples are shown in Fig.10. It can be seen that there was no significant change in the concentration of  $\text{NH}_4^{+}\text{-N}$  ( $26.4\text{--}27.3 \text{ mg dm}^{-3}$ ) between the entry and exit points of the creek with respect of the city. Jumps in the concentration of  $\text{NH}_4^{+}\text{-N}$  are characteristic during pollutant waves and precipitation. Decrease in concentration of  $\text{PO}_4^{3-}\text{-P}$  is notable ( $131\text{--}100 \mu\text{g dm}^{-3}$ ) at the exit section. At the entry section, Séd flows near to agricultural areas, backyard gardens. We correlate the

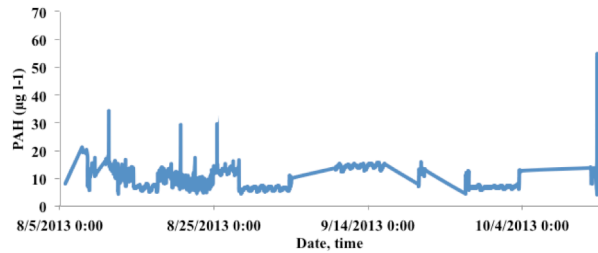


Figure 8: Change in PAH concentration in the investigated timeframe

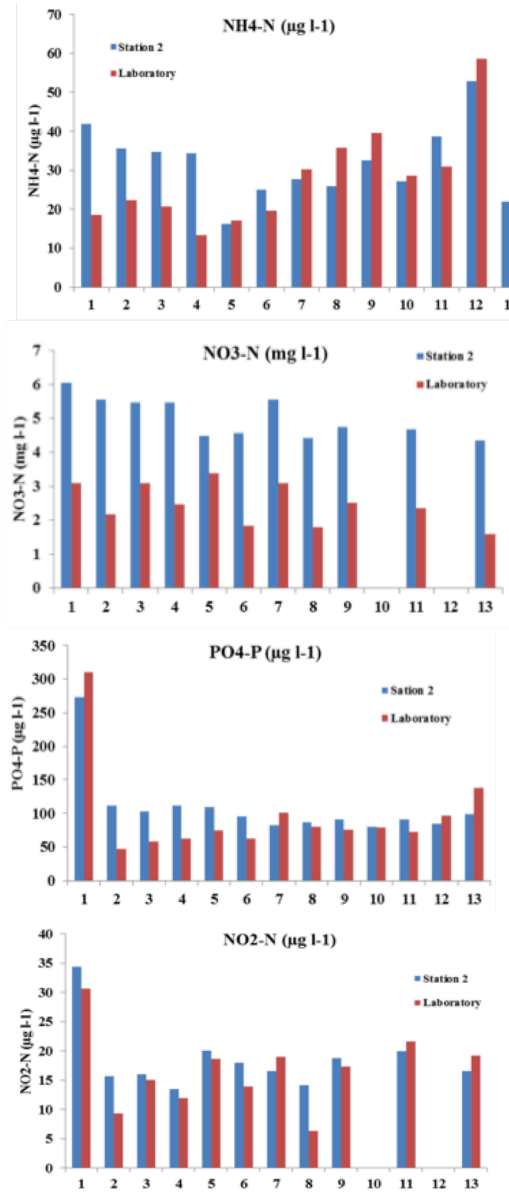


Figure 9: Comparing mobile Monitoring Station 2 and laboratory results

decrease of phosphate concentration within city limits with the presence of pure karst water inflows resulting in significant dilution effect.

In the case of  $\text{NO}_3^{-}\text{-N}$  and  $\text{NO}_2^{-}\text{-N}$  concentrations (Fig.10) an obvious increase can be seen ( $1.3\text{--}2.6 \text{ mg dm}^{-3}$ ;  $4.3\text{--}5.6 \text{ mg dm}^{-3}$ ), which is related to the high nitrate content of the incoming karst water. The discharges from rainwater drains, backyard gardens, the canal of the zoo, and inflow from roads add to the increase of these concentrations.

Table 2: Devices used to measure physical and chemical properties of water samples

	Mobile Monitoring Station 1	Mobile Monitoring Station 2	Laboratory
pH	NEOTEK-PONSEL, PHEHT	SENTEK PI11	Consort C902
conductivity	NEOTEK-PONSEL, C4E	Endress+Hauser InduMaxP CLS 50	Consort C902
turbidity	NEOTEK-PONSEL, NTU sensor	Endress+Hauser TurbiMax W CUS41/CUS41-W	-
PO <sub>4</sub> <sup>3-</sup> -P NH <sub>4</sub> <sup>+</sup> -N NO <sub>3</sub> <sup>-</sup> -N NO <sub>2</sub> <sup>-</sup> -N	-	μMAC C	Lovibond PC Spectro
PAH	Trios, eviroFlu-HC	-	-

Table 3: Comparison of laboratory and online measurement results

	EnviroFlu (μg dm <sup>-3</sup> )	Laboratory (μg dm <sup>-3</sup> )
sample form Séd	13.01	0.13
Séd + 20 μg dm <sup>-3</sup> PAH mix	25.27	13.7
Séd +100 μg dm <sup>-3</sup> naphthaline-disulphonate	21.03	0.15

Table 4: Monthly average values for water quality parameters

	August	September	October
pH	7.64	7.45	7.43
Conductivity, μS cm <sup>-1</sup>	711.22	707.16	720.74
Oxygen saturation, %	84.15	93.4	77.32
Dissolved oxygen, mg dm <sup>-3</sup>	9.39	10.28	8.73
NH <sub>4</sub> <sup>+</sup> -N, μg dm <sup>-3</sup>	33	31	26
NO <sub>2</sub> <sup>-</sup> -N, μg dm <sup>-3</sup>	31	17	15
NO <sub>3</sub> <sup>-</sup> -N, mg dm <sup>-3</sup>	5.12	4.02	4.14
PO <sub>4</sub> <sup>3-</sup> -P, μg dm <sup>-3</sup>	113.79	96.58	92.04

#### Measurement of Polyaromatic Hydrocarbon Concentrations

The two goals of the measurements were the testing the reliability of the results by EnviroFlu and evaluating whether the probe can detect other PAH compounds that are not fluorescent. To check reliability, we used the addition method with EPA TCL Polynuclear Hydrocarbons Mix chemical from Sigma-Aldrich. Furthermore, we also used naphthaline-disulphonate compound for inducing disturbing effect. We measured three solutions as shown in Table 3 with probe and we have taken emission spectra. Laboratory control measurements (MSZ 1484-6) [5] were done by ELGOSCAR 2000.

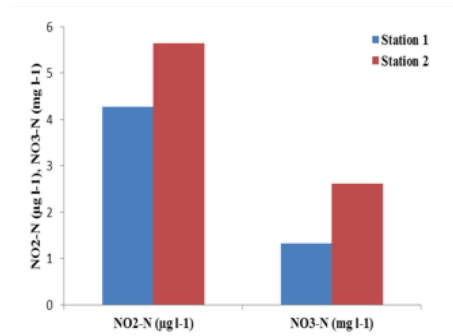
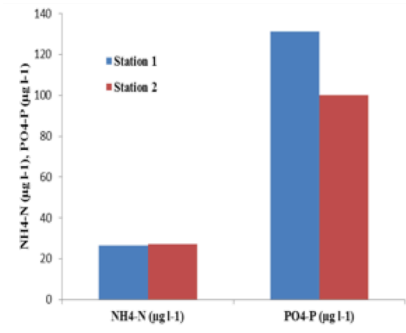


Figure 10: The effect of the city of Veszprém on the investigated section of Séd creek

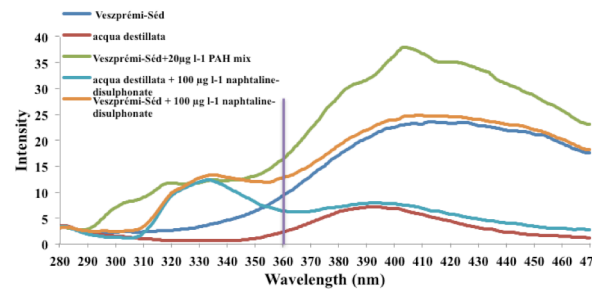


Figure 11: Emission spectra taken with fluorimeter

Comparison of the laboratory and probe results showed significant difference (Table 3). If we deduct the values obtained for the sample from Séd creek as base values, we get similar results. The reliability of results obtained this way was confirmed by spectra taken by a Perkin Elmer LS50B type fluorimeter (Fig.11) [1]. The EnviroFlu probe detects fluorescent light at 360 nm. When looking at the curves at 360 nm, we can see that the proportions of intensity differences between the spectra of a sample from Séd and artificially polluted samples correspond to the concentration differences. The significant difference between the laboratory and probe results comes from the fact that the probe senses all compounds giving fluorescence at a given wavelength. This was further elaborated by the significant concentration difference when the sample contained naphthaline-disulphonate.

#### Water Quality According to Water Framework Directive

The middle section of Séd belongs to Type 3, or alpine, calcic-rough bed material, medium catchment water flow according to Water Management Plan [18] on the basis of Water Framework Plan [19.] We have prepared

water qualification in the observed timeframe in monthly divisions. For dissolved oxygen and oxygen saturation values we used the results of Mobile Monitoring Station 1 and for other components the results of Mobile Monitoring Station 2.

We have calculated monthly average values of water quality parameters (*Table 4*). In addition, we classified each component on a five-level scale and then made class averages. The class minimums provided classifications for each month. The minimum of class average for August, September, and October were 2.5, 3, and 3, respectively; which resulted in water quality that did not reach a good status.

### Conclusions

The advantage of online measurement methods was demonstrated due to the possibility of continuously monitoring the quality of the examined creek. With online devices events can be detected that can be missed by point sampling, such as daily fluctuations, pollution waves in extreme time points.

Another advantage of online methods is the remote controllability, which does not require personnel except for maintenance. A drawback of the larger and more complex Mobile Monitoring Station 2 compared to more portable Mobile Monitoring Station 1 is the need for significant chemical, distilled water and maintenance time.

The measurement stations can reveal trends, the results provided by them are in the same magnitude, but it cannot compete with the accuracy of an accredited laboratory. The goal of online measurements is to detect pollutant waves and extreme values. In order to enhance the accuracy of online measurements follow up laboratory control measurements is needed.

In addition to the entry and the exit sections of the Séd creek, the Catchment Management Plan requires monitoring the physical and chemical parameters of the middle section of Séd that are missing. The results presented in the given paper may help in the drafting of the measurement plans.

### Acknowledgements

This work was supported by the European Union and co-financed by the European Social Fund in the frame of the TÁMOP-4.2.2/B-10/1-2010-0025.

### REFERENCES

[1] KRISTÓF J.: Chemical Analysis II. (Instrumental Analysis), VE 13/2000. Veszprém, Pannon Egyetemi Kiadó, 2000 (in Hungarian)  
 [2] Endress+Hauser Conductivity Sensor InduMaxP CLS 50: Technical Information (TI 182C/07,en, No 51517565), Endress+Hauser in Germany, 2007

[3] Endress+Hauser Solids Content Sensor Turbimax W CUS 41/CUS 41-W: Technical Information (TI 177C/07,en, No 51517577), Endress+Hauser in Germany, 2007  
 [4] Water Management of Central Transdanubia: Significant Water Management Issues 1–13; Northern and Eastern Bakony field land planning sub-unit, Székesfehérvár, 2007 (in Hungarian)  
 [5] MSZ 1484-6:2003: Testing of waters. Determination of polycyclic aromatic hydrocarbons (PAH) content gas chromatographic-mass spectrometry, Hungarian Standards Institution Standards Bulletin, 2003 (in Hungarian)  
 [6] MSZ ISO 5667-1:2007: Water Quality. Sampling; Part 1: Guidance on the design of sampling programmes and sampling techniques, Hungarian Standards Institution Standards Bulletin, 2007 (in Hungarian)  
 [7] MSZ EN ISO 5667-3:2004: Water Quality. Sampling; Part 3: Guidance on preservation and handling of water samples, Hungarian Standards Institution Standards Bulletin, 2004 (in Hungarian)  
 [8] NEOTEK-PONSEL Digital sensorC4E: Conductivity/Salinity Datasheet, NEOTEK-PONSEL in France, 2009  
 [9] NEOTEK-PONSEL Digital sensor Nephelometric Turbidity Datasheet, NEOTEK-PONSEL in France, 2009  
 [10] NEOTEK-PONSEL Digital sensor ODOT: Optical Dissolved Oxygen Datasheet, NEOTEK-PONSEL in France, 2009  
 [11] NEOTEK-PONSEL Digital sensor PHEHT: pH, Redox, Temperature Datasheet, NEOTEK-PONSEL in France, 2009  
 [12] SENTEK Electrochemical Sensor Specialists PI 11 pH elektrode manual, SENTEK in UK, 2008  
 [13] SYSTEA S.p.A: Ammonia in water 0–0.4 ppm N-NH<sub>3</sub> (LFA-NH3-05 rev.1 common.609) , Systea S.p.A., Italy, 2000  
 [14] SYSTEA S.p.A: Nitrate in water DTPA UV reduction 0–100 mg dm<sup>-3</sup> N-NO<sub>3</sub><sup>-</sup>+N-NO<sub>2</sub><sup>-</sup> (LFA-NO3DTPA-02 rev.1 comm. 896) Systea S.p.A., Italy, 2000  
 [15] SYSTEA S.p.A: Nitrite in water and seawater 0–5 ppm N-NO<sub>2</sub><sup>-</sup> (LFA-NO2-01 rev2.comm. 896) Systea S.p.A., Italy, 2000  
 [16] SYSTEA S.p.A: Orthophosphate in water and seawater 0–20 ppm (LFA-PO4-02 rev.1 comm.896) Systea S.p.A., Italy, 2000  
 [17] TriOS GmbH: Trios Optical Sensors enviroFlu-HC manual submersible fluorimeter for the detection of polycyclic aromatic hydrocarbons (PAHs) in water, TriOS GmbH in Germany, 2004  
 [18] Directorate for Water and Environmental Protection: Water Management Plan for the Danube River Basin in Hungary, 2009 (in Hungarian)  
 [19] EU Water Framework Directive: The European Parliament and of the Council, Water Framework Directive (2000/60/EC), OJL 327, 22 December 2000, 1–73

## ADSORPTION AND INTERCALATION OF SMALL MOLECULES ON KAOLINITE FROM MOLECULAR MODELLING STUDIES

ATTILA TÁBOROSI,<sup>1</sup> RÓBERT KURDI,<sup>1</sup> AND RÓBERT K. SZILÁGYI<sup>2</sup>

<sup>1</sup> Surfaces and Nanostructures Laboratory, Institute of Environmental Engineering, University of Pannonia, Veszprém, H-8201, HUNGARY

<sup>2</sup> Department of Chemistry and Biochemistry, Montana State University, Bozeman, MT 59717, U.S.A.  
✉E-mail: taborosia@almos.uni-pannon.hu

Kaolinite is an abundant natural material with considerable industrial potential. Despite its simple composition ( $\text{Al}_2\text{Si}_2\text{O}_5(\text{OH})_4$  and layered structure being a phyllosilicate), it is notable that only little known about the interaction of kaolinite sheets with small organic reagents at the molecular level. These assumed to govern intercalation, delamination, and then the complete exfoliation processes. A common methodology to model the molecular structure of kaolinite is the employment of periodic boundary conditions. The application of molecular cluster models gained importance nowadays by capitalizing on the availability of wide range of theoretical tools for describing structural features and reaction mechanisms. In this study, we present our results using theoretical methodologies and modelling strategies from literature that are applied for adsorption and intercalation of urea, ethylene glycol, and potassium acetate.

**Keywords:** kaolinite, intercalation, adsorption, hydrogen bonding, molecular cluster model

### Introduction

A significant hindrance in the design, optimization, and execution of experimental research involving clay minerals is the lack of our understanding of molecular level processes occurring at the outer (adsorption) or at the inner surface (intercalation) of layers of clay. Molecular modelling approaches have the potential to aid experimental design, mitigating cost of chemicals used, rationalizing unsuccessful trial-and-error experiments, and thus contributing to tailored utilization of clay minerals as industrial raw materials.

Given the periodic nature of the crystalline clay minerals, a common approach in modelling is the use of periodic boundary conditions [1–4]. A competitive approach is based on molecular cluster models [5–9]. An advantage of using the latter is the availability of a broad range of quantum chemical tools for studying the local chemical environment of the site(s) of adsorption and/or intercalation.

In the given study, we have utilized kaolinite, which is a member of the 1:1 class of clay minerals. This implies that the layers of this simplest phyllosilicate are composed of octahedral (O) and tetrahedral (T) sheets. The O-sheet contains hexacoordinate  $\text{Al}^{3+}$  ions, while the T-sheet has tetracoordinate  $\text{Si}^{4+}$  ions. The O- and T-sheets are connected *via* tricoordinate oxide anions, while the separate OT or 1:1 layers are connected through hydrogen bonds (H-bonds) (Fig. 1).

### Computational Methods

The computational models were created from the unit cell of the experimental X-ray diffraction structure of crystalline kaolinite [10]. We will discuss results here for models for separate O- and T-sheets with

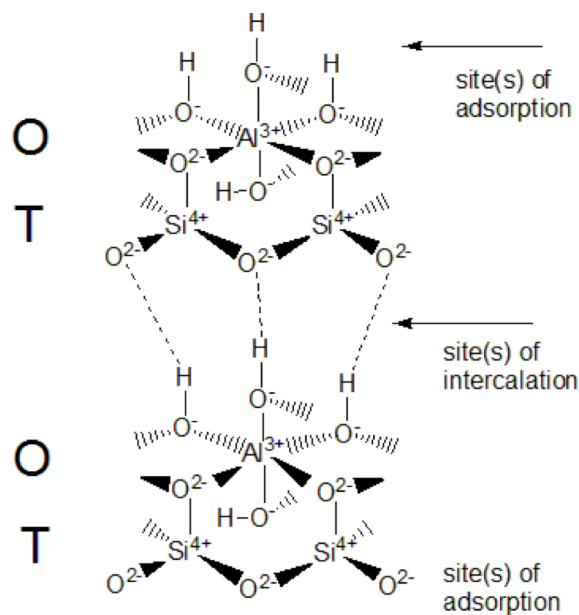


Figure 1: Schematic presentation of adjacent OT layers of delaminated kaolinite

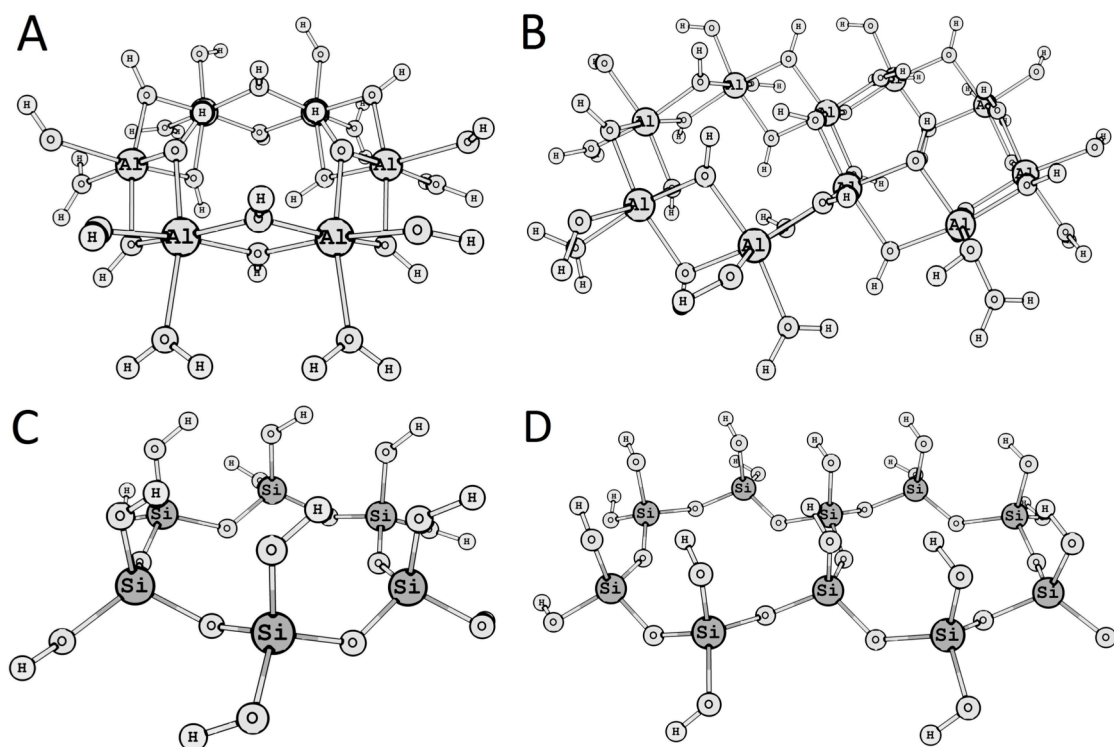


Figure 2: Computational models for the hexagonal honeycomb-like units of [6Al] (A) and [10Al] (B) octahedral, [6Si] (C) and [10Si] (D) tetrahedral cluster models for O- and T-sheets of kaolinite, respectively

stoichiometry of  $\text{Al}_6\text{O}_{24}\text{H}_{30}$  and  $\text{Si}_6\text{O}_{18}\text{H}_{12}$ , respectively (Figs. 2A and C). These are the smallest possible cluster models for the hexagonal, honeycomb like units of the O- and T-sheets. In addition, two larger models of  $\text{Al}_{10}\text{O}_{38}\text{H}_{46}$  and  $\text{Si}_{10}\text{O}_{29}\text{H}_{18}$  were also considered (Figs. 2B and D) for the larger intercalating agents (ethylene glycol, potassium acetate). The unit cell of kaolinite was multiplied in all crystal dimensions to create a super-cell. This was then truncated to the cluster models presented above. The charge neutrality was achieved by terminating dangling bonds with protons at the periphery of the models. The initial positions of the adsorbent reagents were set at the centre of the hexagonal honeycomb-like unit of both O- and T-sheets and it was allowed to fully relax during optimizations.

Given that the computational models shown in Fig. 2 are simplifications of the experimental crystal structure environment, structural constraints were applied during geometry optimizations. In all calculations, the atoms of the organic reagents, the surface hydroxide groups ( $s\text{-HO}^-$ ) of the O-sheet, and the bridging oxide groups ( $b\text{-O}^{2-}$ ) of the T-sheets were allowed to move, while the positions of the rest of the atoms were kept fixed. After structural optimizations, the positions and relative arrangements of the organic reagents with respect of the outer and inner surfaces, the shortest distances of possible ion/dipole interactions or H-bonds were noted. For computational models of T...reagent...O intercalation, the basal spacing was set at the beginning of calculations to the experimental values of 10.7, 9.5, 11.5 Å, and 14.2 Å for urea [11], ethylene glycol [12], and potassium acetate in the absence or in the presence of water [13], respectively.

The calculations were carried out using the B3LYP hybrid density functional [14,15] with LANL2DZ basis set [16] as implemented in Gaussian09 [17]. The interaction energies were not considered in this work due to the modest level of theory and lack of consideration of explicit or implicit solvation shell. The main focus of the given work is to establish initial structural models for rationalizing experimental observations and prepare for more advanced computational modeling. The optimized structures presented in this work were made available at [computational.chemistry.montana.edu/SI](http://computational.chemistry.montana.edu/SI).

## Results and Discussions

### Kaolinite-Urea Interactions

The lowest energy, optimized structure for the adsorbed urea on O-sheet can be characterized by two short O(urea)... $s\text{-HO}^-$  distances of 1.92 and 1.95 Å, while one of the amide groups approaches the opposite  $s\text{-HO}^-$  group within 1.73 Å as shown in Fig. 3A. The presence of both donor and acceptor interactions for the same reagent molecule result in a tilted orientation of the urea. An alternative orientation in which only the carbonyl group is interacting with three  $s\text{-HO}^-$  groups (see below for intercalation model) was not found to be a stationary structure at this level of theory. Figs. 3B and C illustrate the two different orientations of the urea at the T-sheet, where the amide groups are H-bonded to the  $b\text{-O}^{2-}$  groups of the same  $\text{Si}^{4+}$  ion (*geminal*) with  $\text{NH}\dots b\text{-O}^{2-}$  distances of 2.03 and 2.12 Å or two different  $\text{Si}^{4+}$  ions (*vicinal*) with 2.02 and 2.08 Å

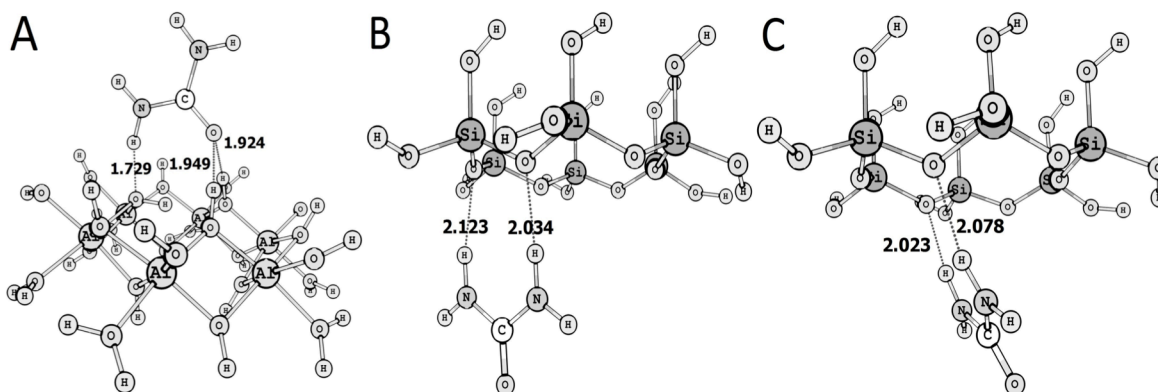


Figure 3: Computational models for urea absorption at O- (A) and T-layers in *geminal* (B) and *vicinal* (C) arrangements

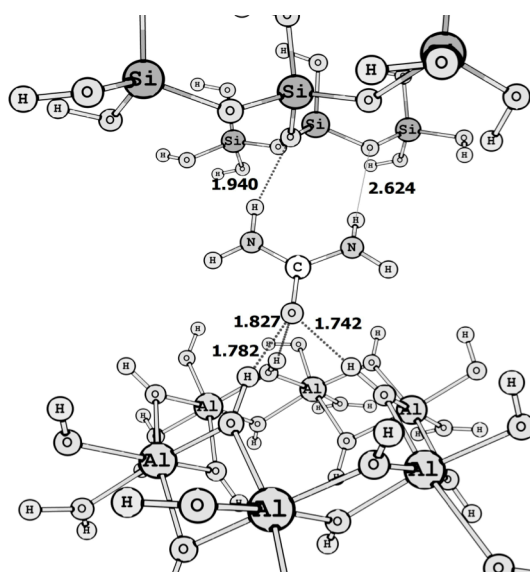


Figure 4: Computational model for intercalation of urea in kaolinite

distances. The energetic difference between the geminal and vicinal coordination is not significant (less than  $10 \text{ kJ mol}^{-1}$ ) at this level of theory.

When the adsorption of urea is considered simultaneously at both the O- and T-sheets, a model can be obtained for a plausible structure of the urea intercalated between two OT-layers (Fig. 4). In this computational model, the carbonyl group of urea forms three H-bonds at 1.74, 1.78, and 1.83 Å distances with three *s*-HO<sup>-</sup> groups of the hexagonal O-sheet cross from each other. At the same time, the intercalated urea forms two H-bonds with the *geminal* *b*-O<sup>2-</sup> groups at 1.94 and 2.62 Å distances. The tilted orientation of the urea is the consequence of the experimental basal spacing of 10.7 Å, which was kept fixed during the structural optimizations. It is important to recognize that according to our computational model, there is not enough room between the expanded layers of kaolinite to accommodate urea perpendicular to the basal planes or with parallel carbonyl groups to the crystallographic ‘c’ axis.

#### Kaolinite-Ethylene Glycol Interactions

Ethylene glycol is generally used in exchange-intercalation as a step followed by initial dimethyl

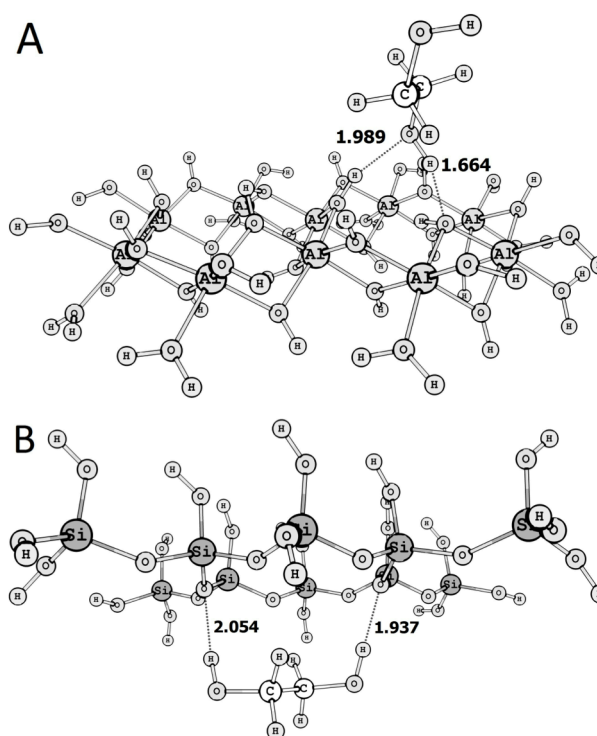


Figure 5: Computational models for the adsorption of ethylene glycol at the (A) O- and (B) T-sheets

sulfoxide or potassium acetate intercalation. As shown in Fig. 5A, the donor interaction between the reagent hydroxyl group and the Al<sup>3+</sup> bound *s*-HO<sup>-</sup> is much shorter (1.66 Å) than those seen for urea adsorption (1.73 Å), while the acceptor interaction is slightly longer (1.99 Å). Given that the *b*-O<sup>2-</sup> groups of the T-sheet can only act as H-bond acceptors with ethylene glycol, the reagent spans the entire hexagonal honeycomb-like unit of the T-sheet by forming longer (2.05 and 1.94 Å), thus weaker H-bond interactions than with the O-sheet.

The complementarity of the O- and T-sheets with respect of being H-bond donor and acceptor, respectively, allows for an ideal orientation of the functional groups of ethylene glycol for maximizing the strength of H-bond interactions. The O-sheet forms a short (1.61 and 1.79 Å) interaction between the O(glycol)...*s*-HO<sup>-</sup> groups. The T-sheet accepts the HO groups of the ethylene glycol at 1.73 and 1.88 Å distances. Comparison of the urea (Fig. 5) and ethylene

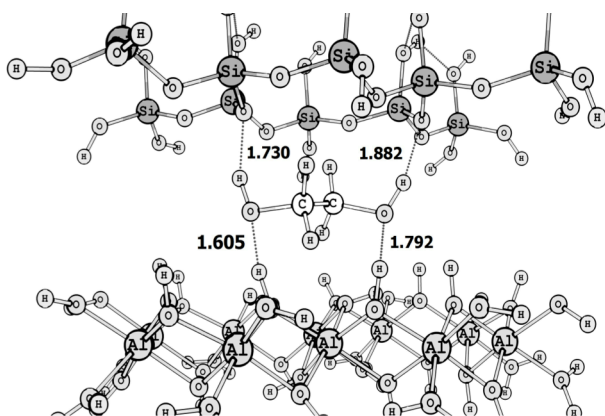


Figure 6: Computational model for ethylene glycol intercalation in kaolinite

glycol (Fig.6) intercalated models, the network of interactions between the layers and reagents parallel well the different experimental basal spacing (10.7 vs. 9.5 Å, respectively). While the urea opens the interlayer space more; however, it anchors the two layers with a stronger set of interactions than ethylene glycol. This can be correlated with the limited reactivity of urea/kaolinite complex in exchange intercalation; while ethylene glycol often provides the last step before complete delamination and exfoliation of clays.

#### Kaolinite-Potassium Acetate Interactions

A limitation of the *in vacuo* models used in this study greatly hinders the dissociation of the potassium ion from acetate and thus in both adsorption models the cation remained at the centre of the hexagonal honeycomb-like model for the O- and the T-sheets in the vicinity of the anion acetate. In addition, the ionized carboxylic group of the reagent form two short and thus strong H-bonding interactions at 1.65 and 1.89 Å distances with two germinal *s*-HO<sup>-</sup> groups of the O-sheet. The shortest acetate C-H...*b*-O<sup>2-</sup> distance in Fig.7B is 2.95 Å, which indicates the presence of weak

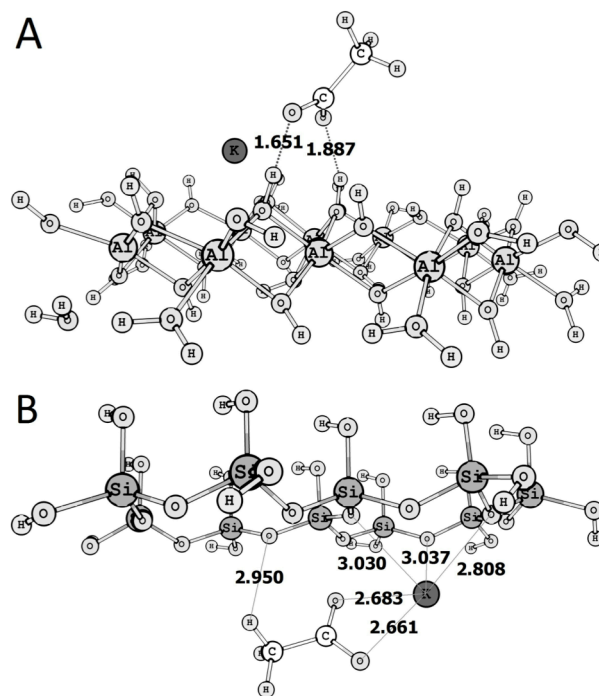


Figure 7: Computational models for the adsorption of potassium acetate on (A) O- and (B) T-sheets

interactions between the methyl group and the *b*-O<sup>2-</sup> groups. In the adsorption model for the T-sheet, the acetate appears to be held in place by the cation at about 2.66 and 2.68 Å.

Some of the plausible structures for the intercalation of potassium acetate were obtained from simulations in the absence (Fig.8A) and presence (Fig.8B) of solvent water. Similarly to the other models the values of basal spacing were set to their corresponding experimental values of 11.5 and 14.2 Å, respectively. The 2.7 Å difference allows for the accommodation of a water molecule as shown in Fig.8B. In agreement with the absorption models in Fig.7, we found short H-bond distances between the carboxylate group and the *s*-HO<sup>-</sup> of the O-sheet at 1.59 and 1.83 Å distances. When water

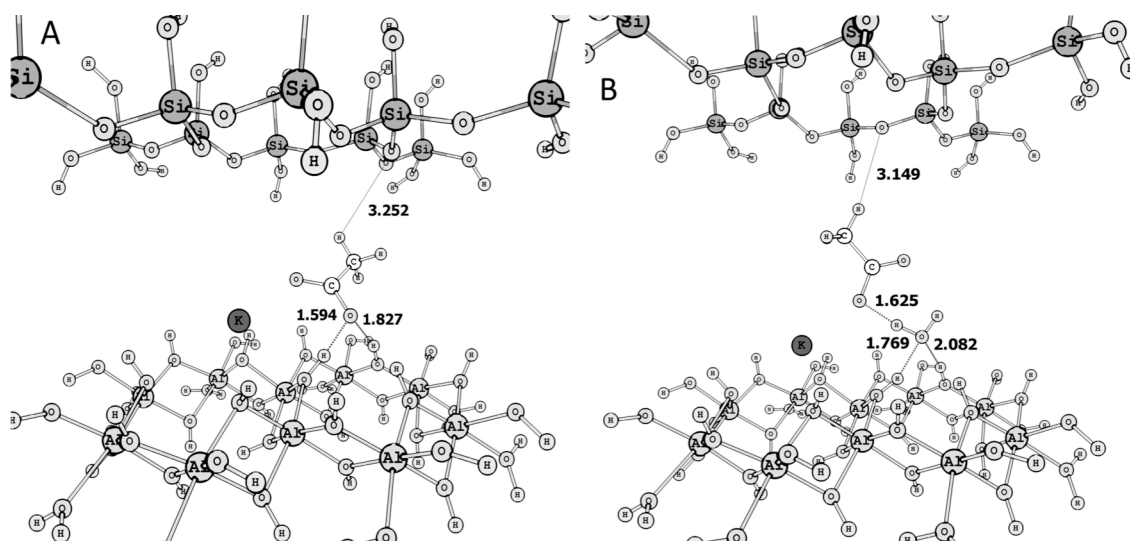


Figure 8: Computational models for potassium acetate intercalation in the (A) absence and (B) presence of solvent water

is present, it is likely to solvate the negatively charged end of the acetate ion with a characteristic  $\text{-COO}^- \dots \text{H-OH}$  distance of 1.63 Å. The interaction of the water and the O-sheet is asymmetrical with 1.77 and 2.08 Å  $\text{O(water)} \dots \text{s-HO}^-$  distances.

Given the energetic preference of the  $\text{O-H} \dots \text{OH}^-$  H-bonding interaction, the methyl group of the acetate will only interact with anionic groups of the T-sheet with representation  $\text{C-H} \dots \text{b-O}^{2-}$  distances of 3.15 and 3.25 Å. The lack of a representative solvent environment is of less importance for the position of the potassium ion in the intercalation models, since the inner environment of this model will likely be only exposed to bulk solvent only to a limited extent.

### Conclusions

We have started with a few notable preliminary results the establishment of a structural database for reference models related to the adsorption and intercalation of small molecules and kaolinite. We found that even a modest level of theory with respect of the basis set can provide reasonable structures. These results allow us for visualizing molecular structures in order to rationalize experimental observables and generate new ideas for research directions. Furthermore, these models can be considered as initial structures for higher-level calculations that are currently in progress in our laboratory.

### Acknowledgement

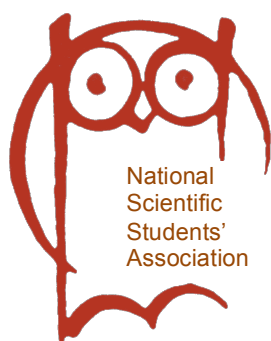
This research was supported by the European Union and the State of Hungary, co-financed by the European Social Fund in the framework of TÁMOP 4.2.4.A/2-11-1-2012-0001 ‘National Excellence Program’ (RKS and AT) and TÁMOP-4.2.2.A-11/1/KONV-2012-0071 (RK). The authors acknowledge the helpful discussions with Prof. JÁNOS KRISTÓF and Prof. ERZSÉBET HORVÁTH. We acknowledge the use of the computational facilities at Montana State University, Bozeman, MT.

### REFERENCES

- [1] SMRCOK L., TUNEGA D., RAMIREZ-CUESTA A.J., IVANOV A., VALUCHOVA J.: The combined inelastic neutron scattering and solid-state DFT study of hydrogen-atoms dynamics in kaolinite-dimethylsulfoxide intercalate, *Clays Clay Minerals*, 2010, 58(1), 52–61
- [2] MERCIER P.H.J., LE PAGE Y.: Rational *ab initio* modeling for low energy hydrogen-bonded phyllosilicate polytypes, *Eu. J. Mineral.*, 2011, 23(3), 401–407
- [3] GEATCHES D.L., JACQUET A., CLARK S.J., GREENWELL H.C.: Monomer adsorption on kaolinite: modeling the essential ingredients, *J. Phys. Chem. C*, 2012, 116(42), 22365–22374
- [4] TUNEGA D., BUCKO T., ZAOUI A.: Assessment of ten DFT methods in predicting structure of sheet silicates: Importance of dispersion corrections, *J. Chem. Phys.*, 2012, 137(11), 114105
- [5] HATÓ Z., MAKÓ É., KRISTÓF T.: Water-mediated potassium acetate intercalation in kaolinite as revealed by molecular simulation, *J. Mol. Mod.* 2014, 20(3), 1–10
- [6] MICHALKOVA A., ROBINSON T.L., LESZCZYNSKI J.: Adsorption of thymine and uracil on 1:1 clay mineral surfaces: comprehensive *ab initio* study on influence of sodium cation and water, *PCCP*, 2011, 13(17), 7862–7881
- [7] DAWLEY M.M., SCOTT A.M., HILL F.C., LESZCZYNSKI J., ORLANDO T.M.: Adsorption of formamide on kaolinite surfaces: A combined infrared experimental and theoretical study, *J. Phys. Chem. C*, 2012, 116(45), 23981–23991
- [8] SCOTT A.M., DAWLEY M.M., ORLANDO T.M., HILL F.C., LESZCZYNSKI J.: Theoretical study of the roles of  $\text{Na}^+$  and water on the adsorption of formamide on kaolinite surfaces, *J. Phys. Chem. C*, 2012, 116(45), 23992–24005
- [9] SONG K.H., WANG X., QIAN P., ZHANG C., ZHANG Q.: Theoretical study of interaction of formamide with kaolinite, *Comp. Theor. Chem.*, 2013, 102, 72–80
- [10] BISH D. L.: Rietveld refinement of the kaolinite structure at 1.5-K, *Clays Clay Minerals*, 1993, 41(6), 738–744
- [11] MAKÓ É., KRISTÓF J., HORVÁTH E., VÁGVÖLGYI V.: Kaolinite-urea complexes obtained by mechanochemical and aqueous suspension technics-a comparative study. *J. Colloid Inter. Sci.*, 2009, 330(2), 367–373
- [12] GARDOLINSKI J.E.F.C., LAGALY G.: Grafted organic derivatives of kaolinite: I. Synthesis, chemical and rheological characterization, *Clay Minerals*, 2005, 40(4), 537–546
- [13] FROST R.L., KRISTÓF J., KLOPROGGE J.T., HORVÁTH E.: Rehydration of Potassium Acetate-intercalated Kaolinite at 298 K. *Langmuir*, 2000, 16(12), 5402–5408
- [14] LEE C.T., YANG W.T., PARR R.G.: Development of the Colle-Salvetti correlation energy formula into a functional of the electron-density, *Phys. Rev. B*, 1988, 37(2), 785–789
- [15] BECKE A.D.: Density-Functional thermochemistry 3 The role of exact exchange, *J. Chem. Phys.* 1993, 98(7), 5648–5652
- [16] DUNNING JR. T.H., HAY P.J., (ED.: SCHAEFER III H.F.): *Modern Theoretical Chemistry: Methods of Electronic Structure Theory*, Plenum, New York 1976, Vol. 3, pp. 1–28
- [17] FRISCH M.J.T., TRUCKS G.W., SCHLEGEL H.B., SCUSERIA G.E., ROBB M.A., CHEESEMAN J.R.; *et al*as: Revision D.01 ed., Gaussian, Inc., Wallingford CT, 2009

## **Acknowledgement**

The dedicated issue of the Hung. J. Ind. & Chem. and in part the organization of the 2014 Spring Scientific Students' Meeting at University of Pannonia were made possible from support provided by the National Talent Program of the Educational Research and Development Institute and the Human Resource Support Program of the Ministry of Human Resources within the framework of "Support of TDK Workshops Recognized by the Council of National Scientific Students' Association" (NTP-TDK-13)



## **Köszönetnyilvánítás**

Jelen kiadvány és részben a 2014. évi Tavaszi Tudományos Diáknapp a Pannon Egyetemen az Emberi Erőforrások Minisztériuma megbízásából az Oktatáskutató és Fejlesztő Intézet és az Emberi Erőforrás Támogatáskezelő által gondozott Nemzeti Tehetség Program „Az Országos Tudományos Diákköri Tanács által elismert TDK-műhelyek támogatása” (NTP-TDK-13) című pályázatának köszönhetően valósult meg.

## IMPACT OF SIZE HETEROGENEITY OF CORE-SHELL PACKING MATERIALS ON CHROMATOGRAPHIC SEPARATION OF LARGE BIOMOLECULES

DIÁNA LUKÁCS AND KRISZTIÁN HORVÁTH<sup>✉</sup>

Department of Analytical Chemistry, University of Pannonia, 8200 Veszprém, Egyetem St. 10., HUNGARY  
<sup>✉</sup>E-mail: raksi@almos.uni-pannon.hu

The effect of particle size heterogeneity of core-shell stationary phases on the efficiency of chromatographic separation of large biomolecules was studied. It was shown that the column efficiency was affected significantly by the breadth of particle size distribution. The chromatographic efficiency decreased as the heterogeneity of particle sizes increased. Although the absolute decrease of separation efficiency was affected by the linear velocity,  $u$ , of the eluent, the relative change of HETP was independent of  $u$  in the practical range of eluent velocities. The results showed that the affect of particle size distribution was the highest in case of fully porous phases, and it decreased as the diameter of the inner core decreased. It was shown that, in the usual range of particle size heterogeneity of core-shell phase, the peak capacities did not change significantly even at high eluent velocities.

**Keywords:** high performance liquid chromatography, particle size heterogeneity, separation efficiency, core-shell phases

### Introduction

Modern analytical applications of liquid chromatography require efficient stationary phases. Before the introduction of core-shell particles – particles with a porous layer surrounding a solid core (*Fig. 1*) – the use of monolithic silica rods [1, 2], or of sub-2  $\mu\text{m}$  particles offered today the most satisfactory results. Due to their excessive radial heterogeneity, however, the efficiency of monolithic columns currently is lower than that of sub-2  $\mu\text{m}$  particles. Columns packed with fine particles, however, have a low permeability [5–7]. Thus, efficiency of columns packed with core-shell particles similar to the columns packed with sub-2  $\mu\text{m}$  particles, but can be operated with the same instruments as those used for conventional columns. The use of core-shell phases is particularly advantageous in the separation of large biomolecules [8]. Recently, core-shell phases were optimized for the separation of large biomolecules [9, 10]. Besides their unique structure, the high efficiency of core-shell phases is in part due to the very narrow particle size distribution, with a relative standard deviation around 5–10% vs. 20–40% for most totally porous particles [7].

In literature, fairly contradictory information can be found about the effect of particle size distribution, PSD, on the separation efficiency. Some results suggest that the large particle size variance has no influence on the column efficiency, while according to other data the wide PSD decreases the efficiency of chromatographic separation. Halász and Naefe [11] were the first ones who examined the effect of particle size distribution

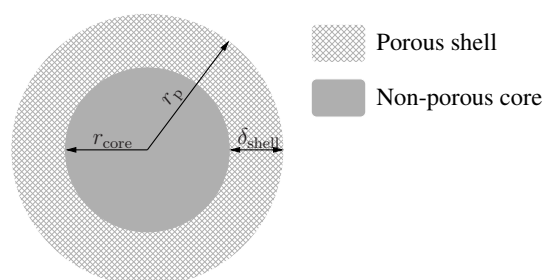


Figure 1: Structure of core-shell particles

on the column efficiency in case of particles that were larger than 50  $\mu\text{m}$ . In their work, no experimental result was found for the change of chromatographic efficiency even in case of wide PSDs ( $\sim 40\%$ ). Two years after Halász's work, significantly smaller, 1-10  $\mu\text{m}$ , particles were tested by Endeke *et al.* [12]. No change in the permeability and in the chromatographic efficiency were observed as long as the average particle size remained the same. Dewaele and Verzele prepared columns packed with mixtures of different compositions of reversed phase particles of 3 and 8  $\mu\text{m}$  and investigated the effect of the PSD on the column efficiency [13] with similar results.

Billen *et al.* found that the breadth of the distribution of the stationary phase particles has no effect on the chromatographic efficiency as long as no fines are present. In the presence of fines, the efficiency decreases significantly [14]. They emphasized that

different conclusions can be drawn about the goodness of a chromatographic column depending on the definition used for the particle size distribution.

The effect of the PSD on the chromatographic efficiency of sub-2  $\mu\text{m}$  particles was studied by Cabooter *et al.* by analyzing kinetic plots of these phases [15]. In their work, they showed that not just the PSD is important but also the separation efficiency one wants to achieve. It was concluded that the greater the achievable number of theoretical plates, the more the PSD affects the separation efficiency. In their experiments, the authors obtained better results by using columns with a narrower PSD than by using columns of the same dimensions but packed with particles with broader PSD.

Recently, Gritti *et al.* found that the chromatographic efficiency of the columns can be optimized if a small amount of greater particles is added to the sub-3  $\mu\text{m}$  particles which leads to better bead homogeneity [16]. Manufacturers practice matches these, because on their confession they add a small amount of larger particles to the bathes to optimize the pressure drop along the column.

Experimental study of the effect of PSD on chromatographic efficiency is rather complex, because the column packing procedure is hardly reproducible. It is particularly true when we work with stationary phases which have different PSDs. The quality of column packing also affects the column efficiency significantly. Theoretical models can provide more reliable data on this field because it does not affected by the variability of column packing. The goal of this work is to study the effect of particle size heterogeneity on the chromatographic efficiency of separation of large biomolecules on core-shell stationary phases on a theoretical basis.

## Theory

In HPLC, one of the measure of separation efficiency is the height equivalent to a theoretical plate, HETP [17]. The higher the plate height, the less efficient the separation is. The general rate model of chromatography [18] permits the calculation of HETP of columns packed by core-shell phases [8]:

$$H(d_p) = \frac{2D_L}{u} + \frac{k_1^2}{1 + k_1^2} \left( \frac{\Omega u d_p^2}{30FD_p} + \frac{u d_p}{3Fk_f} \right), \quad (1)$$

where  $d_p$  is the diameter of particles of packing material,  $u$  the linear velocity of the eluent in the interstitial volume,  $k_1$  the interstitial retention factor,  $F$  the phase ratio,  $D_L$  and  $D_p$  the axial and pores diffusion coefficients, respectively, and  $k_f$  the external mass transfer coefficient.  $\Omega$  is given by the relationship

$$\Omega = (1 - \rho) \frac{1 + 3\rho + 6\rho^2 + 5\rho^3}{(1 + \rho + \rho^2)^2}, \quad (2)$$

where  $\rho$  represents the ratio of the radius of the inner solid core,  $r_{\text{core}}$ , to the radius of the particle,  $r_p$  (see *Fig. 1*):

$$\rho = \frac{r_{\text{core}}}{r_p}. \quad (3)$$

Accordingly,  $\rho$  is zero for fully porous particle and one for non-porous particle.

For a core-shell particle, the interstitial retention factor is

$$k_1 = \frac{(1 - \varepsilon_e)(1 - \rho^3)}{\varepsilon_e} [K_a(1 - \varepsilon_p) + \varepsilon_p], \quad (4)$$

where  $\varepsilon_e$  is the external bed porosity,  $\varepsilon_p$  is the porosity of the porous shell, and  $K_a$  is the adsorption equilibrium constant (Henry constant).

The particle size distribution is usually described by log-normal distribution [19]. The PSD of a packing material with mean  $\mu$  and variance  $\sigma^2$  is

$$f_{d_p} = \frac{1}{d_p \sqrt{2\pi\theta}} \exp \left( -\frac{\left( \ln \frac{d_p}{\mu} + \frac{1}{2}\theta \right)^2}{2\theta} \right), \quad (5)$$

where

$$\theta = \ln \left( \frac{\sigma^2}{\mu^2} + 1 \right). \quad (6)$$

On the basis of the equations above, the probability density function of local HETPs,  $f_H$ , can be derived by applying the change-of-variables rule [20]:

$$f_H = \left| \frac{d}{dH} d_p(H) \right| f_{r_p}(d_p(H)), \quad (7)$$

where  $d_p(H)$  is the inverse function of  $H(d_p)$  (see *Eq. (1)*).

The observable HETP of the column is the first moment of *Eq. (7)*:

$$H_{\text{col}} = \int_0^{\infty} H f_H dH. \quad (8)$$

## Methods of Calculations

For the calculation of  $H_{\text{col}}$  (*Eq. (8)*) a software written in C++ language, using the adaptive quadrature routine provided by GNU Scientific Library (GSL, v. 1.15) [21]. The integration region was divided into subintervals, and on each iteration the subinterval with the largest estimated error was bisected. As a result, the overall error reduced rapidly, as the subintervals became concentrated around local difficulties in the integrand. These subintervals were managed by the GSL library, which handled the memory for the subinterval ranges, results and error estimates too. The relative error of integration was set to  $10^{-10}$ . The source code of the program was compiled by g++ shipped by GNU

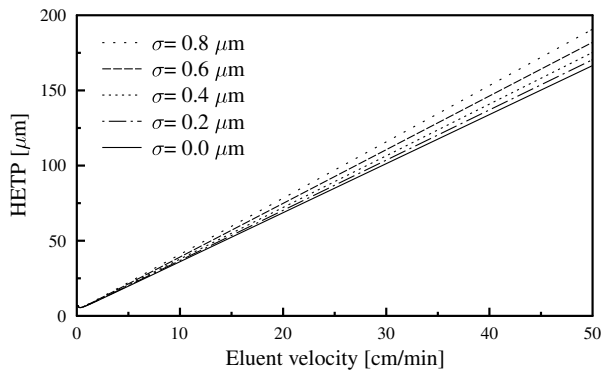


Figure 2: Van Deemter plots of large biomolecules in case of different standard deviations of particle size distributions of 2.6  $\mu\text{m}$  core-shell stationary phases

Compiler Collection ver. 4.7.2 using O1 optimization. The calculations were performed on a Pentium IV computer (2.80 GHz) running GNU Linux operating system (Debian Wheezy).

The function  $f_H$  (Eq.(7)) for the numerical integration was derived symbolically by Mathematica 8.0 (Wolfram Research, Inc.).  $H$  (Eq. (1)) was calculated as it is described in Ref. [8]. The internal ( $\varepsilon_p$ ) and external column porosities ( $\varepsilon_e$ ), were 0.05 and 0.4, respectively. The distribution coefficient of the compounds were set to 3. The ratio of the molecule size and the average pore diameter were assumed to be 0.68. The molecular diffusivity was  $2.5 \times 10^{-5} \text{ cm}^2/\text{min}$ . The value of “eddy” diffusion term, the internal and external obstruction factors were 1.3, 0.31 and 0.6, respectively. The linear velocity of the eluent was varied between 0.1 and 50 cm/min. The average pore size was 80 Å. It was assumed that the quality of the column packing remained identical in all cases.

## Results and Discussion

In Fig. 2 the calculated van-Deemter curves of large biomolecules separated on 2.6  $\mu\text{m}$  core-shell phases can be seen. The ratio of the radius of the inner solid core to the radius of the particle,  $\rho$ , is 0.7 representing the typical core size of commercial core-shell phases. The standard deviation of particle size distribution is varied between 0.0–0.8  $\mu\text{m}$  that corresponds to 0–30% relative standard deviation. Close examination of Fig. 2 highlights that the HETP values of large biomolecules are approximately directly proportional to the eluent velocity.

Fig. 2 shows that the heterogeneity of particle sizes has a significant effect on the separation efficiency of large biomolecules. The separation efficiency is the highest when the variance of particle size distribution is zero (solid black line). Increasing breadth of particle size distribution decreases the efficiency of separation. The decrease in the efficiency is more significant at higher eluent velocities. At 10 cm/min, the difference between

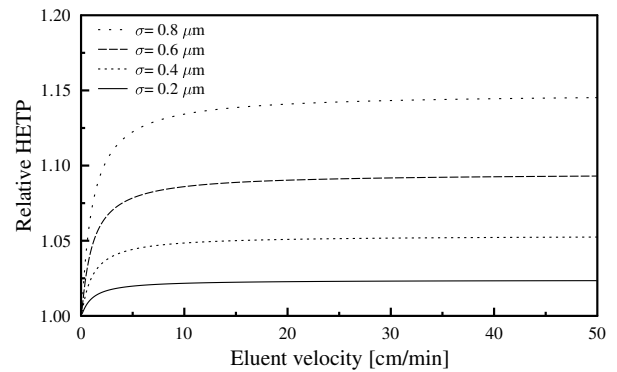


Figure 3: Relative van Deemter plots of large biomolecules in case of different standard deviations of particle size distributions of 2.6  $\mu\text{m}$  core-shell stationary phases

the two extremes ( $\sigma = 0$  and  $\sigma = 0.8$ ) is less than 5  $\mu\text{m}$  that is approximately 15% of the total plate height at this eluent velocity in ideal case ( $\sigma = 0$ ). In case of 30, 40, and 50 cm/min the differences are significantly larger:  $\sim 15$ ,  $\sim 20$ , and  $\sim 25 \mu\text{m}$ , respectively. Note, however, that the relative increase is  $\sim 15\%$  in each case suggesting that the relative change of HETP is independent from the eluent velocity.

In Fig. 3 the relative HETP,  $H_{\text{rel}}$ , values of large biomolecules can be seen as a function of eluent velocity.  $H_{\text{rel}}$  were calculated as

$$H_{\text{rel}} = \frac{H_{\sigma}}{H_0}, \quad (9)$$

where  $H_{\sigma}$  and  $H_0$  are HETP values at  $\sigma^2$  and 0 variance of PSD.

In Fig. 3, it can be seen that raising eluent velocity increases the relative HETP. Above  $\sim 8$  cm/min, however, a plateau is reached and the change of relative HETP becomes negligible. It suggests that, at low eluent velocities, the interstitial dispersion is the governing effect in band dispersion. As the velocity of eluent increases, the pore diffusion becomes more and more significant. Accordingly, in practice ( $u > 10$  cm/min), it is the dominant effect in band dispersion.

Fig. 4 shows the effect of core size on the chromatographic efficiency at different breadth of core-shell particle distribution. The linear velocity of the eluent was 15 cm/min that is a typical value in chromatographic applications. It can be seen that, as expected from Eq. (1), the efficiency of stationary phase increases as the thickness of porous layer decreases. The effect of width of particle size distribution is less significant at larger  $\rho$  values. While in case of fully porous particles, the difference is almost 17  $\mu\text{m}$  between the HETP values of the two extremes ( $\sigma = 0$  and  $\sigma = 0.8$ ), it is slightly more than 4  $\mu\text{m}$  at  $\rho = 0.8$ .

The relative HETPs calculated as in case of Fig. 3 do not change significantly with the diameter of non-porous core until  $\rho = 0.8$  (Fig. 5). Above that value,

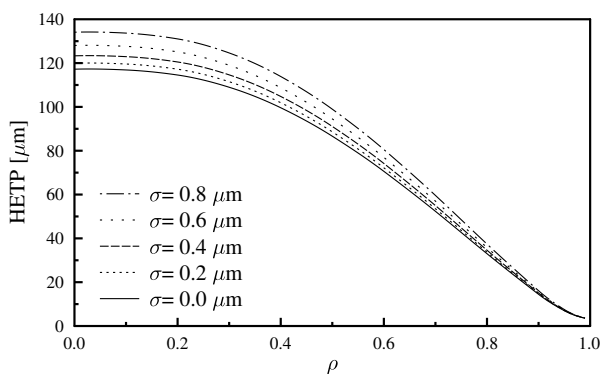


Figure 4: HETP of columns packed with 2.6  $\mu\text{m}$  core-shell particles

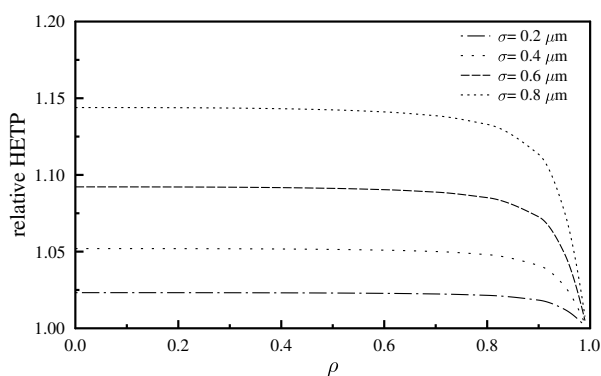


Figure 5: Relative HETPs of columns packed with 2.6  $\mu\text{m}$  core-shell particles

$H_{\text{rels}}$  decrease abruptly, at  $\rho = 1$  there is no difference between the cases. It can be explained by considering that the separation efficiency of large biomolecules is affected mainly by the pore diffusion (second term of Eq. (1)). As the thickness of porous layer of core-shell particles decrease, the diffusion paths reduce as well. As a result, the impact of pore diffusion on band broadening is less and less significant. The difference between the distinct particles vanishes. Finally, at  $\rho = 1$ , only the interstitial band spreading (first term of Eq. (1)) influences the efficiency of separation. Since  $D_L$  is not affected by the particle size distribution,  $H_{\text{rels}}$  become unity.

Besides the plate heights, the change of peak capacities were also studied. Peak capacity,  $n_c$ , is a practical measure of separation potential in HPLC.  $n_c$  is defined as the maximum number of components that can be resolved completely between the peaks of the least and most retained solutes [22]. Several expressions exist for the calculation of peak capacity [23] depending on the mode of chromatography. In case of isocratic mode of separation,  $n_c$  can be calculated as

$$n_c = \frac{1}{4} \sqrt{N} (t_{\text{max}} - t_{\text{min}}) \ln \frac{t_{\text{max}}}{t_{\text{min}}}, \quad (10)$$

where  $t_{\text{max}}$  and  $t_{\text{min}}$  are the retention times of the first and last eluting peaks, and  $N$  the number of theoretical

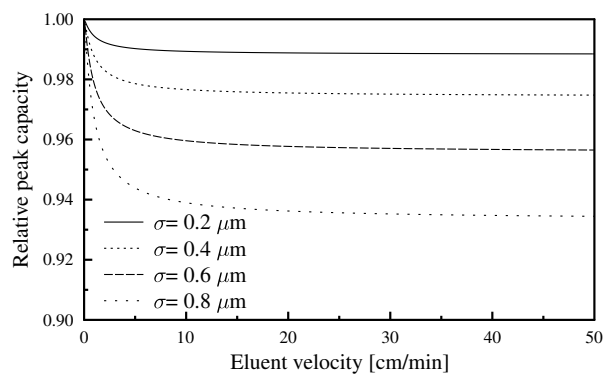


Figure 6: Relative peak capacities of columns packed by 2.6  $\mu\text{m}$  core-shell particles;  $L = 10$  cm,  $t_0 = 10/9$ ,  $t_{\text{max}} = 100/9$

plates ( $N = L/H$ ).

In Fig. 6 the peak capacities of 2.6  $\mu\text{m}$  core-shell phases can be seen as a function of eluent velocity in case of separation of large biomolecules. The calculated peak capacities were normalized for value that belongs to zero variance of PSD. The figure shows that the achievable peak capacity of a column packed with core-shell particles is affected by the heterogeneity of particle sizes. The decrease of peak capacities, however, is significantly smaller than the decrease of column efficiencies (Fig. 2). That is because  $n_c$  is proportional to the reciprocal square root of  $H$ . Accordingly, 15% increase in the plate height results in  $\sim 7\%$  loss of peak capacity that is not significant in practice.

## Conclusions

Since their introduction, core-shell stationary phases became very popular for the analysis of large biomolecules. The morphology of these phases results in less band broadening compared to fully porous particles and thus delivers extremely high efficiencies. In this work, the effect of particle size heterogeneity of core-shell stationary phases on the efficiency of chromatographic separation of large biomolecules was studied. The results showed that slopes of van Deemter curves were affected by the breadth of particle size distribution. As a result of widening PSD the column efficiencies decreased significantly. The analysis of peak capacities showed that the maximum number of large biomolecules that can be resolved by core-shell phases was not affected significantly, even if the PSD was wide. Considering that the relative standard deviations of PDSs of core-shell phases are between 0.2–0.4  $\mu\text{m}$  for 2.6  $\mu\text{m}$  particles, it can be concluded that the efficiency of these phases is affected significantly by the size heterogeneity of the particles. Further efforts from column manufacturers in order to improve the PSD do not give any more advantages and are not profitable.

### Acknowledgements

This research was supported by the European Union and the State of Hungary, co-financed by the European Social Fund in the framework of TÁMOP-4.2.4.A/2-11/1-2012-0001 'National Excellence Program'. The research infrastructure was supported by the Hungarian Scientific Research Fund (OTKA PD104819) and the Hungarian State and the European Union under the TÁMOP-4.2.2.A-11/1/KONV-2012-0071 project.

### REFERENCES

- [1] NAKANISHI K., SOGA N.: Phase Separation in Gelling Silica–Organic Polymer Solution: Systems Containing Poly(sodium styrenesulfonate), *J. Am. Ceram. Soc.*, 1991, 74, 2518–2530
- [2] MINAKUCHI H., NAKANISHI K., SOGA N., ISHIZUKA N., TANAKA N.: Octadecylsilylated porous silica rods as separation media for reversed-phase liquid chromatography, *Anal. Chem.*, 1996, 68, 3498–3051
- [3] KIRKLAND J., LANGLOIS T., DESTEFANO J.: Fused core particles for HPLC columns, *American Laboratory*, 2007, 39, 18–21
- [4] DESTEFANO J.J., LANGLOIS T.J., KIRKLAND J.J.: Characteristics of superficially-porous silica particles for fast HPLC: Some performance comparisons with sub-2- $\mu$  m particles, *J. Chromatogr. Sci.*, 2008, 46, 254–260
- [5] GRITTI F., CAVAZZINI A., MARCHETTI N., GUIOCHON G.: Comparison between the efficiencies of columns packed with fully and partially porous C-18-bonded silica materials, *J. Chromatogr. A.*, 2007, 1157, 289–303
- [6] CAVAZZINI A., GRITTI F., KACZMARSKI K., MARCHETTI N., GUIOCHON G.: Mass-transfer kinetics in a shell packing material for chromatography, *Anal. Chem.*, 2007, 79, 5972–5979
- [7] GRITTI F., LEONARDIS I., SHOCK D., STEVENSON P., SHALLIKER A., GUIOCHON G.: Performance of columns packed with the new shell particles, Kinetex-C18, *J. Chromatogr. A.*, 2010, 1217, 1589–1603
- [8] HORVÁTH K., GRITTI F., FAIRCHILD J.N., GUIOCHON G.: On the optimization of the shell thickness of superficially porous particles, *J. Chromatogr. A.*, 2010, 1217, 6373–6381
- [9] WAGNER B.M., SCHUSTER S.A., BOYES B.E., KIRKLAND J.J.: Superficially porous silica particles with wide pores for biomacromolecular separations, *J. Chromatogr. A.*, 2012, 1264, 22–30
- [10] SCHUSTER S.A., WAGNER B.M., BOYES B.E., KIRKLAND J.J.: Optimized superficially porous particles for protein separations, *J. Chromatogr. A.*, 2013, 1315, 118–126
- [11] HALÁSZ I., NAEFE M.: Influence of column parameters on peak broadening in high-pressure liquid chromatography, *Anal. Chem.*, 1972, 44, 76–84
- [12] ENDELE R., HALÁSZ I., UNGER K.: Influence of the particle size (5–35  $\mu$ m) of spherical silica on column efficiency in HPLC, *J. Chromatogr.*, 1974, 99, 377–393
- [13] DEWAELE C., VERZELE M.: Influence of the particle size distribution of the packing material in reversed-phase high-performance liquid chromatography, *J. Chromatogr.*, 1983, 260, 13–21
- [14] BILLEN J., GUILLARME D., RUDAZ S., VEUTHEY J.L., RITCHIE H., GRADY B., DESMET G.: Relation between the particle size distribution and the kinetic performance of packed columns. Application to a commercial sub-2  $\mu$ m particle material, *J. Chromatogr. A.*, 2007, 1161, 224–233
- [15] CABOOTER D., BILLEN J., TERRY H., LYNEN F., SANDRA P., DESMET G.: Kinetic plot and particle size distribution analysis to discuss the performance limits of sub-2  $\mu$ m and supra-2  $\mu$ m particle columns, *J. Chromatogr. A.*, 2008, 1204, 1–10
- [16] GRITTI F., FARKAS T., HENG J., GUIOCHON G.: On the relationship between band broadening and the particle-size distribution of the packing material in liquid chromatography: Theory and practice., *J. Chromatogr. A.*, 2011, 1218, 8209–8221
- [17] SNYDER L., KIRKLAND J., DOLAN J.: *Introduction to Modern Liquid Chromatography* (John Wiley, Hoboken, NJ) 2010
- [18] GUIOCHON G., FELINGER A., SHIRAZI D.G., KATTI A.M.: *Fundamentals of Preparative and Nonlinear Chromatography* (Academic Press, Amsterdam) 2006
- [19] JOHNSON N.L., KOTZ S., BALAKRISHNAN N.: *Continuous Univariate Distributions*, vol. 1 (Wiley, New York), second edn. 1994
- [20] WEISSTEIN E.W.: Change of Variables Theorem, From MathWorld – A Wolfram Web Resource, URL <http://mathworld.wolfram.com/ChangeofVariablesTheorem.html>
- [21] GALASSI M., DAVIES J., THEILER J., GOUGH B., JUNGMAN G., ALKEN P., BOOTH M., ROSSI F.: *GNU Scientific Library Reference Manual - Third Edition*, Network Theory Ltd. 2009
- [22] HORVATH C., LIPSKY S.R. : Peak capacity in chromatography, *Anal. Chem.*, 1967, 39, 1893–1893
- [23] GRUSHKA E.: Chromatographic peak capacity and the factors influencing it, *Anal. Chem.*, 1970, 42, 1142–1147



HUNGARIAN JOURNAL OF INDUSTRY AND CHEMISTRY

# HJIC

Advertise upcoming meetings,  
conferences and workshops;  
make public announcements;  
introduce your research laboratory;  
a new product or a service

on the pages of the

**Hungarian Journal of Industry and Chemistry**

Please contact us if interested!

---

EDITORIAL OFFICE: UNIVERSITY OF PANNONIA  
P.O. BOX 158, VESZPRÉM H-8201 (HUNGARY)  
Tel.: +36 (88) 624-746, E-mail: [hjic@almos.uni-pannon.hu](mailto:hjic@almos.uni-pannon.hu);  
web: [hjic.mk.uni-pannon.hu](http://hjic.mk.uni-pannon.hu)  
Felelős szerkesztő: Szilágyi Róbert, PhD  
Kiadja: Pannon Egyetem, 8200 Veszprém, Egyetem u. 10.  
Levélcím: H-8201 Veszprém, Postafiók 158, Tel.: (88) 624-000

## EFFECTS OF WASHING OF RAW MATERIAL ON PROPERTIES OF CARBON NANOTUBE CONTAINING POLY(ETHYLENE-TEREPHTHALATE) COMPOSITES

TÍMEA MOLNÁR,<sup>1</sup> CSILLA VARGA,<sup>1</sup> AND LÁSZLÓ BARTHA<sup>1</sup>

<sup>1</sup> Department of MOL Hydrocarbon & Coal Processing, University of Pannonia, Egyetem str.10, Veszprém, H-8200, HUNGARY

✉ E-mail: vcsilla@almos.uni-pannon.hu

Our interest has been focused on mechanical recycling of poly(ethylene-terephthalate) (PET) bottle waste, because recycling of plastic waste has crucial importance nowadays. The present article deals with the effects of washing of the secondary raw materials on properties of carbon nanotube (CNT) reinforced composites. In the first step advantageous washing compounds and their concentration were determined. After selecting the proper washing method extrusion moulding characteristics of PET granulates were investigated, and effects of carbon nanotubes as reinforcing additives and also application of coupling agents on the mechanical and rheological properties of composites were studied.

**Keywords:** carbon nanotubes, coupling agent, poly(ethylene-terephthalate), bottle waste recycling

### Introduction

Almost all human activities result in waste generation either directly or indirectly. Satisfying the daily needs for growing amounts of products results in higher consumption of raw materials, higher quantities of processing waste, and also higher amounts of wastes after the end of product life [1–4].

Selectively collected PET bottles derived from municipal solid waste considered as waste plastics of a specific type, but the liquid stored in them contaminates their surfaces. *Fig.1* shows the typical treatment cycle and possible recycling methods for plastic wastes, especially for the PET bottles collected selectively. Washing the surface of the waste materials is an important issue as biofilm can be formed. Therefore, this raw material will be contaminated with some biological content. Removing biofilm can be carried out in water, acidic or alkaline solvents. Effectiveness of the method is measured by using reactions with Folin reagent.

PET has excellent mechanical and chemical properties, therefore, its resistance against chemicals and irradiation is outstanding; however, it can also have serious impact on the environment, because the biodegradation requires a long time, and expensive pre-treatment methods are needed in order to bring them within reach of decomposing enzymes [3–8].

Carbon nanotubes (CNT) are members of the family of fullerenes with cylindrical shapes, where carbon atoms are located at the surface of a cylinder. Typical diameter is between the 1–50 nm regime, length can exceed even the 10  $\mu\text{m}$  scale. Carbon nanotubes have non-polar character. Their surface contains only a few functional groups, which can react with polymers. In

order to enhance the interaction between nanotubes and polymer matrices, the nanotube surface needs to be modified by application of coupling agents [7–11].

The given study deals with mechanical recycling of PET bottle wastes by applying secondary raw material for polymer matrix of CNT reinforced composites. After selecting the proper washing method, extrusion moulding characteristics of PET granulates were investigated. Furthermore, the effects of carbon nanotubes as reinforcing additives, and application of coupling agents on the mechanical and rheological properties of composites were studied.

### Experimental

#### Materials

Selectively collected PET bottles waste was used as the polymer matrix in the composites in washed and

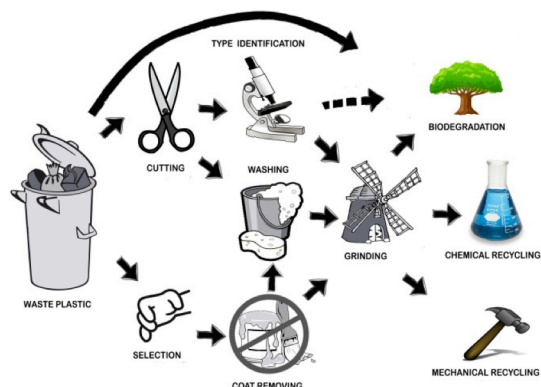
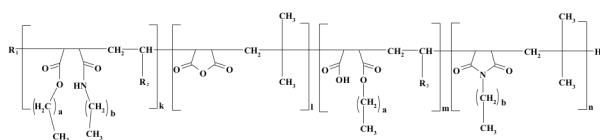
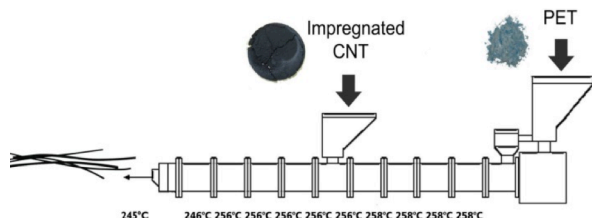


Figure 1: Pre-treatment and recycling of plastic wastes



**Figure 2:** Structure of the ester-amide-imide derivative of the experimental olefin-maleic-anhydride copolymer ( $R_1$ : alkyl group with length of the olefinic monomer ( $C_{16}$ - $C_{18}$ );  $R_2$ : alkyl group with  $R_1$ -2 carbon number; a: 3-40, b: 3-32; k: 0,2-2; l: 1-7; m: 1-7 and n: 0,3-2)



**Figure 3:** Production of PET composites in a twin-screw extruder

unwashed form. MFI values of the PET granulates were measured, and changed in the interval of 10–14 g ( $10 \text{ min}^{-1}$ ) ( $255 \text{ }^\circ\text{C}$ , 2.16 kg). Multi-walled carbon nanotubes (MWCNT) were produced at  $700 \text{ }^\circ\text{C}$  by chemical vapour deposition (CVD) process over Fe-Co bimetallic catalyst at the Department of Chemical Engineering, Institute of Chemical and Process Engineering, University of Pannonia. Purity of MWCNT was higher than 90 wt%, diameter was between 10 nm and 20 nm, the average length was above  $30 \mu\text{m}$  and the BET-surface was  $200 \text{ m}^2 \text{ g}^{-1}$ . Carbon nanotubes were applied in PET matrix in pristine and surface treated form. For treating surface of the carbon nanotubes experimental olefin-maleic-anhydride copolymer based coupling agents (Fig.2) were used with the properties summarized in Table 1. The ratios of the functional groups in coupling agents were determined by measuring acid value and saponification number by classical analytical methods and on the second hand the ratios were estimated by a previously developed FT-IR method [12].

#### Production of Composite Samples

CNT/PET composites were produced by a laboratory twin/screw extruder (LTE 20-44, LabTech Engineering, Fig.3). Temperature profiles and screw rotation speed for production were previously determined [13].

#### Washing of the Waste Material

After the washing process, raw materials from selectively collected PET and PET derived directly from waste deposit were compared. The solutions with 0.05 M concentration were used for both acidic and alkaline washing method. Citric acid and potassium hydroxide were chosen for the acidic and the alkaline wash.

#### Measurements

To determine the tensile properties of the extruded

**Table 1:** Main properties of coupling agents

property	CA-1	CA-2
acid value, mg KOH ( $\text{g sample}^{-1}$ )	12.8	33.1
saponification number, mg KOH ( $\text{g sample}^{-1}$ )	95.3	126.5
molecular weight ( $M_w$ )*, $\text{g mol}^{-1}$	3520	3660
polydispersity factor	1.10	1.40
ratio of functional group, %		
anhydride	7.9	12.0
semi-ester	2.7	37.6
ester-amide	44.7	25.2
imide	44.7	25.2

\* related to PS standard

**Table 2:** BET-surface of different carbon nanotubes

samples	surface area
pristine	$191.1 \text{ m}^2 \text{ g}^{-1}$
20% CA-1 coupling agent	$125.5 \text{ m}^2 \text{ g}^{-1}$
15% CA-2 coupling agent	$172.3 \text{ m}^2 \text{ g}^{-1}$
20% CA-2 coupling agent	$102.1 \text{ m}^2 \text{ g}^{-1}$

strings (namely strength, modulus, and extension) an INSTRON 3345 universal tensile testing machine was used. The temperature in the laboratory was  $23 \text{ }^\circ\text{C}$ , while relative humidity was 37% during the mechanical tests that were carried out at  $90 \text{ mm min}^{-1}$  crosshead-speed. Rheological measurements were carried out in a CEAST Smart RHEO 2000 capillary rheometer at  $265 \text{ }^\circ\text{C}$ . Before measurements, 180 second preheating was applied to all samples.

Structural information about the developed coupling agent was obtained by IR technique using a TENSOR 27 FTIR spectrometer (resolution:  $3 \text{ cm}^{-1}$ , illumination: SiCGlobal light, detector: RT-DLaTGS type) in the  $400\text{--}4000 \text{ cm}^{-1}$  spectral range.

Scanning Electron Microscopy (SEM) was used to study the morphology of fractured faces of specimens and to follow possible interaction between the reinforcements and matrices on a Phillips XL30 ESEM instrument.

## Results and Discussion

### Surface Treating

Effects of surface treatment were studied in two applications. Firstly, the coupling agents on the CNT surface was investigated, thereby properties of pristine CNT were compared to properties of two different coupling agent treated CNTs. BET-surface was measured and surface energy measurements were conducted. Secondly, the effects of concentration of the coupling agent applied on the CNT surface were studied with additive concentration to be 15% and 20%. By the surface treatment the BET surface of pristine CNT reduced at least by 35–40% (Table 2).

On the basis of mesopore volume distribution results (Fig.4), it was determined that coupling agents mainly attached to pores with diameters below 10 nm, because numbers of that pore size decreased the most. Structure

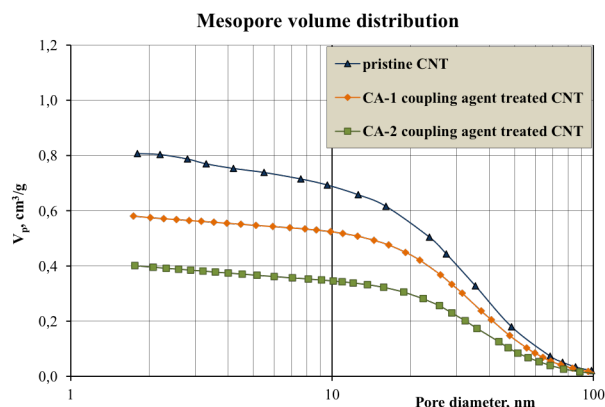


Figure 4: Changes in mesopore volume distribution due to surface treatment (20% coupling agent)

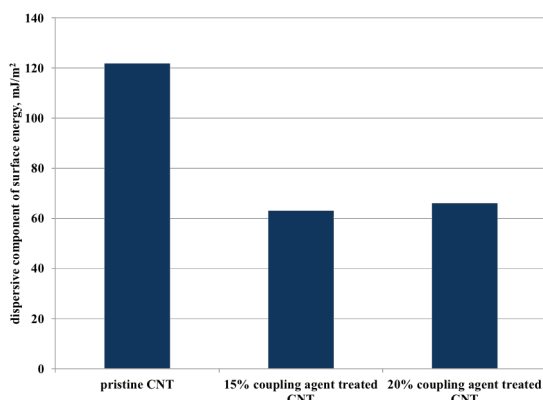


Figure 6: Dispersive surface energy based on Schultz-method (temperature: 70 °C)

of the coupling agent had considerable impact on the distribution since different ratios of decrease were measured in the mesopore volumes, therefore surface interactions with different strength may have evolved between the coupling agent and the CNT.

Concentration of the coupling agent on the CNT surface also influenced the results (Fig.5). Decreasing the concentration from 20% to 15% resulted in an increase in the mesopore volumes to such an extent that almost the values for pristine CNTs were achieved.

Properties of heterogeneous polymer systems are influenced by interfacial interactions and structure; however, no direct method is available to determine strength of interactions. Therefore, models are used generally for their estimation. Inverse gas chromatography measurements can be a useful tool for measuring the surface properties of different fillers and thus, the strength of interactions can be estimated. The dispersive component of surface energy describes London-interactions that can be used for estimation of the non-polar character, while other types of interactions (hydrogen-bond, polar, acid-base, etc....) are included in the specific component (Fig.6). We found that the dispersive surface energy of the coupling agent treated CNT was half of the pristine one at 70 °C (Fig.6). This is indicative of the surface treated carbon nanotubes likely having lower tendency for agglomeration than pristine CNTs. Constant for the acid-base interactions were calculated based on the GUTMANN equation [14] as summarized in Table 3.

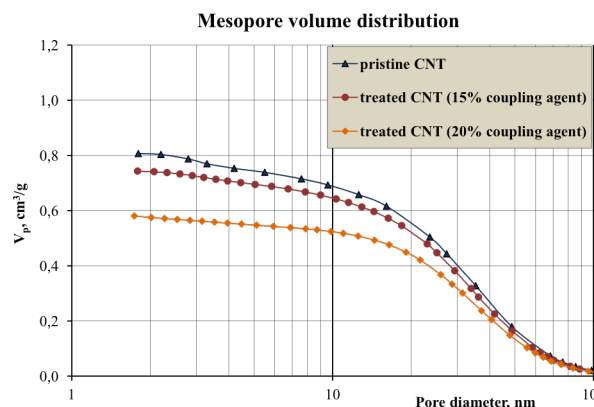


Figure 5: Changes in mesopore volume distribution due to surface treatment with various coupling agent (CA-2) concentrations

Table 3: Acid-base constants calculated by GUTMANN equation [14] at 70 °C

sample			R <sup>2</sup>
pristine CNT	K <sub>a</sub>	0.086	0.928
	K <sub>b</sub>	0.000	
15% coupling agent treated CNT (CA-1)	K <sub>a</sub>	0.086	0.806
	K <sub>b</sub>	0.253	
20% coupling agent treated CNT (CA-1)	K <sub>a</sub>	0.090	0.849
	K <sub>b</sub>	0.213	

On the basis of these results it can be stated that acid character of the pristine CNTs do not change significantly after surface treatment but the basic character improved. On the surface of the treated CNT-s weak basic active centres were predominant over acidic ones.

#### Effects of Washing

Both acidic and alkaline washing were shown to be effective by which biofilm had been removed from surface of PET granulates with 100% efficiency. Since biofilm cannot stick to the surface of PET due to its crystalline structure biofilm can be removed by application of weak acid or lye.

FT-IR spectra of the granules before and after washing gave the opportunity to study the changes in functional groups of the plastic. It is important to highlight that no significant differences were observed between FT-IR spectra of acidic and alkaline washed samples. Therefore, none of the compounds during washing deteriorated structure of PET (Fig.7).

#### Effect of Screw Rotational Speed

PET samples were produced at various screw rotational speeds to study their rheological behaviour and also their mechanical properties. Screw rotational speed during processing caused significant differences in viscosities in the low shear rate regime (beyond 500 s<sup>-1</sup>) (Fig.8).

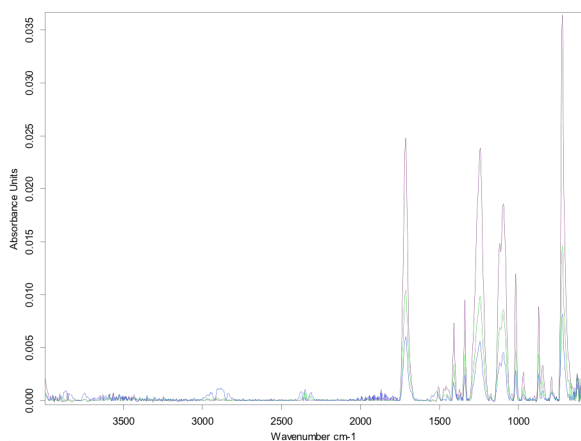


Figure 7: FT-IR spectra of PET sample in the 4000-600 cm<sup>-1</sup> wavenumber range (purple: potassium-hydroxide; green: citric acid; blue: without washing)

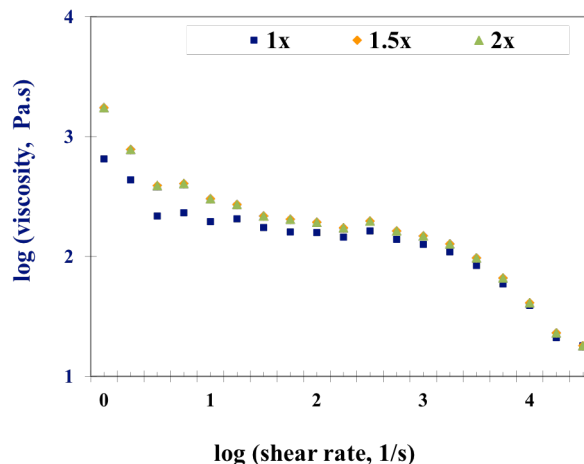


Figure 8: Effect of screw rotational speed on rheological behaviour of PET raw material

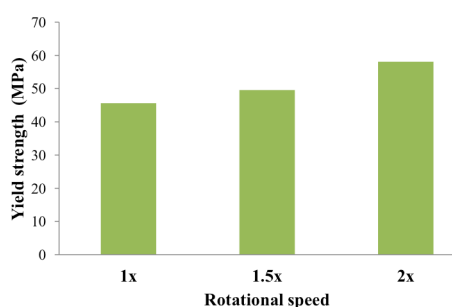


Figure 9: Effect of screw rotational speed on yield strength of PET raw material

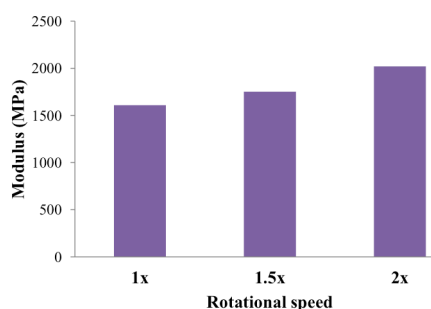


Figure 10: Effect of screw rotational speed on tensile modulus of PET raw material

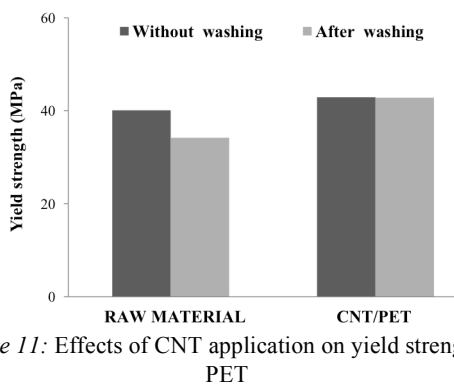


Figure 11: Effects of CNT application on yield strength of PET

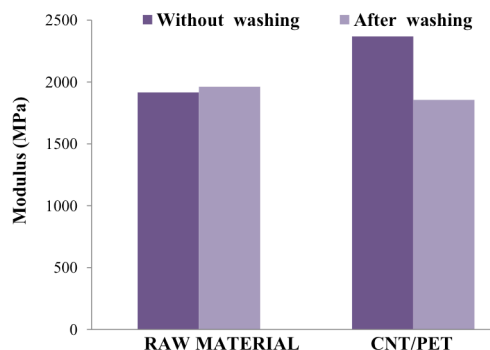


Figure 12: Effects of CNT application modulus of PET

In the medium shear rate region (500-5000 s<sup>-1</sup>) differences among the viscosities of the samples continuously disappeared. No differences were observed at higher shear rates, above 5000 s<sup>-1</sup> dedicated to shear rates characteristic for injection moulding. That indicated that all the samples could probably be injection moulded at the same parameters. All the tensile properties (yield strength, modulus) improved by increasing screw rotational speed during processing (Figs.9 and 10).

The highest values for the tensile properties were measured for samples produced at the highest screw rotational speed. Sample produced at the lowest rotational speed had values nearly identical to literature data [15]. However, samples processed at the highest rotational speed had 35–40% higher yield strength than the original material used for bottle production. It is important to note that washed PET granulates with the

lowest rotational speed could not be produced at the same temperature profile as the plastic melted.

#### PET Composites Containing Pristine CNT

Washing the raw material caused 15% deterioration in yield strength, but the modulus did not change. Untreated CNT could be introduced into the polymer melts at 2 wt% level both into washed and unwashed PET raw materials by the same side feeder screw rotational speeds. Application of pristine CNT did not influence yield strength of the composites (Figs.11 and 12), so yield strength of CNT/PET samples did not depend on the previous washing of the raw material.

The PET raw materials had ca. 2000 MPa tensile modulus either for washed and unwashed plastic, so rigidity of the samples was stated to be the same.

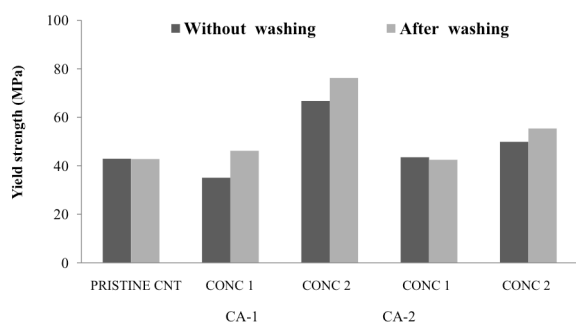


Figure 13: Tensile properties of surface treated CNT containing PET composites

Pristine CNT containing washed PET had 20% lower modulus than unwashed PET based samples had, thereby; the property of the PET raw material was achieved. Adding pristine CNT to washed PET plastic no difference was measured in the modulus compared to the washed PET without any reinforcing.

#### Effects of Type and Concentration of Coupling Agent

Two different, previously successfully applied coupling agents [13] were used on the surface of CNTs. Concentration of the coupling agents varied from 15% (CONC-1) to 20% (CONC-2) related to the weight of the pristine CNT. With respect of processing, surface treated CNTs were much easier to introduce into the polymer melt. CNT concentration could be elevated up to 2.7–2.9 wt% in the polymer matrix at the same processing parameters using coupling agent treated CNTs instead of pristine type.

Yield strengths of washed PET based composites increased with increasing concentration in the presence of both coupling agents compared to the pristine CNT containing PET sample (Figs.13 and 14). Improvement of 78% for CA-1, and 30% for CA-2 was realized in the presence of coupling agents at the higher concentration (20%). Using unwashed PET, as raw material also resulted in enhancement of yield strength, but to a different extent, such as CA-1 resulting in 55%, while CA-2 causing 16% increase.

Based on the above results, the CA-1 additive was worth applying in higher (20%) concentration due to the achieved more than 50% higher yield strength relative to the pristine CNT containing PET composite. Raw material is worth washing before processing if cost of washing could be balanced by the advantage of the 10 MPa increase in yield strength applying CA-1 coupling agent in 20% concentration. In case of CA-2 additive washing did not influence the properties at the lower (CONC-1) concentration level, but with higher additive concentration (CONC-2) a 14% difference was measured between the composites made from the two raw materials.

Comparing the samples with various additive concentrations an increase was observed in the modulus with increasing concentration for both raw materials and coupling agents. Applying unwashed raw material 34% improvement was realized with CA-1 coupling agent and 32% with CA-2 additive if the concentration

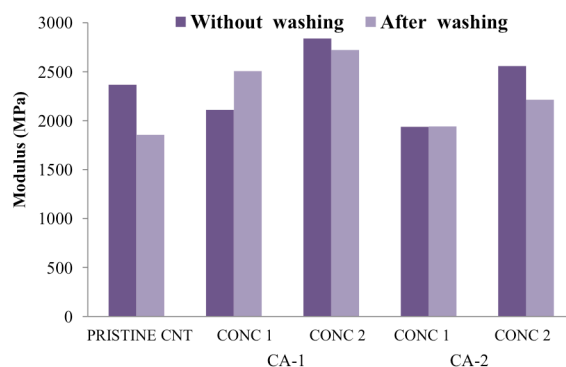


Figure 14: Tensile properties of surface treated CNT containing PET composites

increased from 15% to 20%. A lower degree of improvements were measured for washed PET based samples making the same comparison.

Comparison of pristine and surface treated CNT containing samples showed that coupling agent was advantageous to be applied in higher concentration from the point of view of the modulus either. For unwashed PET based composites application of coupling agents resulted in 10–15% decrease in modulus related to the pristine CNT containing sample. For washed PET based samples making the same comparison changes were calculated to be +45% in case of CA-1, and +20% for CA-2 additive.

The most advantageous observation based on the results is the lack of an effect on the mechanical properties in the investigated interval of raw material quality with respect of washing PET bottle waste, when used as polymer matrix for CNT reinforced composites. This could be realized in easier handling and pre-treating of the raw material before recycling.

#### SEM graphs

Broken surfaces of samples were studied by Scanning Electron Microscopy. CNTs concentrated at one side of the extruded string in pristine CNT containing samples (Fig.15A). Diameter of the probable carbon nanotube nucleation centres varied (Figs.15B and C). There were agglomerates with diameter of 30–40  $\mu\text{m}$  and also with 5–10  $\mu\text{m}$  number of the latter seemed to be higher. In addition, there were only a few nucleation centres both for washed and unwashed PET based composites.

On the cross section of the extruded strings a crystalline part was rendered likely in larger areas in coupling agent treated CNT containing samples than in pristine CNT/PET samples. In PET containing 15% CA-2 coupling agent a likely crystalline part was found at the middle of the extruded sample (Fig.16). More nucleation centres and more homogeneous structure were observed (Fig.16) than in pristine CNT containing sample from the same PET raw material. It is in accordance with the 15% lower CNT content of the pristine CNT/PET composite than the treated CNT containing one. The diameters of the nucleation parts were in the range of 20–30  $\mu\text{m}$ .

Area related to the probable crystalline structure was higher in washed PET based sample on the SEM graphs of the extruded strings (Fig.17A). Nucleation parts were

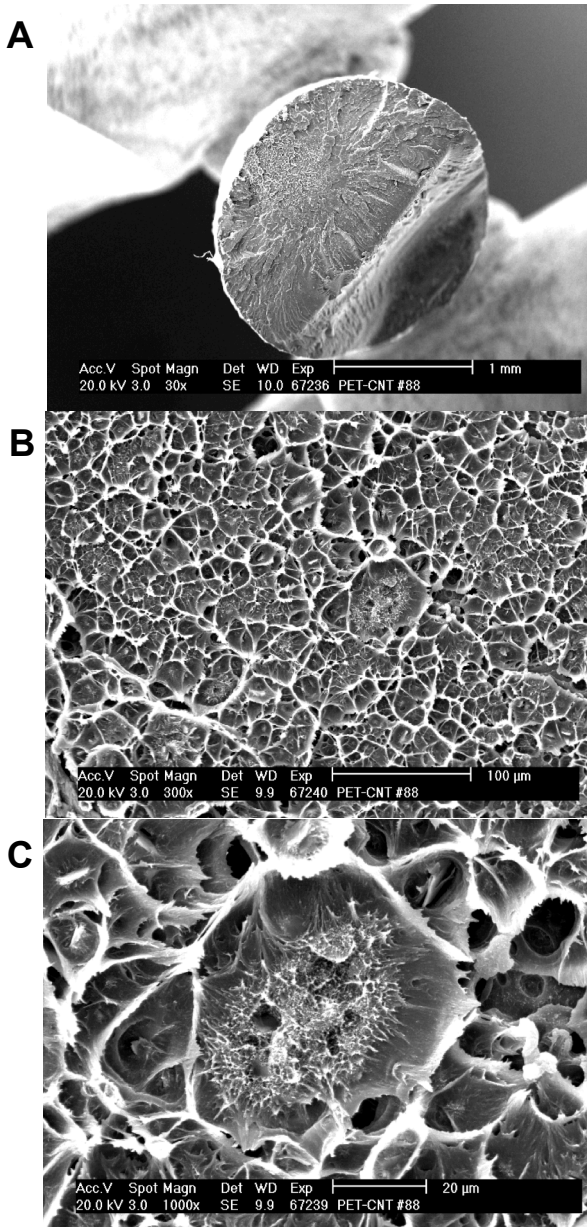


Figure 15: SEM graphs of PET sample containing pristine CNT

located in the middle of the sample and connected to each other diameters were identical to the former sample that was treated (Fig.17B).

Based on the SEM graphs it was concluded that carbon nanotubes were easier to handle and distribute more homogeneously due to surface treating both for washed and unwashed PET raw material, and on the other hand numbers of the nucleation parts and sizes could be influenced.

### Conclusions

The present article gave a brief insight into mechanical recycling of PET bottle wastes by applying that secondary raw material for polymer matrix of CNT reinforced composites. After selecting the proper washing method extrusion moulding characteristics of PET granulates were investigated and it was concluded

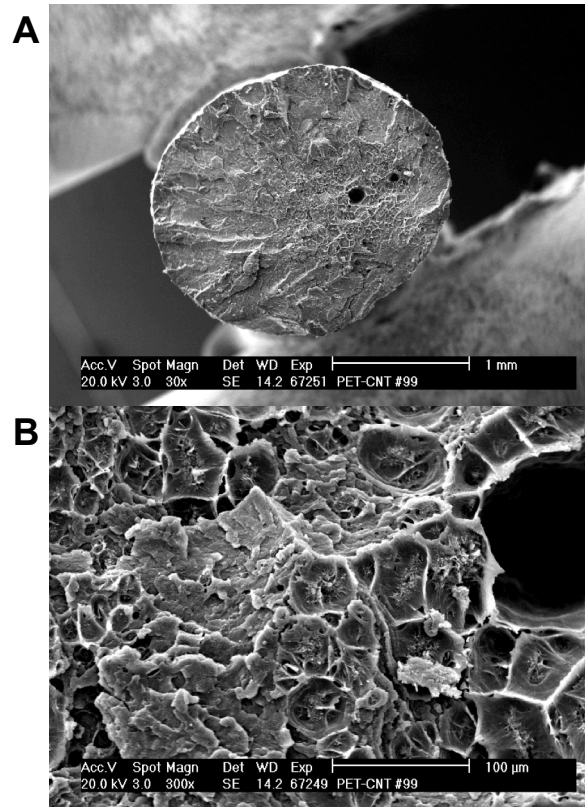


Figure 16: SEM graphs of unwashed PET based sample containing 15% CA-2 coupling agent treated carbon nanotube

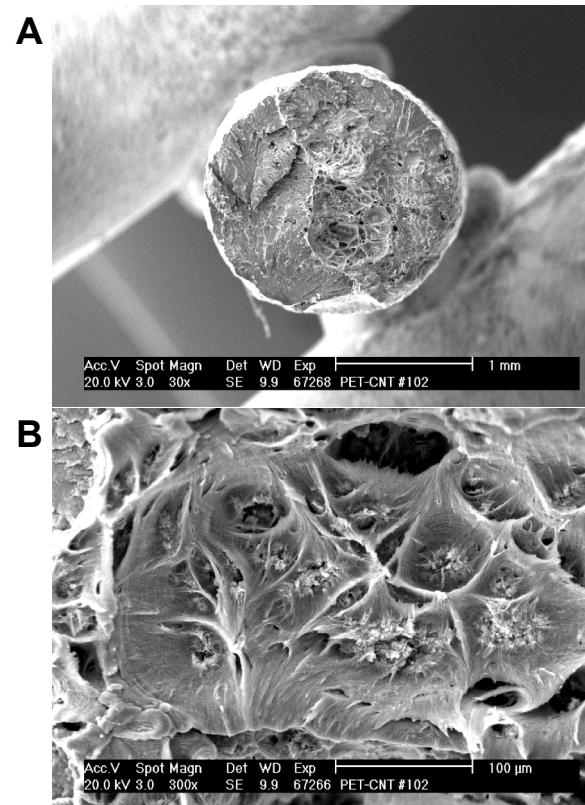


Figure 17: SEM graphs of washed PET based sample containing 20% CA-1 coupling agent treated carbon nanotube

that tensile properties improved by increasing screw rotational speed.

Effects of washing in carbon nanotubes containing PET composites were also investigated where carbon

nanotubes were applied either in pristine or surface treated form. Washing of the waste plastic did not affected yield strength in case of pristine carbon nanotubes containing samples but for coupling agent containing composites mechanical properties significantly changed. If the proper coupling agent was applied in higher concentration, 20% e.g. yield strength improved by higher than 60% while modulus increased at least 20%.

### Acknowledgements

This research was supported by the European Union and the State of Hungary, co-financed by the European Social Fund in the framework of TÁMOP-4.2.4.A/2-11/1-2012-0001 'National Excellence Program'. The authors are also grateful for the financial support of this work by the Hungarian State and the European Union under the TÁMOP-4.2.2.A-11/1/KONV/2012-0071 project.

### REFERENCES

- [1] LA MANTIA F.: Handbook of Plastic Recycling, Shrewsbury, Rapra Technology, 2002
- [2] WÉGNÉR K.: Towards more efficient waste management, Yearbook of Hungarian Plastic and Rubber Industry, 2013, 27–32 (in Hungarian)
- [3] WU G., LI J., XU Z.: Triboelectrostatic separation for granular plastic waste recycling: A review, Waste Mngnt., 2013, 33, 585–597
- [4] FORTELNY I., MICHALKOVÁ D., KRULIS Z.: An efficient method of material recycling of municipal plastic waste, Polym. Degrad. Stabil., 2004, 85, 975–979
- [5] AKSA W., MEDLES K., REZOUG M., BOUKHOULDA M.F., BILICI M., DASCALESCU L.: Two stage electrostatics separator for the recycling of plastic from waste electrical and electronic equipment, J Electrostat., 2013, 71, 681–688
- [6] SÁNCHEZ A.C., COLLINSON S.R.: The selective recycling of mixed plastic waste of polylactic acid and polyethylene terephthalate by control of process conditions, Eu. Polym. J., 2011, 47, 1970–1976
- [7] WANG Y., GAO J., MA Y., AGARWAL U.S.: Study on mechanical properties, thermal stability and crystallization behavior of PET/MMT nanocomposites, Composites Part B, 2006, 37, 399–407
- [8] LOGAKIS E., PISSIS P., POSPIECH D., KORWITZ A., KRAUSE B., REUTER U., PÖTSCHKE P.: Low electrical percolation threshold in poly(ethylene terephthalate)/multi-walled carbon nanotube nanocomposites, Eu. Polym. J., 2010, 46, 928–936
- [9] LI Z., LUO G., WEI F., HUANG Y.: Microstructure of carbon nanotubes/PET conductive composites fibers and their properties, Composites Sci. Techn., 2006, 66, 1022–1029
- [10] FIEDLER B., GOJNY F.H., WICHMANN M.H.G., NOLTE M.C.M., SCHULTE K.: Fundamental aspects of nano-reinforced composites, Composites Sci. Techn., 2006, 66, 3115–3125
- [11] BORRELL A., ROCHA V.G., TORRECILLAS R., FERNÁNDEZ A.: Surface coating on carbon nanofibers with alumina precursor by different synthesis routes, Composites Sci. Tehn., 2011, 71, 18–22
- [12] VARGA CS.: Production and investigation of compatibilizing additives for polymer composites, PhD Thesis, University of Pannonia, Veszprém, 2010 (in Hungarian)
- [13] MOLNÁR T.: Effects of carbon nanotubes and coupling agents in poly(ethylene-terephthalate) polymer, ITDK report, University of Pannonia, Veszprém, 2011 (in Hungarian)
- [14] GUTMANN V.: The donor-acceptor approach to molecular interactions, Plenum Press, New York, 1978
- [15] PÁL K.: Recycling of plastics wastes as secondary raw material, Műanyagipari Szemle, 2006/2

## **Acknowledgement**

The dedicated issue of the Hung. J. Ind. & Chem. and in part the organization of the 2014 Spring Scientific Students' Meeting at University of Pannonia were made possible from support provided by the National Talent Program of the Educational Research and Development Institute and the Human Resource Support Program of the Ministry of Human Resources within the framework of "Support of TDK Workshops Recognized by the Council of National Scientific Students' Association" (NTP-TDK-13)



## **Köszönetnyilvánítás**

Jelen kiadvány és részben a 2014. évi Tavaszi Tudományos Diáknapp a Pannon Egyetemen az Emberi Erőforrások Minisztériuma megbízásából az Oktatáskutató és Fejlesztő Intézet és az Emberi Erőforrás Támogatáskezelő által gondozott Nemzeti Tehetség Program „Az Országos Tudományos Diákköri Tanács által elismert TDK-műhelyek támogatása” (NTP-TDK-13) című pályázatának köszönhetően valósult meg.

## INVESTIGATION THE PROPERTIES OF Y-BA-Cu-OXIDE SUPERCONDUCTORS PREPARED BY HYDRAULIC PRESSING AND MOLDING

ANNA MALOVECZKY,✉ MARGIT ENISZ-BÓDOGH, AND TAMÁS KULCSÁR

Institute of Materials Engineering, University of Pannonia, Egyetem str. 10., Veszprém, 8200, HUNGARY  
✉E-mail: anna.maloveczky@gmail.com

Levitation applications of superconductors require the fabrication of bulk ceramic superconductors with special shapes. The conventional hydraulic pressing is not suitable for the production of superconductors with complicated forms, so we have applied slip casting to shape bulk superconductors. Superconducting powders with different  $\text{YBa}_2\text{Cu}_3\text{O}_y$  (123) and  $\text{Y}_2\text{BaCuO}_5$  (211) phase content and different (Pt, Pb, Ce) additives were prepared by solid-state reactions. The non-superconducting (211) particles can be considered as flux pinning centres; thus the magnetic properties can be influenced by their amount and particle sizes. The addition of a few weight percent of dopant in the nominal composition can modify the particle size and distribution of the (211) grains. We have investigated and compared the phase compositions, morphologies and magnetic levitation forces of bulk superconductors formed by hydraulic pressing and moulding. The shielding abilities of a moulded superconductor were simulated with the COMSOL Multiphysics 4.4 software.

**Keywords:** YBCO superconductor, moulding, shielding, modelling

### Introduction

The use of superconductivity is promoted by the need for stable high magnetic fields. The high-temperature superconductors are attractive for engineering applications, such as contactless superconducting bearings, trapped field magnets, levitation trains, fusion reactors, and NMR spectrometers. An important application of superconducting magnets is the Magnetic Resonant Imaging (MRI). Superconducting magnetic shielding can be used simultaneously to protect the personnel and other medical equipment from the strong magnetic fields produced by an MRI system.

The relative magnetic permeability of Type I superconductor is theoretically zero, which means when we use it for shielding, it expels the magnetic fluxes from itself. The high-Tc superconductors can also be used for shielding sensitive electronic devices from external electromagnetic fields. Due to the MEISSNER effect [1,2], it is sufficient to surround the volume to be protected by a thin film. For quasi-monocrystalline films of  $\text{YBaCuO}$  thickness of 1  $\mu\text{m}$  would be sufficient for virtually perfect shielding. A granular ceramic layer would require a larger thickness, but in all cases the thickness and weight of the superconducting shields would be much less than those of magnetic materials providing a comparable effect. For these applications of high-Tc superconductors outstanding magnetic properties and special shapes are required.

The scientific literature suggests two main ways for improving the magnetic properties of superconductors that are structure damaging or doping [3–9]. Both

methods work the same way, such as by increasing the amount of pinning centres (such as 211 phase) in the superconducting (123) material and decreasing the size of these centres by addition of different dopants. The damaging method could be done by ion or neutron radiation to destruct the bulk of the material and generate faults.

Preparation of high-Tc superconductors with special, complicated forms is a particular challenge due to their brittle nature. Slip casting, namely pouring low viscosity water-containing slurry into moulds is the oldest ceramic forming method for production of special shapes. For superconductors slip casting of shapes is also possible although the use of water as liquid phase is not optimal due to hydrolysis and other reactions. Another preparation method for ceramic superconductors is tape casting of viscous slurry containing ceramic particles in organic solvent [10].

### Materials and Methods

In this work, Y-Ba-Cu-oxid-based superconductive powders were prepared with different 123/211 phase content and different (Pt, Pb, Ce) additives. Shaped bulk superconductors were produced from these powders with hydraulic pressing and moulding. The effects of these parameters were investigated on the phase compositions, morphologies and magnetic levitation forces of the sintered bulk superconductors.

For modelling the superconductor as a shield in different geometries, COMSOL Multiphysics 4.4 software was used that provides a simulating and

Table 1: The peak intensity of the crystalline phases

	Samples Binder	Solvent	Peak intensity, counts				
			123	211	011		
			d=2.72 Å	d=2.99 Å	BaCuO <sub>2</sub> d=3.05 Å	CuO d=2.52 Å	BaCO <sub>3</sub> d=3.72 Å
1.	polyvinyl formal	dioxane	4460	1122	562	956	-
2.	metylan	dest. water	2952	919	737	725	-
3.	metylan	ethanol	1477	765	679	459	-

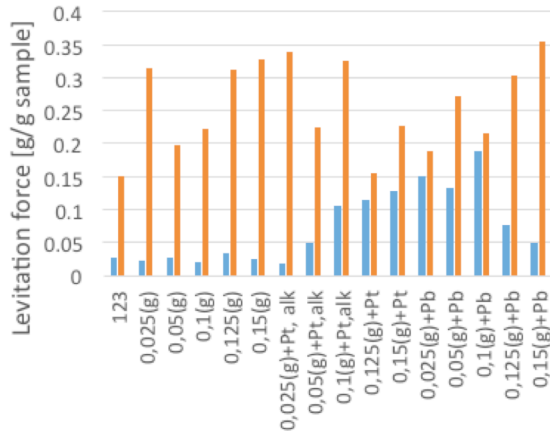


Figure 1: Levitation forces of the heat treated samples

modelling environment using the finite element method. Instead of the original AC-DC module of COMSOL, a module by ROBERTO BAMBILLA was used, which was developed for modelling YBCO superconductors.

## Results and Discussions

### Samples Made by Hydraulic Pressing

The superconducting samples were prepared by using  $Y_2O_3$ ,  $Ba(OH)_2 \cdot 8H_2O$  and CuO. The latter was obtained by the calcinations of  $Cu(OH)_2 \cdot CuCO_3 \cdot nH_2O$  with a specific surface area of  $18.4 \text{ m}^2 \text{ g}^{-1}$ ,  $PtCl_4$ ,  $PbO$  and  $Ce(NO_3)_3 \cdot 6H_2O$  starting materials. The 123:211 molecular ratio of the nominal compositions was changed in the range of 1.00:0.15. Samples were prepared without additives as well as with 2.0 wt% Ce + 0.5 wt% Pt, and 2.0 wt% Ce + 0.5 wt% Pb dopants.

For sample preparations, barium-hydroxide was ground in agate mortar, but in some cases the pulverization and grinding was made in the presence of alcohol. The mixture of raw materials was homogenized by thoroughly mixing with alcohol in an agate mortar and compacted into disks of  $25 \text{ mm} \times 3 \text{ mm}$  by hydraulic pressing at 70 MPa. Firstly, the samples were pre-reacted at  $960 \text{ }^\circ\text{C}$  for 4 hours to obtain the desired (123+211) phases by solid-state reaction. The heat-treated samples were ground and the powders were pressed into pellets by hydraulic pressing using a pressure of 70 MPa. The relatively dense structure was obtained by liquid state sintering at  $1010 \text{ }^\circ\text{C}$  peak temperature for 6 hours in oxygen atmosphere [11].

The levitation force of the samples after the heat treatments is shown in Fig.1. As described in the

literature, we also found that the levitation force shows an increasing trend with increasing amount of 211 phases. In the case of Ce+Pt and Ce+Pb dopant containing samples higher levitation forces can be obtained after the first heat treatment at  $960 \text{ }^\circ\text{C}$ . It is notable that the samples prepared from barium hydroxide ground in the presence of alcohol showed improved magnetic properties.

### Samples Made by Moulding

Part of the pre-reacted at  $960^\circ\text{C}$  ground samples were used for shaping superconductors by moulding. Previously, superconductive slurries were prepared with different organic liquid additives and those were burnt out during the annealing. From these materials only a few were good enough for further studies. Samples providing a proper cohesion and appearing to be homogeneous were selected for future analysis. After heat treatment, X-ray diffraction analysis was used to study the phase composition changes caused by addition of organic materials for deciding if any of the dopants has a negative influence on the superconductor properties.

As shown in Table 1, the metylan reduces the amount of the superconducting phase (123) and this leads to the tetragonal, non-superconducting structure. Polyvinyl formal did not have a negative influence on the formation of 123 phase. Thus, the polyvinyl formal binder was chosen with dioxane for further experiments. With respect of ideal concentrations, it was found that 1 wt% of polyvinyl formal/dioxane must be added to the superconducting powders to obtain a slurry with a density of  $2.4 \text{ g cm}^{-3}$ , which was dense enough, but still can be poured. The second step was to find the appropriate mould form.

Different types of materials were investigated, such as stainless steel, glass, plastic, gypsum, and silicone rubber. The prepared slurries stuck to most of these materials rendering them useless for moulding with the exception of silicone rubber as sample could be removed perfectly. Using this type of moulds we can make superconductors with complex geometry.

The moulded samples were heat treated at the same program as used for hydraulic pressed samples. The moulding technique applies no pressing thus provides a porous structure. However, the pores can lead to poor superconductor properties. To decrease the porosity melt-producing dopants were applied. Ag and Pb with Ce proved to be good in the case of hydraulic pressed samples.

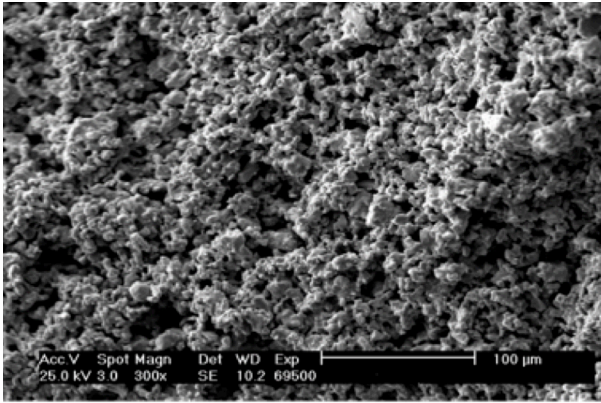


Figure 2: SEM micrograph of the moulded sample ground conventionally

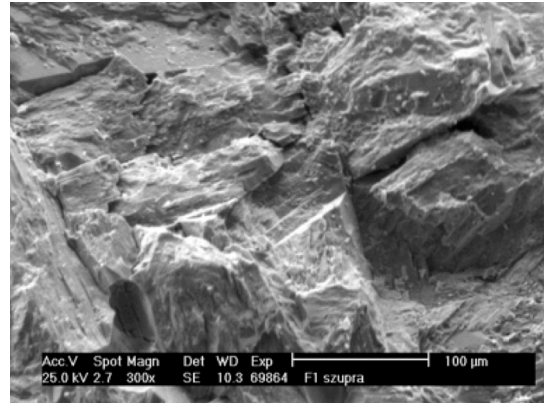


Figure 3: SEM micrograph of the moulded sample ground in alcohol

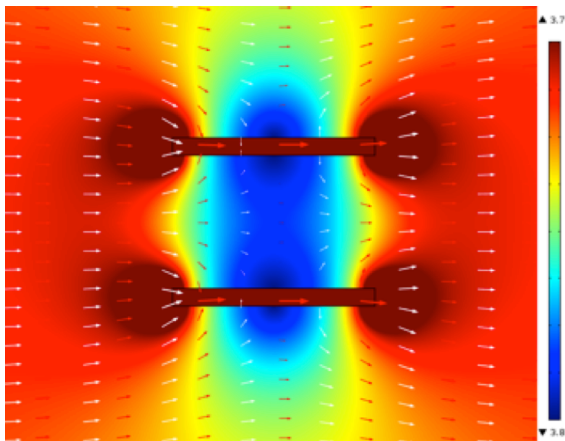


Figure 4: Simulation of iron shield

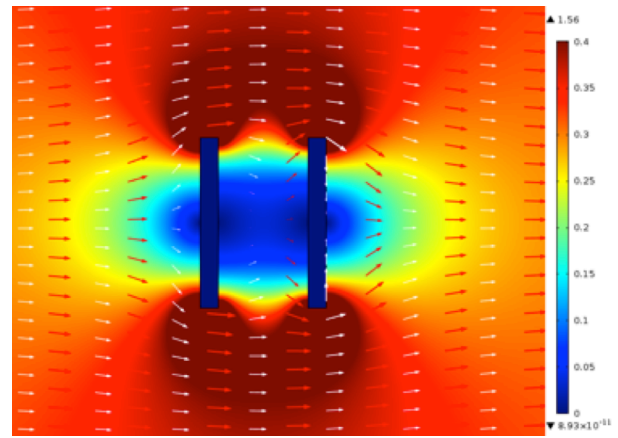


Figure 5: Simulation of superconductor shield

It was found that only in the moulded samples prepared from barium hydroxide ground in alcohol provide enough melt for efficiently fill the pores. The use of dopants alone toward this goal was not sufficient. Furthermore, with this grinding technique, the peritectic temperature of the superconducting phase (123) decreased, which allowed for a more economical heat treatment. It can be proposed that this grinding resulted in particle size reduction of barium hydroxide and the higher specific surface area leading to higher reactivity. In this case bulk superconductor with higher density can be obtained, which has an oriented, large plate-like 123-crystals containing structure (Figs.2 and 3).

#### Modelling YBCO as Magnetic Shield

YBCO can shield from magnetic fluxes due to the MEISSNER effect. It works the opposite way than the commonly used ferromagnetic materials, which means that superconductor expels the magnetic fluxes from itself, while iron collects them. Using the COMSOL Multiphysics 4.4 package, the shields of iron and superconductor were compared in Figs.4 and 5.

The shielding ability of the superconductor is comparable with iron, and even better. It has the advantage that in alternating magnetic field it does not get heated. The ferromagnetic materials shield poorly in too small and too big fields because they have saturation flux density. Superconductors are being used as shields in various devices [12–16].

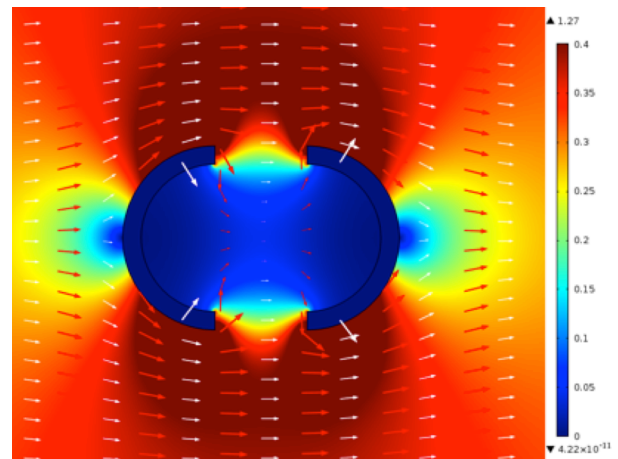


Figure 6: Simulation of shielding for shell geometry

With a geometry shown in Fig.6, very sensitive magnetic devices could be fully shielded and *vice versa* the environment could be protected from a device, which induces strong magnetic field. With the shape in Fig.7, for example a skull could be protected in the MRI in case of presence of metal implants in the head.

Theoretically moulding could be used to prepare these shields. It would be cheaper and thin layers could be made, thus more economical wall could be produced by a few thin layers.

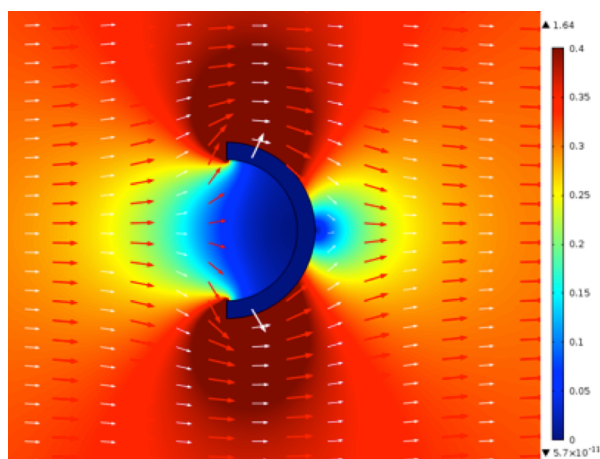


Figure 7: Simulation of shielding using a semi-sphere geometry

### Conclusion

In the case of the hydraulic pressed pellets, the results confirmed those from the literatures. Improved magnetic properties were noticed with the increasing of the 211 phase content. This was further enhanced by the presence dopants. It was found that Pb performs as good as Pt or even a little bit better, which is preferred due to the price of Pt. The grinding of barium-hydroxide in the presence of alcohol provided a denser structure and more melt phase leading to better superconducting properties. Furthermore, it seems that this method decreases the peritectic temperature of the superconducting 123 phase. The homogenization needs to take place after grinding in alcohol to be effective.

The adequate liquid-to-material ratio to make a slurry with 1 wt% polyvinyl formal in dioxane and the ideal moulding form of silicone rubber were determined. This allowed for making complex shaped superconductors. The melt-producing dopants cannot reduce the porosity enough to sufficiently improve the levitation force. Alternative heat treatment programs with slow annealing up to 500 °C, while all of the organic materials burn out, can avoid the cracks in the structure. Application of vacuum during the moulding can also be useful, since it can eliminate trapped air bubbles from the mass.

Simulations carried out using Comsol Multiphysics 4.4 software indicated YBCO being a good shielding material. Utilization of complex geometries, sensitive devices can be protected, such as skull protection during MRI measurements.

### REFERENCES

- [1] TAKASH M., TOMIOKA Y., MIYAUCHI T., SATO S., MURAI A., IDO T., WAKITA K., TERADA H., OHKIDO S., MATSUBARA M.: Characterization of a large-scale non-doped  $\text{YBa}_2\text{Cu}_3\text{O}_{7-x}$  superconductor prepared by plastic forming without high-pressure molding, *J. Amer. Ceram. Soc.* 2007, 90(7), 2032–2037
- [2] EVETTS J.: Concise Encyclopaedia of Magnetic and Superconducting Materials, Pergamum Press, Oxford, 1992, pp. 532–533
- [3] MONOT I., LEBLOND C., MARINEL S.M., DESGARDIN G.: Precursor and microstructure control for melt texturing of high-Tc superconductive YBCO ceramics, Development of high-temperature superconducting alternators combining rotating and levitating principles, Russian Academy of Science, Saint-Petersburg, 2002, pp. 27–45
- [4] SHLYK L., NENKOV K., KRABBES G., FUCHS G.: Melt-processed YBCO with Pt or Ce additions: comparison of pinning behaviour, *Physica C* 2005, 423, 22–28
- [5] RICHES J.D., ALARCO J.A., BARRY J.C.: Effects of  $\text{PtO}_2$  and  $\text{CeO}_2$  additives on the microstructures of the quenched melts of Y–Ba–Cu–O materials *Physica C Superconductivity*, 2000, 336, 43–56
- [6] LEBLOND C., MONOT I., PROVOST J., DESGARDIN G.: Optimization of the texture formation and characterization of large size top-seeded-melt-grown YBCO pellets, *Physica C*, 1999, 311, 211–222
- [7] HARDY V., SIMON C., PROVOST J., GROULT D.: Pinning forces in Bi-2212 single crystals irradiated by 6 GeV Pb ions, *Physica C*, 1993, 206, 220–226
- [8] WESCHE R.: Magnetic relaxation and flux pinning in  $\text{YBa}_2\text{Cu}_3\text{O}_7$  a high-Tc oxide irradiated by 5.3 GeV Pb ions, *Physica North-Holland C* 1992, 190, 289–298
- [9] HORVAT J., WANG X.L., DOU S.X.: Vortex pinning in heavily Pb-doped Bi2212 crystals *Physica C* 1999, 324, 211–219
- [10] GRADER G.S., JOHSON D.W.: Forming methods for high Tc superconductors, *Thermochimica Acta*, 1991, 174, 239–251
- [11] KOMLAI K.: Investigation of the the properties of the incongruent melting reaction of  $\text{YBa}_2\text{Cu}_3\text{O}_y$  superconductor phase, M.Sc. Thesis, University of Pannonia, 2013 (in Hungarian)
- [12] TAVERNIER S.P.K., VAN DEN BOGAERT F., VAN LANCKER L.: The design of a magnetic shielding for an array of photomultipliers in a strong external field, *Nucl. Instrum. Methods*, 1979, 167, 391–398
- [13] BITTER T., EISERT F., EL-MUZEINI P., KESSLER M., KINKEL U., MEMT E., LIPPERT W., MEIENBURG W., WERNER R.: A large volume magnetic shielding system for the ILL neutron-antineutron oscillation experiment, *Nucl. Instrum. Methods Phys. Res.*, 1991, A309, 521–529
- [14] TRIPATHI A., VEDAVATHY T.S.: Electromagnetic shielding using superconductors, Pergamon Press Ltd, Oxford, Vol. 2, No. I, 1994, pp. 1–5
- [15] SPILLANTINI P.: Active shielding for long duration interplanetary manned missions, *Adv. Space Res.*, 2010, 45, 900–916
- [16] YUSUF S.M., OSGOOD III R.M., JIANG J.S., SOWERS C.H., BADER S.D., FULLERTON E.E., FELCHER G.P.: Magnetic profile in Nb/Si superconducting multilayers, *J. Magnet. Magnetic Mat.*, 1999, 198–199, 564–566

## EFFECTS OF ULTRASONIC DISINTEGRATION, HOT-COMPRESSED LIQUID WATER PRE-TREATMENT, AND STEAM EXPLOSION ON SOLVOLYSIS AND DIGESTIBILITY OF GRAIN SORGHUM STOVER

DÁNIEL CAPÁRI,<sup>✉</sup> AND ANDRÁS DALLOS

Department of Physical Chemistry, University of Pannonia, Egyetem str. 10, Veszprém, H-8200, HUNGARY  
<sup>✉</sup>E-mail: capari.daniel@gmail.com

One of the most promising renewable energy crops and biomass feedstock for biogas production in Europe is the C4 plant grain sorghum due to its high photosynthetic efficiency. The release of lignocellulosic material and therefore the acceleration of degradation processes of sorghum stalks and leaves can be achieved using mechanical and thermal pre-treatments, which assist to hydrolyse the cell walls and speed the solvolysis of biopolymers. This study is focused on hot-compressed liquid water, steam explosion and ultrasonic pre-treatments of grain sorghum stover. The effectiveness of pre-treatments was evaluated by means of soluble chemical oxygen demand, biochemical oxygen demand, and by the biogas and methane productivities. The results show that the pre-treatments disintegrated the lignocellulosic structure, increased and accelerated the biogas and methane production, and increased the mesophilic anaerobic digestion potential of grain sorghum stover. Our laboratory tests demonstrated that the steam exploded grain sorghum stover possess the highest biogas productivity.

**Keywords:** grain sorghum stover; hot-compressed liquid water pre-treatment; steam explosion; ultrasonic disintegration, biogas digestion.

### Introduction

The grain sorghum is a possible carbohydrate resource for the simultaneous production of bioethanol and biogas due to its advantages over the traditional agricultural crops. The plants have remarkably good CO<sub>2</sub> absorption ability. Grain sorghum is the fifth most important cereal crop grown in the world. The drought tolerance of sorghum is greater than that of corn. Furthermore, it is able to regenerate after a period of drought. Its productivity is also higher than that of corn, even in dry periods or in lower quality soils. In Hungary, sorghum grows in arid areas as a substitution for fodder corn. Therefore sorghum could be used to cultivate alternative feedstock for bioethanol production [1] and could be a sustainable crop for energy production in Europe. The sorghum grain contains approximately the same amount of starch compared to corn kernels, which makes it attractive as raw material for the production of bioethanol. The agricultural by-product of sorghum-based bioethanol production, the sorghum stover is a valuable bioenergy substrate for biogas digesters, despite the complex lignocellulosic structures of sorghum stalks and leaves and its resistance to decomposition. The utility and the economic feasibility in biogas power plants can be highly increased by different pre-treatment methods, to assist the disruption of the cell wall structure and to speed-up the solubilisation of the biopolymers in the

biogas feedstock [2–4]. The purpose of pre-treatments is to remove lignin and hemicellulose, reduce cellulose crystallinity, and increase porosity [5,6] (*Fig. 1*).

Liquid hot-compressed water (LHCW) pre-treatment is a commonly used hydrothermal method. High temperature and high pressure are applied to maintain liquid phase and to avoid vaporization. During the pre-treatment, water is penetrated into the cell structure of the biomass, hydrating cellulose, solubilizing hemicellulose, and slightly removing lignin. LHCW pre-treatment is highly effective for enlarging the accessible and susceptible surface area of cellulose and improving cellulose degradability for microbes and their enzymes [7,8]. After the hydrothermal treatment, the biogas production was increased for pig manure, for municipal sewage sludge and for fruit/vegetable waste

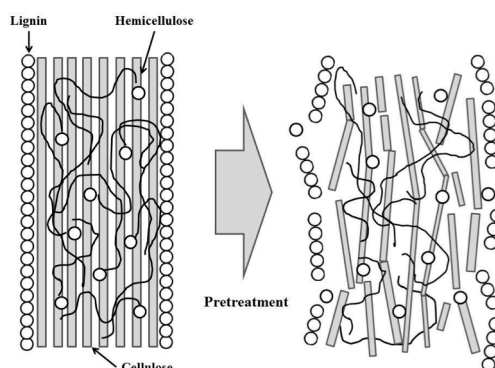


Figure 1: The disintegration of lignocellulosic material by pre-treatments

[9]. The hot water treatment increases the enzymatic hydrolysis and digestion of corn leaf, stalk and fibre [10,11] and the dissolution of solids and xylan of destarched corn fibre [12]. The liquid hot water pre-treatment of sorghum bagasse produced higher solubilisation of hemicellulose and cellulose content enrichment [13]. Combining hydrothermal treatment and enzymatic hydrolysis of sorghum bagasse resulted in improvement of cellulose and total polysaccharides hydrolysis [14].

Steam explosion (SE) is one of the most effective methods for the pre-treatment of lignocellulosic biomass. In this process, the biomass is heated with high-pressure steam for a certain period, then the pressure is reduced to atmospheric pressure as quickly as possible. The biomass is undergone on an explosive decompression by this swift reduction of pressure [6,7]. The high efficiency of the steam explosion treatment is due to the thermo-mechano-chemical destruction applied in the method. Steam-explosion has been used to treat various kinds of lignocellulosic biomass (i.e. softwood, sugarcane bagasse, corn stalk) for enhanced bioethanol and biogas production [15–19]. SIPOS *et al.* [20] demonstrated the efficient effect of pre-treatment by steam on sorghum bagasse characterized by high degree of cellulose hydrolysis. ZHANG *et al.* [21] compared four pre-treatment processes including liquids, steam explosion, lime and dilute acid for enzymatic hydrolysis of sorghum bagasse and pointed out that steam-explosion showed the greatest improvement on enzymatic hydrolysis.

The biogas yields of anaerobic digestion can be also increased by ultrasonic treatments (UT) to support the solubilisation of raw materials. During the ultrasonic treatment, a cyclic sound pressure is used to disintegrate the cell walls by cavitation. The parameters of the sonication are the power, frequency and time of sonication [3,22]. ZHANG *et al.* [23] showed that ultrasonic pre-treatments caused indistinctive effects on bio-hydrogen production. The ultrasonic treatment accelerated the enzymatic hydrolysis of corn stover and sugar cane bagasse cellulose [24] and improved the liquefaction and saccharification of sorghum flour [25]. IMAM *et al.* [26] pointed out the positive effects of ultrasonic plus hot water pre-treatment on the conversion of sweet sorghum to hexose and pentose sugars and on lignin, cellulose and hemicellulose concentrations.

However, no systematic studies on pre-treatments of grain sorghum stover are available in literature. A correct comparison of the various pre-treatments and the selection of the suitable processes for the disintegration of grain sorghum stover as feedstock for enhanced biogas production are the goals and the novelty of this paper. However, the main message of this work is that a perfect testing is only possible, if there are no differences in the microbial communities in different biogas fermenters, in the inocula used, in the substrates cultivated and in the methods applied to assess pre-treatments: chemical analysis, batch tests or continuous AD.

Therefore this work is focused on liquid hot-compressed water, steam explosion and ultrasonic pre-treatments of grain sorghum stover using both fast analytical, biochemical and biomethane potential AD tests to study and comparison the effects of pre-treatments on anaerobic digestion without addition of chemicals. The influence of temperature, contact time of thermal treatments, and the effect of sonication energy on decomposition of lignocellulose on a chemical level were determined using laboratory scale experimental techniques. The effectiveness of thermal and ultrasonic treatments was evaluated by SCOD and BOD<sub>5</sub> concentrations and by the biogas and methane productivities during mesophilic fermentations.

## Experimental

### Materials

Sorghum stover investigated in this work consists of leaves and stalks of commercial grain sorghum (Milo) hybrid named *Mexican Sweet* (code: HF1) harvested from the B12 field at Kétegyháza, Hungary, and used for pre-treatments and biogas production experiments. This easily grown hybrid with mid-early maturation was developed by J. FECZAK (Agroszemek Ltd., Szeged, Hungary). Post-harvest residue grain sorghum stover samples were chopped, homogenized, and analysed for dry substance (DS, 93.6%), organic dry substance (94.5%), and ash (5.5%). Deionized water was used in all experiments after cation and anion exchange.

### Liquid Hot-Compressed Water Treatments

The LHCW pre-treatments were carried out in a 2 L capacity Parr 4843 type high-pressure reactor at the temperatures of 100, 150 and 175 °C (0.1, 0.5 and 0.9 MPa, respectively) and at various treating time from 10 to 120 minutes. 25 g of grain sorghum stover were used in each experiment and were added to 1000 g of water. The suspension was introduced in the thermal reactor at room temperature and heated to the set temperature. The pulp slurry was mixed by a built-in stirrer at 300 rpm during the entire treating process to avoid temperature gradients. After treatment, the reactor was cooled down to 30 °C by the built-in cooling system of the reactor using cold water-flow and the treated slurry was removed from the vessel.

### Steam Explosion Pre-treatments

SE treatments were performed in a steam explosion laboratory unit (*Fig.2*) consisted of a steam generator (2), a digester vessel (6) and a separator cyclone (8). A 2 L capacity PARR 4843 reactor was used for the production of steam with temperatures of 185, 200, and 215 °C and working pressures of 1.1 MPa, 1.6 MPa, and 2.1 MPa, respectively. The SE unit operated in batches and equipped with a digester vessel (6) of 200 cm<sup>3</sup> volume. The digester vessel was filled with 10 g

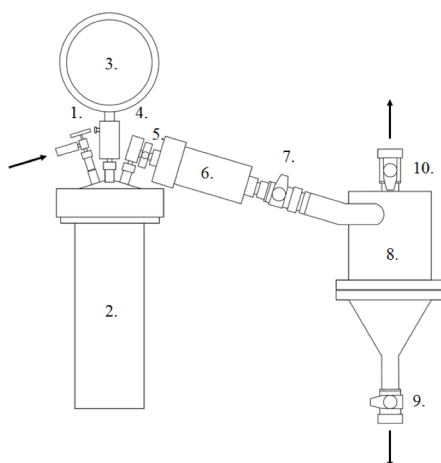


Figure 2: Scheme of the steam explosion apparatus (1. input valve, 2. steam generator, Parr 4843 reactor, 3. pressure gauge, 4. evacuation valve, 5. steam inlet valve, 6. digester vessel, 7. expansion valve, 8. cyclone, 9. sampling valve, 10. steam outlet valve)

feedstock per batch and was heated to the desired temperature, directly with saturated steam led to the vessel, by opening the steam inlet valve (5). No catalysts (additional chemicals) were applied in the process. After the steaming time (1–10 minutes), the expansion valve (7) was opened to rapidly reduce the vessel pressure to the atmospheric one. The steamed sample slurry explosively released into the separator cyclone (8).

#### Ultrasonic treatments

The ultrasonication was performed in a Vibracell VCX 750 (Sonics & Materials, USA) ultrasonic processor operated at constant sonication frequency of 20 kHz with maximum power input of 750 W. The radiation was carried out by a 25.4 mm diameter titan alloy (Ti-6Al-4V) probe with removable tip and maximum amplitude of 35  $\mu\text{m}$ . Samples of the mixture of grain sorghum stover (1 g) and water (99 g) placed in a temperature-controlled vessel. They were subjected to ultrasonic pre-treatment without additional agitation at different power inputs by adjustment of the amplitude (50, 70 and 100%) and at various sonication durations of from 1 to 10 minutes for each power level. The temperature of the vessel was held constant at 25 °C during the treatment by a high-precision thermostat (Huber Kältemaschinenbau GmbH, Germany).

Aliquot parts of the resulting sorghum stover pulp slurries of samples obtained from pre-treatments were used as substrate in AD test. The rests were filtered to separate the solid fraction from the liquid fraction for analytical measurements (SCOD, BOD<sub>5</sub>, pH). A set of untreated, blank samples was also tested for chemical analysis and methane potential by AD as the control points of reference for the treated samples.

#### Mesophilic Anaerobic Digestions

The anaerobic degradability of untreated, LHCW, SE, and UT pre-treated grain sorghum stover slurries was determined in laboratory scale, using a fermenter system

contained 12 Pyrex batch reactors of 1 L capacities. Inoculum for the AD tests was taken from the effluent line of an anaerobic pilot fermenter [27] treating a mixture of swine manure and corn stillage (spent mash remaining after bioethanol distillation) at biogas test facility of DENK Ltd (Kövegyűrpusztá, Hungary). The batch reactors were inoculated by 700 g inocula. Afterwards a batch of 100 g of grain sorghum stover pulp slurry samples was added under nitrogen atmosphere. Furthermore, the digester materials were bubbled with nitrogen gas for 10 minutes to get rid of the air from the liquid phase before each experiment. The batch reactors were kept in a temperature-controlled water bath at 37 °C until they stopped producing biogas. The mesophilic AD tests performed for grain sorghum stover substrates including controls were all done in duplicate. During the 36–40 days mesophilic AD tests the flows of the produced biogas were on-line measured by digital flow meters and the daily and cumulated biogas volumes were stored digitally. The methane content was determined by gas chromatography.

#### Analytical and Biochemical Measurements

The SCOD, pH, and BOD<sub>5</sub> measurements were carried out on the liquid fractions after 10 min centrifugation at 14,000 rpm and 20 °C with a refrigerated universal high-speed, filtration (0.45  $\mu\text{m}$ ) centrifuge (UniCen MR, Herolab, Germany). Colorimetric SCOD concentration was measured by the Standard Methods procedure [28] using a Nanocolor Vario Compact heating block (MACHEREY-NAGEL, Germany) and a MultiDirect photometer (Tintometer/Lovibond, Germany) according to DIN ISO 15705. Biochemical oxygen demand (BOD<sub>5</sub>) was determined according to EN 1899-1 and EN 1899-2 by using OxiTop Control 6 OC 100 (WTW, Germany) system. The pH values were measured by a C831 type pH meter (Consort, Belgium) with an RA-0903P sensor (Radelkis, Hungary) after two-point pH calibration (pH = 4.01  $\pm$  0.01 and pH = 7.00  $\pm$  0.01) using DuraCal pH buffers (Hamilton, Switzerland). The surfaces of the grain sorghum stalk were investigated by a PHILIPS XL30ESEM environmental scanning electron microscope (ESEM) with 20 kV accelerating voltage and resolution of 3.5 nm, in secondary electron image mode (SEI), and backscattered electron image mode (BEI).

## Results and Discussion

#### Liquid Hot-Compressed Water Treatments

The influence of LHCW pre-treatments at various temperatures and treating times on SCOD concentration of grain sorghum stover slurry is visualized by 3D mesh segmentation on Fig. 3.

The results of LHCW pre-treatments show that hot-compressed water has a positive effect in grain sorghum stover disintegration, leading to significant increments in SCOD concentration: +262% at 100 °C, +419% at

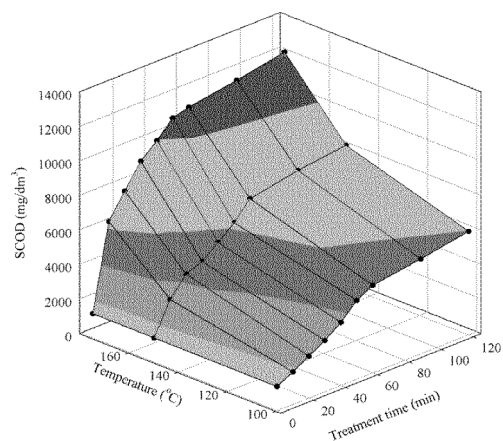


Figure 3: Effects of temperatures and contact times of LHCW pre-treatments on SCOD concentration of grain sorghum stover suspension (●: experimental data points)

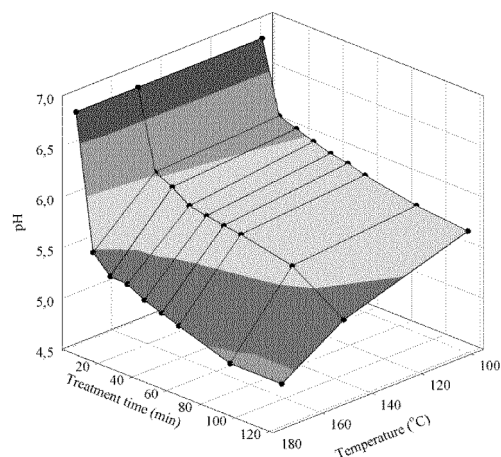


Figure 4: Acidity of grain sorghum stover slurries as the function of LHCW contact time and temperature (●: experimental data point)

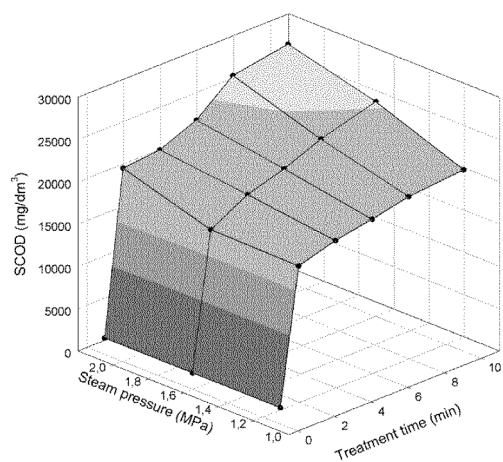


Figure 5: Effects of steam pressures on SCOD concentration levels of grain sorghum stover slurries as the function of the contact time during steam explosion (●: experimental data points)

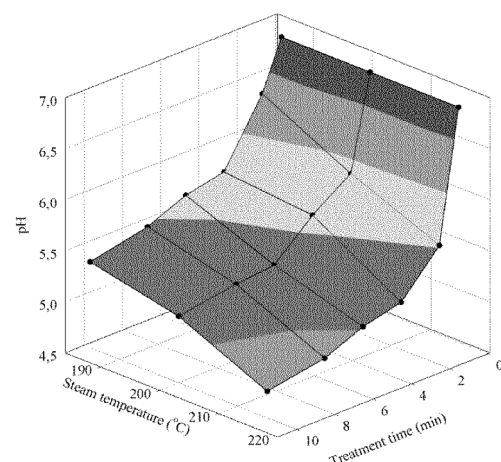


Figure 6: The effect of steam explosion on pH values of treated grain sorghum stover slurry at various steam pressures as the function of the treatment time (●: experimental data points)

150 °C and + 698% at 175 °C with an operating time of 60 min, respectively. The control experiments were performed using untreated grain sorghum stover suspension. Both temperature and time have positive, but not linear effects on SCOD and not to the same degree. The temperature raising has more effect on the solubilisation of grain sorghum stover after 60 minutes than the treating time in agreement with the results of VALO *et al.* [29] who found that treating time had less influence than temperature during thermal treatment of sludge. It is notable that higher solvolysis temperatures resulted in more acidic products as reflected by the low pH level of the grain sorghum stover slurry (Fig.4).

#### Steam Explosion Pre-Treatments

The pressures and temperatures of SE pre-treatments had significant effect on digestibility of grain sorghum stover. Elevated pressures and temperatures resulted in enhanced solubilisation (Fig.5). The positive pressure effect may be explained by the increased disintegration caused by higher-pressure drop at the end of treatment. Compounds that are more soluble were released from the grain sorghum stover during the steam explosion

and made the resulting slurry available to subsequent bacterial degradation.

The pressure effect is quasi-linear and the effect of contact time can be modelled by an exponential-to-maximum function. Compared to the untreated grain sorghum stover, the SCOD concentrations of the slurries increased by a factor of 8.9, 9.6, 10 at 185, 200, and 215 °C, respectively, with an operating time of 3 min, respectively. Additional, the pH value decreased with pre-treatment pressure (steam temperature) and with the contact time (Fig.6). The formation of acidic degradation products during disintegration of grain sorghum stover slurry by steam explosion agree well with the observation of GUO *et al.* [30] at corn stalk steam explosion.

#### Ultrasonic Treatments

The efficiency of ultrasonic irradiation of grain sorghum stover was quantified by SCOD concentration of the slurry as a function of contact time and power input in terms of ultrasonic amplitude level (%) and specific sonication energy. Results of ultrasonic treatments are shown in Fig.7, where the values of the SCOD

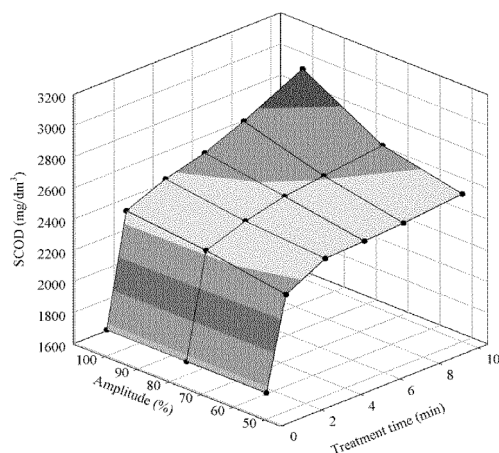


Figure 7: The effect of sonication energy on SCOD concentration level of grain sorghum stover slurry as the function of sonication time and relative ultrasound amplitude (●: experimental data points)

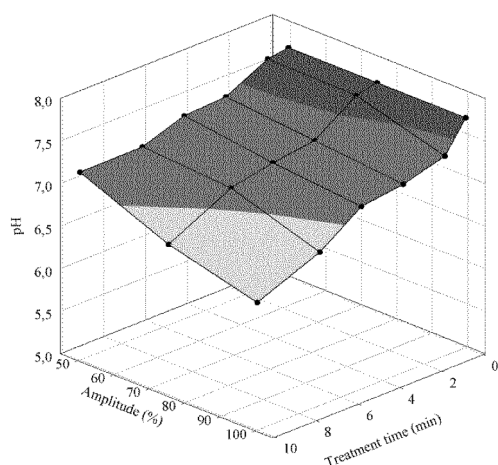


Figure 9: The effect of sonication power on the pH values of grain sorghum stover slurries as the function of the sonication time (●: experimental data points)

concentrations are presented for each value of the ultrasonic amplitude level (%), and sonication time. The SCOD of the pulps increased with the ultrasonic power demonstrating the effectiveness of the cavitation energy to disrupt the cell walls of the plant parts. The SCOD concentration excess reached +105%, +109%, and +133% at 50%, 70%, and 100% amplitude level, respectively, with a contact time of 3 min.

The ultrasonic power and the pre-treatment time affect the SCOD to a different degree. The raising of SCOD values by treating time is stabilized after 3 minutes. These can be described by an exponential-to-maximum function. The effect of energy-input on SCOD is quasi-linear ( $R^2 = 0.942$ ) as demonstrated by the data shown in Fig. 8, where SCOD values are plotted against the specific sonication energy. The SCOD concentrations were increased by the sonication energy; however, no power-saturation phenomenon was observed. The sonication energy over the minimal energy of  $1 \text{ kJ g}^{-1} \text{ DS}$  is the most effective for breaking up cells [31].

The pH values of the sonicated grain sorghum stover slurries decreased monotonously with pre-treatment time and sonication power on a small scale (Fig. 9)

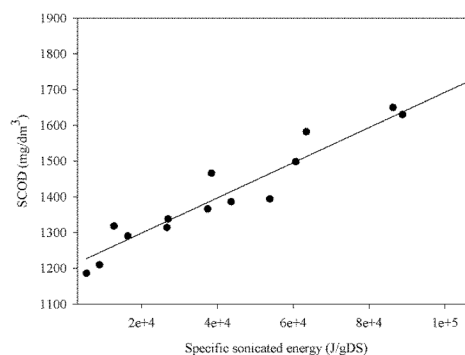


Figure 8: SCOD change in grain sorghum stover slurry as a function of specific sonication energy (●: experimental data points)

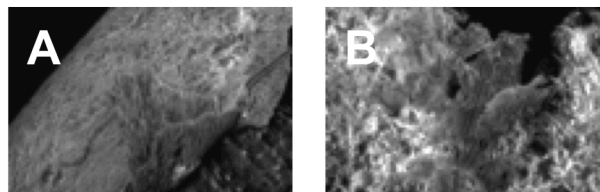


Figure 10: ESEM pictures of the surface on untreated (A) and by ultrasonic treated (B) grain sorghum stalks at 100× magnification

suggesting that local temperature effects caused by cavitation bubbles were not enough to accelerate the hydrolytic processes resulted in acidic degradation product.

#### Environmental Scanning Electron Microscopy

The ESEM pictures of the surfaces on untreated and by ultrasonic treated grain sorghum stalks are shown in Fig. 10 at 100× magnification. The surface of the treated sorghum stalk was altered (Fig. 10B) from the appearance of defective plant tissues. Fig. 10B shows a heterogeneous appearance compared to the homogeneous surface of the untreated stalk (Fig. 10A). The comparison of the pre-treatment results of the chemical analysis, the SCOD concentration, and pH changes of grain sorghum stover slurries suggested that the most effective disintegration method is the steam explosion to disrupt the lignocellulosic structure of grain sorghum stover and partial hydrolysis of its molecular components. However, results of these fast methods can only indicate how much structures of lignocellulosic materials broke down on a chemical level. Nevertheless, greater decomposition of the lignocellulose structures does not necessarily prove enhanced biogas production, because inhibitors for methanogenesis reactions can also be produced through hydrolytic processes during steam explosion. Furthermore, one has to take into account the high energy needs of treatments at elevated temperatures. According to the results of fast chemical analyses (SCOD and pH), the optimal conditions for the LHCW, steam explosion and ultrasonic treatment of grain sorghum stover were established as  $150 \text{ }^\circ\text{C} / 30 \text{ min}$ ,  $200 \text{ }^\circ\text{C} / 3 \text{ min}$  and 100% ultrasound amplitude / 3 min (at  $25 \text{ }^\circ\text{C}$ ), respectively. However, to study the real effect of optimal conditions of the investigated pre-

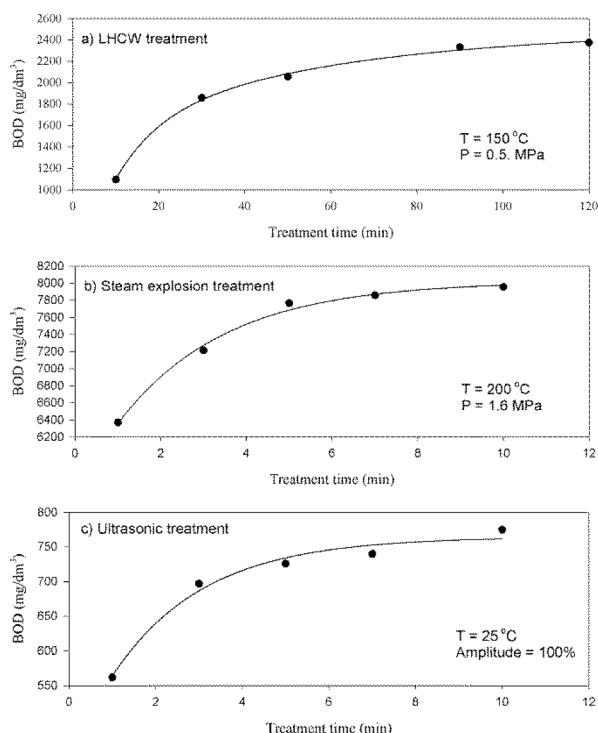


Figure 11: Comparison of the BOD<sub>5</sub> test of filtrates of grain sorghum stover slurries after various pre-treatment methods

treatments additional biochemical tests like BOD and biomethane potential determinations are necessary.

#### Biochemical Oxygen Demand

A comparison of the biochemical oxygen demands of filtrates of grain sorghum stover slurries after pre-treatments at the optimal conditions is given in Fig.11. The results of the BOD<sub>5</sub> tests support the observations from chemical analysis. Actually, all three methods investigated are appropriate for pre-treatment of grain sorghum stover, because the BOD<sub>5</sub> values systematically increased in filtrates of grain sorghum stover slurries with the treatment time under the conditions investigated. However, the highest BOD<sub>5</sub> values were obtained in filtrates after steam explosion, therefore the steam explosion seems to be the most effective disintegration method to disrupt the lignocellulosic structure of grain sorghum stover and to partially hydrolyse its molecular species, resulting in the formation of bacterially digestible substrate.

#### Biogas Production by Mesophilic Anaerobic Digestions

Biogas and biomethane production tests were carried out using grain sorghum stover slurries pre-treated under stated optimal conditions (LHCW: 150 °C / 30 min, steam explosion: 200 °C / 3 min, and ultrasonic treatment: 100% ultrasound amplitude / 3 min at 25 °C). Daily as well as the final biogas and methane production (normalized volumes at 0 °C and 101.15 kPa) were determined. The results are shown as a function of the digestion time in Figs.12 and 13. The specific gas productions were calculated by dividing the

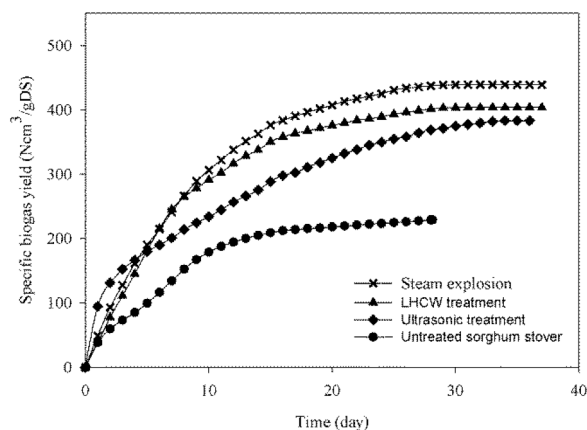


Figure 12: Specific cumulative biogas yield (Ncm<sup>3</sup>/g DS) of grain sorghum stover substrates after pre-treatments

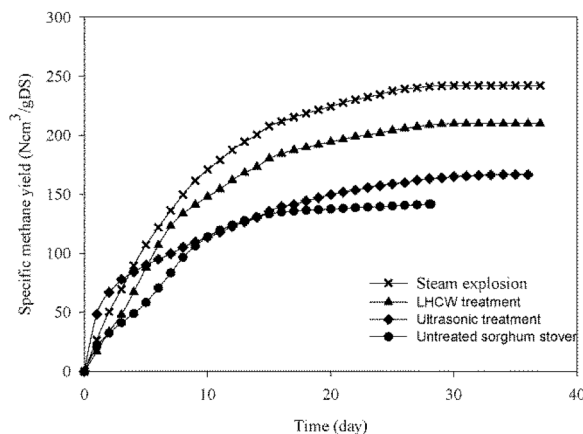


Figure 13: Specific cumulative methane yield (Ncm<sup>3</sup> g<sup>-1</sup> DS) of grain sorghum stover substrates after pre-treatments

accumulated gas amount with the total DS of the substrates. As reference, the untreated material was used in the same amount. In agreement with the results of chemical analytical and biochemical tests after pre-treatments, the specific total biogas and methane yields obtained for treated grain sorghum stover substrates were significantly higher than that of the untreated control.

As seen in Fig.12, biogas productions began immediately, without a lag period after starting the degradation of grain sorghum stover. The fastest biogas production at the beginning was detected at the ultrasonicated substrate. However, the highest biogas production was observed during the fermentation of steam-exploded substrate. The biogas production proceeded in constant and high daily biogas production for treated substrates until the 30<sup>th</sup> day of hydraulic retention time. This observation is notable, because the application of pre-treatments can decrease the usual cycle time for biogas fermentation and increase the production of biogas with higher methane content. The comparison of the biomethane yields is given in Fig.13. Methane production, as the major result of anaerobic digestion of pre-treated grain sorghum stover, was markedly increased by the three pre-treatments. The highest biomethane production rate was observed at the substrates after ultrasonic and steam explosion pre-treatments. The biomethane production rate of LHCW

treated substrate was lower, probably due to the low pH of the pre-treated grain sorghum stover slurry.

Our laboratory tests have shown that the steam exploded substrate possess has the highest biogas production potential ( $439 \text{ Ncm}^3 \text{ g}^{-1} \text{ DS}$ ) during hydraulic retention times of 36 days with 55% methane content. The steam explosion pre-treatment increased the biomethane yield by +72% to  $242 \text{ Ncm}^3 \text{ g}^{-1} \text{ DS}$ . The LHCW pre-treated substrate has the second highest biogas production potential ( $403 \text{ Ncm}^3 \text{ g}^{-1} \text{ DS}$ ) during hydraulic retention times of 36 days with 52% methane content, the LHCW pre-treatment increased the biomethane yield by 49% to  $210 \text{ Ncm}^3 \text{ g}^{-1} \text{ DS}$ . This yield increment is higher than that was obtained by QIAO *et al.* [9] for various biomass wastes after hydrothermal treatment. The substrate after ultrasonic pre-treatment has a biogas production potential of  $383 \text{ Ncm}^3 \text{ g}^{-1} \text{ DS}$  during hydraulic retention times of 36 days with 44% methane content, the ultrasonic pre-treatment increased the biomethane yield by 18% to  $167 \text{ Ncm}^3 \text{ g}^{-1} \text{ DS}$ . The low biogas and methane yields of ultrasonic treated grain sorghum stover can be explained by the superficial effect of ultrasonic cavitation.

### Conclusions

The results of chemical, biochemical analyses and biogas/biomethane potential test obtained by mesophilic anaerobic digestion were presented. It was found that LHCW treatment and steam explosion are the most effective biomass pre-treatment for increasing the solubilisation of the organic matters of grain sorghum stover. Laboratory testing of anaerobic digestibility of pre-treated slurries have shown that the grain sorghum stover has high biogas potential. It can serve as biogas feedstock and could reduce the energy consumption of sorghum-based bioethanol production in the future. The LHCW and steam explosion biomass pre-treatment techniques can reduce the cycle time and improve the biogas production via disintegration of the complex and compact plant structures of grain sorghum stover.

### ACKNOWLEDGEMENTS

This research was supported by TÁMOP 4.2.4. A/2-11-1-2012-0001 „National Excellence Program – Elaborating and operating an inland student and researcher personal support system”. The project was subsidized by the European Union and co-financed by the European Social Fund. Authors also gratefully acknowledge the support of the Hungarian State and European Union under the TÁMOP-4.2.2.A-11/1/KONV-2012-0071 project.

### REFERENCES

- [1] SALDIVAR S.R.O.S., CARRILLO E.P., ALVAREZ M.M.: Method for obtaining bioethanol from sorghum grain (*Sorghum Bicolor* L.Moench) comprising steps involving decortication and hydrolysis with proteases. Patent application number: US 20110014671 A1, 2011
- [2] MCMILLAN J.D.: Pre-treatment of Lignocellulosic Biomass, in: *Enzymatic Conversion of Biomass for Fuels Production* (Eds: M.E.HIMMEL, J.O.BAKER, R.P.OVEREND), ACS Symposium Series, 1994, 566, 292–324
- [3] CESARO A., NADDEO V., AMODIO V., BELGIORN V.: Enhanced biogas production from anaerobic codigestion of solid waste by sonolysis, *Ultrasonics Sonochemistry*, 2012, 19(3), 596–600,
- [4] HARUN M.Y., RADIAH A.Z.D., ZAINAL ABIDIN Z., YUNUS R.: Effect of physical pre-treatment on dilute acid hydrolysis of water hyacinth (*Eichhornia crassipes*), *Biores. Technol.*, 2011, 102(8), 5193–5199
- [5] SUN Y., CHENG J.: Hydrolysis of lignocellulosic materials for ethanol production: a review, *Biores. Technol.*, 2002, 83(1), 1–11
- [6] HAGHIGHI MOOD S., HOSSEIN GOLFESHAN A., TABATABAEI M., SALEHI JOUZANI G., NAJAFI G.H., GHOLAMI M., ARDJMAND M.: Lignocellulosic biomass to bioethanol, a comprehensive review with a focus on pre-treatment. *Renew. Sustain. Energy Rev.*, 2013, 27, 77–93
- [7] ZHENG Y., ZHAO J., XU F., LI Y.B.: Pre-treatment of lignocellulosic biomass for enhanced biogas production, *Prof. Energy Comb. Sci.*, 2014, 42, 35–53
- [8] VAN WALSUM G.P., ALIEN S.G., SPENCER M.J., LASER M.S., ANTAL JR. M.J., LYND L.R.: Conversion of lignocellulosics pretreated with liquid hot water to ethanol. *Appl. Biochem. BioTechnol. A*, 1996, 57–58, 157–170
- [9] QIAO W., YAN X., YE J., SUN Y., WANG W., ZHANG Z.: Evaluation of biogas production from different biomass wastes with/without hydrothermal pre-treatment. *Renewable Energy*, 2011, 36 (12), 3313–3318
- [10] SU D., SUN J., LIU P., LÜ Y.: Effects of Different Pre-treatment Modes on the Enzymatic Digestibility of Corn Leaf and Corn Stalk, *Chinese J. Chem. Engng.*, 2006, 14(6), 796–801
- [11] DIEN B.S., LI X.L., ITEN L.B., JORDAN D.B., NICHOLS N.N., O'BRYAN P.J., COTTA M.A.: Enzymatic saccharification of hot-water pretreated corn fiber for production of monosaccharides, *Enzyme Microbial Technol.*, 2006, 39(5), 1137–1144
- [12] WEIL J., SARIKAYA A., RAU S., GOETZ J., LADISCH C., BREWER M., HENDRICKSON R., LADISCH M.: Pre-treatment of corn fiber by pressure cooking in water, *Appl. Biochem. Biotech.*, 1998, 73(1), 1–17
- [13] ROHOWSKY B., HÄULER T., GLADIS A., REMMELE E., SCHIEDER D., FAULSTICH M.: Feasibility of simultaneous saccharification and juice co-fermentation on hydrothermal pretreated sweet sorghum bagasse for ethanol production, *Appl. Energy*, 2013, 102, 211–219,

- [14] DOGARIS I., KARAPATI S., MAMMA D., KALOGERIS E., KEKOS D.: Hydrothermal processing and enzymatic hydrolysis of sorghum bagasse for fermentable carbohydrates production, *Biores. Technol.*, 2009, 100(24), 6543–6549
- [15] SÖDERSTRÖM J., PILCHER L., GALBE M., ZACCHI G.: Two-step steam pre-treatment of softwood by dilute H<sub>2</sub>SO<sub>4</sub> impregnation for ethanol production, *Biomass Bioene.*, 2003, 24(6), 475–486
- [16] KAAR W.E., GUTIERREZ C.V., KINOSHITA C.M.: Steam explosion of sugarcane bagasse as a pre-treatment for conversion to ethanol, *Biomass Bioene.*, 1998, 14(3), 277–287
- [17] XU G.Z., FAN S.Y., ZHANG B.L., LIU J.B.: Anaerobic Fermentation Characteristics of Corn Straw Pretreated by Steam Explosion, *Adv. Mat. Res.*, 2012, 512–515, 334–337
- [18] WANG X.T., CAI H.Z., LIU L.S.: Experimental Study on Anaerobic Fermentation of Steam Explosion Pretreated Corn Stalk, *Adv. Mat. Res.*, 2011, 183–185, 1975–1978
- [19] VARGA E., RÉCZEY K., ZACCHI G.: Optimization of steam pre-treatment of corn stover to enhance enzymatic digestibility, *Appl. Biochem. Biotechnol.*, 2004, 113–116, 509–23
- [20] SIPOS B., RÉCZEY J., SOMORAI ZS., KÁDÁR ZS., DIENES D., RÉCZEY K.: Sweet Sorghum as Feedstock for Ethanol Production: Enzymatic Hydrolysis of Steam-Pretreated Bagasse, *Appl. Biochem. Biotechnol.*, 2009, 153(1–3), 151–162
- [21] ZHANG J., MA X., YU J., ZHANG X., TAN T.: The effects of four different pre-treatments on enzymatic hydrolysis of sweet sorghum bagasse, *Biores. Technol.*, 2011, 102(6) 4585–4589
- [22] APUL O.G., SANIN F.D.: Ultrasonic pre-treatment and subsequent anaerobic digestion under different operational conditions, *Biores. Technol.*, 2010, 101(23) 8984–8992
- [23] ZHANG K., REN N., GUO C., WANG A., CAO G.: Effects of various pre-treatment methods on mixed microflora to enhance biohydrogen production from corn stover hydrolysate, *J. Env. Sci.*, 2011, 23(12), 1929–1936
- [24] YACHMENEV V., CONDON B., KLASSON T., LAMBERT A.: Acceleration of the enzymatic hydrolysis of corn stover and sugar cane bagasse celluloses by low intensity uniform ultrasound, *J. Biobased Mat. Bioene.*, 2009, 3(1), 25–31
- [25] SHEWALE S.D., PANDIT A.B.: Enzymatic production of glucose from different qualities of grain sorghum and application of ultrasound to enhance the yield, *Carbohydr. Res.*, 2009, 344(1), 52–60
- [26] IMAM T., CAPAREDA S.: Ultrasonic and high-temperature pre-treatment, enzymatic hydrolysis and fermentation of lignocellulosic sweet sorghum to bio-ethanol, *Int. J. Ambient Ene.*, 2012, 33(3), 152–160
- [27] FÖRHÉCZ J., REGÖS J., GÖBLÖS SZ., DALLOS A.: Planning, construction and testing of a biogas pilot plant with mesophilic biodigester, Prof. 37th International Conference of Slovak Society of Chemical Engineering, Tatranské Matliare, Slovakia, Ed.: MARKOS, J., 2010, pp. 325
- [28] APHA, Standard Methods for the Examination of Water and Wastewater, 20th ed. American Public Health Association, Washington, DC, USA, 1999,
- [29] VALO A., CARRÈRE H., DELGENÈS J.P.: Thermal, chemical and thermo-chemical pre-treatment of waste activated sludge for anaerobic digestion, *J. Chem. Technol. Biotechnol.*, 2004, 79, 1197–1203
- [30] GUO P., MOCHIDZUKI K., CHENG W., ZHOU M., GAO H., ZHENG D., WANG X., CUI Z.: Effects of different pre-treatment strategies on corn stalk acidogenic fermentation using a microbial consortium, *Biores. Technol.*, 2011, 102(16), 7526–7531
- [31] BOURGRIER C., CARRÈRE H., DELGENÈS J.P.: Solubilisation of waste-activated sludge by ultrasonic treatment, *Chem. Eng. J.*, 2005, 106, 163–169

## DEVELOPMENT OF A REACTION STRUCTURE IDENTIFICATION ALGORITHM

JÁNOS KONTOS,<sup>1✉</sup> LÁSZLÓ RICHÁRD TÓTH,<sup>2</sup> AND TAMÁS VARGA<sup>2</sup>

<sup>1</sup> Department of Physical Chemistry, University of Pannonia, Egyetem St. 10, Veszprém, H-8200, HUNGARY

<sup>2</sup> Department of Process Engineering, University of Pannonia, Egyetem St. 10, Veszprém, H-8200, HUNGARY

✉E-mail: kontosjan@gmail.com

The most important step in the design procedure of a chemical reactor is the understanding the chemical reaction network (CRN), which will take place in that reactor. The structure of a CRN as representation of the reaction mechanism contains all the elementary reaction steps that are required to convert the reagents into products. The aim of the reaction mechanism analysis is the identification of the route how the system goes from its initial to the end state. In order to do this, a lot of knowledge is required about chemistry supplemented with some analytical measurements. In this work, we focus on the development of an algorithm, which requires a few data inputs to reveal all the reaction steps that are important in the reactor design point of view. It is trivial that the structure of a dynamic system cannot be determined without the identification of the model parameters that belong to that structure. Hence, the algorithm reported here can be used to obtain the parameters of the reaction rate equations for each identified chemical reaction. First, the structure is identified followed by its parameters. In this study the processed data are obtained by a CRN generator, which is applied to generate random CRNs based on some specified parameters to reach maximal reaction order. Concentration profiles, which characterize each CRN at a specific reaction rate constants combination, are obtained as a result of simulations based on the randomly generated CRNs. The developed algorithm for reaction mechanism identification is based on a modified type of linear least-squares method (LLSM) in which the searching variables must be higher than zero, since the reaction rate constants cannot have negative values. The developed algorithm is tested in different cases to check the applicability of LLSM in reaction structure identification procedure and the obtained results show that with some further improvements the proposed algorithm can be applied solving more complex identification tasks.

**Keywords:** chemical reaction network, structure identification, non-negative least-squares method, CRN generator

### Introduction

One of the most important tasks during the design procedure of any chemical technology is the engineering design of the conversion subsystem and to ensure the optimal and safe operation. Hence, before starting the design of a technology phenomena with impact on the dynamic behaviour of the subsystem must be identified. The most crucial part of the conversion subsystem is the chemical reactor in which we try to control the processes that was identified on the basis of laboratory experiments. In this work we proposed a method to support the identification of the individual reaction steps and their rates in a chemical reaction network (CRN).

Numerous literature examples can be found that describe different methodologies to generate the structure of CRNs, as representations for reaction mechanisms [1, 2]. The reaction mechanism of a reaction system represents all the elementary reaction steps, which are required to convert the reagents into products. Hence, the aim of reaction mechanism identification is the determination of the intermediate steps, which take the starting materials to the final products. Trivially, it is challenging to follow and model

the movements of all the molecules in a system in full detail. However, we can describe a reaction system on the basis of the cumulative effects of great number of molecules in specific states. Such specific states are the formation of stable intermediates.

The intermediates are chemical species produced in the elementary reaction steps. Often, it is possible to detect them by experimental methods. The produced amount of these intermediates is sometimes very low and they react very fast to produce another intermediate or final product. Hence, the identification of the latter components and the measurement of their concentrations can be challenging. Most of the reactions take place through multiple intermediate steps. These scenarios are called multi-step reactions. In a single reaction step, the sign of stoichiometric coefficients represent that a given molecule is a reagent (-) or product (+), and the absolute value of these coefficients give how many moles are consumed/formed.

The transient states of a reaction system and the intermediates can be investigated with two kinds of methods on the basis of whether *a priori* knowledge of reaction kinetics is available or not [3]. The foundation of the reaction mechanism analysis is the precise identification of all intermediates and their

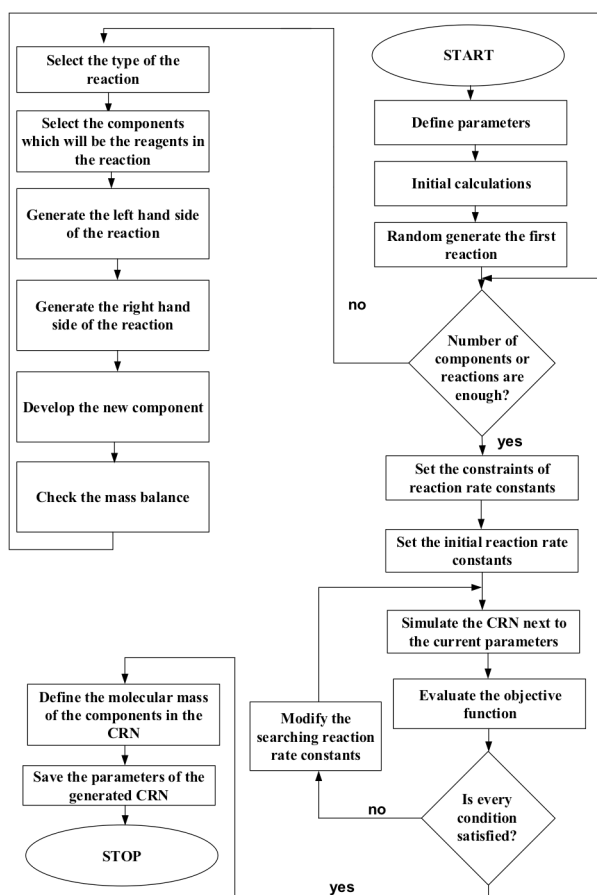


Figure 1: The scheme of the proposed CRN generator

concentration. With the lack of this information the stoichiometry of the reaction cannot be revealed reliably. The nature and the amount of the products can contain as much information as a well-qualified chemist requires identifying the reaction mechanism of an unknown reaction system. The proposed algorithm can support this process in case we have lack of experience in the identification of the structure of a CRN and parameters of kinetic expressions, which describe the rate of the reaction steps considered in the CRN.

The essence of the parameter identification process is the solution of a constrained minimization problem in which the objective function can be the sum of squared error between the measured and the calculated component concentration profiles. The searching variables are the unknown parameters in the kinetic expressions (i.e. pre-exponential factor, activation energy, reaction order).

The role of the structure identification is the definition of correlated variables and their mathematical formalization. In our case, the identification means the selection of reaction steps that can take place in the reactor. The identification tasks can be solved by the application of linear least-squares method (LLSM) [4]. The main challenges using this method are the definition of the correct initial conditions for the applied searching algorithm and the speed up of the identification procedure.

One of the most important simultaneous methods is the incremental approach, which applies a hierarchical modelling methodology to decompose the complex

identification problem into simpler sub-problems [5]. The method applies target factor analysis to identify the suitable structure of the unknown CRN. This method has been successfully applied in reaction mechanism identification process in a multi-phase system based on concentration and calorimetric measurements [6].

Correlation metric method was developed to analyse the strength of the connections between the components in the system, which is based on the qualitative analysis of the measured data [7]. Qualitative trend analysis was also applied in reaction mechanism identification algorithms to divide the entire experimental time into shorter periods in which the correlations are analysed between the concentrations of components [8].

In this work, our aim is to develop a simple, but reliable method for structure identification of CRNs, which need as few data as possible. In our case the input of the algorithm is only the list of components and concentration profiles, which are the result of the simulation based on randomly generated CRNs. These CRNs were generated based on user specified parameters, such as maximal reaction order. On the basis of the randomly generated CRNs, the concentration profiles for each CRN at a specific reaction rate constants combination are determined. The algorithm developed for reaction mechanism identification is based on a modified LLSM method, in which the searching variables must be higher than zero, since the reaction rate constants cannot have negative values.

## Development of Simulation Methods

Since our aim is to develop a generally applicable algorithm to support the identification process of CRNs with unknown structure, we developed a CRN generator, which can be applied to randomly generate CRNs based on some structural parameters, such as the maximum number of components or reactions in CRN.

There are many examples in literature for developing a CRN generator that analyses the affinity of molecules taking part in reactions [9], applies mixed integer programming to build up reaction networks [10], or using group contribution method to generate the structure of the CRN and the kinetic parameters of the reaction steps in that network [11].

In this work we developed a simple CRN generator that randomly generates a CRN from randomly generated components. In this generator, we define probabilities in situations for building different kinds of CRNs. For example, if we would like to have more decomposition reactions in the CRN then the probability of this type of reaction is increased. The scheme of the developed CRN generator can be seen in *Fig. 1*.

The first step of the algorithm of the CRN generator is the definition of the parameters of the desired CRN, such as the probabilities of the different types of reactions. In this step the maximal number of building block types in a component and the maximal number of specific building blocks in a component are defined.

The next step is the development of the first reaction step in which we define a new component next to the components that are already in the component list. The stoichiometric coefficients of the reaction are randomly generated based on the user-defined parameters. The composition and the chemical formula of the added component are determined based on the material balance of the reaction. With the first reaction step, it is checked whether the numbers of components and reactions in the generated CRN are enough.

If the user defined value of these parameters are higher than the current values the CRN generator starts to build a new reaction with selecting the reaction type, the components. Based on the CRN parameters it randomly generates stoichiometric factors for that new reaction and checks the material balance. Components that are involved in more reactions have a smaller chance to be chosen for the next new reaction building iteration.

If there are enough components or reactions in the generated CRN, the algorithm steps to the next phase in which it randomly generates the reaction kinetic constants for reactions in the CRN. In this phase, the algorithm randomly generate kinetic parameters, while maintaining the same order of magnitude of the reaction rates, to make it harder to find out the structure of the generated CRN. Particle swarm optimization method has been applied to solve this constrained optimization problem, where the objective function is defined as the difference of the integral of reaction rates over the time [12].

#### General Reactor Model

The kinetic experiments are usually performed in a tempered flask that can be modelled as an isothermal batch reactor. All the reagents are added to the unit with or without catalyst and samples are taken from the reaction mixture in specific times. As mentioned earlier the simplest case is considered as we have only concentration measurements from a batch reactor. However, the developed algorithm can be improved and the processability of data can be widened with the application of mathematical models of other reactor types.

Hence, at this point of the development of the proposed algorithm, we consider that the unit in which the kinetic experiments are performed is a well-mixed, isothermal batch reactor. The model of a batch reactor should be developed first to contain component mass balance equations. Applying the well-mixed assumption the component mass balances can be simplified and we obtain the equations:

$$\frac{dc_i}{dt} = R_i \quad i = \{A; B; C; \dots\}, \quad (1)$$

where  $I$  identifies the components in the system in which we have  $N_c$  components;  $c_i$  is the concentration of the  $i^{\text{th}}$  component [ $\text{mol m}^{-3}$ ];  $R_i$  is the component source of the  $i^{\text{th}}$  component [ $\text{mol m}^{-3} \text{s}^{-1}$ ], which can be calculated as:

$$R_i = \sum_{j=1}^{N_R} \nu_{ji} \cdot r_j, \quad (2)$$

where  $j$  identifies the reaction in the system;  $N_R$  gives the number of reactions considered;  $\nu_{ji}$  is the stoichiometric coefficient of the  $i^{\text{th}}$  component in the  $j^{\text{th}}$  reaction;  $r_j$  is the reaction rate of the  $j^{\text{th}}$  reaction [ $\text{mol m}^{-3} \text{s}^{-1}$ ], which is calculated with following expression:

$$r_j = k_j \prod_{i=\{A;B;C;\dots\}} c_i^{n_{ji}}, \quad (3)$$

where  $n_{ji}$  denotes the order of  $i^{\text{th}}$  component in  $j^{\text{th}}$  reaction [1],  $k_j$  is the reaction rate constant of the  $j^{\text{th}}$  reaction [the unit is dependent on the order of the reaction,  $\text{mol}^{1-n} \text{m}^{3n-1} \text{s}^{-1}$ ], where  $n$  is the summarized reaction order in  $j^{\text{th}}$  reaction:

$$n = \sum_{i=\{A;B;C;\dots\}} n_{ji}. \quad (4)$$

This summarized reaction order is equal to the absolute value of the stoichiometric coefficient of the  $i^{\text{th}}$  component in the  $j^{\text{th}}$  reaction, if the given component is a reagent in a given reaction, otherwise it is 0. The developed general reactor model has been implemented in MATLAB.

#### Proposed Algorithm for Structure Identification of CRN

Our primary aim is to develop an algorithm, which can be efficiently applied in reaction mechanism identification tasks on the basis of concentration profiles. In this phase, we considered that the concentration profiles are known for all the components in the system. It is a simplification with respect of practical problems; however, in this work we aim to evaluate if a simple method of LLSM is suitable for a complex task.

LLSM is based on the minimization of a special model error, which is based on comparing the measured to the calculated time series. In our case, the time series are the numerical derivatives of the concentration profiles. Based on the measured concentration profiles the change in concentration during two sampling steps can be calculated as a numerical derivative with respect to length of that time step. If we have  $N_k$  samples, the difference in  $k^{\text{th}}$  sample can be defined as follows:

$$\frac{\Delta \hat{c}_i}{\Delta t}(k) = \hat{c}_i(k) - \hat{c}_i(k-1), \quad (5)$$

where  $k$  is the current sample;  $\Delta \hat{c}_i$  is the difference of the measured concentration of  $i^{\text{th}}$  component in between  $k$  and  $k-1$  sampling steps;  $\Delta t$  is the time difference between  $k$  and  $k-1$  sampling steps.

If we calculate this difference for all the components and in every sampling steps we get a matrix which has  $k-1$  rows and as many columns as many components we assume in the system. Based on the calculated concentration profiles another matrix can be built with the calculated variables. In our case the sum of the

squared differences between these two matrices is defined as the model error, which should be minimized during the identification process:

$$E = \sum_{i=\{A,B,C,\dots\}} \sum_{k=1}^{N_k} \left( \frac{\Delta \hat{c}_i}{\Delta t}(k) - \frac{\Delta c_i}{\Delta t}(k) \right)^2, \quad (6)$$

where  $E$  is the calculated model error, which is basically the difference of the measured and calculated component sources defined with *Eq.(2)*;  $\Delta c_i$  is the calculated changes in concentrations of  $i^{\text{th}}$  component from *Eq.(1)*, but the steps is equal with the sample times of measurement.

To make it easier to follow the process we define *Eq.(6)* using vectors instead of sums:

$$E = \left( \overline{\Delta \hat{c}} - \overline{\Delta c} \right)^T \left( \overline{\Delta \hat{c}} - \overline{\Delta c} \right), \quad (7)$$

where the length of vectors are  $N_c(N_k-1)$  (i.e. the change in concentrations of components should be calculated in every sample time except in the initial phase) and defined with the following structures:

$$\overline{\Delta \hat{c}} = \begin{bmatrix} \Delta \hat{c}_A(1) \\ \Delta \hat{c}_B(1) \\ \vdots \\ \Delta \hat{c}_A(2) \\ \Delta \hat{c}_B(2) \\ \vdots \\ \Delta \hat{c}_A(k) \\ \Delta \hat{c}_B(k) \\ \vdots \end{bmatrix}, \quad \overline{\Delta c} = \begin{bmatrix} \Delta c_A(1) \\ \Delta c_B(1) \\ \vdots \\ \Delta c_A(2) \\ \Delta c_B(2) \\ \vdots \\ \Delta c_A(k) \\ \Delta c_B(k) \\ \vdots \end{bmatrix}. \quad (8)$$

The task in LLSM is the minimization of the model error defined in *Eq.(7)* by manipulating the model parameters, such as the reaction rate constants of all the possible reaction steps, which are the building blocks of the unknown CRNs. Hence, to use LLSM in reaction mechanism identification process first we need to collect all the possible reaction steps, which can take place in the system based on the defined component list. To get the necessary reaction steps, we generate all the possible combination of reactions, which satisfy the material balances. A given reaction step has to be further processed, since some reaction steps can be produced from each other with linear combinations. Thus, only the independent reactions should be kept in the reaction set. The resulted reaction set is represented in a matrix (i.e. in stoichiometric matrix):

$$\overline{\mathbf{v}}_{RS} = \begin{matrix} & A & B & \dots \\ \begin{matrix} 1 \\ 2 \\ \vdots \end{matrix} & \begin{bmatrix} \mathbf{v}_{1A} & \mathbf{v}_{1B} & \dots \\ \mathbf{v}_{2A} & \mathbf{v}_{2B} & \dots \\ \vdots & \vdots & \ddots \end{bmatrix} \end{matrix}, \quad (9)$$

which has the same number of rows and columns as the number independent reactions and components are considered in the system, respectively.

After the possible reaction steps have been automatically collected, all the reaction steps of the set are considered as the part of the unknown CRNs. Based on the reaction set the mathematical model of the system is automatically generated based on *Eqs.(1)-(3)*. The unknown parameters in this model are the reaction rate constants for all reactions in the reaction set.

The calculated concentration differences in *Eq.(7)* can be obtained using *Eq.(10)* on the basis of the general reactor model (*Eqs.(1-3)*):

$$\overline{\Delta c} = \overline{\mathbf{v}} \overline{\mathbf{k}} \overline{\mathbf{c}}, \quad (10)$$

where  $\overline{\mathbf{c}}$  denotes a special matrix in which a diagonal matrix is repeated from sample time to sample time and in the diagonal matrices we calculate the concentration product term in *Eq.(3)* in every sample time. The following general matrix shows the structure of the resulting diagonal matrix in this step if we have  $N_R$  reactions in the reaction set:

$$\overline{\mathbf{c}} = \begin{bmatrix} \prod_{i=\{A,B,C,\dots\}} (c_i(0))^{n_{i1}} & 0 & \dots \\ 0 & \prod_{i=\{A,B,C,\dots\}} (c_i(0))^{n_{i2}} & \dots \\ \vdots & \vdots & \ddots \\ \prod_{i=\{A,B,C,\dots\}} (c_i(1))^{n_{i1}} & 0 & \dots \\ 0 & \prod_{i=\{A,B,C,\dots\}} (c_i(1))^{n_{i2}} & \dots \\ \vdots & \vdots & \ddots \\ \prod_{i=\{A,B,C,\dots\}} (c_i(k-1))^{n_{i1}} & 0 & \dots \\ 0 & \prod_{i=\{A,B,C,\dots\}} (c_i(k-1))^{n_{i2}} & \dots \\ \vdots & \vdots & \ddots \end{bmatrix} \quad (11)$$

$\overline{\mathbf{v}}$  denotes a special matrix in which the stoichiometric matrix representing the reaction set (*Eq.(9)*) is repeated as many times as the sample times minus one:

$$\overline{\mathbf{v}} = \begin{bmatrix} \overline{\mathbf{v}}_{RS} \\ \overline{\mathbf{v}}_{RS} \\ \vdots \end{bmatrix} \quad (12)$$

$\overline{\mathbf{k}}$  indicates reaction rate constant vector for all the reactions in the reaction set.

By applying LLSM, the structure of the unknown CRN can be identified since the reaction rate constants that can be the part of the unknown CRN will have different values than zero at the end of the identification process and all the other reactions in reaction set get zero value. Based on *Eqs.(7)* and *(10)* we can solve the minimization problem and the following expression is the result for the calculation of reaction rate constants for all reactions in the generated reaction set:

Table 1: A randomly generated CRN with CRN generator

	A	B	C	D	E	$k [-]$
<b>R01</b>	-1	-1	1	1	0	1.5590
<b>R02</b>	2	0	0	1	-1	1.0184

$$\bar{k} = \left[ \left( \left( \bar{v} \right)' \times \bar{c} \right)' \times \left( \left( \bar{v} \right)' \times \bar{c} \right)' \right]^{-1} \times \left( \left( \bar{v} \right)' \times \bar{c} \right)' \times \bar{\Delta c} \quad (13)$$

Reactions with zero reaction rate constants indicate that they cannot be part of the unknown CRN. This means that at the end of the identification process we get the reaction rate constants as well, next to the structure of the CRN.

### Results and Discussion

Since we do not have measurements from a real system in this work the developed CRN generator has been applied to randomly generate some CRNs. *Table 1* shows two reaction steps in the unknown CRN. We have defined five components (**A-E**) in the system. **A** and **B** components are reagents in the first reaction step (**R01**), in which **C** and **D** components are produced. However, in the second reaction (**R02**) only **E** is consumed while 2 moles of **A** and 1 mole of **D** are produced. The last column of *Table 1* shows the exact values of reaction rate constants. The unit of reaction rate constants can be determined for the  $j^{\text{th}}$  reaction based on the sum of the reaction orders of each component in that reaction:

$$\left( \frac{\text{mol}}{\text{m}^3} \right) \left( 1 - \sum_{i=\{A:B:C:\dots\}} n_{ji} \right) \cdot \frac{1}{s} \quad (14)$$

*Table 2* shows the five components (**A-E**) that are built from nine (**a-j**) building elements. These building elements can be imagined as atoms or groups. The numbers in the matrix represents the stoichiometric coefficients of composition. The last row shows a fictitious molecular mass of the components in the system.

Based on the molecular mass and the number of building elements in the components all the independent reaction steps were generated as shown in *Table 3*. The 22 possible reaction steps can be found for the five components from *Table 2*. The unknown reaction mechanism should be built from these reaction steps. In *Table 1* we saw that we need only two of these steps and as it can be seen in the last column of *Table 3* with the proposed algorithm we can find these two reactions of **RS01** and **RS16**. However, the algorithm identifies a third possible reaction step, **RS13**, which can be the part of the unknown CRN. As can be seen in the last column of *Table 3*, the reaction rate constant corresponding to this reaction step is very low. This means **RS13** should not be considered as the part of the unknown CRN.

Table 2: The generated compound matrix

	A	B	C	D	E
<b>a</b>	9	0	1	8	26
<b>b</b>	10	0	8	2	22
<b>c</b>	7	1	1	7	21
<b>d</b>	2	10	7	5	9
<b>e</b>	4	12	13	3	11
<b>f</b>	12	0	1	11	35
<b>g</b>	8	0	6	2	18
<b>h</b>	11	5	7	9	31
<b>j</b>	6	1	3	4	16
M [mass mol <sup>-1</sup> ]	359	195	252	302	1020

Table 3: The resulted reaction step matrix with the identified reaction rate constant

RS ID	A	B	C	D	E	$k [-]$
<b>RS01</b>	-1	-1	1	1	0	1.626
<b>RS02</b>	-3	-1	1	0	1	0
<b>RS03</b>	-2	0	0	-1	1	0
<b>RS04</b>	-2	6	3	-4	0	0
<b>RS05</b>	-3	5	4	-3	0	0
<b>RS06</b>	-4	4	5	-2	0	0
<b>RS07</b>	-5	3	6	-1	0	0
<b>RS08</b>	0	4	5	0	-2	0
<b>RS09</b>	-3	3	6	0	-1	0
<b>RS10</b>	5	-3	-6	1	0	0
<b>RS11</b>	3	-3	-6	0	1	0
<b>RS12</b>	4	-4	-5	2	0	0
<b>RS13</b>	0	-4	-5	0	2	0.004
<b>RS14</b>	3	-5	-4	3	0	0
<b>RS15</b>	2	-6	-3	4	0	0
<b>RS16</b>	0	-6	-3	3	1	0
<b>RS17</b>	2	0	0	1	-1	1.051
<b>RS18</b>	0	-2	2	3	-1	0
<b>RS19</b>	1	1	-1	-1	0	0
<b>RS20</b>	0	2	-2	-3	1	0
<b>RS21</b>	3	1	-1	0	-1	0
<b>RS22</b>	0	6	3	-3	-1	0

After the above simple task, we tested our method in nine other cases. We defined a quantitative measure to check the correctness of the identified kinetic parameters as the mean average difference between the known and the identified reaction rate constants:

$$MAE = \frac{1}{N_{\text{dr}}} \sum_{l=1}^{N_{\text{dr}}} \left| \hat{k}_l - k_l \right| \quad (15)$$

where  $N_{\text{dr}}$  is the number of reactions in unknown CRN;  $l$  identifies the current reaction rate constant;  $\hat{k}$  is the reaction rate constant value what we are looking for, such as the last column in *Table 1* for **CRN01**.

*Table 4* presents the number of reaction steps in the unknown CRN ( $N_{\text{dr}}$ ), the number of components ( $N_c$ ) in the system, the number of the possible reaction steps ( $N_r$ ) as a representation of the size of the reaction set, if the algorithm can find the perfect reaction steps or not, and MAE values when available from *Eq.(15)*.

Table 4: Testing the developed algorithm in case of 10 CRNs

CRN ID	$N_{dr}$	$N_c$	$N_r$	match	MAE [-]
CRN01	2	5	22	y	0.0498
CRN02	3	5	40	n (1/3)	-
CRN03	3	5	11	y	0.0983
CRN04	2	5	17	y	0.0268
CRN05	4	5	26	y	0.1197
CRN06	2	5	13	y	0.0146
CRN07	3	5	10	y	0.0216
CRN08	4	5	119	n (0/4)	-
CRN09	3	5	85	n (0/3)	-
CRN10	4	5	19	y	0.0748

Based on the results in Table 4 it can be seen that the proposed algorithm has some limitations in this phase. However, if the size of the reaction set is relatively small it gives very good agreement with the desired parameters. This means that we should improve this method to make possible the analysis of more complex problems with it. If the algorithm cannot find the perfect match for the unknown CRN a ratio is given which shows how many of the reaction steps are correctly identified from the unknown mechanism.

### Conclusions

The structure of a CRN represents all the elementary reaction steps that are required to convert the reagents into products. Hence, the aim of reaction mechanism identification is to discover the intermediate steps, which connect starting materials with the final product. The proposed algorithm can support this process even in the case, when we lack knowledge about the reaction mechanism and/or kinetic parameters.

The applied structure identification method is based on linear least-square method. The measured and calculated concentration profiles are compared and the difference between these profiles is minimized during the identification process. The proposed algorithm for reaction mechanism identification was implemented in MATLAB.

The results of initial testing showed promising results for this simple method being applicable for a complex task; however, the proposed algorithm should be improved toward processing reaction sets. The given implementation of the algorithm for batch reactor models can be easily extended to other reactor models, which enables to employ our method to realistic problems from chemical industry.

### Acknowledgements

This research was supported by the European Union and the State of Hungary, co-financed by the European Social Fund in the framework of TÁMOP 4.2.4.A/2-11-1-2012-0001 'National Excellence Program'.

### REFERENCES

- [1] DELVIN S.: Organic Reaction Mechanism, Sarup & Sons, New Delhi, 2002
- [2] GROSSMAN R.B.: The Art of Writing Reasonable Organic Reaction Mechanisms, Springer, New York, 2003
- [3] FRIESS S.L., LEWIS E.S.: Investigation of Rates and Mechanisms of Reactions, John Wiley & Sons, New York, 1963
- [4] WALTER E.: Identification of Parametric Models from Experimental Data, Springer-Verlag, Berlin 1997
- [5] BENDEL M.L., BONVIN D., MARQUARDT W.: Incremental identification of kinetic models for homogeneous reaction systems, Chem. Eng. Sci., 2006, 61, 5404–5420
- [6] SRINIVASAN S., BILLETER J., BONVIN D.: Extent-based incremental identification of reaction systems using concentration and calorimetric measurements, Chem. Eng. J., 2012, 207–208, 785–793
- [7] SAMOILOV M., ARKIN A., ROSS J.: On the deduction of chemical reaction pathways from measurements of time series of concentrations, Chaos, 2001, 11, 108–114
- [8] VARGA T.: Qualitative Analysis Based Reaction Mechanism Identification, Chem. Eng. Trans., 2013, 35, 769–774
- [9] RATKIEWICZ A., TRUONG T.N.: Application of Chemical Graph Theory for Automated Mechanism Generation, J. Chem. Inf. Comput. Sci., 2003, 43, 36–44
- [10] FIRST E.L., GOUNARIS C.E., FLOUDA C.A.S.: Stereochemically Consistent Reaction Mapping and Identification of Multiple Reaction Mechanisms through Integer Linear Optimization, J. Chem. Inf. Model, 2012, 52, 84–92
- [11] WEST R.H., ALLEN J.W., GREEN W.H.: Automatic Reaction Mechanism Generation with Group Additive Kinetics, ChemInform., 2012, 43, 36–258
- [12] KENNEDY J., EBERHART R.: Particle swarm optimization in Neural Networks, Proc. IEEE International Conference on Neural Networks, Perth, Australia, 1995, 4, 1942–1948

## A COMPARISON OF ADVANCED NON-LINEAR STATE ESTIMATION TECHNIQUES FOR GROUND VEHICLES

GYÖRGY MAX<sup>✉</sup> AND BÉLA LANTOS

<sup>1</sup> Department of Control Engineering and Informatics, Budapest University of Technology and Economics,  
Magyar tudósok körútja 2, Budapest, 1117, HUNGARY  
<sup>✉</sup>Email: max@iit.bme.hu

This paper presents a comparative examination of state-of-the-art non-linear state estimation techniques. First, the Sigma-Point (SPKF) stochastic estimators are investigated on the basis of the Unscented Transformation. This is followed by the technique of non-linear symmetry-preserving observers for non-linear dynamics on the basis of symmetrical LIE groups. The variety of the deterministic and stochastic state estimation algorithms is studied the kinematics of ground vehicles. Two cases are described that deal with the reliability of path tracking, the convergence and speed of off-line calibration.

**Keywords:** state estimation, invariant observers, unscented KALMAN filter, vehicle kinematics

### Introduction

Vehicles are indispensable in modern society, and vehicle safety is consequently of importance in everyday life. A lack of information about the state of vehicle and parameters presents a major obstacle for the development of vehicle control systems.

The effectiveness of vehicle stability control largely depends on the accuracy of the vehicle state parameters that are measured by appropriate sensors. Unfortunately, measurements from these sensors contain bias, as well as electrical noise, and can drift with temperature changes. However, the state estimation method is also able to dramatically reduce errors introduced by measurement and process noise contained in the signal.

The focus of this work is the non-linear state estimation techniques. Firstly, the ‘Sigma-Point KALMAN filter family’ (SPKF) is discussed on the basis of the ‘Unscented Transformation’ (UT) and STERLING’s interpolation [3, 5, 6]. Secondly, the symmetry-preserving observer is presented [15, 16, 18], which is based on Lie-transformation of invariant frames. The various state estimation procedures are then examined and compared through an illustrative non-linear example of vehicle kinematics.

### Sigma-Point KALMAN Filters

Sigma-Point KALMAN filter [2, 4, 7] is a collective name for derivativeless KALMAN filters that employs the deterministic sampling based Sigma-point approach to calculate the optimal terms of the state estimation. Common methods use the Scaled Unscented Transformation [4] and STERLING’s polynomial interpolation.

The former replaces the original set of sigma-points with a transformed set in order to minimize the errors of higher order terms, the latter approximates the derivation of the divided difference filter [10, 11] and central difference filter in [12].

### The Scaled Unscented Transformation

The Scaled Unscented Transformation (SUT) has two steps. First, a fixed number of sigma points is chosen to capture the desired moments (at least mean and covariance) of the original distribution. Then the sigma points are propagated through the non-linear function and the moments of the transformed variables are estimated. The advantage of SUT over the Taylor series based approximation is that SUT is better at capturing the higher order moments caused by the non-linear transformation, as discussed in [1, 8-10].

Consider a non-linear function  $y = g(x)$  and assume  $x$  has mean  $\bar{x}$  and covariance  $P_x$ . The first two moments of  $y$  are calculated by the following two steps:

1) Weighted Sigma-point selection:

$$\begin{aligned} X_0 &= \bar{x} \\ X_i &= \bar{x} + \left( \sqrt{(L+\lambda)P_x} \right)_{i=1..L} \\ X_i &= \bar{x} - \left( \sqrt{(L+\lambda)P_x} \right)_{i=L+1..2L} \end{aligned} \quad (1)$$

with weights

$$\begin{aligned} w_0^m &= \frac{\lambda}{L+\lambda} & w_0^c &= \frac{\lambda}{L+\lambda} + (1 - \alpha^2 + \beta) \\ w_i^m &= w_i^c & &= \frac{\lambda}{2(L+\lambda)} \end{aligned} \quad (2)$$

where  $w_i^m$ , and  $w_i^c$  are associated with the  $i^{\text{th}}$  sigma-point such that  $\sum_{i=0}^{2L} w_i = 1$ . Symbols  $\lambda$ ,  $\alpha$ , and  $\beta$  denote scaling parameters and  $\left(\sqrt{(L+\lambda)P_x}\right)_i$  is the  $i^{\text{th}}$  column of the matrix square root of the weighted  $(L+\lambda)P_x$  covariance matrix.

2) Propagation:  $Y_i = g(X_i)$

$$\begin{aligned} \bar{y} &\approx \sum_{i=0}^{2L} w_i^m Y_i & P_y &\approx \sum_{i=0}^{2L} w_i^c (Y_i - \bar{y})(Y_i - \bar{y})^T \\ P_{xy} &\approx \sum_{i=0}^{2L} w_i^c (X_i - \bar{x})(Y_i - \bar{y})^T \end{aligned} \quad (3)$$

where  $\bar{y}$ ,  $P_y$ , and  $P_{xy}$  are the approximated mean, covariance and cross-covariance respectively.

### The Unscented KALMAN Filter (UKF)

The algorithm of the UKF according to Refs. [3, 7, 8] consists of the following steps:

1) Initialization:

$$\hat{x}_0 = E[x_0], \quad P_{x_0} = E[(x_0 - \bar{x}_0)(x_0 - \bar{x}_0)^T] \quad (4)$$

$$\hat{x}_0^a = E[\hat{x}_0^a] = \begin{bmatrix} \hat{x}_0^T & \bar{v}_0^T & \bar{n}_0^T \end{bmatrix}^T \quad (5)$$

$$P_0^a = \begin{bmatrix} P_{x_0} & 0 & 0 \\ 0 & R_v & 0 \\ 0 & 0 & R_n \end{bmatrix} \quad (6)$$

2) State estimation for  $k = 1 \dots \infty$ :

a) Calculate Sigma-points:

$$X_{k-1}^a = \begin{bmatrix} \hat{x}_{k-1}^a & \hat{x}_{k-1}^a + \gamma \sqrt{P_{k-1}^a} & \hat{x}_{k-1}^a - \gamma \sqrt{P_{k-1}^a} \end{bmatrix} \quad (7)$$

b) Time-update:

$$\begin{aligned} X_{i,k|k-1}^x &= f(X_{i,k-1}^x, X_{k-1}^v, u_{k-1}), \quad i = 0, \dots, 2L \\ \hat{x}_k^- &= \sum_{i=0}^{2L} w_i^m X_{i,k|k-1}^x \\ P_{x_k}^- &= \sum_{i=0}^{2L} w_i^c (X_{i,k|k-1}^x - \hat{x}_k^-)(X_{i,k|k-1}^x - \hat{x}_k^-)^T \end{aligned} \quad (8)$$

c) Measurement-update:

$$\begin{aligned} Y_{i,k|k-1} &= h(X_{i,k|k-1}^x, X_{k-1}^n), \quad i = 0, \dots, 2L \\ \hat{y}_k^- &= \sum_{i=0}^{2L} w_i^m Y_{i,k|k-1} \\ P_{\hat{y}_k}^- &= \sum_{i=0}^{2L} w_i^c (Y_{i,k|k-1} - \hat{y}_k^-)(Y_{i,k|k-1} - \hat{y}_k^-)^T \\ P_{x_k, y_k} &= \sum_{i=0}^{2L} w_i^c (X_{i,k|k-1}^x - \hat{x}_k^-)(Y_{i,k|k-1} - \hat{y}_k^-) \end{aligned} \quad (9)$$

$$\begin{aligned} K_k &= P_{x_k, y_k} P_{\hat{y}_k}^{-1} \\ \hat{x}_k &= \hat{x}_k^- + K_k (y_k - \hat{y}_k^-) \\ P_{x_k} &= P_{x_k}^- - K_k P_{\hat{y}_k} K_k^T \end{aligned} \quad (10)$$

where  $x_k^a = [x_k^T \ v_k^T \ n_k^T]^T$  and  $X_k^a = [(X_k^x)^T \ (X_k^v)^T \ (X_k^n)^T]^T$  are the  $L$  dimension vectors of the augmented states and Sigma-points respectively,  $R_v$  and  $R_n$  are the covariances of the process and measurement noise respectively,  $\gamma = \sqrt{L+\lambda}$ ,  $\lambda = \alpha^2(L+\kappa)+L$ ,  $\alpha = 10^{-3}$ ,  $\kappa = 0$ ,  $\beta = 2$ , and  $w_i$  is the weighting parameter defined in Eq.(2).

### The Central-Difference KALMAN Filter

This approach is based on STERLING's polynomial interpolation, which was used in the derivations of divided difference filter [10, 11] and central difference filter in Ref. [12]. The result of this approximation can be used for sigma-point approach as in the case of SUT. The algorithm consists of the following steps:

1) Weighted Sigma-point selection:

$$\begin{aligned} X_0 &= \bar{x} \\ X_i &= \bar{x} + \left(h\sqrt{P_x}\right)_{i=1 \dots L} \\ X_i &= \bar{x} - \left(h\sqrt{P_x}\right)_{i=L+1 \dots 2L} \end{aligned} \quad (11)$$

with weights

$$w_0^m = \frac{h^2-L}{h^2}, \quad w_i^m = \frac{1}{2h^2}, \quad w_i^{c1} = \frac{1}{4h^2}, \quad w_i^{c2} = \frac{h^2-1}{4h^2}, \quad (12)$$

where  $w_i^m$ , and  $w_i^c$  are associated with  $i = 1, \dots, 2L$  sigma-point.

2) Initialization: the same as defined in Eqs.(4-6)

3) State estimation for  $k = 1, \dots, \infty$ :

a) Sigma-points for time-update:

$$\hat{x}_{k-1}^{a_v} = \begin{bmatrix} \hat{x}_{k-1} & \bar{v} \end{bmatrix}, \quad P_{k-1}^{a_v} = \begin{bmatrix} P_{x_{k-1}} & 0 \\ 0 & R_v \end{bmatrix} \quad (13)$$

$$X_{k-1}^{a_v} = \begin{bmatrix} \hat{x}_{k-1}^{a_v} & \hat{x}_{k-1}^{a_v} + h\sqrt{P_{k-1}^{a_v}} & \hat{x}_{k-1}^{a_v} - h\sqrt{P_{k-1}^{a_v}} \end{bmatrix} \quad (14)$$

b) Time-update:

$$\begin{aligned} X_{i,k|k-1}^x &= f(X_{i,k-1}^x, X_{k-1}^v, u_{k-1}), \quad i = 0, \dots, 2L \\ \hat{x}_k^- &= \sum_{i=0}^{2L} w_i^m X_{i,k|k-1}^x \\ P_{x_k}^- &= \sum_{i=1}^L w_i^{c1} (X_{i,k|k-1}^x - X_{L+i,k|k-1}^x)^2 + \\ &\quad \sum_{i=1}^L w_i^{c2} (X_{i,k|k-1}^x + X_{L+i,k|k-1}^x - 2X_{0,k|k-1}^x)^2 \end{aligned} \quad (15)$$

c) Sigma-points for measurement-update:

$$\hat{x}_{k|k-1}^{a_n} = \begin{bmatrix} \hat{x}_k^- & \bar{n} \end{bmatrix}, P_{k|k-1}^{a_n} = \begin{bmatrix} P_{x_k}^- & 0 \\ 0 & R_n \end{bmatrix} \quad (16)$$

$$X_{k|k-1}^{a_n} = \begin{bmatrix} \hat{x}_{k|k-1}^{a_n} & \hat{x}_{k|k-1}^{a_n} + h\sqrt{P_{k|k-1}^{a_n}} & \hat{x}_{k|k-1}^{a_n} - h\sqrt{P_{k|k-1}^{a_n}} \end{bmatrix} \quad (17)$$

d) Measurement-update:

$$\begin{aligned} Y_{i,k|k-1} &= h(X_{i,k|k-1}^x, X_{i,k|k-1}^n), \quad i = 0, \dots, 2L \\ \hat{y}_k^- &= \sum_{i=0}^{2L} w_i^m Y_{i,k|k-1} \\ P_{\hat{y}_k} &= \sum_{i=0}^{2L} w_i^{c_1} (Y_{i,k|k-1} - Y_{L+i,k|k-1})^2 + \\ &\quad \sum_{i=0}^{2L} w_i^{c_2} (Y_{i,k|k-1} + Y_{L+i,k|k-1} - 2Y_{0,k|k-1})^2 \quad (18) \\ P_{x_k y_k} &= \sqrt{w_1^{c_1} P_{x_k}^-} (Y_{1:L,k|k-1} - Y_{L+1:2L,k|k-1})^T \\ K_k &= P_{x_k y_k} P_{\hat{y}_k}^{-1} \\ \hat{x}_k &= \hat{x}_k^- + K_k (y_k - \hat{y}_k^-) \\ P_{x_k} &= P_{x_k}^- - K_k P_{\hat{y}_k} K_k^T \end{aligned}$$

### Symmetry-Preserving Observers

Among many problems in control theory, the symmetric nature of the system can be utilized, such as in the case of optimal control for feedback or regulations. The symmetry properties can also be used in the design of observers. Symmetry-preserving observers are also known as invariant observers that are based on the differential geometric background of abstract LIE-groups [15, 16, 18].

The constructive algorithm can be defined for designing invariant observers, which is based on the group transformation of symmetry. The aim is to produce invariant frames and invariant output errors to transform a locally asymptotically convergent observer around an equilibrium point into an invariant one, retaining its first-order approximation. The method in Refs. [16, 18] benefits from the fact that the error equations and the first-order approximation can be calculated explicitly and the relationships can be defined globally. In addition, the invariant error equations make stability issues easier to deal with [19-21].

#### Assumptions

Suppose  $G$  is a LIE-group with identity  $e$  on manifold  $\Sigma$ . The group transformation  $(\varphi_g)_{g \in G}$  on  $\Sigma$  is a smooth mapping

$$(g, \xi) \in G \times \Sigma \rightarrow \varphi_g(\xi) \in \Sigma \quad (19)$$

such that  $\varphi_e(\xi) = \xi$  and  $\varphi_{g_2}(\varphi_{g_1}(\xi)) = \varphi_{g_2 g_1}(\xi)$  for  $\zeta, g_1$ , and  $g_2$ . The transformation group is local if  $\varphi_g(\xi)$  is defined only when  $g$  lies sufficiently near to  $e$ . We consider only local transformations.

Invariant observers are designed for the smooth nonlinear system

$$\frac{d}{dt}x = f(x, u), \quad y = h(x, u) \quad (20)$$

where  $x, u$ , and  $y$  belong to the open subsets  $X \subset \mathbb{R}^n$ ,  $U \subset \mathbb{R}^m$ , and  $Y \subset \mathbb{R}^p$  respectively and  $p \leq n$ . Let  $r \leq n$  be the dimension of the LIE-group. We assume that for each  $x$  the mapping  $x \rightarrow \phi_g(x)$  is full rank. Time functions  $u(t)$  and  $y(t)$  are known.

#### Invariant Pre-Observer

For the differential geometric description of the symmetric observers [14], the following definitions and theorems should be introduced:

**Definition 1.** The group of local transformation on manifold  $X \times U$  is expressed by

$$(X, U) = (\phi_g(x), \psi_g(u)) \quad (21)$$

where  $\phi_g(x), \psi_g(u)$  is local diffeomorphism and  $g \in G$

**Definition 2.** System  $\frac{d}{dt}x = f(x, u)$  is  $G$ -invariant, if  $f(\phi_g(x), \psi_g(u)) = D\phi_g(x) \cdot f(x, u)$  for  $g, x, u$ . Thus, the system remains unchanged for the local transformation,  $\dot{X} = f(X, U)$ .

**Definition 3.** The output  $y = h(x, u)$  is  $G$ -equivariant, if there exists  $\rho_g$  transformation on  $Y$ , such that  $g \in G$  and  $h(\phi_g(x), \psi_g(u)) = \rho_g(h(x, u))$  for  $g, x, u$ . Thus, the output remains unchanged for the local transformation,  $Y = h(X, U)$ .

**Definition 4.** The vector field  $w$  is  $G$ -invariant on manifold  $X$ , if  $\frac{d}{dt}x = w(x)$  is invariant to the transformation, i.e.  $w(\phi_g(x)) = D\phi_g(x) \cdot w(x)$  for  $g, x$ .

**Definition 5.** An invariant frame  $(w_1, w_2, \dots, w_n)$  consists of  $n$  linearly point-wise independent  $G$ -invariant vector fields on  $X$  thus  $(w_1(x), w_2(x), \dots, w_n(x))$  is a basis of the tangent space  $T_X(x)$ .

**Lemma 1.** The invariant frame can be constructed from the canonical basis of  $X$ . The vector field defined by

$$w_i(x) = (D\phi_{\gamma(x)})^{-1} \cdot \frac{\partial}{\partial x_i} \quad (22)$$

for  $i = 1, \dots, n$  forms an invariant frame.

**Definition 6.** The system  $\frac{d}{dt}\hat{x} = F(\hat{x}, u, y)$  is a pre-observer, if  $F(x, u, h(x, u)) = f(x, u)$  is satisfied for  $x$  and  $u$ . Furthermore, if  $\lim_{t \rightarrow \infty} \hat{x}(t) = x(t)$  as  $t \rightarrow \infty$ , then the pre-observer is asymptotic.

**Definition 7.** The pre-observer is G-invariant, if

$$F(\varphi_g(\hat{x}), \psi_g(u), \rho_g(y)) = D\varphi_g(\hat{x}) \cdot F(\hat{x}, u, y) \quad (23)$$

is satisfied for  $g$ ,  $\hat{x}$ ,  $u$ , and  $y$  i.e. the observer remains unchanged for the group transformation on  $X, U, Y$ .

Thus,  $X = \phi_g(x)$ ,  $U = \psi_g(u)$ ,  $Y = \rho_g(y)$ , and

$$\frac{d}{dt} \hat{X} = F(\hat{X}, U, Y).$$

An invariant observer is an asymptotic G-invariant pre-observer. Moreover, if the pre-observer is G-invariant and  $\text{rank}(F) = \dim y$ , then the output map  $y$  is G-equivariant.

**Definition 8.** Smooth map  $(\hat{x}, u, y) \rightarrow E(\hat{x}, u, y) \in \mathbb{R}^p$  is an invariant output error if

- $y \rightarrow E(\hat{x}, u, y)$  is invertible for  $\hat{x}$ ,  $u$ , and  $y$
- $E(\hat{x}, u, h(\hat{x}, u)) = 0$  for  $\hat{x}$  and  $u$
- $E(\phi_g(\hat{x}), \psi_g(u), \rho_g(y)) = E(\hat{x}, u, y)$  for  $\hat{x}$ ,  $u$ , and  $y$ .

The first two properties mean  $E$  is an output error, the third expresses the invariance. The introduction of the invariant error is necessary, because the output error  $\hat{y} - y$  does not usually preserve the geometry of the system [21].

The following three theorems [15, 16] support the construction of the symmetry-preserving observers.

**Theorem 1.** The observer  $\frac{d}{dt} \hat{x} = F(\hat{x}, u, y)$  is a G-invariant pre-observer for the G-invariant non-linear Eq.(20) with a G-equivariant output if and only if

$$F(\hat{x}, u, y) = f(\hat{x}, u) + \sum_{i=1}^n L_i(I(\hat{x}, u), E(x, u, y)) w_i(\hat{x}) \quad (24)$$

where  $E$  is an invariant output error,  $(\hat{x}, u) \rightarrow I(\hat{x}, u) \in \mathbb{R}^{n+m-r}$  is a full rank function,  $L_i$  is a smooth function, such that  $L_i(I(\hat{x}, u), 0) = 0$  and  $(w_1, w_2, \dots, w_n)$  is an invariant frame. Since  $L_i(I, E) = \bar{L}_i(I, E)E$

$$\begin{aligned} \sum_{i=1}^n L_i(I, E) w_i &= \sum_{i=1}^n w_i (\bar{L}_i(I, E) E) \\ &= \begin{pmatrix} w_1 & \dots & w_n \end{pmatrix} \begin{pmatrix} \bar{L}_1(I, E) \\ \vdots \\ \bar{L}_n(I, E) \end{pmatrix} E \end{aligned} \quad (25)$$

The observer can be written as follows

$$F(\hat{x}, u, y) = f(\hat{x}, u) + W(\hat{x}) L(I(\hat{x}, u), E(\hat{x}, u, y)) E(\hat{x}, u, y). \quad (26)$$

**Theorem 2.** The following statements are valid:

- $(\hat{x}, u, y) \rightarrow E(\hat{x}, u, y)$  invariant output error exists,
- there is a  $(\hat{x}, u) \rightarrow I(\hat{x}, u) \in \mathbb{R}^{n+m-r}$  invariant function,
- every other invariant output error has the form of

$$\tilde{E}(\hat{x}, u, y) = L(I(\hat{x}, u), E(\hat{x}, u, y)) \quad (27)$$

where  $L$  is a smooth function such that  $L(I, 0) = 0$  and  $E \rightarrow L(I, E)$  is invertible.

**Theorem 3.** Consider the equilibrium of a non-linear system

$$f(\bar{x}, \bar{u}) = 0 \quad \text{and} \quad \bar{y} = h(\bar{x}, \bar{u})$$

Assume that the linearized system  $A, B, C, D$  around this equilibrium is observable, where

$$A = \frac{\partial f}{\partial x}(\bar{x}, \bar{u}), \quad B = \frac{\partial f}{\partial u}(\bar{x}, \bar{u}), \quad C = \frac{\partial h}{\partial x}(\bar{x}, \bar{u}), \quad D = \frac{\partial h}{\partial u}(\bar{x}, \bar{u})$$

and let  $L$  be such that  $A + LC$  is a stable matrix. From the locally asymptotically convergent observer

$$\frac{d}{dt} \hat{x} = f(\hat{x}, u) + L(\hat{y} - y), \quad \hat{y} = h(\hat{x}, u) \quad (28)$$

an invariant observer can be constructed by the same linear approximation

$$\frac{d}{dt} \hat{x} = f(\hat{x}, u) + W(\hat{x}) \bar{L}(I(\hat{x}, u), E(\hat{x}, u, y)) E(\hat{x}, u, y) \quad (29)$$

where  $\bar{L} = -W(x)^{-1} L V^{-1}$  and  $V = \frac{\partial E}{\partial y(\bar{x}, \bar{u}, \bar{y})}$  is an invertible matrix of  $p \times p$  dimensions.

There is no general algorithm for designing the  $L_i$  gain functions of *Theorem 1*. However, if we consider the following invariant state error

$$\eta(x, \hat{x}) = \phi_{\gamma(x)}(\hat{x}) - \phi_{\gamma(x)}(x) \quad (30)$$

instead of the  $\hat{x} - x$  state error, where  $\gamma(x)$  is the solution of

$$\phi_g^a(x) = c \quad (31)$$

with respect to  $g$ , then the invariant error will only depend on the  $I(x, u)$  trajectories.

### Constructive Algorithm

Consider an invariant system, i.e. unchanged by transformation Eq.(21) with an equivariant output (*Definition 3*). The non-linear observer design for non-linear dynamic systems [10, 11] can be divided into the following steps:

- Choose a G LIE-group and a group transformation taking into account the symmetrical properties of the system.
- Solve the normalization Eq.(31). Build an invariant error  $E$  and the complete set of scalar invariants  $I$ .
- Construct the invariant frame Eq.(22).
- Determine the pre-observer Eq.(25).
- Linearize the system  $f(\bar{x}, \bar{u}) = 0$  around the equilibrium and obtain  $A, B, C, D$  matrices. Check the observability and design an invariant observer from the chosen linear observer by using *Theorem 3*. Choose an appropriate  $\bar{L}$ .
- Choose the parameters of the linearized error equations, based on the invariant state-errors  $\eta$ , such that the invariant system will be asymptotically stable.

Then the non-linear symmetry-preserving observer is asymptotically stable, and converges locally and exponentially along all system trajectories.

### Case Study: A Non-Holonomic Vehicle

In this section, the previously introduced state estimation procedures are employed for an example of a non-holonomic vehicle tracking control. The well-known model in the robotics of the simplified vehicle kinematics is considered. The tracking is maintained by satisfying the kinematic constraints with the appropriate choice of reference signals.

#### Kinematic Model

The simplified kinematic model of the vehicle can be written in the following form

$$\begin{pmatrix} \dot{x} \\ \dot{y} \\ \dot{\theta} \end{pmatrix} = \begin{pmatrix} u \cos \theta \\ u \sin \theta \\ v \end{pmatrix}, \quad h(x, y, \theta) = (x, y) \quad (32)$$

where  $u$  is the velocity,  $v$  is the curvature, i.e. a function of the steering angle and  $h$  is the measured output. All signals contain additive Gaussian noise. The model assumes that the contact point of the wheel and the ground does not slip. Notice, that the linearized system is not observable.

#### Tracking

For path tracking the control signals are set to satisfy the kinematic constraints, thus  $u$  and  $v$  are calculated as follows:

$$u(t) = \sqrt{\dot{x}_r^2(t) + \dot{y}_r^2(t)} \quad \text{and} \quad v(t) = \frac{\ddot{y}_r(t)\dot{x}_r(t) - \dot{x}_r(t)\ddot{y}_r(t)}{u^3(t)} \quad (33)$$

where  $x_r(t)$  and  $y_r(t)$  are time functions of the reference signal. The initial conditions for tracking control is

$$\theta_r(0) = \tan^{-1} \left( \frac{\dot{y}_r(0)}{\dot{x}_r(0)} \right). \quad (34)$$

Hence, the reference signals for the vehicle velocity and steering function can be calculated. In the simulations, sinusoidal path tracking is implemented using the reference signals

$$x_r(t) = t, \quad \text{and} \quad y_r(t) = A \sin(\omega t).$$

#### Invariant Observer Design

##### Group Transformation

Eq.(32) is independent of the origin and of the orientation of the frame chosen, i.e. it is invariant with

regards to the group of rotations and translations. We chose the Lie-group  $G = SE(2)$  and defined the group transformation as follows:

$$\begin{aligned} \phi_{(x_g, y_g, \theta_g)}(x, y, \theta) &= \begin{pmatrix} x_g \\ y_g \\ \theta_g \end{pmatrix} \cdot \begin{pmatrix} x \\ y \\ \theta \end{pmatrix} = \\ &= \begin{pmatrix} x \cos \theta_g - y \sin \theta_g + x_g \\ x \sin \theta_g + y \cos \theta_g + y_g \\ \theta + \theta_g \end{pmatrix} \end{aligned} \quad (35)$$

$$\psi_{(x_g, y_g, \theta_g)}(u, v) = \begin{pmatrix} u \\ v \end{pmatrix}$$

$$\rho_{(x_g, y_g, \theta_g)}(x, y) = \begin{pmatrix} x \cos \theta_g - y \sin \theta_g + x_g \\ x \sin \theta_g + y \cos \theta_g + y_g \end{pmatrix}$$

One can check that Eq.(32) is invariant to the transformations  $\phi$ , and  $\psi$  in terms of Definition 1 and the output is equivariant to transformation  $\rho$  in terms of Definition 3.

#### Invariant Output Errors

The normalization Eq.(31) for  $c = 0$ :

$$\begin{aligned} 0 &= x \cos \theta_\gamma - y \sin \theta_\gamma + x_\gamma \\ 0 &= x \sin \theta_\gamma + y \cos \theta_\gamma + y_\gamma \\ 0 &= \theta + \theta_\gamma \end{aligned} \quad (36)$$

The solution of Eq.(36), the scalar invariants and output errors can be written as follows respectively

$$\begin{pmatrix} x_\gamma \\ y_\gamma \\ \theta_\gamma \end{pmatrix} = \begin{pmatrix} x \\ y \\ \theta \end{pmatrix}^{-1} = \begin{pmatrix} -x \cos \theta - y \sin \theta \\ x \sin \theta - y \cos \theta \\ -\theta \end{pmatrix} = \gamma \begin{pmatrix} x \\ y \\ \theta \end{pmatrix} \quad (37)$$

$$I(x, y, \theta, u, v) = \psi_\gamma(x, y, \theta)(u, v) = \begin{pmatrix} u \\ v \end{pmatrix} \quad (38)$$

$$\begin{aligned} E &= \rho_{(x_\gamma, y_\gamma, \theta_\gamma)}(\hat{x}, \hat{y}) - \rho_{(x_\gamma, y_\gamma, \theta_\gamma)}(x, y) \\ &= \begin{pmatrix} \cos \hat{\theta} & \sin \hat{\theta} \\ -\sin \hat{\theta} & \cos \hat{\theta} \end{pmatrix} \begin{pmatrix} \hat{x} - x \\ \hat{y} - y \end{pmatrix} \end{aligned} \quad (39)$$

#### Invariant Frame

$$\begin{aligned} W &= (D\phi_\gamma(x, y, \theta)(x, y, \theta))^{-1} \frac{\partial}{\partial (x, y, \theta)} = \\ &= D\psi_\gamma(x, y, \theta)(x, y, \theta) = \begin{pmatrix} \cos \theta & -\sin \theta & 0 \\ \sin \theta & \cos \theta & 0 \\ 0 & 0 & 1 \end{pmatrix}. \end{aligned} \quad (40)$$

### Invariant pre-observer

$$\frac{d}{dt} \begin{pmatrix} \hat{x} \\ \hat{y} \\ \hat{\theta} \end{pmatrix} = \begin{pmatrix} u \cos \hat{\theta} \\ u \sin \hat{\theta} \\ uv \end{pmatrix} + \begin{pmatrix} \cos \hat{\theta} & -\sin \hat{\theta} & 0 \\ \sin \hat{\theta} & \cos \hat{\theta} & 0 \\ 0 & 0 & 1 \end{pmatrix} \bar{L} \times \begin{pmatrix} \cos \hat{\theta} & \sin \hat{\theta} \\ -\sin \hat{\theta} & \cos \hat{\theta} \end{pmatrix} \begin{pmatrix} \hat{x} - x \\ \hat{y} - y \end{pmatrix} \quad (41)$$

where  $\bar{L}$  is a smooth  $3 \times 2$  gain matrix, whose elements depend on the invariant error  $E$  and the invariants  $I$ .

### Error Equations and Error Dynamics

$$\eta = \begin{pmatrix} \eta_x \\ \eta_y \\ \eta_\theta \end{pmatrix} = \gamma(\hat{x}, \hat{y}, \hat{\theta}) \begin{pmatrix} \hat{x} \\ \hat{y} \\ \hat{\theta} \end{pmatrix} - \gamma(\hat{x}, \hat{y}, \hat{\theta}) \begin{pmatrix} x \\ y \\ \theta \end{pmatrix} = \begin{pmatrix} (\hat{x} - x) \cos \hat{\theta} + (\hat{y} - y) \sin \hat{\theta} \\ -(\hat{x} - x) \sin \hat{\theta} + (\hat{y} - y) \cos \hat{\theta} \\ (\hat{\theta} - \theta) \end{pmatrix} \quad (42)$$

$$\begin{pmatrix} \dot{\eta}_x \\ \dot{\eta}_y \\ \dot{\eta}_\theta \end{pmatrix} = \begin{pmatrix} u(1 - \cos \eta_\theta) + (uv + \bar{L}_{31}\eta_x + \bar{L}_{32}\eta_y)\eta_y \\ u \sin \eta_\theta - (uv + \bar{L}_{31}\eta_x + \bar{L}_{32}\eta_y)\eta_x \\ 0 \end{pmatrix} + \bar{L} \begin{pmatrix} \eta_x \\ \eta_y \end{pmatrix} \quad (43)$$

It can be seen that the invariant error equations are independent of the trajectory and only depend on the relative quantities  $\eta_x$ ,  $\eta_y$ , and  $\eta_\theta$  and the  $I$  invariants.

### Stability and Convergence

The weighting matrix is defined as follows

$$\bar{L} = \begin{pmatrix} -|u|a & ubE_y - uv \\ uv - ubE_y & -|u|c \\ 0 & -ub \end{pmatrix}, \quad (44)$$

where  $a$  and  $b$  are care positive scalars and  $E_y = \eta_y$ . The invariant error dynamics can be made locally asymptotically stable. Furthermore, the resulting symmetry-preserving observer is almost globally

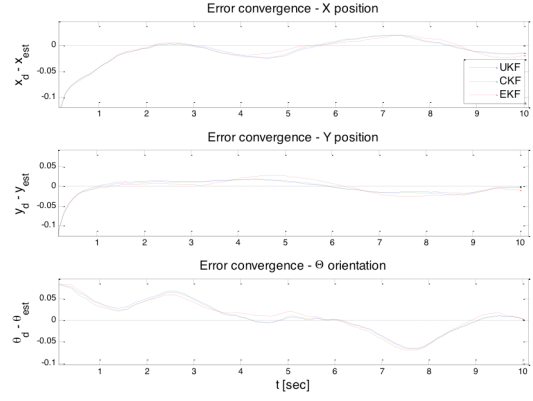


Figure 2: Estimation errors of the sigma-point and extended KALMAN filters from Example 1

asymptotically convergent, i.e. it converges any initial condition except for one as described in Refs. [15-16].

### Simulation Results

The state estimation techniques are illustrated in two tracking examples. For comparative purposes, the following algorithms have been implemented: Extended KALMAN Filter (EKF), Central Difference and Unscented KALMAN Filter (CKF, UKF) and the symmetry preserving observer (SYM) discretized by the sample time of the sigma-point estimators.

The reference paths are  $x_r(t) = t$ , and  $y_r(t) = A \sin(\omega t)$ , where  $A = 3$  m and  $\omega = \pi/5$  rad  $s^{-1}$ . Zero mean additive Gaussian noise is assumed with standard deviations of 0.01 and 0.005 for the process noise and 0.02 for the measurement noise. The sampling time is  $T_s = 0.1$  s. The initial values are  $x_0^{est} = y_0^{est} = \theta_0^{est} = 1$ , and  $x_0 = y_0 = 0$ .

#### Example 1

The vehicle starts from the origin of the  $xy$ -plane with large initial estimation error and tracks a sinusoidal path. Fig.1 shows the estimated output positions of the vehicle using sigma-point KALMAN filters and symmetry-preserving observers. The estimation errors of different algorithms can be seen in Figs.2 and 3.

The errors are smaller and show smoother signals in the case of the SPKF estimators, which was expected, since the SYM observer is deterministic. Large errors appear at the peak values of the reference signals; however, both estimation techniques achieved the same satisfactory results in spite of the relatively small sampling frequency.

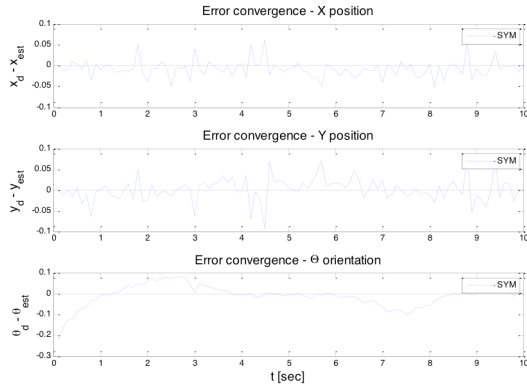


Figure 3: Estimation errors of the symmetry-preserving observer (SYM) from Example 1

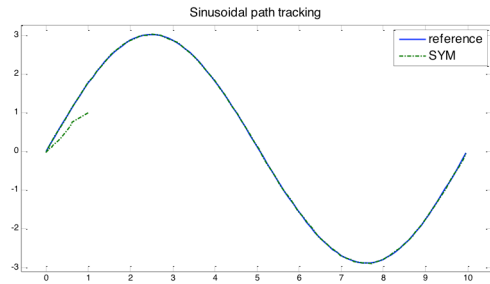


Figure 5: Estimated output position of the vehicle using symmetry-preserving observer (SYM) from Example 2

Table 1: Root-mean-squared errors of the estimated signals from Example 1

RMSE	$x, m$	$y, m$	$\theta, rad$
UKF	0.1368	0.1587	0.0338
CKF	0.1366	0.1577	0.0336
EKF	0.1371	0.1551	0.0352
SYM	0.1371	0.1628	0.0455

Table 2: Root-mean-square errors of the estimated signals from Example 2

RMSE	$x, m$	$y, m$	$\theta, rad$
UKF	0.0998	0.1180	0.0627
CKF	0.0993	0.1175	0.0628
EKF	0.1013	0.1165	0.0648
SYM	0.1264	0.1453	0.0760

Root-mean-square errors can be seen in Table 1. We can conclude that among the processes of state estimation techniques the SYM observer is competitive with SPKF estimators.

### Example 2

In this example the vehicle performs an off-line estimation before movement starts, followed by an on-line estimation along a sinusoidal path. It is notable that in the stationary state the velocity is zero and at the beginning of movement the velocity changes to a non-zero value abruptly, see Eq.(33). Figs.4-7 illustrate the estimated output positions and the measurement errors for the sigma-point estimators and the invariant observers respectively

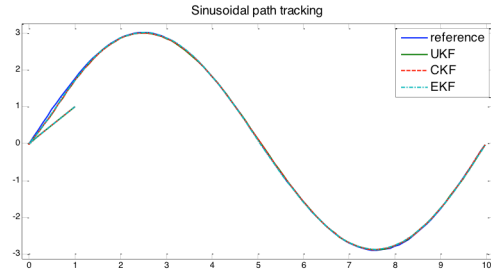


Figure 4: Estimated output position of the vehicle using sigma-point state estimation (UKF, CKF) and extended KALMAN Filter (EKF) from Example 2

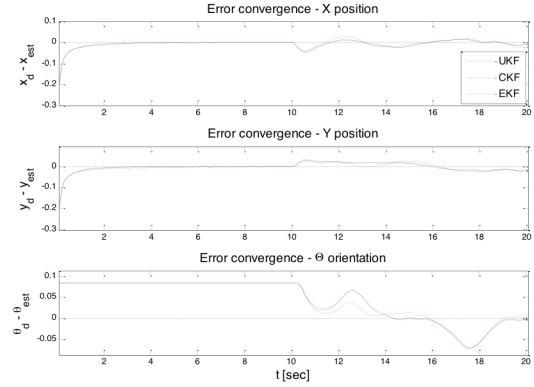


Figure 6: Estimation errors of the sigma-point and the extended KALMAN filters from Example 2

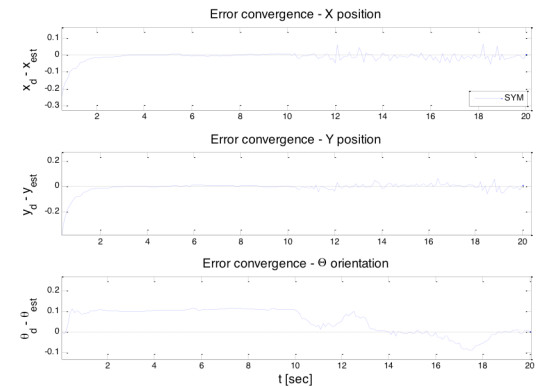


Figure 7: Estimation errors of the symmetry-preserving observer (SYM) from Example 2

The error signals show a quick convergence in the case of the symmetry-preserving observer. The speed of convergence depends on the parameters set in the  $\bar{L}$  matrix; however, high gains can cause the observer to be divergent and make larger errors. Since there are no  $u$  and  $\delta$  signals in the stationary position and the orientation is not directly measured, the orientation can only be estimated after the vehicle starts moving.

The error signal oscillates around zero in a similar way to Example 1. Due to calibration, smaller errors appear. The invariant observer and sigma-point estimators have the same magnitude of error components. The root-mean-square errors of the simulation can be seen in Table 2.

## Conclusion

In this paper we presented a comparison of two different recently developed state estimation techniques. The Sigma-Point (SPKF) stochastic estimator is based on the Unscented Transformation and the non-linear symmetry-preserving observers are based on the group transformation of symmetrical LIE groups and invariant frames. Two examples are considered for the estimation of vehicle kinematics: the first example deals with the path tracking reliability of the vehicle; the second example examines the convergence and the speed of the off-line calibration followed by path tracking.

The examples illustrate that for non-linear systems in noisy environments the use of stochastic state-estimators is needed. Moreover the Sigma-point approach provides more accurate estimation results than the commonly used non-linear EKF state estimators.

The symmetry preserving observers for non-linear systems benefit from their constructive design method, which provides local asymptotic convergence. This method can be utilized by non-linear applications in which the physical and mechanical symmetry properties of the system can be exploited.

## REFERENCES

- [1] BAR-SHALOM Y., LI X.-R., KIRUBARAJAN T.: Estimation with Applications to Tracking and Navigation, Wiley Interscience, New York, NY, U.S.A., 2001
- [2] SÄRKKÄ S.: Recursive Bayesian inference on stochastic differential equations, PhD Thesis, Helsinki University of Technology, Helsinki, Finland, 2006
- [3] JULIER S.J., UHLMANN J.K.: Unscented filtering and non-linear estimation, Proc. IEEE, 2004, 92(3), 401–422
- [4] VAN DER MERWE R., WAN E.A., JULIER S.: Sigma-Point KALMAN Filters for Nonlinear Estimation and Sensor-Fusion: Applications to Integrated Navigation, Proc. AIAA Guidance, Navigation & Control Conference (GNC), Providence, RI, U.S.A. 2004
- [5] VAN DER MERWE R.: Sigma-Point KALMAN Filters for Probabilistic Inference in Dynamic State-Space Models, PhD Thesis, Oregon Health & Science University, Eugene, OR, U.S.A., 2004
- [6] JULIER S.J., UHLMANN J.K.: Corrections to unscented filtering and non-linear estimation, Proc. IEEE, 2004, 92(12), 1958–1958
- [7] JULIER S.J., UHLMANN J.K.: Unscented filtering and non-linear estimation, Proc. IEEE, 2004, 92(3), 401–422
- [8] WAN E.A., VAN DER MERWE R.: The unscented KALMAN filter, in KALMAN Filtering and Neural Networks, Ed.: HAYKIN S., John Wiley and Sons, New York, NY, U.S.A., 2001, Chapter 7
- [9] NORGAARD M., POULSEN N., RAVN O.: Advances in Derivative-Free State Estimation for Non-linear Systems Tech. Rep. IMM-REP-1998-15, Dept. Math. Modelling, Technical University of Denmark, Lyngby, Denmark, 2000
- [10] NORGAARD M., POULSEN N., RAVN O.: New Developments in State Estimation for Nonlinear Systems, Automatica 2000, 36(11), 1627–1638
- [11] ITO K., XIONG K.: Gaussian Filters for Nonlinear Filtering Problems, IEEE Trans. Automatic Control 2000, 45(5), 910–927
- [12] VAN DER MERWE R., WAN E.: Efficient Derivative-Free KALMAN Filters for Online Learning, Proc. 9th Eur. Symp. Artificial Neural Networks (ESANN) Bruges, Belgium, 2001, 205–210
- [13] VAN DER MERWE R., WAN E.: The Square-Root Unscented KALMAN Filter for State- and Parameter-Estimation, Proc. IEEE Int. Conf. Acoustics, Speech, and Signal Processing (ICASSP), Salt Lake City, UT, 2001, 6, 3461–3464
- [14] SALAM ERAN: Filtering Algorithms and Avionics Systems for Unmanned Aerial Vehicles, PhD Thesis, MINES ParisTech, Paris, France, 2010
- [15] BONNABEL S., MARTIN P., ROUCHON P.: Non-linear Symmetry Preserving Observers on LIE-Groups, IEEE Transactions on Automatic Control, 2009, 54(7), 1709–1713
- [16] BONNABEL S., MARTIN P., ROUCHON P.: Symmetry-preserving Observers, IEEE Transactions on Automatic Control, 2008, 53(11), 2514–2526
- [17] BONNABEL S., MARTIN P., ROUCHON P.: A non-linear symmetry-preserving observer for velocity aided inertial navigation, Proc. 2006 American Control Conference, Minneapolis, MN, U.S.A., 2006
- [18] AYHANMAN N., ROUCHON P.: On invariant asymptotic observers, CDC, 2002
- [19] ROUCHON P., GUILLAUME D.: Observation and Control of Simplified Car, IFAC, 1998
- [20] BONNABEL S.: Symmetries in observer design: review of some recent results and application to EKF-based SLAM, Robot Motion and Control 2011, Lecture Notes in Control and Information Sciences 2012, 422, 3–15
- [21] COLLON C., RUDOLPH J., WOITENNEK F.: Invariant Feedback Design for Control Systems with Lie-symmetries – a kinematic car example, Discrete Cont. Dyn. Sys. 2011, 2(11), 312–321

## TELEMEDICAL HEART RATE MEASUREMENTS FOR LIFESTYLE COUNSELLING

MARIO SALAI,<sup>✉</sup> GERGELY TUBOLY, ISTVÁN VASSÁNYI, AND ISTVÁN KÓSA

Faculty of Information Technology, University of Pannonia, Egyetem u. 10., Veszprém, 8200, HUNGARY  
<sup>✉</sup>Email: mario.salai@gmail.com

In this paper we analyse a low-cost commercial chest belt to be integrated into a lifestyle counselling system as a source of heart rate data. We compared data from a Schiller ECG Holter device, which serves as a reference to a CardioSport device. Due to missing data in the CardioSport device caused by loss of contact with the body, the creation of special algorithms was necessary for synchronization and data validation. The results show that when using our synchronization algorithms the average absolute percentage error between the two signals was 2% with correlation of more than 99%. Using a data validation algorithm, we were able to get on average more than 70% of the signal with an absolute percentage error of 3% and a high average correlation of 99%. The mean RR interval values and standard deviation of RR intervals are very close to those of the reference device using both the synchronization and data validation algorithms. When using the data validation algorithm, the reference measurements produced only slightly better results with regard to false detections of atrial defibrillation than the CardioSport device. In conclusion, we found that with a simple pre-processing algorithm, CardioSport as a low-cost device can be safely integrated into a lifestyle support system as a telemedical solution.

**Keywords:** telemedicine, lifestyle counselling, heart rate monitor

### Introduction

Low-cost telemedical sensors are often used in modern ambient assisted living (AAL) telemonitoring and self-management systems for providing inputs to medical intelligence algorithms [1]. Such systems extend the scope of traditional health care that is based purely on data measurement. However, the proper interpretation and reliability of the results depends on the reliability of the measured data and the sensor itself. Nevertheless, there are still surprisingly few reviews reported in the literature to date on the validation of the information content of such low-cost sensors compared to the clinically accepted reference device. An example of a device that was tested for validity is the SenseWear HR Armband [2]. In this study, they used the reference device simultaneously with the tested device as a way of validating data. However, most of the compared devices are expensive high-end devices, which present an obstacle for their wide use in telemedicine.

In this proof-of-concept paper, we analyse a simple commercial chest belt chosen to be integrated into the Lavinia lifestyle mirror system [3] as a source of heart rate (HR) data. In the Lavinia system, the HR signal of the patient will be used to (i) estimate the calories burnt by physical activity, (ii) calculate the heart rate variability (HRV) in order to detect periods of mental or emotional stress, and (iii) analyse arrhythmia patterns (Poincare plots) for atrial fibrillation detection. Our approach involves the comparison of the HRV and

Poincare plots computed from the filtered chest belt signal, with those parameters computed from a reference Holter device.

### Methods

#### *Measurements*

Two devices were used simultaneously by a healthy volunteer over a 24 hour period. A Schiller MT-101/MT-200 Holter device was our reference device designed for clinical use. The chest belt was a CardioSport TP3 Heart Rate Transmitter device. Since this device does not have its own memory for storing data, we used a Nexus 7 tablet with Android version 4.4.2 to connect the device via the Bluetooth 4.0 protocol and store the measured data on the tablet.

Although both devices were worn by volunteers for 24 hours, only 12 hours of the overall signal were used for analysis due to frequent detachments of the device from the body during nighttime. The measurements of 12 hours were repeated on 4 additional healthy male subjects.

#### *Signal Analysis*

The direct comparison of measured data was not possible due to the different designs of the reference and the telemedical devices. However, we wanted to

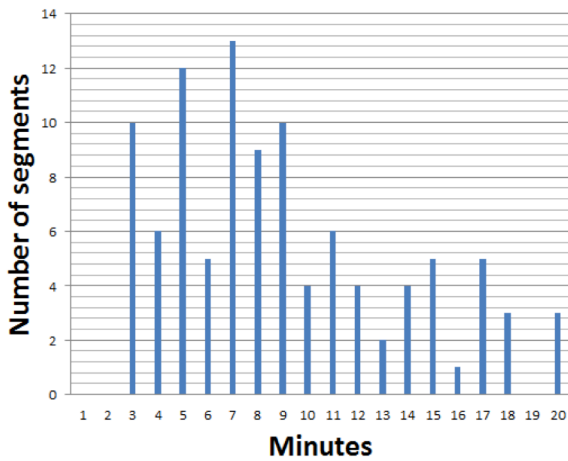


Figure 1: The distribution of strongly correlated segment lengths for all subjects

compare signals directly in terms of time and also to develop a data validation algorithm for removing the noisy parts of the CardioSport device measurements reliably without using the reference data. The problem was that the chest belt was not firmly attached to the body and sudden movements of the device caused signal loss. Therefore, we needed to create a software module for synchronization and data validation before any analysis. Data validation means removing obviously bad data (artefacts) and keeping only ‘good’ data segments of sufficient length, because, as a rule of thumb, both HRV and Poincare plot computations require data chunks of at least 5 minutes. Even though the data validation algorithm removed a considerable amount of data from the original signal, we still had enough useful data for analysis from the daytime.

#### The Synchronization Algorithm

Our simple algorithm for signal synchronization uses a sliding window that passes from the beginning of the chest belt signal to the end and calculates the absolute error between the two signals. When sliding finishes, the location of the sliding window with the minimum absolute error is considered as the point where the two signals should be synchronized. This applies only if the correlation of the data in the sliding window and the same amount of data from the reference device are higher than a minimum set by the user. If these conditions are met, the algorithm copies data from the sliding window into a newly generated third signal, which represents the chest belt signal fully synchronized with the reference signal. If conditions are not met, the third signal is filled with zeros. Finally, the algorithm extracts all the highly correlated segments from the third signal ignoring zero values. Also, a file with all the merged segments is generated for general analysis. The algorithm uses the following 5 main parameters that can be set up by the user:

1. window size: amount of data copied from the signal into the sliding window (default: 200),

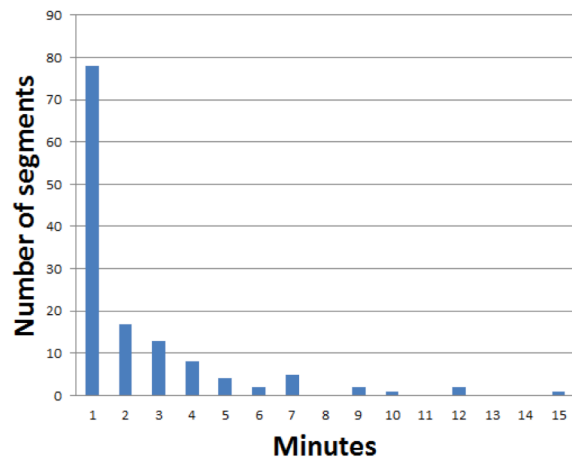


Figure 2: The distribution of weakly correlated segment lengths for all subjects

2. window shift step: the number of samples by which we shift the sliding window in each iteration (default: 50),
3. absolute error window: amount of data used for calculating the minimum absolute error (default: 200),
4. maximum error distance: the number of samples by which we shift the absolute error window in order to find the minimum absolute error (default: 1000),
5. minimum correlation: minimum correlation, expressed as a percentage, required for the two signals to consider data in the chest belt signal as accurate (default: 97%).

Each parameter’s default value was determined empirically. After running the synchronization process, we obtained segments of highly correlated data. *Fig.1* shows the distribution of the lengths of signal segments. We can see that most segments are 3 to 18 minutes long. The longest highly correlated segment with the reference data is 110 minutes long. The default parameter settings minimize the number of overly short (< 5 min) segments. Most of the bad segments (*Fig.2*) are shorter than one minute, and only one bad segment was 60 minutes long.

#### Data Validation Algorithm

Another type of algorithm was used in the real telemedical scenario for finding good parts of the signal without relying on reference data. This implies finding gaps and abnormal values and omitting them. First, we compared the timestamp of each data point with the timestamp of the previous one. If the difference between the timestamps was longer than 3 seconds, we marked this as a ‘gap’. The 3-second gap detection was enabled by the chest belt’s buffering system that can tolerate short detachments of the device from the body. In the second step we identified abnormal values in the signal that were treated as gaps. The abnormal values are identified by observing the mean value of 20 neighbouring data points (10 before and 10 after a given point). If the mean value differs from the value of the

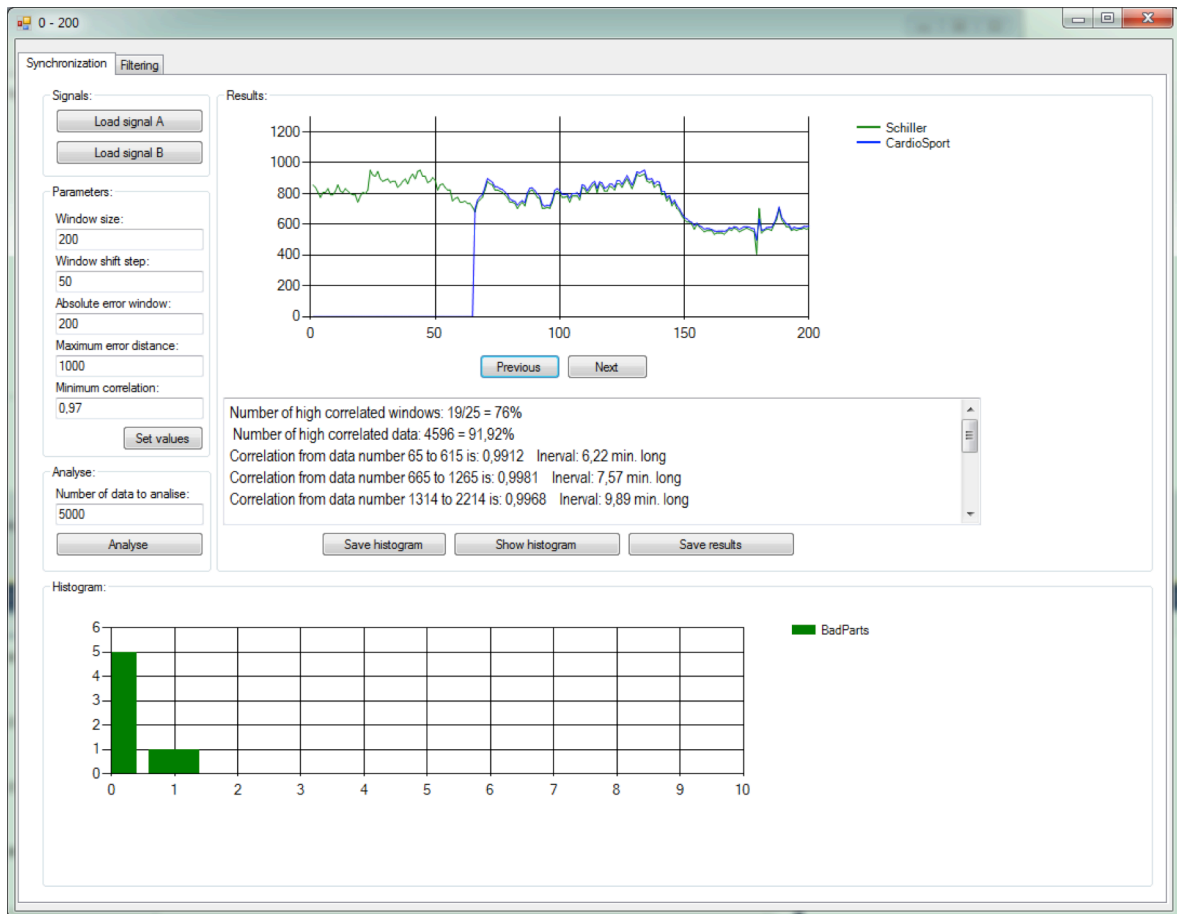


Figure 3: Synchronization and data validation software

current sample by more than 300 units, we consider it invalid and mark it as a gap/error in the signal. Finally, we extract the good segments from the signal with a length of more than 5 minutes.

We implemented the above algorithm in a simple software tool (Fig. 3). On the left-hand side we can load the two signals and set the parameter values as well as the amount of data to be analysed. The graph shows two signals after the synchronization process was completed. The user can examine signals by clicking the Previous and Next buttons. General statistics are shown in the middle part of the screen, while in the lower part, we can see the histogram, and save the histogram and results as a file. Two tabs in the top left-hand corner allow the user to switch between synchronization and data validation algorithms.

### Statistical Analysis

Time and frequency domain analyses, correlation comparisons, mean absolute percentage errors, and the slopes of scatter plot diagrams were compared between two measurements for HRV analysis. The specificities of a self-developed atrial fibrillation detector algorithm were compared for atrial fibrillation analysis. The latter algorithm is based on the k-means clustering of Poincaré plots (consisting of RR intervals)

The time and frequency domain analyses for HRV were performed using Kubios HRV analysis software,

Table 1: Signal duration after the synchronization process

Subject	Duration (h:m:s)
#1	10:53:28
#2	8:45:40
#3	10:30:17
#4	7:46:56

while the rest of the analysis for HRV and atrial fibrillation was performed in Microsoft Excel. Atrial fibrillation detection was done using the MATLAB environment and the results were saved as Microsoft Excel workbooks.

## Results and Analysis

### Heart Rate Variability

After the synchronization process, we got strongly correlated (greater than 97%) synchronized data segments of various durations. Table 1 summarizes the duration of signals analysed.

Table 2 shows results in the time domain for Schiller and CardioSport devices after using the algorithm for the synchronization of signals. Time domain analysis shows similar values for mean RR values and standard deviation (STD RR in Eq.(1)). The average Mean RR values for the Schiller and CardioSport devices are 851 and 871 respectively. The average STD RR for the Schiller device is 108 and 110 for the CardioSport device.

Table 2: Time domain analysis after synchronization

Subject	Mean RR (ms) <sup>a</sup>		STD RR (ms) <sup>b</sup>	
	Schiller	CardioSport	Schiller	CardioSport
#1	738	755	123	125
#2	704	720	91	93
#3	908	929	90	93
#4	855	875	145	148
#5	937	959	107	109
Average	851	871	108	111

<sup>a</sup> with 2% error, <sup>b</sup> with 1-3% error

Table 3: Frequency domain analysis after synchronization

Subject	Schiller				CardioSport				Error			
	Absolute power (ms <sup>2</sup> )				Absolute power (ms <sup>2</sup> )				% % % %			
	VLF	LF	HF	LF/HF	VLF	LF	HF	LF/HF	VLF	LF	HF	LF/HF
#1	7937.6	3086	1578	1.956	8444	3224	1330	2.4235	6	4	19	19
#2	5431.5	626.6	245	2.557	5723	659.3	250.9	2.6281	5	5	2	3
#3	4251.2	1927	494.4	3.898	4543	2055	538.8	3.8146	6	6	8	2
#4	12682	1790	636.5	2.813	13514	1869	621.5	3.0077	6	4	2	6
#5	6139.8	1212	476.7	2.542	6465	1274	481.4	2.6459	5	5	1	4

Table 4: Signal duration after data validation

Subject	Duration (h:m:s)
#1	1:28:10
#2	11:20:03
#3	6:15:38
#4	9:27:07
#5	4:29:44

$$STD\ RR = \sqrt{\frac{1}{N-1} \sum_{j=1}^N (RR_j - \overline{RR})^2} \quad (1)$$

The frequency domain analysis for the synchronization process is presented in Table 3. The absolute power was compared for very low frequencies (VLF: 0-0.04 Hz), low frequencies (LF: 0.04-0.15 Hz), high frequencies (HF: 0.15-0.4 Hz) and ratios between low frequencies and high frequencies (LF/HF). Results show no significant difference between Schiller and CardioSport device values. The average mean absolute percentage error (MAPE) between two signals is 2% with a high average correlation of close to 100%.

Using the data validation algorithm, we extracted data points from the collected signals. The duration of the resulting signal is shown in Table 4. It is important to note that due to the noise on Schiller device recordings, we had to remove noisy parts from the original signal. Therefore, even though the signal was recorded continuously for 12 hours, overall duration is

much less. Calculations show that in the worst scenario only 45% of the signal can be used for analysis using this data validation method, while in the best scenario this number reaches 95%. This leads to a conclusion that results are rather subject dependent.

The results of data analysis in the time domain after the removal of bad parts using the validation algorithm can be seen in Table 5. The mean RR intervals for Schiller and CardioSport devices are 851 and 871 and standard deviations are 104 and 106, respectively. The

Table 5: Time-domain analysis after data validation

Subject	Mean RR (ms) <sup>a</sup>		STD RR (ms) <sup>b</sup>	
	Schiller	CardioSport	Schiller	CardioSport
#1	701	724	136	139
#2	700	717	91	93
#3	899	921	100	100
#4	846	866	139	142
#5	958	981	88	90
Average	851	871	105	106

<sup>a</sup> with 2% error, <sup>b</sup> with 0-2% error

CardioSport device has slightly greater values, but these are practically identical.

The frequency domain analysis for the data validation process is presented in Table 6. The absolute power was compared for very low frequencies (VLF: 0-0.04 Hz), low frequencies (LF: 0.04-0.15 Hz), high frequencies (HF: 0.15-0.4 Hz), and ratios between low frequencies and high frequencies (LF/HF). As in the synchronization process, the results show no significant difference between the Schiller and CardioSport device values.

The minimum, maximum and average percentage errors on whole signals were calculated using 5 minute long sliding windows with one minute long shift steps (Table 7). Only one subject had a high maximum error value of 34%. By visual examination, it was determined that the cause of such a high error was the artefact of the Schiller device. In spite of that, the average error remained low (2%).

Table 6: Frequency domain analysis after data validation

Subject	Schiller				CardioSport				Error			
	Absolute power (ms <sup>2</sup> )				Absolute power (ms <sup>2</sup> )				% % % %			
	VLF	LF	HF	LF/HF	VLF	LF	HF	LF/HF	VLF	LF	HF	LF/HF
#1	10414	2297	1171	1.96	10847	2442	1004	2.43	4	6	17	19
#2	5446	631	245	2.57	5718	654	245	2.67	5	3	1	4
#3	5163	1990	523	3.80	5424	2054	540	3.80	5	3	3	0
#4	11683	1769	616	2.87	12149	1831	594	3.08	4	3	4	7
#5	4356	1235	317	3.89	4522	1303	330	3.95	4	5	4	1

Table 7: The minimum, maximum and average percentage errors

Subject	Minimum error	Maximum error	Average error
#1	0.1%	3.5%	1.5%
#2	0.0%	7.7%	2.1%
#3	0.0%	33.9%	3.2%
#4	0.1%	6.7%	1.9%
#5	0.1%	5.1%	2.2%
Average	0.1%	13.4%	2.4%

Fig.4 represents a typical relationship between CardioSport and Schiller devices. All gradient values are close to 1. The lowest slope value is 0.98 while the highest value is 1.02. The average mean absolute percentage error (MAPE) between two signals was 3% with a strong average correlation of 99%.

### Atrial Fibrillation

We carried out the detection of atrial fibrillation (AFib) by analysing POINCARÉ plots consisting of 30 RR intervals. We considered 30 RR intervals per iteration and in each iteration after constructing the POINCARÉ plot we calculated the dispersion around the diagonal line and used k-means based cluster analysis to determine the number of the clusters. If the dispersion was too high (greater than 0.06) and the number of clusters was 1, or the number of clusters was more than 9; we assigned "AFib" to that series of RR intervals, otherwise to "Non-AFib". The details of the algorithm can be seen in our previous study [16]. Since our data

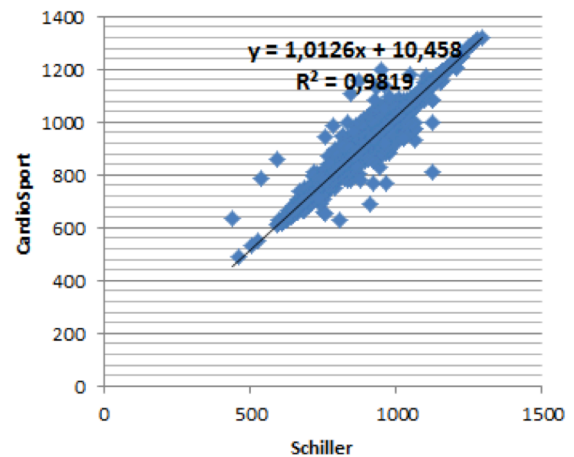


Figure 4: Comparison of the CardioSport and Schiller devices after data validation

set did not contain real AFib cases, only specificity could be calculated with regard to the efficiency of detection. The evaluation of atrial fibrillation detection results for synchronized data validation can be seen in Tables 8 and 9.

### Conclusion

Even though the CardioSport device may suffer from signal loss due to its design, we managed to determine that it can be safely used for telemedical purposes of measuring HRV and atrial fibrillation. We found only a few usable data segments that were less than 5 minutes long. With our algorithm that detects gaps and errors in

Table 8: Results from the synchronized data related to atrial fibrillation detection

Subject	Number of iterations	Schiller MT-101/MT-200 system				CardioSport TP3 Heart Rate Transmitter			
		AFib cases		Non-Afib cases		AFib cases		Non-Afib cases	
#1	331	26	8%	305	92%	31	9%	300	91%
#2	1796	9	1%	1787	99%	3	>1%	1793	~100%
#3	1120	7	1%	1113	99%	5	1%	1115	99%
#4	1427	11	1%	1416	99%	16	1%	1411	99%
#5	964	46	5%	918	95%	45	5	919	95%
Min	-	-	1%	-	92%	-	>1%	-	91%
Max	-	-	8%	-	99%	-	9%	-	~100%
Mean	-	-	3%	-	97%	-	3%	-	97%
STD	-	-	3%	-	3%	-	4%	-	4%

Table 9: Results from the data validation process related to atrial fibrillation detection

Patient	Number of iterations	Schiller MT-101/MT-200 system				CardioSport TP3 Heart Rate Transmitter			
		AFib cases		Non-Afib cases		AFib cases		Non-Afib cases	
#1	241	3	1%	238	99%	8	3%	233	97%
#2	1879	29	2%	1850	98%	2	>1%	1877	~100%
#3	808	15	2%	793	98%	3	>1%	805	~100%
#4	1296	10	1%	1286	99%	20	2%	1276	98%
#5	544	6	1%	538	99%	7	1%	537	99%
Min	-	-	1%	-	99%	-	>1%	-	97%
Max	-	-	2%	-	99%	-	3%	-	~100%
Mean	-	-	1%	-	99%	-	1%	-	99%
STD	-	-	>1%	-	>1%	-	1%	-	11%

the signal and removes them with an average effectiveness of more than 70%, which translates into having enough data to calculate HRV and atrial fibrillation from daytime measurements.

Regarding atrial fibrillation detection, we can conclude that by using the developed data validation algorithm the reference Schiller MT-101/MT-200 measurements produced only slightly better results with regard to false detections than the CardioSport TP3 Heart Rate Transmitter. In two cases the CardioSport measurements proved to be even better than Schiller records, which implies that some relatively simple heart rate recorders are equivalent to some Holter devices after signal processing using the data validation algorithm. We have to emphasize; however, that we have not performed any measurements on actual atrial fibrillating patients yet. Therefore, the investigation of the sensitivity of our atrial fibrillation detection algorithm under the presented circumstances could be the subject of further studies. In summary, the CardioSport as a low-cost device can easily be integrated into a lifestyle support system as a telemedical solution.

#### ACKNOWLEDGMENTS

This research was supported by the European Union and co-funded by the European Social Fund “Telemedicine-

focused research activities in the field of Mathematics, Informatics and Medical Sciences” TÁMOP-4.2.2.A-11/1/KONV-2012-0073.

#### REFERENCES

- [1] PATEL S., PARK H., BONATO P., CHAN L., RODGERS M.: A review of wearable sensors and systems with application in rehabilitation, *J. Neuroengng. Rehab.*, 2012, 9(21), 1–17
- [2] KRISTIANSEN J., KORSHØJ M., SKOTTE J.H., JESPERSEN T., SØGAARD K., MORTENSEN O.S., HOLTERMANN A.: Comparison of two systems for long-term heart rate variability monitoring in free-living conditions - a pilot study, *Biomed Eng. Online*, 2011, 10(27), 1–14
- [3] KÓSA I., VASSÁNYI I., NEMES M., KÁLMÁNNÉ K.H., PINTÉR B., KOHUT L.: A fast, Android based dietary logging application to support the lifestyle change of cardio-metabolic patients, *Global Telemedicine and eHealth Updates: Knowledge Resources*, Eds.: M. JORDANOVA, F. LIEVENS, 2014, 7, 553–556
- [4] SALAI M., TUBOLY G., VASSANYI I., KOSA I.: Reliability of telemedical Heart Rate meters, *IME J.*, 2014, 8(5), 49–55

## THE APPLICATION OF UNKNOWN INPUT ESTIMATORS TO DAMP LOAD OSCILLATIONS OF OVERHEAD CRANES

BÁLINT PATARTICS<sup>✉</sup> AND BÁLINT KISS

Department of Control Engineering and Information Technology, Budapest University of Technology and Economics,  
Magyar Tudósok krt. 2, Budapest, 1111, HUNGARY  
<sup>✉</sup>E-mail: patarticsbalint@gmail.com

This paper focuses on the development of state estimation methods for mechanical systems with uncertain frictional parameters. The goal of the study is to provide reliable angle estimation for state-feedback-based crane control solutions, designed to reduce load sway. Cranes are underactuated systems, usually unequipped with the sensors necessary to measure the swinging angle, therefore the damping of their oscillatory behaviour is a challenging task. Two estimators are proposed for the calculation of the unmeasured states. One is based on an 'unknown input Kalman filter' (UIKF), the other applies the 'unscented Kalman filter' (UKF) with load prediction. Simulation results are provided to demonstrate the accuracy of the algorithms.

**Keywords:** overhead crane, state estimation, nonlinear systems, unknown inputs, Kalman filter

### Introduction

The sway of the load carried by cranes is an unwanted phenomenon. Friction may decouple load motion from the remaining crane mechanism. This causes difficulty for inexperienced operators, especially when they try to land the cargo. The friction present in the crane mechanism makes the reduction of the swinging particularly demanding. Therefore the goal of the design of crane control systems is often to ensure minimal swinging along a specified trajectory [1–6].

There are numerous algorithms available in the literature for the solution to this problem. The design of such a control system can be addressed using soft computing methods such as fuzzy logic and neural network with genetic algorithm. These solutions require however the measurement of the load position, which is often based on workspace visualization [1]. Hard commuting techniques are also widely applied for sway reduction. An  $H_2$  optimal solution is described in Ref.[2], which also relies on image processing for the measurement of the load coordinates. There are a variety of algorithms taking advantage of the flatness property (or exact linearizability) of overhead cranes [7]. The control systems in Refs.[3] and [4] consider all the states measurable, however an estimator is proposed in Ref.[3] for the computation of the uncertain parameters.

In the case of navy cranes, local asymptotic stability can be achieved without the measurement of the swinging angle, if trajectory planning exploits the flatness property of the system [6]. There is also a tracking control algorithm specifically designed for overhead cranes, that

is capable of effectively reducing the sway despite the friction [5]. For the calculation of the unmeasured states, this controller uses a linear observer. In this paper we propose new methods of state observation for systems that take into account friction, and are applicable to overhead cranes. These estimators can replace the linear observer in Ref.[5] or the need to measure the load coordinates in any other state-feedback-based method to enhance the precision of the control. Our estimation methods are based on the assumption that the effect of the friction on the inputs can be reduced. This is true for most mechanical systems (including overhead cranes), where the actuating signals are usually forces and torques.

In the following section, the modelling of Lagrangian mechanical systems is overviewed, and it is shown how the friction can be handled as an input disturbance. In the next section the state estimation techniques are presented based on the possible approaches of interpreting the friction. The next section describes the results of the application of these methods to the state estimation problem of overhead cranes and presents the simulation results.

### Lagrangian-Based Models of Mechanical Systems

The nonlinear dynamics of the controlled system can be obtained using the Euler-Lagrange equations. If the generalized coordinates are  $q = (q_1 \ q_2 \ \dots \ q_n)^T$  and the generalized forces are  $\tau = (\tau_1 \ \tau_2 \ \dots \ \tau_n)^T$ , the Euler-Lagrange equations read

$$\frac{d}{dt} \frac{\partial \mathcal{L}}{\partial \dot{q}_i} - \frac{\partial \mathcal{L}}{\partial q_i} = \tau_i, \quad (1)$$

where  $\mathcal{L}$  is the so-called Lagrangian, the difference between the kinetic and potential energy of the system,  $\dot{q}_i = \frac{dq_i}{dt}$  and  $i = 1, 2, \dots, n$ .

Using these equations, under some conditions the controlled system's model can be written in the form

$$H(q)\dot{q} + h(q, \dot{q}) + h_s(s) = \tau, \quad (2)$$

where  $H(q)$  is the inertia matrix,  $h(q, \dot{q})$  comprises the centrifugal, Coriolis and gravitational terms, and  $h_s(s)$  is the frictional term with  $s$  being the vector of the frictional forces. In this form  $h_s(s)$  can be reorganized to the right-hand-side of the equation. Introducing the disturbance torques as  $\tilde{\tau} = \tau - h_s(s)$ , Eq.(2) yields

$$H(q)\dot{q} + h(q, \dot{q}) = \tilde{\tau}. \quad (3)$$

The state-space representation of the model is

$$\begin{aligned} \dot{x} &= f(x, u) \\ y &= g(x), \end{aligned} \quad (4)$$

where  $x$  is the state,  $u$  is the input,  $y$  is the output of the system, and  $f$  and  $g$  are nonlinear functions. This form can be obtained from Eq.(5) assuming that  $x^T = (q^T \ \dot{q}^T)$ , and the output is not directly dependent on the torques. The state-space equations read

$$\begin{aligned} \dot{x} &= \begin{pmatrix} \dot{q} \\ -H^{-1}(q)h(q, \dot{q}) \end{pmatrix} + \begin{pmatrix} 0 \\ H^{-1}(q) \end{pmatrix} \tilde{\tau} \\ y &= g(x). \end{aligned} \quad (5)$$

The inputs of mechanical systems are usually forces and torques, consequently they are only dependent on  $\tilde{\tau}$ . This means, that the effect of the friction can be reduced to the actuated degrees of freedom of the system.

If it is necessary for the design of the control system, the nonlinear dynamics can be approximated by a first order Taylor series expansion around a setpoint  $(x_0, u_0)$ . The linear model then becomes

$$\begin{aligned} \delta\dot{x} &= A\delta x + B\delta u \\ \delta y &= C\delta x, \end{aligned} \quad (6)$$

where the quantities prefixed with  $\delta$  mean the distance from the setpoint, e.g.  $\delta x = x - x_0$ , and the matrices are Jacobians [8].

### State Estimation Methods

Since the friction can be interpreted in our setup as an input disturbance, we consider two ways for its compensation in the state estimation. Either all input variables can be disregarded, or the additive disturbance can be estimated using a load predictor. These ideas form the basis of the two estimator design techniques described as follows.

The computations of the controllers implemented in embedded systems are based on sampled signals. Hence the design of the estimators is done in discrete-time.

### Unknown Input Approach

Consider the discrete-time linear stochastic system model

$$\begin{aligned} x[k+1] &= \Phi x[k] + \Gamma_d d[k] + \omega[k] \\ z[k] &= Cx[k] + v[k], \end{aligned} \quad (7)$$

where  $x$  is the state,  $d$  is the unknown input (disturbance) of the system and  $z$  is the measurement of the output  $y[k] = Cx[k]$ .  $\Phi$  and  $\Gamma_d$  are obtained from the matrices of Eq.(6) in the form of

$$\Phi = e^{AT_s}, \quad \Gamma_d = \int_0^{T_s} e^{At} B dt, \quad (8)$$

where  $T_s$  is the sample time. The measurement and process noise  $v$  and  $\omega$  are assumed to be additive, white, and Gaussian with mean of zero. Notice, that in Eq.(7), all of the system inputs are considered to be disturbances.

The state and the unknown input of such a system can be estimated using an 'unknown input Kalman filter' (UIKF) [9], if the system satisfies the conditions

$$\dim\{d\} \leq \dim\{y\} \quad (9)$$

$$\text{rank}\{C\} = \dim\{y\} \quad (10)$$

$$\text{rank}\{\Gamma_d\} = \dim\{d\} \quad (11)$$

$$\text{rank}\{C\Gamma_d\} = \dim\{d\}. \quad (12)$$

### Additive Disturbance Approach

In the case of input disturbances, load prediction is often applied. Let us introduce the discrete-time nonlinear model of a system in the form

$$\begin{aligned} x[k+1] &= \phi(x[k], \tilde{u}[k]) + \omega[k] \\ z[k] &= g(x[k]) + v[k], \end{aligned} \quad (13)$$

where  $\tilde{u}$  is the disturbed input of the system, and  $\phi$  and  $g$  are nonlinear functions. We will follow the assumption, that the disturbance is additive to the input, thus  $\tilde{u}[k] = u[k] + \Lambda d[k]$ , where  $u$  is the vector of actuating signals, and  $\Lambda$  is a constant matrix.

We also assume a constant disturbance model with process noise  $\omega_d$ ,  $d[k+1] = d[k] + \omega_d[k]$ , resulting in the model

$$\begin{aligned} \tilde{x}[k+1] &= \tilde{\phi}(\tilde{x}[k], u[k]) + \tilde{\omega}[k] \\ z[k] &= \tilde{g}(\tilde{x}[k]) + v[k]. \end{aligned} \quad (14)$$

In Eq.(14)  $\tilde{x}^T = (x^T \ d^T)$  is the extended state and  $\tilde{\omega}^T = (\omega^T \ \omega_d^T)$  is the extended process noise. The extended nonlinear mappings of the system are given by  $\tilde{g}(\tilde{x}[k]) = g(x[k])$  and

$$\tilde{\phi}(\tilde{x}[k], u[k]) = \begin{pmatrix} \phi(x[k], u[k] + \Lambda d[k]) \\ d[k] \end{pmatrix}. \quad (15)$$

In most cases the continuous-time differential equation of the observed system is available, in the form

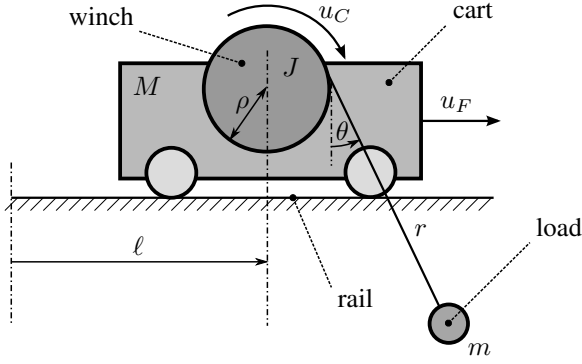


Figure 1: The two-dimensional overhead crane

of Eq.(4). The discrete-time state-transition equation can then be obtained by

$$\phi(x[k], u[k]) = x[k] + \int_{kT_s}^{(k+1)T_s} f(x, u[k]) dt, \quad (16)$$

where the input is piecewise constant and  $u[k] = u(kT_s)$ . If the integral in Eq.(16) cannot be given in closed form and  $T_s$  is sufficiently small, the left rectangle rule approximation

$$\int_{kT_s}^{(k+1)T_s} f(x, u[k]) dt \approx T_s f(x[k], u[k]). \quad (17)$$

can be used. Substituting this into Eq.(15), the expression reads

$$\tilde{\phi}(\tilde{x}[k], u[k]) = \begin{pmatrix} x[k] + T_s f(x[k], u[k] + \Lambda d[k]) \\ d[k] \end{pmatrix}. \quad (18)$$

For the observation of the system described by Eq.(14) and Eq.(18) the 'unscented Kalman filter' (UKF) [10] is applicable. We chose one of the implementation variants of this filter from Ref.[10].

## Application of the Methods to Overhead Cranes

### System Dynamics

We will now consider the state estimation problem of the two-dimensional overhead crane (Fig.1). Let us denote the horizontal displacement of the cart by  $\ell$ , the length of the rope by  $r$  and the angle between the vertical and the rope by  $\theta$ . The generalized coordinates of the system are chosen to be  $q = (\ell \ r \ \theta)^T$ , and the state is  $x = (\ell \ r \ \theta \ \dot{\ell} \ \dot{r} \ \dot{\theta})^T$ . Based on the sensors available, the output is  $y = (\ell \ r \ \dot{\ell} \ \dot{r})^T$ .

Overhead cranes is a typical example of underactuated systems. It is actuated by two motors, one applying the force  $u_F$  on the cart, and another delivering the

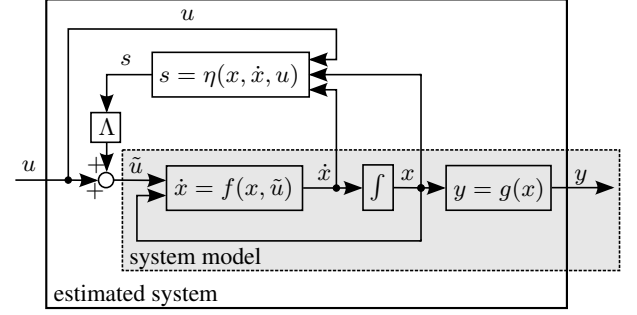


Figure 2: Dynamics of the estimated system

torque  $u_C$  to the winch. The system input consists of these,  $u = (u_F \ u_C)^T$ .

The parameters of the system are the mass of the cart  $M$ , the mass of the load  $m$ , the moment of inertia of the winch  $J$  and the radius of the winch  $\rho$ . The acceleration in the gravitational field is denoted by  $g$ .

The following assumptions are made of the system.

- The rope connecting the load to the winch is massless and behaves as a rigid rod during the motion.
- The load is a point mass.
- $M$ ,  $m$ ,  $J$  and  $\rho$  are known.
- In the initial state of the system the unmeasured states are zero:  $\theta = 0$  rad and  $\dot{\theta} = 0$  rad/s.
- The effect of the aerodynamic resistance is negligible.

The Lagrangian of overhead cranes reads

$$\mathcal{L} = \frac{1}{2} (M + m) \dot{\ell}^2 + \frac{1}{2} \frac{J}{\rho^2} \dot{r}^2 + \frac{1}{2} m (\dot{r}^2 + r^2 \dot{\theta}^2) + m \dot{r} \sin \theta + m \dot{r} \dot{\theta} \cos \theta + m g r \cos \theta. \quad (19)$$

Using Eq.(1), the model can be written in the form of Eq.(2), where the expressions become

$$H(q) = \begin{pmatrix} (M + m \sin^2 \theta) & m \sin \theta & 0 \\ m \sin \theta & \left(\frac{J}{\rho^2} + m\right) & 0 \\ \cos \theta & 0 & r \end{pmatrix}, \quad (20)$$

$$h(q, \dot{q}) = - \begin{pmatrix} m(r \dot{\theta}^2 + g \cos \theta) \sin \theta \\ m r \dot{\theta}^2 + m g \cos \theta \\ -2 \dot{r} \dot{\theta} - g \sin \theta \end{pmatrix}, \quad (21)$$

$$h_s(s) = - \begin{pmatrix} s_F \\ s_C \\ 0 \end{pmatrix}, \quad \tau = \begin{pmatrix} u_F \\ -\frac{u_C}{\rho} \\ 0 \end{pmatrix}, \quad (22)$$

where  $s_F$  is the frictional force between the cart and the rail and  $s_C$  is the frictional force applied to the winch.

The continuous-time linear model of the crane is computed around the setpoint  $x_0 = (0 \ r_0 \ 0 \ 0 \ 0 \ 0)^T$ ,  $u_0 = (0 \ m g \rho)^T$ , and  $s_F = s_C = 0$  is substituted

Table 1: Numeric values of the parameters

	Value	Unit
$M$	5	kg
$m$	0.05	kg
$J$	$3.802 \cdot 10^{-4}$	kg m <sup>2</sup>
$\rho$	0.02	m
$g$	9.81	m s <sup>-2</sup>
$T_s$	1	ms
$r_0$	0.47	m
$\ell_D$	0.5	m

into Eq.(5). The resulting Jacobians are

$$\begin{aligned}
 A &= \begin{pmatrix} 0 & 0 & 0 & 1 & 0 & 0 \\ 0 & 0 & 0 & 0 & 1 & 0 \\ 0 & 0 & 0 & 0 & 0 & 1 \\ 0 & 0 & \frac{m}{M}g & 0 & 0 & 0 \\ 0 & 0 & 0 & 0 & 0 & 0 \\ 0 & 0 & -\frac{m+M}{Mr_0}g & 0 & 0 & 0 \end{pmatrix}, \\
 B &= \begin{pmatrix} 0 & 0 \\ 0 & 0 \\ 0 & 0 \\ \frac{1}{M} & 0 \\ 0 & -\frac{\rho}{m\rho^2+J} \\ -\frac{1}{Mr_0} & 0 \end{pmatrix}, \\
 C &= \begin{pmatrix} 1 & 0 & 0 & 0 & 0 & 0 \\ 0 & 1 & 0 & 0 & 0 & 0 \\ 0 & 0 & 0 & 1 & 0 & 0 \\ 0 & 0 & 0 & 0 & 1 & 0 \end{pmatrix}.
 \end{aligned} \tag{23}$$

Substituting Eq.(22), the disturbance torque term in Eq.(3) reads

$$\tilde{\tau} = \begin{pmatrix} u_F + s_F \\ -\frac{1}{\rho}(u_C - \rho s_C) \\ 0 \end{pmatrix}. \tag{24}$$

Eq.(24) shows, that the disturbed input of the system can be introduced in the form  $\tilde{u} = u + \Lambda s$ , where

$$\Lambda = \begin{pmatrix} 1 & 0 \\ 0 & -\rho \end{pmatrix}. \tag{25}$$

The frictional forces usually depend on the actuating signals, state variables, and the derivative of the state as well. The general characteristics of the friction reads as  $s = \eta(x, \dot{x}, u)$ . The block diagram of the dynamics of the system is illustrated in Fig.2. Only the system model block is used for estimator design, which is Eq.(5) if the effect of the friction is disregarded,  $h_s(s) = 0$ .

**Proposition 1.** *The discrete-time linear crane model obtained from the matrices in Eq.(23) and using Eq.(8) satisfies the design conditions of the UIKF in Eq.(9-12).*

*Proof.* It is clear that  $\dim\{y\} = 4$ ,  $\dim\{d\} = 2$  and  $\text{rank}\{C\} = 4$ , thus Eq.(9) and (10) are satisfied. Us-

ing Eq.(8) and the numerical values in Table 1,

$$\begin{aligned}
 \Gamma_d &= 10^{-2} \begin{pmatrix} 0.0001 & 0 \\ 0 & -0.025 \\ -0.0002 & 0 \\ 0.2 & 0 \\ 0 & -49.975 \\ -0.4255 & 0 \end{pmatrix}, \\
 C\Gamma_d &= 10^{-2} \begin{pmatrix} 0.0001 & 0 \\ 0 & -0.025 \\ 0.2 & 0 \\ 0 & -49.975 \end{pmatrix}.
 \end{aligned} \tag{26}$$

We obtain  $\text{rank}\{\Gamma_d\} = 2$  and  $\text{rank}\{C\Gamma_d\} = 2$ , which are both equal to the number of unknown inputs. This satisfies Eqs.(11) and (12). The continuity argument holds for the rank of the matrices in Eq.(26), therefore there exists a neighbourhood around our parameter set where the design conditions are still satisfied.

### Simulation

The estimation results were obtained by simulation of overhead cranes in a closed-loop scenario using a simple discrete-time pole-placement-based linear controller. The simulation also took into account friction. There are various models of the friction phenomenon, ours included Coulomb, Stribeck, viscous friction, and stiction [11]. The numerical values of the parameters used in the simulation are given in Table 1.

Because of friction, but mainly stiction, the position of the crane can not be accurately controlled without integrators in the controller. Consequently we included the integral of the measurable positions in the controller design as proposed on page 309 of Ref. [8].

The outputs to be integrated are  $y_I = (\ell \ r)^T$ . Integrals of these quantities are approximated by the left rectangle rule as

$$x_I[k+1] = x_I[k] + T_s y_I[k] = x_I[k] + T_s C_I x[k], \tag{27}$$

where  $C_I$  is defined so that  $y_I[k] = C_I x[k]$ . In our case  $C_I$  is the first two rows of  $C$  in Eq.(23). Using Eq.(27) and Eq.(7) a new system model is introduced in the form

$$\begin{aligned}
 \tilde{x}[k+1] &= \tilde{\Phi}\tilde{x}[k] + \tilde{\Gamma}u[k] \\
 y[k] &= \tilde{C}\tilde{x}[k].
 \end{aligned} \tag{28}$$

where the expanded state is  $\tilde{x}^T = (x^T \ x_I^T)$  and the matrices are

$$\begin{aligned}
 \tilde{\Phi} &= \begin{pmatrix} \Phi & 0 \\ T_s C_I & I \end{pmatrix}, \quad \tilde{\Gamma} = \begin{pmatrix} \Gamma_d \\ 0 \end{pmatrix}, \\
 \tilde{C} &= (C \ 0).
 \end{aligned} \tag{29}$$

For the controller design the process and measurement noises are omitted.

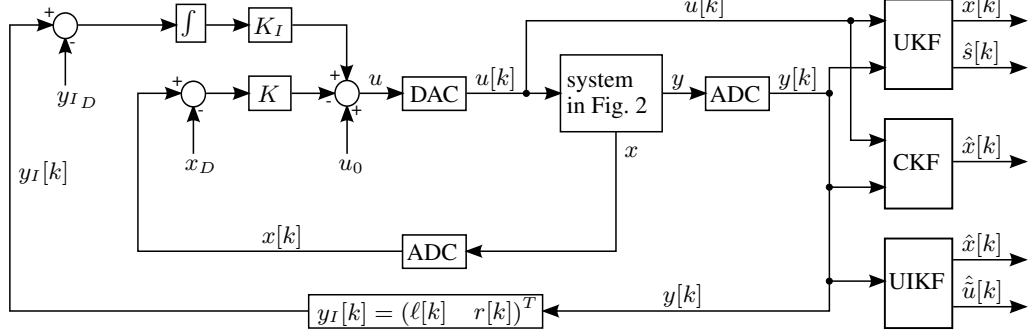


Figure 3: Closed-loop estimation setup used in the simulation

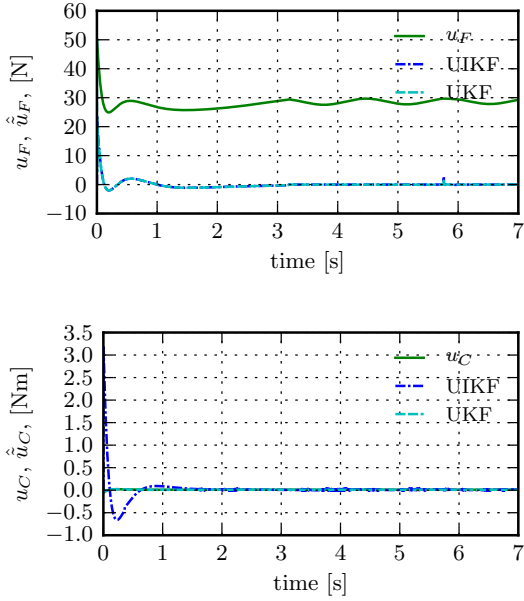


Figure 4: Actuating signals and the estimated inputs of the system

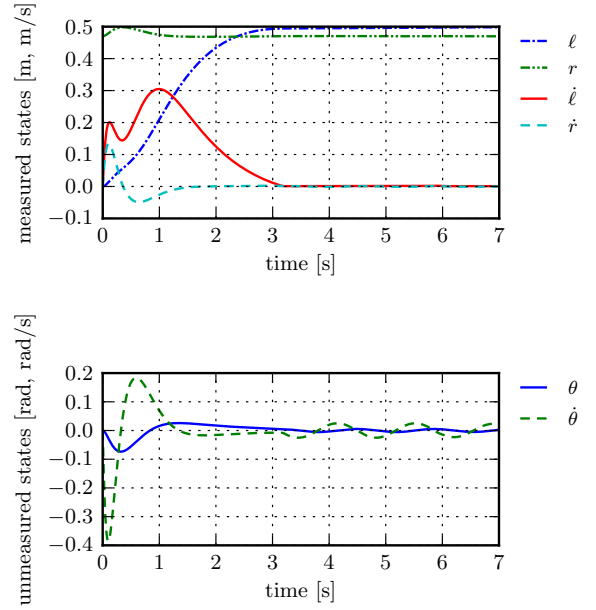


Figure 5: State evolution of the controlled crane using the true states as feedback

We want the state-feedback controller to output  $u[k] = -\tilde{K}\tilde{x}[k] = -Kx[k] - K_I x_I[k]$ . The gain  $\tilde{K}$  can be computed using the eigenvalue placement method implemented in Matlab's `place` algorithm:  $\tilde{K} = \text{place}(\tilde{\Phi}, \tilde{\Gamma}, \lambda)$ , where  $\lambda$  contains the chosen eigenvalues of the closed-loop system. In continuous time they are  $-1 + 0.5j$ ,  $-1 - 0.5j$ ,  $-5.1$ ,  $-5.2$ ,  $-5.3$ ,  $-5.4$ ,  $-5.5$ , and  $-5.6$ . The controller gains are

$$K = \begin{pmatrix} 100.594 & -0.1273 \\ 0.6011 & -1.6765 \\ -185.407 & 0.0458 \\ 81.4011 & -0.0558 \\ 0.0562 & -0.3166 \\ -4.2257 & -0.0195 \end{pmatrix}^T, \quad \text{and} \quad (30)$$

$$K_I = \begin{pmatrix} 46.641 & 1.6026 \\ -0.074 & -2.955 \end{pmatrix}.$$

The closed-loop setup is illustrated in Fig.3. Here the integration is done using the left rectangle rule, and the

ADC and DAC blocks are analogue-digital and digital-analogue converters respectively. The DAC uses the zero-order hold method for signal reconstruction. The desired state of the system is  $x_D = (\ell_D \ r_0 \ 0 \ 0 \ 0 \ 0)^T$ ,  $\ell_D$  is the desired position of the cart and  $y_{ID} = C_I x_D$ .

Since we only want to demonstrate the results of the state estimation, first the real states are fed back to the controller. To compare the accuracy of our methods to a traditional solution, the classical Kalman filter (CKF) [12] is also implemented. As a result, the Kalman filters compute the estimated state of the system  $\hat{x}[k]$ , and they also provide information about the input.

The UIKF estimates the friction loaded actuating signals directly, while the UKF estimates the frictional forces superposed to the actuating signals. The actuating signals along with the estimates of the real inputs provided by the filters can be seen in Fig.4. Here, the estimated input of the UKF is computed as  $\hat{u} = u[k] + \Lambda \hat{s}[k]$ .

Because of friction, the real inputs are estimated to be

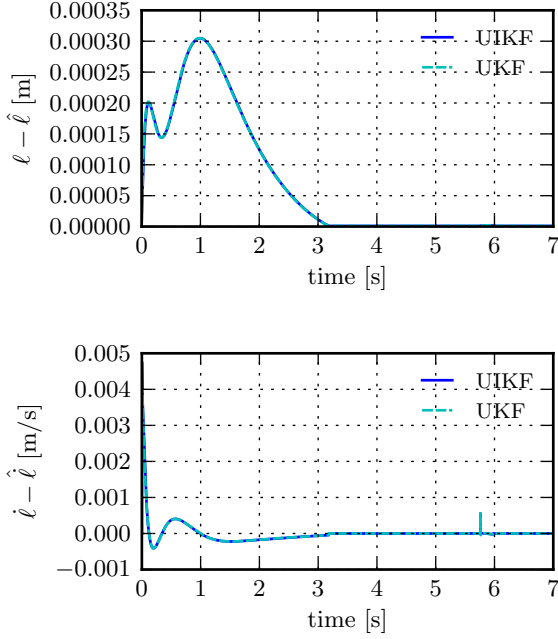


Figure 6: Error of the position and velocity estimations

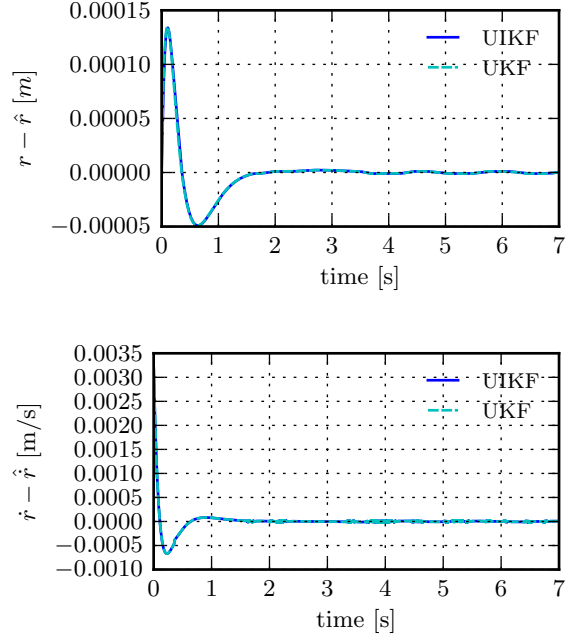


Figure 7: Error of the rope length and hoisting velocity estimations

much less than the actuating signals. The large offset in Fig.4 is a consequence of the stiction, the cart will not move until  $u_F$  becomes greater than a certain value (in our case about 28 N). When the cart finally stops moving, the fluctuation of  $u_F$  tries to counter the load sway, during which the measured states do not change. This is the reason why the estimators find the input to be zero.

Fig.5 shows the transient of the states in a closed-loop. Results show that the controller can bring the system into the desired state, but friction prevents it from stopping the low amplitude swinging of the load, because it makes quick, short motions impossible. Error estimates are illustrated by Figs. 6 and 7. In all cases, the error becomes zero when the crane reaches the desired state.

This is not true for the angle and its derivative in Fig.8. The error decreases at the end of the state transient, but does not become zero. When the cart stops and the load swings, the measurements are all constant thus they carry no information regarding  $\theta$  and  $\dot{\theta}$ . In these situations the cart and winch are usually also motionless due to friction. Consequently, the estimation error of these quantities never becomes zero.

It is possible to decrease the estimation error using two laser slot sensors. With the help of such devices,  $\theta$  can be measured accurately in two positions and through the application of proper sensor fusion techniques the estimation of the angle can become more precise in between the chosen positions as well.

In Fig.9 the estimation error of  $\theta$  and  $\dot{\theta}$  is illustrated using CKF. The filter was designed for the dynamics given by Eq.(7) except that it does not consider the inputs unknown. The results show that the error is substantially higher than in the case of the UIKF or UKF.

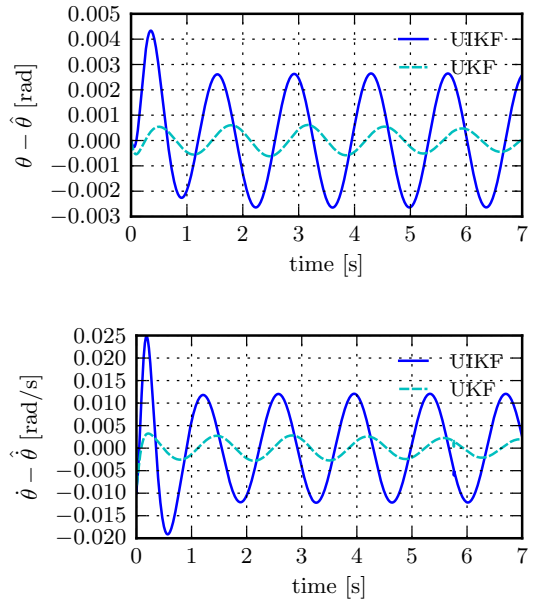


Figure 8: Error of the angle and angular velocity estimations

Fig.8 shows the estimation error of the UKF to be less. We applied this estimator in a closed-loop scenario identical to the one presented in Fig.3, but instead of  $x[k]$  the  $\hat{x}[k]$  of the UKF was used in the feedback loop. The state evolution of the crane in this simulation is illustrated in Fig.10. The system's behaviour is only slightly different from the case when the actual states were used in the feedback control in Fig.5.

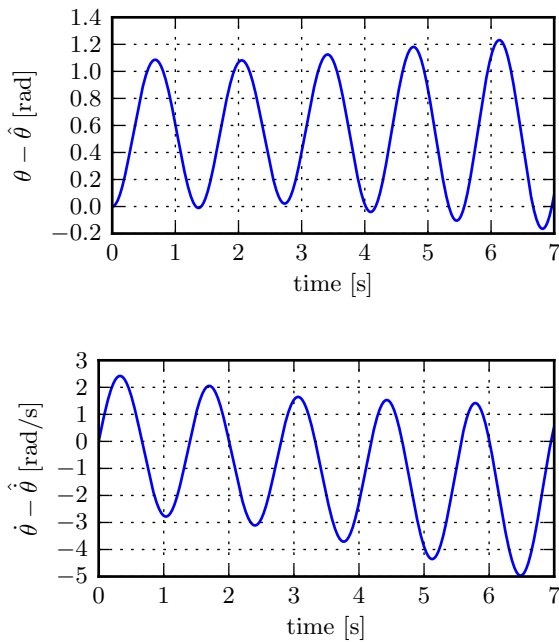


Figure 9: Error of the angle and angular velocity estimations using CKF

### Conclusion

It was shown that in most mechanical systems the disturbing effect of friction can be reduced to the actuating signals. Based on this statement, two estimation methods were provided for the computation of the unmeasured states. One of these techniques considers the inputs completely unknown and uses UIKF for the estimation. The other algorithm treats the inputs as distorted by an additive disturbance, and applies UKF with a load predictor extension. Simulation results in a closed-loop controlled scenario were provided to prove the applicability of the concepts. It was also pointed out, that the precision of the estimators could be improved using laser slot sensors. This will be the subject of a forthcoming paper.

### REFERENCES

- [1] HYLA P.: The crane control systems: A survey, Proc. 17th Int. Conf. Methods and Models in Automation and Robotics (MMAR), 2012, 505–509
- [2] SCHINDELE D., MENN I., ASCHEMANN H.: Non-linear optimal control of an overhead travelling crane, Proc. 18th IEEE Int. Conf. Control Applications, 2009, 1045–1050
- [3] BOUSTANY F., D'ANDREA NOVEL B.: Adaptive control of an overhead crane using dynamic feedback linearization and estimation design, Proc. IEEE Int. Con. Robotics and Automation, 1992, 1963–1968

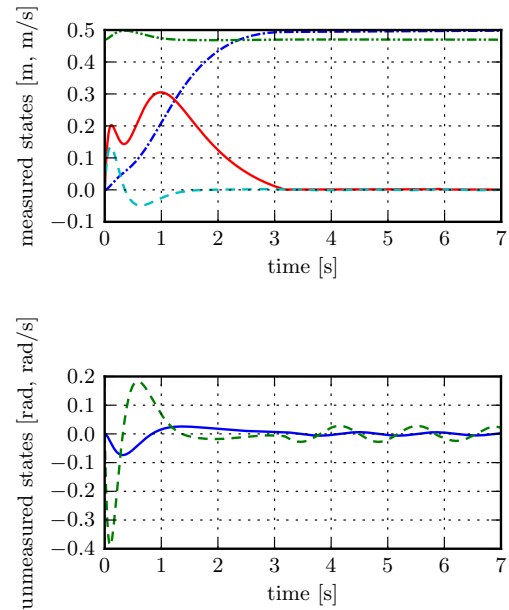


Figure 10: State evolution of the controlled crane using the UKF's estimated states as feedback

- [4] NEUPERT J., HILDEBRANDT A., SAWODNY O., SCHNEIDER K.: Trajectory tracking for boom cranes using a flatness based approach, Proc. Int. Joint Conf. SICE-ICASE, 2006, 1812–1816
- [5] RÓZSA T., KISS B.: Tracking control for tow-dimensional overhead crane, Proc. 8th Int. Conf. Informatics in Control, Automation, and Robotics, ICINCO, 2011, 1, 427–432
- [6] KISS B., LEVINE J., MÜLLHAUPT P.: A simple output feedback PD controller for nonlinear cranes, Proc. 39th IEEE Conference on Decision and Control, 2000, 5, 5097–5101
- [7] KISS B., LÉVINE J., MÜLLHAUPT P.: Modelling, flatness and simulation of a class of cranes, Electrical Engineering, 1999, 43, 215–225
- [8] LANTOS B.: Theory and design of control systems I., Akadémia Kiadó, 2001 (in Hungarian)
- [9] DAROUACH M., ZASADZINSKI M., ONANA A.B., NOWAKOWSKI S.: Kalman filtering with unknown inputs via optimal state estimation of singular systems, Int. J. Sys. Sci., 1995, 26(10), 2015–2028
- [10] HAYKIN S.S.: Kalman filtering and neural networks, John Wiley & Sons, Inc., 2001
- [11] ARMSTRONG-HÉLOUVRY B., DUPONT P., DE WIT C.C.: A survey of models, analysis tools and compensation methods for the control of machines with friction, Automatica, 1994, 30, 1083–1138
- [12] KALMAN R.E.: A new approach to linear filtering and prediction problems, Journal of basic Engineering, 1960, 82, 35–45



HUNGARIAN JOURNAL OF INDUSTRY AND CHEMISTRY

HJIC

Advertise upcoming meetings,

conferences, workshops,

new products or services;

make public announcements,

introduce your research laboratory

on the pages of the

**Hungarian Journal of Industry and Chemistry**

Please contact us if interested!

---

EDITORIAL OFFICE: UNIVERSITY OF PANNONIA

P.O. BOX 158, VESZPRÉM H-8201 (HUNGARY)

Tel.: +36 (88) 624-746, E-mail: [hjic@almos.uni-pannon.hu](mailto:hjic@almos.uni-pannon.hu);

web: [hjic.mk.uni-pannon.hu](http://hjic.mk.uni-pannon.hu)

Felelős szerkesztő: Szilágyi Róbert Károly, PhD

Kiadja: Pannon Egyetem, 8200 Veszprém, Egyetem u. 10.

Levél cím: H-8201 Veszprém, Postafiók 158, Tel.: (88) 624-000

Felelős kiadó: a Pannon Egyetem, Mérnöki Kar dékánja

## CHALLENGES OF ENTERPRISE POLICY COMPLIANCE WITH SMARTPHONE ENABLEMENT OR AN ALTERNATIVE SOLUTION BASED ON BEHAVIOUR-BASED USER IDENTIFICATION

SÁNDOR DOBOS<sup>✉</sup> AND ATTILA KOVÁCS

Department of Information Technology, ELTE University Budapest, Budapest, 1117, HUNGARY  
<sup>✉</sup>Email: sandor.dobos@hu.ibm.com

Current trends show the intense growth in the role and importance of mobile technology (smartphones, tablets, etc.) in business due to economic, social and technological reasons. The social element drives a powerful convenience expectation called “Bring Your Own Device” (BYOD) for taking notes and accessing internal and external network resources. Apparently, the future is leading toward a more extensive enablement of smartphones and tablets with their enterprise applications. Internal security standards along with applicable regulatory ones to achieve ‘policy enforcement’ as types of solutions and controls; however, this allows for merely one aspect of compliance. An alternative solution could be behaviour-based analysis to identify the user, attacker or even a malicious program accessing resources on phone or internal networks. Complex networks can be defined by graphs, such as connections to resources on smartphones and serve as a blueprint. In case the motif is different from the user’s actual behaviour, the company can initiate specific actions to avoid potential security violations. This document reviews the IT security challenges related to smartphones as well as the concept of graph-based user identification. The challenges of the latter are the identification of motif, selection of search algorithm and defining rules for what is considered a good or bad behaviour.

**Keywords:** mobile device security, “Bring Your Own Device” (BYOD) management, secure data communication, behaviour-based identification of threat, graph-based user identification

### Introduction

Enterprise policy enforcement with current mobile technology management tools (Mobile Device Management (MDM), virus detection, and other necessary modules) ensure only the compliance of piece of equipment. Within enterprise, MDM Servers initiate the compliant actions, if the smartphone client fails the access privilege is taken away; however, this has an immediate impact on revenue through operational efficiency affecting the business. The enterprise compliance of the smartphone device is only a validated response, which can be altered by understanding the mobile technology, such as the application structures or the way MDM technology works. Hackers are heavily attacking smart devices with malicious software (Malware). These can be viruses, spyware, adware, and other types of attacks. A specific example is the “Obad.a Trojan”, which is now being distributed *via* mobile botnets. The trojans are occupying a larger space and becoming more complex, which shows the need for IT security to find new ways to detect them.

The secure enterprise environment is crucial for organizations to ensure the business strategy and continuity of operation, irrespective of its environment being production, service delivery, or customer support related. Companies are following the trend to ensure

efficiency and simplify service accessibility for their customers, business partners or employees. It is an essential element of the IT security strategy to be aligned with the business strategy due to (i) the intense growth of mobile technology and (ii) pressure from enterprise that has transformed business operations.

Forrester Research from the Q2 Foresights Security Survey shows (*Fig. 1*) that mobile security is of primary concern amongst enterprise leaders. CEOs are concerned about the risk of data loss, particularly due to device loss or theft. Another worry regards data protection or data leak prevention usually in connection with data related to finance and innovation.

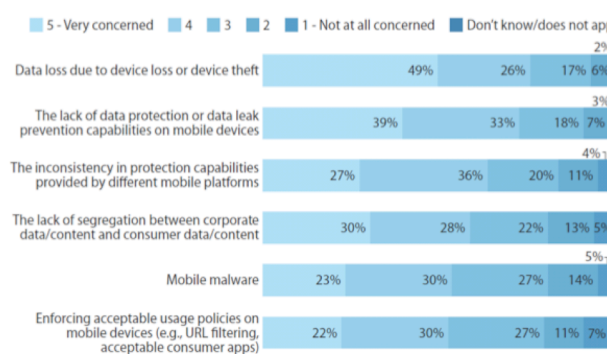


Figure 1: Degree of concern of CEOs from Forrester Research, Foresights Security Survey

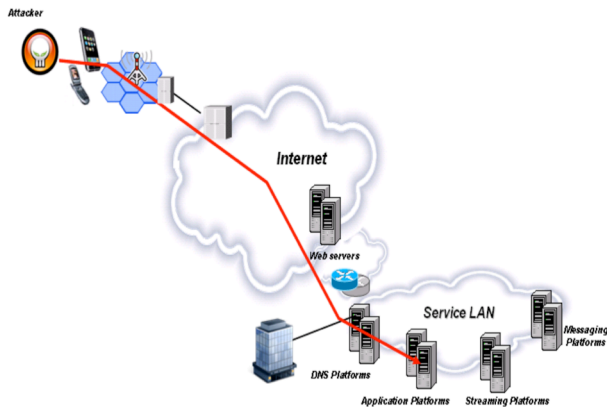


Figure 2: Graphical illustration of mobile phone technology security threats

### Current Challenges

Within today's economic environment, profit-driven organizations are challenged from revenue, growth or profit target perspectives. In order to meet such expectations, organizations are under high pressure to offer innovative products (services) within newly identified channels and more accessible yet-to-be-penetrated markets to a demanding customer base, especially in the area of providing smartphone solutions. On the other hand, regulatory bodies are alarmed at mobile enablement and organizations in general striving to protect critical financial systems better, in particular via identity and access management. At the same time, organizations need to maintain operational resiliency and perform risk management assessments as an integrated part of day-to-day operations. The cost perspective is an important factor for customers facing the task of achieving a lower total cost of ownership (TCO) although, by this shift in paradigm, they move from reactive protection to proactive value creation mode.

The alignment of the current IT strategy to business strategy is a challenge for corporations as IT is a service provider within an enterprise also offering business enablement leads. Companies need to manage security policy at the corporate level, assess the security health of the heterogeneous IT environment, monitor the security weakness(es) in processes and systems and, of course, meet the plethora of banking laws, regulations and standards including SOX, BASEL III, GLBA, and PCI compliance.

With the adaptation of the BYOD concept in business practices, mobile technology itself contributes to additional and more complex challenges. Enterprises are not the owners of those smart devices with access to enterprise networks and their data. Fig.2 illustrates how smartphones with applications developed by unknown sources could be a threat to enterprise's sensitive data.

### Business Drivers for Change

As introduced above an active need is emerging for more effective mobile solutions. It is not only a

reflection of the compliance requirements but a real protective solution against mobile threats without any restrictions on financial growth or cutbacks on efficiency initiatives. There are compelling reasons to act and change now including data potentially at risk, pressure from regulatory bodies and audit firms to be compliant with the applicable data handling regulations, and the implementation of mobile security into an existing security structure.

### Highlights of a Political-Economic-Social-Technology (PEST) Analysis

Politicians are setting high standards for data management regardless of platforms, even if they are related to mobile devices or mobile applications. These regulations mostly focus on the handling of financial data such as The Sarbanes-Oxley Act of 2002 (SOX). There are new developments regarding data (pictures, text, etc.) ownership such as The Stop Online Privacy Act (SOPA). The Preventing Real Online Threats to Economic Creativity and Theft of Intellectual Property Act or in short PROTECT IP Act (PIPA) will have an even more rigorous norm for enterprises who need to meet these regulations in order to obtain permission to operate in a certain field or market (market player).

The economic situation puts more pressure on businesses as the trend still shows stagnancy on a macro level while in some segments it is still in decline. Firms have high demands for business achievements measured by revenue and profit perspectives to meet shareholder expectations. One way to do so is to improve cost structures with mobile enablement (particularly BYOD).

Society wants to live more comfortably by searching for easily accessible services, such as online mobile-enabled bank transfers or online mobile retail orders. Companies aim to reach their customers via mobile applications that are more easily accessible through user-friendly interfaces, such as social network platforms. As usual, this trend is typical for major market areas, such as North America or, Western Europe; however, other regions are expected to follow.

The trend in technology continues to be more vivid from a computing power and portability perspective. Internet Service Providers are granting access to higher bandwidth networks for new applications and online content.

### Policy Enforcement and its Weaknesses

To manage the various types of mobile devices in an enterprise, a solution was introduced in 2008 by STRICKLEN, MCHALE, CAMINETSKY and REDDY based on Pattern Definition for Mobile Device Management (MDM). MDM is the most common approach how mobile devices (including smartphones, tablets) are managed within the enterprise as a management tool for monitoring and policy enforcement. Even though this technology is available and wide-spread, according to ABI research, mobile threats grew by 261% just in the

last quarter of 2012; however, MDM technology is not growing at a comparable rate to the number of vulnerabilities and attacks.

One of the components of MDM is the registration module, which is responsible for identifying mobile devices within the enterprise network, where the identifier indicates the platform of each mobile device, e.g. smartphone and tablet. The other significant element is the management module. Its job is to receive a management function definition performed on mobile devices using identifiers from mobile devices. The management module is responsible for instructions for the first platform to perform the management tasks and provides instructions for the other modules specific to the second platform to perform the management task on at least the second device.

However, MDM is not the ultimate solution for mobile device security within the enterprise environment due to some concerns regarding the verifiable device integrity. There are attempts at identifying MDM solutions to detect modifications of the underlying platform, but since the MDM agent has limited privileges and was susceptible to compromise by malicious privileged software, these stand little chance of detecting a targeted attack. The US National Security Agency (NSA) describes an immutable cryptography, as the ‘root of trust’ on a specific platform, to be available for leveraging by MDM or other software, providing a means of countering this type of threats. Encryption enables devices to attest their integrity on an enterprise and carry out any local policy decisions. The availability of this ‘root of trust’ to other software can vigorously complement a chain of trust that begins when booting and extends into the system runtime. An additional benefit of an immutable root of trust is that it allows a company to bind the unique identifier of that device together with other credentials to restrict company access to only those devices. In effect, the device itself can become one of the factors of a multi-factor access.

In summary, MDM’s current capabilities support the BYOD and enterprise-owned use of mobile devices with certain gaps for high-security issues. Management capabilities are limited to those provided for MDM products by the underlying mobile OS (iOS, Android, and other platforms), and therefore, these capability gaps cannot be closed by MDM providers alone. Ongoing cooperation between enterprise customers, OS vendors, and MDM vendors is critical to the continued advancement of enterprise-level security for mobile devices. Closing stated holes will enable the deployment of commercially available mobile devices to tackle high-security use issues common in sensitive industrial and governmental environments.

Secure data networks need to guarantee integrity, confidentiality and availability; this is when security is fulfilled. Policy enforcement with the MDM can be too liberal, but then there is no real need for MDM or strictly constraining users thus limiting the value-add. The proposed solution is to identify the user based on behaviour and compare behaviour changes.

## Behaviour Analysis and Challenges

Growing recognition drove the importance of network science related to the behaviour of sophisticated systems that is shaped by relations among their constituent elements. The rising availability and tractability of large and high quality data sets on a wide range of complex systems [1-3] have led to a primary insight: substantially diverse complex systems often share core key organizational principles. These can be quantitatively characterized by the same parameters, which means that they show remarkably similar macroscopic behaviour despite reflective differences in the low-level details of the components of each system or their mechanisms of interaction.

The behaviour as described above can be modelled by mathematical graphs, where the graphs are defined simply as a set of nodes called vertices linked together in direct or indirect ways by connections (edges). From a mathematical point of view,  $G(V, E)$  are canonical graphs as the vertices and edges are labelled. In network science, methodological advances permit research to quantify other topological properties of complex systems, such as modularity [4], hierarchy [5], centrality [6] and the distribution of network hubs [7,8]. There have also been significant efforts to form the development or evolution of complex networks [9], to link network topology to network dynamics, and to explore network robustness and vulnerability. These topics are likely to become more relevant in relation to behavioural studies.

Structural and functional behaviour maps can be created using graph theory through the following four steps:

1. Define the network nodes.
2. Estimate a continuous measure of association between nodes.
3. Generate an association model by compiling all pairs of associations between nodes and usually apply a threshold to each element of this model to produce a binary adjacency matrix or undirected graph.
4. Calculate the network parameters of interest in this graphical model of the behaviour network and evaluate them against the equivalent parameters of a population of random networks.

The elements such as defined network nodes, relationship of nodes, generated association matrix and network parameters give the basis of the behaviour type of “blueprint” of a user. A mobile user can be defined as an identity based on certain features of this behavioural “blueprint” as the key points of a fingerprint within the enterprise company. In *Fig.3* the darker highlighted edges could be the essential elements for the identifier.

Access to resource driven networks is defined in the graph theory as a set of nodes or vertices and the edges or lines, plus the connections between them. The graph topology can be quantitatively captured by a wide variety of measures used to generate the key points of the blueprint. The most important measurement is the node degree. The degree of a node is the number of

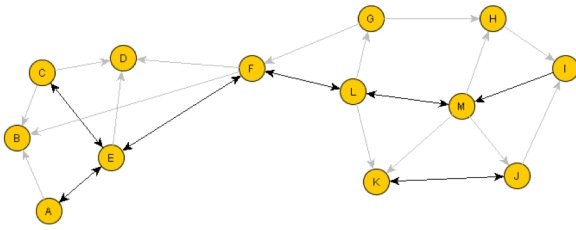


Figure 3: An example of a mobile user's identity on the basis of a "blueprint" network

connections it links to the rest of the network. Based on this definition, it is the most elementary network measure, and most other measures are ultimately linked to the node degree. The degrees of all the network's nodes identified form a degree distribution [10]. In randomly selected networks all of the connections are equally probable, i.e. the result is a Gaussian distribution. However, complex networks in general have non-Gaussian distributions, often with a long tail towards higher degrees. The degree distributions of the scale-free networks follow a power law [11]. This landmark study [11] was the first to describe the scale-free organization of many complex networks and proposed a simple growth rule for their formation.

The number of connections could give a large graph network that could be used for usability needs to define clustering, coefficients, and motifs. If the nearest neighbours of a node are also directly linked to each other, they form a cluster, and the clustering coefficient quantifies the number of connections that subsist between the nearest neighbours of a node as a quantity of the maximum number of possible connections [12]. The randomly selected networks exhibit low average clustering, whereas compound networks displays high clustering. Interactions between neighbouring nodes can also be counted by counting the occurrence of small motifs of interconnected nodes [13]. The distribution of different motif classes (nodes EFL and KMJ in Fig.3) in a network provides information about the types of local interactions that the network can support [14].

The numbers of reachable nodes and hops needed for connectivity are defined by the path length and efficiency. The path length is the minimum number of edges that must be passed through to start moving from one node to another. Random, complex networks have short mean path lengths; they exhibit high global efficiency of parallel information transfer, whereas regular patterns exhibit long mean path lengths. Efficiency is inversely related to path length. Nevertheless it is numerically easier to estimate topological distances between elements of disconnected graphs. Moreover, the link density or cost of the route provides further description. The connection density is the actual number of the network edges in the graph as a proportion of the total number of possible edges and is the simplest estimator of the physical cost of the network.

Hubs are nodes of high degree, where the centrality of a node measures how many of the shortest paths exist between all other node pairs in the network passing through it. It can be asserted that nodes with high

centrality are thus crucial to efficient communication [15]. The importance of an individual node to network effectiveness can be assessed by deleting it and estimating the efficiency of the severed network. The robustness property refers either to the structural integrity of the network following the deletion of nodes, edges or effects of perturbations on local or global network states.

Finally, modularity is the property that has significant influence on the "blueprint" of the behaviour. There are algorithms that estimate the modularity of the network on the basis of hierarchical clustering [16]. Each module contains several densely interconnected nodes, and there are relatively few connections between these nodes in different modules. Airline hubs described this as a function of their roles in community structure [17]. Provincial hubs are connected mainly to nodes in their modules where the connector hubs are connected to nodes in other modules.

### Graph Based Analysis of Smartphone Usage

Previously, the challenges of using mobile devices in the enterprise environment were discussed. It is important to identify the activities on the device in order to take either preventive or corrective actions.  $G(V, E)$  used for the behaviour identification and description graphs. Vertices are defined as applications, more precisely, vertices within the device or network addresses and sites. Edges are the connections between the vertices applications called websites, network addresses, user- or process-initiated connections.

- Network nodes can be defined as the resource access, i.e. applications, programs, and device elements access initiated by the user or application calls.
- Association between network nodes could be defined as the connections of the applications (calls, connections, as web access), usually resources are connecting together.
- Based on the above elements, network nodes and associations provide the details to calculate the association matrix.
- The following steps include network parameter analysis calculated from the above.

The question is not whether mobile activity can be defined as a complex network and describable by graph, but whether the process identifies a user by a motif. However, before this question can be answered certain challenges need to be faced:

- identify motifs as maximum independent set,
- search motif in the complex network,
- define „approved behaviours" according to the identification of user behaviour.

### Identification of the Motif in the Graph

The task is to find the Maximum Independent Set (MIS) of a particular graph as was defined by GAREY and JOHNSON [18] as NP-complete and remains so even for bounded degree graphs. According to FEIGE *et al.* [19] MIS cannot be approximated even within a factor of  $|V|^{1-o(1)}$  in polynomial time.

The greedy algorithm (GMIS) can provide a solution for the identification of the maximum independence set. The algorithm selects a vertex of minimum degree, deletes that vertex and all of its neighbours from the graph, and repeats this process until the graph becomes empty. A recent detailed analysis of the GMIS algorithm has shown that it produces reasonably good approximations of the MIS for bounded- and low-degree graphs defined by HALLDORSSON and RADHAKRISHNAN [20]. In particular, for a graph  $G$  with a maximum degree  $\Delta$  and an average degree  $\bar{d}$ , the size  $|I|$  of the MIS satisfies *Eq.(1)*.

$$|I| \leq \min \left( \frac{\Delta+2}{3} |\text{GMIS}(G)|, \frac{\bar{d}+2}{2} |\text{GMIS}(G)| \right) \quad (1)$$

where  $|\text{GMIS}(G)|$  is the size of the approximate MIS found by the GMIS algorithm.

*Eq.(1)* provides an upper-bound of the number of edge-disjoint embeddings of a particular sub-graph, and will use this bound to obtain a computationally tractable problem formulation that is guaranteed not to miss any sub-graphs that can potentially be frequent.

### Searching for a Discover Motif in the Graph

The GROCHOW-KELLIS method [21] can be used to find all examples of sub-graphs of a given size, similar to exhaustive methods. In the background, all non-isomorphic graphs are generated of a particular size using MCKAY'S tools [22]. Then for each graph, the method evaluates its significance. Due to symmetries, a set sub-graph of  $G$  may be mapped to a set query graph  $H$  multiple times. Therefore, a simple mapping-based search for a query graph will locate every case of the query graph as many times as the graph has symmetries. To avoid this, the method computes and enforces several symmetry-breaking conditions, which ensure that there is an exclusive map from the query graph  $H$  for each case of  $H$  in  $G$ , so that the search only spends time finding each instance once

```

IsomorphicExtensions (f,H,G[,C(h)]):
Finds all isomorphic extensions of partial map f :
  H → G [satisfying C(h)]
Start with an empty list of isomorphism.
Let D be the domain of f.
If D=H, return a list consisting solely of f.
  (Or write to disk.)
Let m be the most constrained neighbour of any d ∈ D
  (constrained by degree, neighbours mapped)
For each neighbour n of f (D)
If there is a neighbour d ∈ D of m such that n is not
  neighbours with f(d),
or if there is a non-neighbour d ∈ D of m such that n
  is neighbours with f(d)

```

```

[or if assigning f (m)=n would violate a symmetry-
  breaking condition in C (h)],
then continue with the next n.
Otherwise, let f=f on D, and f (m)=n.
Find all isomorphic extensions of f.
Append these maps to the list of isomorphism.
Return the list of isomorphism

```

The symmetries of a graph  $H$  equals automorphism (self-isomorphism). The collection of automorphism of  $H$  is indicated by  $Aut(H)$ . For a set  $A$  of automorphism, two nodes are stated to be “A-equivalent” if there is some automorphism in  $A$  which maps one to the other, or just “equivalent” if  $A = Aut(H)$ . Given a set of conditions  $C$ ,  $\alpha$  preserves the conditions  $C$  if, given a labelling  $L1$  of  $H$  which satisfies  $C$ , the corresponding labelling  $L2: H \rightarrow Z$  given by  $L2(n) = L1(\alpha(n))$  also satisfies  $C$ . We are thus searching for setting  $C$ , such that the only automorphism preserving  $C$  is the identity. This ensures exactly one map from  $H$  onto each of its instances in  $G$  to satisfy the conditions. To find these conditions, an  $Aut(H)$ -equivalence class  $\{n_0, \dots, n_k\}$  of nodes of  $H$ , and the condition  $L(n_0) < \min(L(n_1), \dots, L(n_k))$  imposed. Any automorphism must send  $n_0$  to one of the  $n_i$ , since these are all of the nodes equivalent to  $n_0$ . However to preserve this state, an automorphism must send  $n_0$  to itself. Then the process continues recursively, replacing  $Aut(H)$  with set  $A$  of automorphisms that send  $n_0$  to itself. Because FindSubgraphInstances starts with a particular node that node can be considered already fixed.

The main reasons for the selection of the GROCHOW and KELLIS method are summarized as follows:

- Capable of finding more significant motifs by enabling exhaustive discovery of motifs up to seven nodes. To find even larger motifs, the method samples a connected subgraph, and then finds all its occurrences and assesses their significance using this method. This practice has enabled the algorithm to find motifs of up to fifteen nodes and examine subgraphs of up to thirty-one nodes;
- Capable of querying a particular subgraph by querying whether a particular subgraph is significant;
- Capable exploring motif clustering; because the algorithm finds all occurrences of a given subgraph, it can be used to examine how these cases cluster together to form larger structures;
- Time and space applied to all subgraphs of a set size, takes exponentially a smaller amount of time than previous methods, even when implementing the previous method with the hashing scheme.

### Conclusions

Apparently the current policy enforcement solutions are not sufficient because they mainly focus on policy compliance based on the response of the device. The installation of malicious applications could alter the mobile devices response (jailbreak on IOS or Android

and software imitating a response to the MDM server) taking to more serious security issues. Similarly to the recently identified malware `Oldboot.B`, which can install malicious applications in the background, it can inject malicious modules into the system process that prevents malware applications from uninstalling. `Oldboot.B` can change the browser setup (set a new and unwanted home page), and it also can uninstall or disable installed Mobile Antivirus software, and even steal data such as credit card information or any other critical data. This malware is especially dangerous as it implements evasion techniques to stay undetected. In order to optimize current threat detection, which is also in line with business requirements, additional and different methodologies are required such as user identification based on the blueprint of the behaviour of the user.

To create a working model of the graph-based user identification, several tasks await completion. The running tasks are the edges started by the system or user defined as the connections between them. Once the complex network and graph are set up the motif can be identified with a greedy algorithm and search of the global graph with the GROCHOW-KELLIS Algorithm. In order to have a behaviour-based decision making system, all of the above algorithms will be tested to further develop the behaviour-based system.

#### REFERENCES

- [1] AMARAL L.A.N., SCALA A., BARTHELEMY M., STANLEY H.E.: Classes of small-world networks, *Proc. Natl Acad. Sci. USA* 2000, 97, 11149–11152
- [2] AMARAL L.A.N., OTTINO J.M.: Complex networks. Augmenting the framework for the study of complex systems, *Eur. Phys. J. B* 2004, 38, 147–162
- [3] BARABÁSI A.L., OLTVAI Z.N.: Network biology: understanding the cell's functional organization, *Nature Rev. Genet.* 2004, 5, 101–113
- [4] GIRVAN M., NEWMAN M.E.J.: Community structure in social and biological networks. *Proc. Natl Acad. Sci. USA* 2002, 99, 7821–7826
- [5] RAVASZ E., BARABÁSI A.L.: Hierarchical organization in complex networks, *Phys. Rev. E Stat. Nonlin. Soft Matter Phys.* 2003, 67, 026112
- [6] BARTHÉLEMY M.: Betweenness centrality in large complex networks, *Eur. Phys. J. B* 2004, 38, 163–168
- [7] GUIMERA R., AMARAL L.A.N.: Functional cartography of complex metabolic networks, *Nature* 2005, 433, 895–900
- [8] GUIMERA R., MOSSA S., TURTSCHI A., AMARAL L.A.: The worldwide air transportation network: anomalous centrality, community structure and cities' global roles, *Proc. Natl Acad. Sci. USA* 2005, 102, 7794–7799
- [9] KASHTAN N., ALON U.: Spontaneous evolution of modularity and network motifs, *Proc. Natl Acad. Sci. USA* 2005, 102, 13773–13778
- [10] AMARAL L.A.N., SCALA A., BARTHELEMY M., STANLEY H.E.: Classes of small-world networks, *Proc. Natl Acad. Sci. USA* 2000, 97, 11149–11152
- [11] BARABÁSI A.L., ALBERT R.: Emergence of scaling in random networks, *Science* 1999, 286, 509–512
- [12] WATTS D.J., STROGATZ S.H.: Collective dynamics of “small-world” networks, *Nature* 1998, 393, 440–442
- [13] AMARAL L.A.N., OTTINO J.M.: Complex networks. Augmenting the framework for the study of complex systems, *Eur. Phys. J. B* 2004, 38, 147–162
- [14] BARABÁSI A.L., OLTVAI Z.N.: Network biology: understanding the cell's functional organization. *Nature Rev. Genet.* 2004, 5, 101–113
- [15] FREEMAN L.C.: A set of measures of centrality based on betweenness, *Sociometry* 1977, 40, 35–41
- [16] GIRVAN M., NEWMAN M.E.J.: Community structure in social and biological networks. *Proc. Natl Acad. Sci. USA* 2002, 99, 7821–7826
- [17] GUIMERÀ R., MOSSA S., TURTSCHI A., AMARAL L.A.: The worldwide air transportation network: anomalous centrality, community structure and cities' global roles. *Proc. Natl Acad. Sci. USA* 2005, 102, 7794–7799
- [18] GAREY M.R., JOHNSON D.S.: *Computers and Intractability: A Guide to the Theory of np-completeness*. New York: W. H. Freeman and Company, 1979
- [19] FEIGE U., GOLDWASSER S., LOVASZ L., SAFRA S., SZEGEDY M.: Approximating clique is almost NP complete, *Proc. 32<sup>nd</sup> IEEE Symposium on Foundations of Computer Science (FOCS)*, 1991, 2–12
- [20] HALLDORSSON M.M., RADHAKRISHNAN J.: Greed is good: Approximating independent sets in sparse and bounded-degree graphs, *Algorithmica*, 1997, 18(1), 145–163
- [21] GROCHOW J.A., KELLIS M.: *Network Motif Discovery using Subgraph Enumeration and Symmetry-Breaking*, Computer Science and AI Laboratory, M.I.T. Broad Institute of M.I.T. and Harvard, 2007
- [22] MCKAY B.D.: Isomorph-free exhaustive generation, *J. Algorithms*, 1998, 26, 306–324

## MEASUREMENT-BASED MODELLING AND SIMULATION OF A HYDROGEN-GENERATING DRY CELL FOR COMPLEX DOMESTIC RENEWABLE ENERGY SYSTEMS

ATTILA GÖLLEI,<sup>✉</sup> PÉTER GÖRBE, ATTILA MAGYAR, AND LÁSZLÓ NEUKIRCHNER

Department of Electrical Engineering and Information Systems, University of Pannonia, Egyetem u. 10.,  
Veszprém, 8200, HUNGARY  
<sup>✉</sup>E-mail: golleia@almos.uni-pannon.hu

Nowadays, the growing need for energy from renewable sources and growing revulsion towards fossil and nuclear fuels puts sustainable and green energy in the limelight. Producing (electrical) energy in domestic power plants from renewable sources (mainly solar and wind) hardly results in difficulties, but the storage of energy not consumed immediately is a great engineering challenge. In the present paper a complex model has been developed by investigating renewable energy sources, the surplus energy not actually consumed and stored in electrical vehicle (EV) batteries, the conversion to hydrogen for storage purposes and how the main grid is fed. A measurement-based model of a hydrogen generating cell developed for the simulation of complex energetic systems. The parameter estimation of the static model was based on the collected measurement data coming from the detailed examination of a built demonstration cell. The novel element of this work is the Matlab Simulink model for the hydrogen generation cell. Using this model, a dynamic simulator of a complex domestic power plant is made available using renewable energy sources and hydrogen generation cells. Hydrogen generation enables the lossless long-term storage of surplus electric energy collected, but not consumed or injected into the low voltage grid. The generated hydrogen can be consumed for transportation purposes in suitable vehicles or it can be applied in fuel cells generating direct electrical energy for energy-deficient low voltage network situations. Energetic situations potentially occurring in practice were simulated in our complex model. Simulations showed that the presented model is suitable for domestic scale low voltage complex energetic systems.

**Keywords:** hydrogen generation, renewable energy sources, domestic power plants, modelling and simulation, measurement-based modelling

### Introduction

Producing hydrogen gas ( $H_2$ ) from excess energy is not a new idea. This is an alternative way to store and convert renewable energy for further utilization. The produced hydrogen can be stored or used in power cells to be converted back to electric energy or in vehicles for hydrogen propulsion [1]. Although the described procedure is efficient and able to produce a high quantity of  $H_2$  it is not suitable for application in combination with domestic power plants.

The most relevant from of  $H_2$  production is when the energy consumption and quantity of produced  $H_2$  are controlled. When power consumption and generation are continuous (and not necessarily deterministic) functions of time, the  $H_2$  production depends solely on the excess energy of the grid. The best solution is the usage of Supervisory Control and data Acquisition Systems (SCADA) of management [2]. The domestic applicability of this technology in the future depends on the cost of SCADA system installation.

Producing hydrogen and oxygen gases from water using electricity in a laboratory is a simple electrochemical process that can be performed easily

and in a very demonstrative way. Producing hydrogen on a large scale or in industrial quantities calls for an optimized or near-optimized cell model. In an energy demanding process only a few percent of variance in efficiency could mean a significant energy surplus or shortage [3]. The electrochemical parameters of a dry cell (*Fig. 1*) that are used here are discussed to simulate hydrogen and oxygen gas production. Compared to wet oxyhydrogen (HHO) cells where the entire unit is underwater, the plates of dry cells are separated with rubber seals. These seals stop the water from leaking from the cell. The electrical connections and edges of

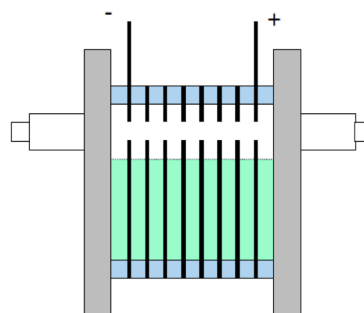


Figure 1: The theoretical setup of a dry HHO block

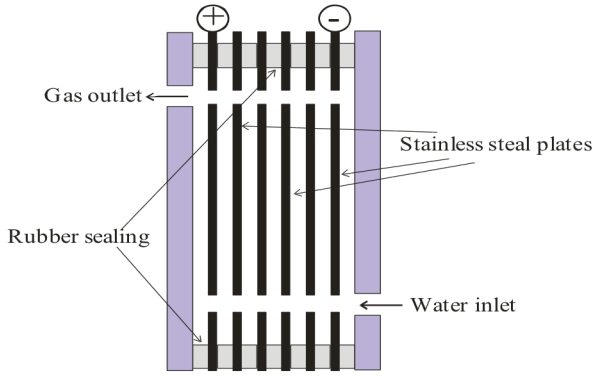


Figure 2: The setup of a HHO gas generator cell block

the plates do not touch the electrolyte. These parts of the unit stay dry, thus the name dry cell. To make sure the gas made from the electrolyte gets out of the cell and the solution flows between the plates, there are holes on the top (for the gas) and bottom (for the electrolyte) on the metal slats (Fig. 1).

The application of dry HHO units has two main advantages. The surface of the dry cell plates enables one to use smaller amounts of electrolyte compared to with wet cells; therefore, the volume and weight of the cell is smaller. Furthermore, the connectors of dry cells remain dry, i.e. they do not corrode unlike to wet cells, where the connectors are underwater therefore their surface slowly corrodes [4].

### Electrochemical Foundations

Electrochemical cells can be considered as galvanic batteries where the electrochemical reactions are supported by an external current supply. They are composed of two electrodes and a conductive electrolyte fluid. If the electrode material does not participate directly in the electrode reaction, it is called an indifferent electrode (e.g. graphite). During electrolysis, if there is more than one possible type of electrochemical reaction, then a simple anion will detach from the positive anode (e.g. chloride), without this anion,  $\text{HO}^-$  will be created by water splitting. The dissolution voltage of water is 1.23 V at 25 °C, the temperature coefficient is -0.85 mV/K, which means that at 100 °C this voltage decreases to 1.17 V. Therefore, in the light of these data, the specific energy demand to make hydrogen *via* electrolysis at 25°C can be calculated from Eqs.(1-4).

The amount of charge needed to evolve 1 kg of  $\text{H}_2$  gas is

$$q = zFM = 2 \cdot 96487 \cdot 0.5 = 96487 \text{ A s mol}^{-1} = 26801 \text{ Ah kg}^{-1} \quad (1)$$

$$w_{\text{H}_2} = qE_{\text{MF}} = 26801 \cdot 1.23 = 32966 \text{ Wh kg}^{-1} \quad (2)$$

Since the volume of 1 kg of standard state  $\text{H}_2$  is 12474  $\text{dm}^3$ , the amount of energy required to produce 1  $\text{dm}^3$  of  $\text{H}_2$  gas is:

$$w_{\text{H}_2} = \frac{32966}{12474} = 2.64 \text{ Wh dm}^{-3} \quad (3)$$

Table 1: Experimental results

Electrolyte concentration, $\text{g dm}^{-3}$	MMW <sup>a</sup> , $\text{cm}^3 \text{ min}^{-1} \text{ W}^{-1}$	Gas production, $\text{dm}^3 \text{ min}^{-1}$	Power of unit, W
1	2.13	0.20	10.8
2	2.66	0.75	34.4
3	2.66	1.37	55.8
4	2.59	1.51	82.2
5	2.72	1.90	90.6
6	2.63	2.52	119.5
7	2.67	2.96	140.0
8	2.65	2.76	125.0
9	2.46	2.28	105.6
10	1.82	2.15	103.2

<sup>a</sup> millilitres per minute per watt

To generate 1  $\text{dm}^3$  of hydrogen gas, 1.5  $\text{dm}^3$  of HHO gas is needed and thus the energy demand of producing 1  $\text{dm}^3$  of HHO gas (0.667  $\text{dm}^3 \text{ H}_2$ ) is:

$$w_{\text{H}_2(\text{HHO})} = 0.667 \cdot 2.64 = 1.76 \text{ Wh dm}^{-3} \quad (4)$$

The unit has been measured at 10 different electrolyte concentrations, using different currents. At the same time, the voltage on the plates and amount of gas produced by electrolysis has also been measured.

### The HHO Cell Unit

The setup of one block of the unit is shown in Fig.2. Usually five cells make up one block giving one gas-producing block. The block's electrical connections are on the ends of two plates (Fig.1). Four of the six electrode plates are neutral electrodes, as there is no voltage connected to them. The potential is divided between the neutral plates according to voltage division in series connections. It means that the voltage between two electrodes is one fifth of the voltage on one whole block. In the experiment, a unit with three blocks connected in parallel has been used. Besides the HHO cell, a water reserve tank to infuse the electrolyte into the cell was necessary. A tube between the gas outlet and the tank has also been installed since due to bubbling, electrolyte comes out of the tube that needs to be recycled back into the system. Then, as the electrolyte drips back into the tank, the gas can escape into the bottle through another hose. The produced  $\text{H}_2$  volume and the production speed are measured with this bottle. A power supply (Manson SPS9600) has been connected to the electrical connections of the HHO unit, in this way the input current was controlled (Table 1).

### Matlab Model of the Dry Cell

The model of the dry cell considered was implemented in Matlab Simulink using the SimPowerSystems Toolbox. Two unknown functional relationships between the generated  $\text{H}_2$  volume, the cell current and the KOH concentration and between cell voltage, cell current and KOH concentration were approximated using fourth and third order polynomials, respectively

Table 2: Coefficients of the polynomial relationship describing the cell voltage

	Value		Value		Value
$p_{00}$	1.429	$p_{10}$	0.2548	$p_{01}$	-0.1226
$p_{20}$	-0.008571	$p_{11}$	-0.01191	$p_{02}$	0.008257
$p_{30}$	0.0001141	$p_{21}$	-8.76e-05	$p_{12}$	0.0009697

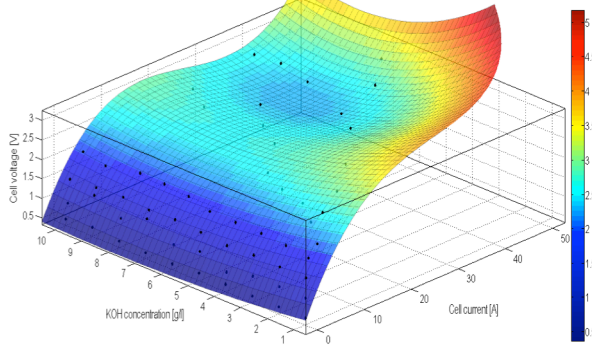


Figure 3: Simulation of the cell model with a constant current of 5 A for 1 day

using the Matlab Surface Fitting Tool. As the fitted polynomials do not have a physical connection to the given device, the model is applicable to any similar electrochemical  $H_2$  generation device with an electric two-pole system. In the different linear and non-linear physical and chemical models different coefficients become dominant. The voltage relationship is given by Eq.(5), where  $i_{cell}$  denotes the cell current and  $c_{KOH}$  stands for the KOH concentration. Parameters can be found in Table 2.

$$u_{cell}(i_{cell}, c_{KOH}) = p_{00} + p_{10} i_{cell} + p_{01} c_{KOH} + p_{20} i_{cell}^2 + p_{11} i_{cell} c_{KOH} + p_{02} c_{KOH}^2 + p_{30} i_{cell}^3 + p_{21} i_{cell}^2 c_{KOH} \quad (5)$$

The volume of the generated  $H_2$  is given by Eq.(6).

$$H_2(i_{cell}, c_{KOH}) = p_{00} + p_{10} i_{cell} + p_{01} c_{KOH} + p_{20} i_{cell}^2 + p_{11} i_{cell} c_{KOH} + p_{02} c_{KOH}^2 + p_{30} i_{cell}^3 + p_{21} i_{cell}^2 c_{KOH} + p_{12} i_{cell} c_{KOH}^2 + p_{03} c_{KOH}^3 + p_{40} i_{cell}^4 + p_{31} i_{cell}^3 c_{KOH} + p_{22} i_{cell}^2 c_{KOH}^2 + p_{13} i_{cell} c_{KOH}^3 \quad (6)$$

Table 3 and Figs.3-4 show representative results for the model. As expected, the  $H_2$  generation speed decreases and the cell finally stops working as the amount of water decreases and the KOH concentration increases.

A Simulink block scheme of the cell model is depicted in Fig.5. This Simulink model was validated by considering a system with the same parameters as the layout of the experimental cell. In this layout, we ran a simulation for 24 h using this model, decreasing water and increasing KOH concentrations. The results of this simulation can be seen in Fig.6. It can be seen that the hydrogen gas generated is reduced because of the rising KOH concentration. The exact values are in good agreement with our measurements.

Table 3: Coefficients of the polynomial relationship for the generated  $H_2$  gas

	Value		Value		Value
$p_{00}$	-0.1695	$p_{10}$	0.1687	$p_{01}$	-0.01765
$p_{20}$	-0.007486	$p_{11}$	-0.03234	$p_{02}$	0.03446
$p_{30}$	-0.0001077	$p_{21}$	0.00412	$p_{12}$	-0.004094
$p_{03}$	-0.004061	$p_{40}$	-4.269e-06	$p_{13}$	6.169e-05
$p_{22}$	-0.0005518	$p_{13}$	0.0009544		

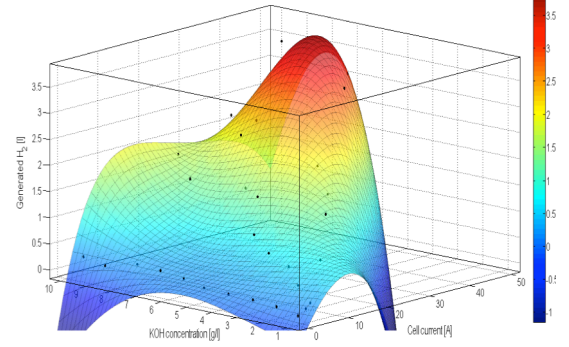


Figure 4: Generated  $H_2$  as a function of KOH concentration and dry cell current

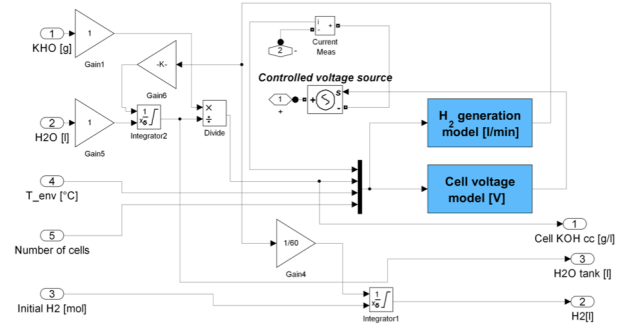


Figure 5: Matlab Simulink model of the HHO cell. The functional blocks implementing Eqs. (5) and (6) are denoted by different background colours

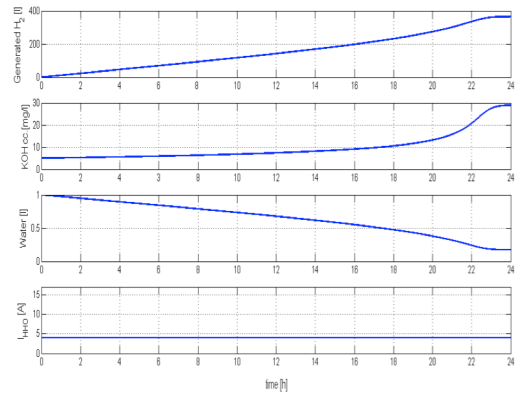


Figure 6: Simulation of a cell model with a constant current of 5 A for 1 day

### Dry Cell Model in Complex Energetic Systems

The model for  $H_2$  generating cells described in the previous section was investigated in the Matlab Simulink simulation environment that studies the energy flow conditions of a complex energetic system consisting of a renewable source with a grid-

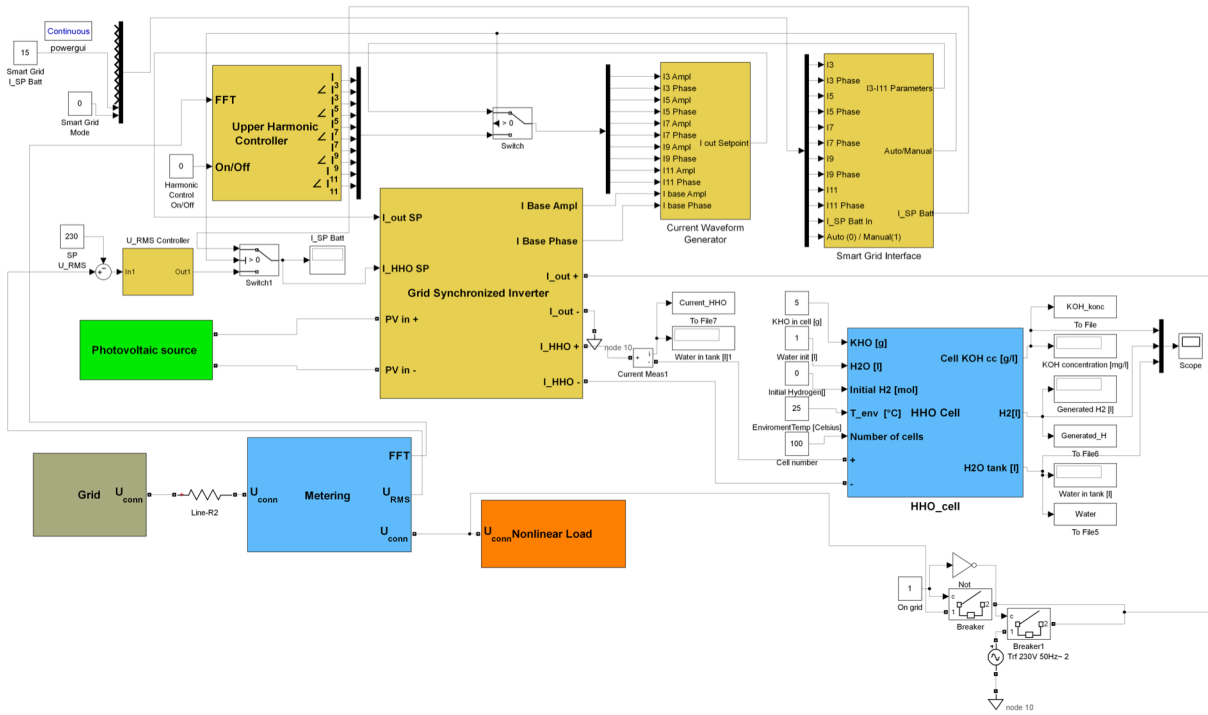


Figure 7: Simulink model of a complex energetic system with an HHO cell model inside

synchronized inverter, a low voltage grid, an intermediate voltage controller [3,5] and a lithium ion battery. We replaced the lithium ion battery in this cell model, which reduces the potential energy flow modes, because this cell can only adsorb current for storing energy in hydrogen production. It cannot reverse the electrochemical process for electrical energy generation from hydrogen gas. The structure of the system can be seen in Fig.7, where it is apparent that the cell model is connected directly only to the grid-synchronized inverter module of the system. The system depicted in Fig.7 operates in different discrete states according to the energy flow direction. Four cases can be defined:

- Normal inverter mode: The energy flows from the renewable source to the grid only (Fig.8A).

- Normal inverter and hydrogen generation mode: The energy flows from the renewable source to both the dry cell and the grid (Fig.8B).
- Hydrogen generation only mode: The energy flows from the grid to the dry cell only (Fig.8C).
- Distortion reduction only mode: The energy flows from the grid into the intermediate capacitance and from the intermediate capacitance into the grid. The energy balance is zero for a period, and the active power is zero (Fig.8D).

Model verification was performed by changing the energy flow modes in subsequent time intervals, and this was implemented by changing the energy balance of the system with outer current loads ( $I_{outer\ load}$ ). The different values for the simulations as parameters can be

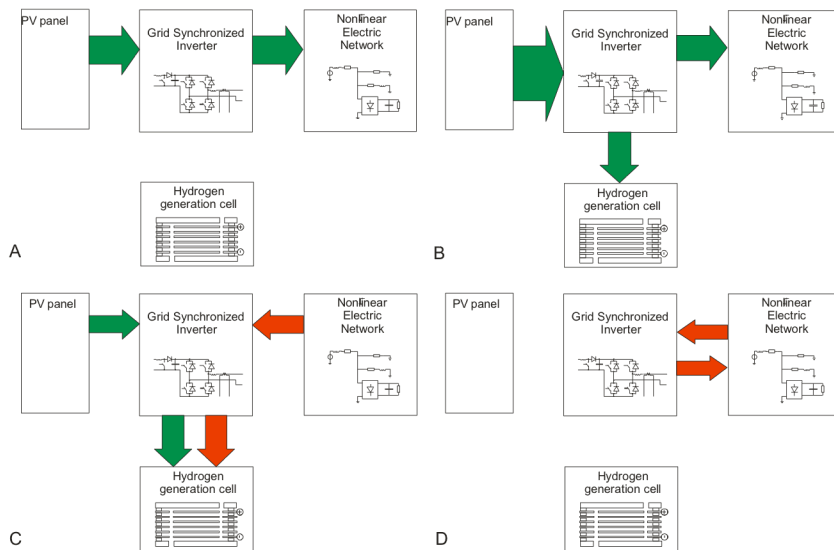


Figure 8: Complex energetic system energy flow modes: A: normal inverter mode, B: inverter and hydrogen generator mode, C: hydrogen generation only mode, D: distortion reduction only mode

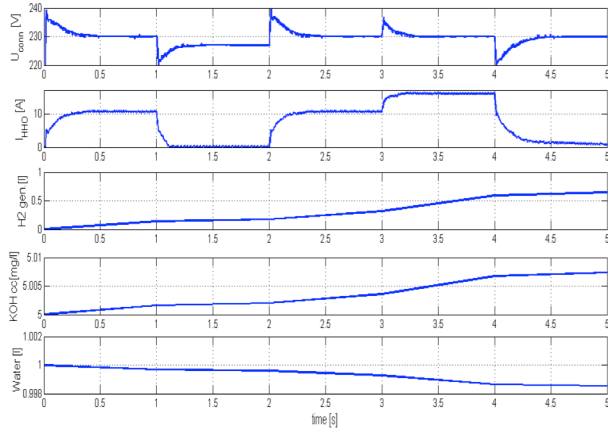


Figure 9: Simulation results of a complex energetic system using a cell model short time range (5 sec)

seen in Table 4. The simulation results are shown in Fig. 9, where  $U_{\text{conn}}$  is the effective value of the voltage at the connection point,  $I_{\text{HHO}}$  is the current value of the dry cell,  $V_{\text{H}_2}$  is the volume of generated hydrogen gas,  $c_{\text{KOH}}$  is the KOH concentration of the electrolyte and  $V_{\text{water}}$  is the volume of water inside the cell system. These values are plotted as a function of time. The results of the simulation show that the behaviour of the simulated electronic two-pole system is identical to that of the measured database.

### Conclusion

We developed a complex model to investigate renewable energy sources, for the conversion of surplus energy to hydrogen gas for storage and to represent how a main grid is fed. We built a measurement-based model of a hydrogen-generating cell for the simulation of complex energy systems in MATLAB SIMULINK environment. We estimated the parameters of the model based on measurements collected during the detailed examination of a demonstration cell. We carried out a series of experiments on a HHO gas producing dry cell to find the optimal electrolyte concentration, current value, etc. or change the setup by altering the distance between the plates with KOH electrolyte solution. We monitored the experimental setup in several regards, for example cell voltage, and gas production. The novel element is the temperature and concentration dependent Matlab Simulink model of the hydrogen generation cell, which was found to be suitable for simulation purposes. We tested it in a simulation of a complex domestic

power plant using a renewable energy source and hydrogen generation cell. Hydrogen generation enables the long-term storage of surplus electrical energy collected, but not consumed or injected into the low voltage grid. The generated hydrogen can be consumed by vehicles for transportation purposes or it can be applied in fuel cells generating direct electrical energy for energy-deficient low voltage network situations. We simulated all the potential energetic situations in this complex model of an energetic system. The simulations showed that the presented model of a hydrogen-generating cell performed well.

### ACKNOWLEDGEMENT

We acknowledge the financial support of this work by the Hungarian State and the European Union under the TAMOP-4.2.2.A-11/1/ KONV-2012-0072 project.

### REFERENCES

- [1] KOUTSONIKOLASA D.E., KALDISA, S.P., PANTOLEONTOSB, G.T., ZASPALISAC, V.T., SAKELLAROPOULOSC, G.P.: Techno-Economic Assessment of Polymeric, Ceramic and Metallic Membranes Integration in an Advanced IGCC Process for H<sub>2</sub> Production and CO<sub>2</sub> Capture, Chem. Engng. Trans. 2013, 35, 715-720
- [2] ZIOGOUA C., ELMASIDESB C., PAPADOPOULOUCA S., VOUTETAKISA S.: Supervisory Control and Unattended Operation of an Off-Grid Hybrid Power Generation Station with Hydrogen Storage Chem. Engng. Trans. 2013, 35, 529-534
- [3] GÖRBE P., MAGYAR A., HANGOS K.M.: Line Conditioning with Grid Synchronized Inverter's Power Injection of Renewable Sources in Nonlinear Distorted Mains, Proc. 10<sup>th</sup> International PhD Workshop on Systems and Control, 2009, 978-980
- [4] AL-ROUSAN A.A.: Reduction of fuel consumption in gasoline engines by introducing HHO gas into intake manifold, Int. J. Hydrogen Energy, 2010, 35, 12930-12935
- [5] GÖRBE P., MAGYAR A., HANGOS K.M.: THD Reduction with Grid Synchronized Inverter's Power Injection of Renewable Sources, Proc. 20<sup>th</sup> Int. Symp. Power Electronics, Electrical Drives, Automation and Motion (SPEEDAM) 2010, 1381-1386



HUNGARIAN JOURNAL OF INDUSTRY AND CHEMISTRY

HJIC

Advertise upcoming meetings,

conferences, workshops,

new products or services;

make public announcements,

introduce your research laboratory

on the pages of the

**Hungarian Journal of Industry and Chemistry**

Please contact us if interested!

---

EDITORIAL OFFICE: UNIVERSITY OF PANNONIA

P.O. BOX 158, VESZPRÉM H-8201 (HUNGARY)

Tel.: +36 (88) 624-746, E-mail: [hjic@almos.uni-pannon.hu](mailto:hjic@almos.uni-pannon.hu);

web: [hjic.mk.uni-pannon.hu](http://hjic.mk.uni-pannon.hu)

Felelős szerkesztő: Szilágyi Róbert Károly, PhD

Kiadja: Pannon Egyetem, 8200 Veszprém, Egyetem u. 10.

Levél cím: H-8201 Veszprém, Postafiók 158, Tel.: (88) 624-000

Felelős kiadó: a Pannon Egyetem, Mérnöki Kar dékánja

## QUASI-POLYNOMIAL REPRESENTATION-BASED CONTROL OF MECHANICAL SYSTEMS

LÁSZLÓ NEUKIRCHNER<sup>✉</sup> AND ATTILA MAGYAR

Department of Electrical Engineering and Information Systems, University of Pannonia, Egyetem u. 10.,  
Veszprém, 8200, HUNGARY  
<sup>✉</sup>E-mail: neu.groszber@gmail.com

A simple kinematic model of a differential steering mobile robot is investigated using a nonlinear technique based on the quasi-polynomial representation of the dynamical model. Dynamical systems can be embedded in the generalized Lotka-Volterra (or quasi-polynomial) form under mild conditions. Quasi-polynomial systems are good candidates for a general nonlinear system representation, since their global stability analysis is equivalent to the feasibility of a linear matrix inequality. The stabilizing quasi-polynomial state feedback controller design problem is equivalent to the feasibility of a bilinear matrix inequality. The classical stabilizing state feedback problem for quasi-polynomial systems was extended with the ability of tracking time-dependent reference signals. It is shown that the stabilizing quasi-polynomial controller design is equivalent to a bilinear matrix inequality. The results are applied to the model of the differential steering mobile robot. The goal reaching quasi-polynomial controller is shown to be a special kind of proportional state feedback.

**Keywords:** quasi-polynomial, robotics, differential drive robot, control systems, kinematics, Lotka-Volterra system

### Introduction

Trajectory and goal tracking of mobile robots is an intensively studied field of modern robotics as well as modern control theory. Several papers deal with an adaptive output feedback approach [1]. On the other hand some groups try to apply neural network-based methods for the task [2]. Another direction is to describe the problem as an optimal control problem and apply optimal control results for it [3]. The class of quasi-polynomial (QP) systems plays an important role in the theory of nonlinear dynamical systems because nonlinear systems with smooth nonlinearities can be transformed into quasi-polynomial form Ref.[4]. This means, that any applicable method for quasi-polynomial systems can be regarded as a general technique for nonlinear systems [5]. The aim of this work is to widen the applicability of the quasi-polynomial representation-based methods to the class of mechanical systems, more precisely to mobile robots. The goal reaching problem of a differential steering mobile robot is reformulated as a globally stabilizing feedback design problem in the quasi-polynomial framework.

### Basic Notions

#### *Differential Drive Mobile Robot Kinematics*

The chosen mechanical system is the kinematic model of a two wheeled differential drive mobile robot Eq.(1). The

model deals with the geometric relationships that govern the system. It calculates the motion without considering the affecting forces. The system's states are the Cartesian coordinates  $x$ , and  $y$  and the orientation  $\theta$  of the mobile robot. The basic kinematic model of the differential drive robot is given by

$$\begin{aligned}\dot{\theta} &= \frac{r}{2a}(\omega_{\text{left}} - \omega_{\text{right}}) \\ \dot{x} &= \frac{r}{2} \cos(\theta)(\omega_{\text{left}} + \omega_{\text{right}}) \\ \dot{y} &= \frac{r}{2} \sin(\theta)(\omega_{\text{left}} + \omega_{\text{right}}),\end{aligned}\quad (1)$$

where  $a$  is half the shaft's diameter,  $r$  is the radius of the wheels and  $\omega$  is the angular velocity of the right or left wheel. To order the robot to reach a specific goal, it is acceptable to design a proportional controller to govern the expected trajectory Eq.(2) [6]. In this case, the model is modified to calculate the state errors between the ordered and the present value. The new error model with proportional gain is

$$\begin{aligned}\dot{x} &= K_v(e_{\text{dis}} \cos(\theta) - x(t)) \\ \dot{y} &= K_v(e_{\text{dis}} \sin(\theta) - y(t)) \\ \dot{\theta} &= K_h(e_{\text{ang}} - \theta(t)) \\ e_{\text{dis}} &= \sqrt{(x_g - x(t))^2 + (y_g - y(t))^2} \\ e_{\text{ang}} &= \arctan\left(2 \frac{y_g - y(t)}{x_g - x(t)}\right),\end{aligned}\quad (2)$$

where  $K_v$  is the velocity control gain,  $K_h$  is the rotational velocity control gain,  $e_{\text{dis}}$  is the distance error,  $e_{\text{ang}}$  is the

angular error, and  $x_g, y_g$  are the Cartesian coordinates to reach.

### Quasi-Polynomial Representation of Nonlinear Systems

Some basic notions of quasi-polynomial and Lotka-Volterra systems are summarised in this section.

### Generalised Lotka-Volterra Form

Representing an ODE in generalised Lotka-Volterra (GLV) form can increase the structural simplicity in exchange for increasing its dimension. The GLV or quasi-polynomial (QP) form:

$$\begin{aligned} \dot{x}_i &= x_i \left( \lambda_i + \sum_{i=1}^m A_{ij} \cdot \prod_{k=1}^n x_k^{B_{ik}} \right), \\ i &= 1, \dots, n, \\ m &\geq n \end{aligned} \quad (3)$$

where  $\mathbf{A}$  and  $\mathbf{B}$  are  $n \times m$ ,  $m \times n$  real matrices, and  $\boldsymbol{\lambda} \in \mathbb{R}^n$  is a vector. The set of non-linear ODEs can be embedded into QP form if it meets two requirements: (i) The non-linear ODEs should follow this form:

$$\begin{aligned} \dot{x}_s &= \sum_{i_{s1} \dots i_{sn}, j_s} a_{i_{s1} \dots i_{sn}, j_s} x_1^{i_{s1}} \dots x_n^{i_{sn}} f(\bar{x})^{j_s}, \\ x_s(t_0) &= x_s^0, \\ s &= 1 \dots n \end{aligned} \quad (4)$$

where  $a_{i_{s1} \dots i_{sn}, j_s} \in \mathbb{R}$ ,  $s = 1 \dots n$ , and  $f(\bar{x})$  is some scalar function which cannot be reduced to quasi-monomial form. (ii) The partial derivatives of the system Eq.(4) should fulfil:

$$\frac{\partial f}{\partial x_s} = \sum_{e_{s1} \dots e_{sn}, e_s} b_{e_{s1} \dots e_{sn}, e_s} x_1^{e_{s1}} \dots x_n^{e_{sn}} f(\bar{x})^{e_s}, \quad (5)$$

where  $b_{e_{s1} \dots e_{sn}, e_s} \in \mathbb{R}$ ,  $s = 1 \dots n$ . By embedding, we introduce the new auxiliary variable:

$$\begin{aligned} y &= f^q \prod_{s=1}^n x^p s_s, \\ q &\neq 0 \end{aligned} \quad (6)$$

Differentiating the new, substituted equations we get the QP representation of the original equation Eq.(4):

$$\begin{aligned} \dot{x}_s &= x_s \left[ \sum_{i_{s1} \dots i_{sn}, j_s} \left( a_{i_{s1} \dots i_{sn}, j_s} y^{j_s/q} \right. \right. \\ &\quad \left. \left. \prod_{k=1}^n x_k^{i_{sk} - \delta_{sk} - j_s p_k / q} \right) \right], \\ s &= 1 \dots n \end{aligned} \quad (7)$$

where  $\delta_{sk} = 1$  if  $s = k$  and 0 otherwise. A new additional

dimension appears as the ODE of the new variable  $y$ :

$$\begin{aligned} \dot{y} &= y \left[ \sum_{i_{s1} \dots i_{sn}, j_s} \left( p_s x_s^{-1} \dot{x}_s + \right. \right. \\ &\quad \left. \left. + \sum_{\substack{i_{s\alpha}, j_s \\ e_{s\alpha}, e_s}} a_{i_{s\alpha}, j_s} b_{i_{s\alpha}, j_s} q y^{(e_s + j_s - 1)/q} \times \right. \right. \\ &\quad \left. \left. \times \prod_{k=1}^n x_k^{i_{sk} + e_{sk} + (1 - e_s - j_s) p_k} \right) \right]. \\ \alpha &= 1 \dots n \end{aligned} \quad (8)$$

It is important to mention that the new ODE is not unique because we can choose the parameters  $p_s$  and  $q$ .

The quasi-monomial transformation is defined as:

$$\begin{aligned} x_i &= \prod_{k=1}^n x_k^{C_{ik}}, \\ i &= 1 \dots n \end{aligned} \quad (9)$$

where  $\mathbf{C}$  is an arbitrary invertible matrix. The matrices of GLV can be modified as  $\hat{\mathbf{B}} = \mathbf{B} \cdot \mathbf{C}$ ,  $\hat{\mathbf{A}} = \mathbf{C}^{-1} \cdot \mathbf{A}$ , and  $\hat{\boldsymbol{\lambda}} = \mathbf{C}^{-1} \cdot \boldsymbol{\lambda}$ , and the transformed set is also in GLV form.

### Lotka-Volterra Models

The above family of models is split into classes of equivalence according to the values of the products  $\mathbf{M} = \mathbf{B} \mathbf{A}$  and  $\mathbf{N} = \mathbf{B} \mathbf{L}$ . The *Lotka-Volterra form* gives the representative elements of these classes of equivalence. If  $\text{rank}(\mathbf{B}) = n$ , then the set of ODEs in Eq.(3) can be embedded into the following  $m$ -dimensional set of equations, the so-called Lotka-Volterra model:

$$\dot{z}_j = z_j \left( N_j + \sum_{i=1}^m M_{ji} z_i \right), \quad j = 1, \dots, m \quad (10)$$

where

$$\mathbf{M} = \mathbf{B} \mathbf{A}, \quad \mathbf{N} = \mathbf{B} \mathbf{L},$$

and each  $z_j$  represents a so-called *quasi-monomial*:

$$z_j = \prod_{k=1}^n y_k^{B_{jk}}, \quad j = 1, \dots, m. \quad (11)$$

### Input-Affine QP Model

The well known input-affine model of nonlinear systems is given in the following state space model:

$$\dot{x} = \mathbf{f}(x) + \sum_{j=1}^p \mathbf{g}_j(x) u_j$$

where  $\mathbf{f} \in \mathbb{R}^n \rightarrow \mathbb{R}^n$ , and  $\mathbf{g}_j \in \mathbb{R}^n \rightarrow \mathbb{R}^n$  are QP functions and the input variable  $\mathbf{u}$  is  $p$ -dimensional. In

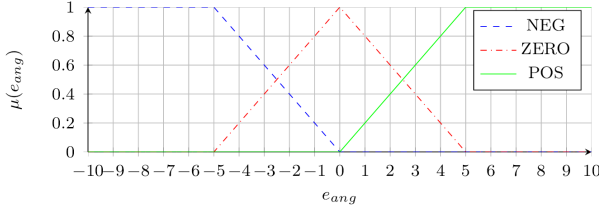


Figure 1: Membership functions for angular error

this case we need a QP form with the matrices from the GLV form ODE set:

$$\begin{aligned} \dot{x}_i &= x_i \left( \lambda_i + \sum_{j=1}^m A'_{ij} \prod_{k=1}^n x_k^{B_{jk}} \right) + \\ &+ \sum_{l=1}^p x_i \left( \mu_{li} + \sum_{j=1}^m C_{lij} \prod_{k=1}^n x_k^{B_{jk}} \right) u_l. \\ i &= 1 \dots n \end{aligned} \quad (12)$$

It can be proven that if  $u = H(x)$  state feedback is in QP form, the closed-loop system remains in QP form as well, but the quasi-monomials of the system will be greater, than the system's without the feedback.

#### Global Stability Analysis

Global equilibrium points can be obtained by finding a Lyapunov function  $V(\cdot)$ . For LV systems there is a well known Lyapunov function family:

$$\begin{aligned} V(z) &= \sum_{i=1}^m c_i \left( z_i - z_i^* - \ln \frac{z_i}{z_i^*} \right), \\ c_i &\geq 0, i = 1 \dots m \end{aligned} \quad (13)$$

and the time derivative:

$$\begin{aligned} \dot{V}_z &= \frac{\partial V(z)}{\partial z} \cdot \frac{\partial z}{\partial t} = \\ &= \frac{1}{2} (z - z^*) (C M + M^T C) (z - z^*), \end{aligned} \quad (14)$$

where  $z^* = (z_1^* \dots z_m^*)^T$  is the unique positive equilibrium point,  $C = \text{diag}(c_1, \dots, c_m)$  and  $M$  is the invariant coefficient matrix of the LV form. If  $C M^T + M C$  is negative semi-definite then  $z^*$  is stable and if negative definite then  $z^*$  is asymptotically stable. The global stability analysis is thus equivalent to the linear matrix inequality

$$\begin{aligned} C M^T + M C &\leq 0 \\ C &> 0. \end{aligned} \quad (15)$$

The presented Lyapunov function Eq.(13) can be extended to GLV systems by embedding the system using the LV coefficient matrix  $M = B A$ . It is necessary to

solve the LMI system Eq.(15) for the stability analysis of the QP and LV system:

$$\begin{pmatrix} C & 0 \\ 0 & -C M^T - M C \end{pmatrix} > 0 \quad (16)$$

#### Controller Design in Quasi-Polynomial Representation

The globally stabilizing QP state feedback design problem for QP systems can be formulated as follows [7]. Consider arbitrary quasi-polynomial inputs in the form:

$$u_l = \sum_{i=1}^r k_{il} \hat{q}_i, \quad l = 1 \dots, p \quad (17)$$

where  $\hat{q}_i = \hat{q}_i(y_1, \dots, y_n)$ ,  $i = 1, \dots, r$  are arbitrary quasi-monomial functions of the state variables of the system and  $k_{il}$  is the constant gain of the quasi-monomial function  $\hat{q}_i$  in the  $l$ -th input  $u_l$ . The closed-loop system will also be a QP system furthermore, the closed-loop LV coefficient matrix  $\hat{M}$  can also be expressed in the form

$$\hat{M} = \hat{B} \hat{A} = M_0 + \sum_{l=1}^p \sum_{i=1}^r k_{il} M_{il}. \quad (18)$$

Then the global stability analysis of the closed-loop system with unknown feedback gains  $k_{il}$  leads to the following *bilinear matrix inequality*

$$\begin{aligned} \hat{M}^T C + C \hat{M} &= M_0^T C + C M_0 + \\ &\sum_{l=1}^p \sum_{i=1}^r k_{il} (M_{il}^T C + C M_{il}) \leq 0. \end{aligned} \quad (19)$$

The variables of the BMI are the  $p \times r$   $k_{il}$  feedback gain parameters and the  $c_j$ ,  $j = 1, \dots, m$  parameters of the Lyapunov function. If the BMI above is feasible then there exists a globally stabilizing feedback with the selected structure.

#### Quasi-Polynomial Control of a Differential Drive Mobile Robot

##### Quasi-Polynomial Representation of the Kinematic Model

With the given differential drive robot model Eq.(1) and the explained error model Eq.(2) the QP representation can be built. The first step as mentioned, is to find the new auxiliary variables, that help to eliminate the non-QP expressions. The newly chosen auxiliary variables are:

$$\begin{aligned} \alpha &= \cos(\theta), \\ \beta &= \sin(\theta), \\ \gamma &= \arctan \left( 2 \frac{y_g - y}{x_g - x} \right), \\ \delta &= (x_g - x)^2 + (y_g - y)^2, \text{ and} \\ \epsilon &= \sqrt{\delta} + (x_g - x). \end{aligned} \quad (20)$$

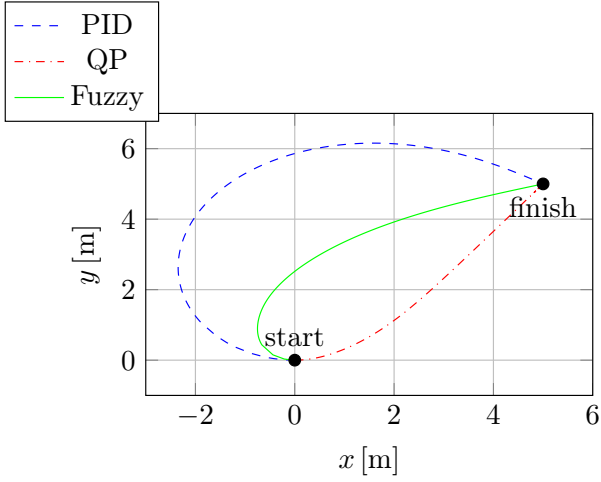


Figure 2: Comparison of different controllers

By substituting them into the original system *Eq.(2)* and performing the differentiation of the new equations *Eq.(20)*:

$$\begin{aligned}
 \dot{x} &= x \left( \frac{K_v \sqrt{\delta} \alpha}{x} - K_v \right) \\
 \dot{y} &= y \left( \frac{K_v \sqrt{\delta} \beta}{y} - K_v \right) \\
 \dot{\theta} &= \theta \left( \frac{K_h \gamma}{\theta} - K_h \right) \\
 \dot{\alpha} &= \alpha \left( -\frac{\beta}{\alpha} \right) \\
 \dot{\beta} &= \beta \left( \frac{\alpha}{\beta} \right)
 \end{aligned} \tag{21}$$

$$\dot{\gamma} = \gamma \cdot \begin{pmatrix} -\frac{2K_v \beta \sqrt{\delta}}{\gamma \epsilon} & +\frac{K_v y}{\gamma \epsilon} & -\frac{K_v x_g \beta}{\gamma \epsilon} & +\frac{K_v x \beta}{\gamma \epsilon} \\ +\frac{K_v x_g y}{\gamma \epsilon \sqrt{\delta}} & -\frac{K_v x y}{\gamma \epsilon \sqrt{\delta}} & +\frac{K_v y_g \alpha}{\gamma \epsilon} & -\frac{K_v y \alpha}{\gamma \epsilon} \\ -\frac{K_v y_g x}{\gamma \epsilon \sqrt{\delta}} & +\frac{K_v x y}{\gamma \epsilon \sqrt{\delta}} & & \end{pmatrix} \tag{22}$$

$$\dot{\delta} = \delta \begin{pmatrix} -\frac{2K_v x_g \alpha}{\sqrt{\delta}} & +\frac{2K_v x_g x}{\delta} & +\frac{2K_v x \alpha}{\sqrt{\delta}} & -\frac{2K_v x^2}{\delta} \\ -\frac{2K_v y_g \beta}{\sqrt{\delta}} & +\frac{2K_v y_g y}{\delta} & +\frac{2K_v y \beta}{\sqrt{\delta}} & -\frac{2K_v y^2}{\delta} \end{pmatrix} \tag{23}$$

$$\dot{\epsilon} = \epsilon \begin{pmatrix} -\frac{K_v x_g \alpha}{\epsilon} & +\frac{K_v x \alpha}{\epsilon} & +\frac{K_v x_g x}{\epsilon \sqrt{\delta}} & -\frac{K_v x^2}{\epsilon \sqrt{\delta}} \\ -\frac{K_v y_g \beta}{\epsilon} & +\frac{K_v y \beta}{\epsilon} & +\frac{K_v y_g y}{\epsilon \sqrt{\delta}} & -\frac{K_v y^2}{\epsilon \sqrt{\delta}} \\ +\frac{K_v \alpha}{\epsilon} & -\frac{K_v \beta}{\epsilon \sqrt{\delta}} & & \end{pmatrix} \tag{24}$$

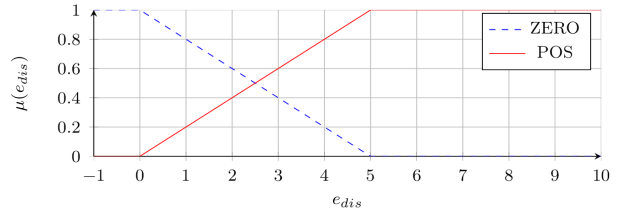


Figure 3: Membership functions for distance error

The closed-loop QP system *Eq.(21-24)* has 29 quasi-monomials.

$$\begin{aligned}
 x &: \alpha \sqrt{\delta} x^{-1} \\
 y &: \beta \sqrt{\delta} y^{-1} \\
 \theta &: \gamma \theta^{-1} \\
 \alpha &: \beta \alpha^{-1} \\
 \beta &: \alpha \beta^{-1} \\
 \gamma &: \beta \sqrt{\delta} \gamma^{-1} \epsilon^{-1}, \quad y \gamma^{-1} \epsilon^{-1}, \quad \beta \gamma^{-1} \epsilon^{-1}, \\
 & \quad x \beta \gamma^{-1} \epsilon^{-1}, \quad y \gamma^{-1} \delta^{-1/2} \epsilon^{-1}, \quad \alpha \gamma^{-1} \epsilon^{-1}, \\
 & \quad y \alpha \gamma^{-1} \epsilon^{-1}, \quad x \gamma^{-1} \delta^{-1/2} \epsilon^{-1} \\
 \delta &: \alpha \delta^{-1/2}, \quad x \delta^{-1}, \quad x \alpha \delta^{-1/2}, \\
 & \quad x^2 \delta^{-1}, \quad \beta \delta^{-1/2}, \quad y \delta^{-1}, \\
 & \quad y \beta \delta^{-1/2}, \quad y^2 \delta^{-1} \\
 \epsilon &: \alpha \epsilon^{-1}, \quad x \alpha \epsilon^{-1}, \quad x \epsilon^{-1} \delta^{-1/2}, \\
 & \quad x^2 \epsilon^{-1} \delta^{-1/2}, \quad \beta \epsilon^{-1}, \quad y \beta \epsilon^{-1}, \\
 & \quad y \epsilon^{-1} \delta^{-1/2}, \quad y^2 \epsilon^{-1} \delta^{-1/2},
 \end{aligned} \tag{25}$$

The QP system *Eq.(21-24)* can obtain the GLV form invariants with the help of monomials.

These matrices are:  $\mathbf{A}$  the coefficient matrix,  $\mathbf{B}$  the exponential matrix and  $\boldsymbol{\lambda}$  the constant's matrix. The invariant matrix product  $\mathbf{B} \mathbf{A}$  results in the LV coefficient matrix  $\mathbf{M}$ , which is necessary for the global stability analysis.

### Controller Design

As the original model *Eq.(2)* already contains the proportional controller parameters  $K_h$  and  $K_v$ , they naturally appear in the QP and Lotka-Volterra forms, respectively.

The closed-loop Lotka-Volterra coefficient matrix  $\mathbf{M}$  contains the proportional gains in a linear manner *Eq.(26)* [7]

$$\mathbf{M} = \mathbf{M}_0 + K_h \mathbf{M}_h + K_v \mathbf{M}_v, \tag{26}$$

where  $\mathbf{M} \in \mathbb{R}^{29 \times 29}$ . This means, that the globally stabilizing feedback design BMI can be formulated, and checked for feasibility.

The controller design is practically solved as a control-Lyapunov function-based state feedback. The prescribed Lyapunov function parameters are  $c_{1,2,3} = 0.1$ ,  $c_{4,5} = 1$  and  $c_{6-29} = 0$ . The control gains are obtained by solving an LMI version of the feedback design BMI by substituting  $\mathbf{C}$  into *Eq.(19)*. The obtained values are  $K_h = 2.78$  and  $K_v = 0.8$ .

Table 1: Rules for the fuzzy controller

$\wedge$		$\Rightarrow$	$\wedge$	
$e_{ang}$	$e_{dis}$		$\omega_{left}$	$\omega_{right}$
ZERO	ZERO		ZERO	ZERO
POS	ZERO		POS	NEG
	ZERO		NEG	POS
ZERO	POS		POS	POS
POS	POS		POS	ZERO
	POS		ZERO	POS

### Comparison of Results for Different Controller Types

The first and most basic method was the proportional controller approach. This was explained in the second chapter. This is a more systematic approach, but with the increasing non-linearities it is becoming a more difficult method to solve. *Fig.3* shows that the robot moves on a significantly wider curve compared to the other two designs.

Secondly a fuzzy controller was designed to compare the original design to. This is a much more intuitive approach, the physical nonlinearities were easily implementable with the cost of inaccuracy. This can be seen in *Fig.3*, where the robot travels on a much smaller curve. *Table 1* shows the definition of the rules. The membership functions follow simple triangular shapes according to the acceptable rate of angular and velocity changes. The QP controller performance can be seen in *Fig.3*. where a classical PID controller and a fuzzy logic controller are also shown. It is apparent, that the QP controller performs well by means of the length of the trajectory.

### Conclusions

A quasi-polynomial representation-based nonlinear control design method has been applied to the kinematics of a differential steering mobile robot in this work. It has been shown, that the quasi-polynomial model of the mobile robot's kinematics extended with the tracking error dynamics has 29 quasi-monomials, i.e. the sizes of matrices appearing in the bilinear matrix inequality that should be solved for a globally stabilizing feedback controller

### Acknowledgement

This research was supported by the European Union and the State of Hungary, co-financed by the European Social are reasonably great. The resulting controller and the trajectory were compared to the trajectories of a reference PID controller and a fuzzy logic controller. It can be seen that the controller performs satisfactorily. Possible future directions include the application of the LMI and /or BMI cost function to introduce some optimality measure to the problem to be minimised. A next step would be the application of a time dependent goal position (i.e. a trajectory). Fund in the framework of the TÁMOP 4.2.4. A/2-11-1-2012-0001 'National Excellence Programme'.

### REFERENCES

- [1] HUANG J., WEN C., WANG W., JIANG Z.-P.: Adaptive output feedback tracking control of a nonholonomic mobile robot, *Automatica*, 2004, 50(3), 821–831
- [2] MOHARERI O., DHAOUADI R., RAD A.B.: Indirect adaptive tracking control of a nonholonomic mobile robot via neural networks, *Neurocomputing*, 2012, 88, 54–66
- [3] LI J., GUO X., LI Z., CHEN W.: Stochastic Adaptive Optimal Control of Under-actuated Robots Using Neural Networks, *Neurocomputing*, 2014, 142, 190-200
- [4] HERNÁNDEZ-BERMEJO B., FAIRÉN V.: Nonpolynomial vector fields under the Lotka-Volterra normal form, *Phys. Lett. A*, 1995, 206, 31–37
- [5] MAGYAR A., FODOR A.: Quasi-polynomial Control of a Synchronous Generator, *Hung. J. Ind. Chem.*, 2013, 41(1), 55–61
- [6] TZAFESTAS S.G.: Mobile Robot Control I: The Lyapunov-Based Method, in *Introduction to Mobile Robot Control* (TZAFESTAS S.G., ed.) Elsevier, Oxford, 2014, 137–183
- [7] MAGYAR A., SZEDERKÉNYI G., HANGOS K. M.: Globally stabilizing feedback control of process systems in generalized Lotka-Volterra form, *J. Proc. Contr.*, 2008, 18(1), 80–91



HUNGARIAN JOURNAL OF INDUSTRY AND CHEMISTRY

HJIC

Advertise upcoming meetings,

conferences, workshops,

new products or services;

make public announcements,

introduce your research laboratory

on the pages of the

**Hungarian Journal of Industry and Chemistry**

Please contact us if interested!

---

EDITORIAL OFFICE: UNIVERSITY OF PANNONIA

P.O. BOX 158, VESZPRÉM H-8201 (HUNGARY)

Tel.: +36 (88) 624-746, E-mail: [hjic@almos.uni-pannon.hu](mailto:hjic@almos.uni-pannon.hu);

web: [hjic.mk.uni-pannon.hu](http://hjic.mk.uni-pannon.hu)

Felelős szerkesztő: Szilágyi Róbert Károly, PhD

Kiadja: Pannon Egyetem, 8200 Veszprém, Egyetem u. 10.

Levél cím: H-8201 Veszprém, Postafiók 158, Tel.: (88) 624-000

Felelős kiadó: a Pannon Egyetem, Mérnöki Kar dékánja

## A NETWORK MODEL FOR SIMULATING THE DYNAMIC BEHAVIOUR OF AN ENERGY DISTRIBUTION NETWORK

LEVENTE BÁLINT,<sup>1</sup>✉ TIBOR DULAI,<sup>2</sup> ÁGNES STARK-WERNER,<sup>2</sup> GERGELY APOSTOL,<sup>1</sup> AND ÁDÁM TOMPOS<sup>1</sup>

<sup>1</sup> Faculty of Information Technology, University of Pannonia, Egyetem u. 10., Veszprém, 8200 HUNGARY

✉E-mail: balintlevente.z@gmail.com

<sup>2</sup> Department of Electrical Engineering and Information Systems, Faculty of Information Technology, University of Pannonia, Egyetem u. 10., Veszprém, 8200 HUNGARY

The aim of this paper is to present the planning and implementation of a network model for an energy distribution network for simulating its dynamical behaviour. The model includes different types of energy sources, distribution centres and consumers. The prepared simulation environment makes it possible to add/remove/modify any type of node – to/form/in the model. Other actions that may be carried out are the initiation/termination of an energy source or change to its production level. The main goal of the simulation is to investigate the effect of an immediate event (such as a power plant failure, decreased production, etc.) on the network and search for the most appropriate substitute possible. The search may happen either on cost bases or time bases. The system created is based on web technology, any user is able to create/save/load his own model and do simulations on it. This work serves as a basis for further work, which involves more complex electrical knowledge and possibilities regarding the network.

**Keywords:** energy distribution network, energy sources, dynamical behaviour, network model, simulation

### Introduction

Energy efficiency has an increasing importance due to cost- and environment-related factors. At the same time, the customer demands have to be satisfied. These circumstances result in a largely heterogeneous energy producing and distributing environment. Renewable energy is applied to a considerable degree in addition to the electricity produced by traditional power plants [1]. This resulted in a system, where different types of energy sources – with different properties, like cost, response time, etc. – are applied in a mixed way. It is a non-trivial task to decide, which sources to apply even in the case of pre-determined demands. Moreover, in practice the amount of the demand appears only when needed.

Earlier efforts implemented simulation environments for analysing the effect of the hybrid manner of an electric network [2, 3]. However, the problem becomes more complex when an immediate negative event happens, e.g. an energy source becomes unavailable or has to decrease its output suddenly. The optimal answer depends on many factors: e.g. how quickly a new energy source can be applied or how much it will cost. Moreover, some types of energy sources are only able to produce discrete levels of output power.

This paper describes a web-based system, which makes it possible to create and modify an energy distribution network (including different types of energy sources and customers, too) with the goal of simulating different immediate events. The requirements to be

collected and the network model and its elements are introduced, followed by details of the implementation and simulation.

### Requirements: The Desired Properties of the System

Functional requirements include mainly the creation and manipulation of network models and simulations. *Fig.1* presents the possible applications of the system. The interface contains a tree graph-based model whose root is the power source, the inner nodes are the network stations and the leaves are the consumers. The graph's edges are the connections between the components. There are multiple projects in the system, each project contains a model. The main functions of the system are available through the modeling and simulation interfaces. During the simulation the components can be switched on and off. After two hours of simulation a statistic diagram can be viewed for each component of the model, showing its consumption or production. Information about components can be edited while the system is not simulating. Next to the functional requirements, the system-related requirements are that:

- the system has to be web-based,
- no user authentication is needed,
- the reaction time is less than 1 s, even if there are 100 users, and
- any system or communication failure has to be presented by an unambiguous alert to the user.

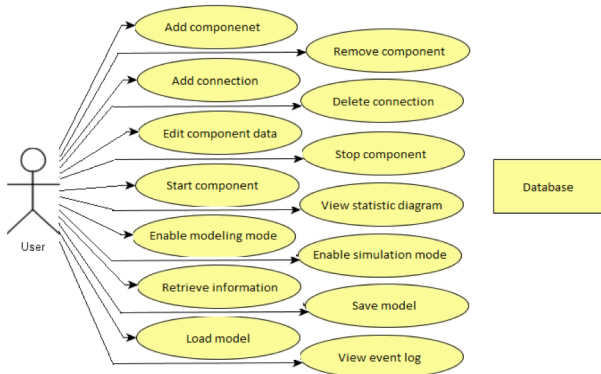


Figure 1: Example uses of the prepared system

## The Interface

The interface of the system contains four important elements. On the upper edge is the modelling control bar with the component adding buttons, background theme switcher and save/load buttons. By pressing the load button, the system opens the project selector. The save button must be pressed before loading another project in order to save the current one. Under the right side of the control bar, there is the simulation control panel. There are buttons on it for editing corporate and residential priority orders, and sliders for the importance of certain properties while calculating the priority order of the power sources. There are buttons for starting, stopping, and restarting simulation time. The simulation time begins at 6:00 am and the step time can be set from 1 to 60 minutes. In the bottom left-hand corner, the event-log is located, which indicates the basic events like start/stop simulation, add/remove components in black and important events like system failure or insufficient power in red. All events have a time-stamp. While hovering the mouse over a component, the system shows the detailed properties of the element. Double clicking selects a component or deletes a connection. While a component is selected, the edit, delete and diagram buttons appear in the modelling control bar. The diagram button works only after a minimum of two hours of simulation. In simulation mode the modelling control bar is hidden and double clicking switches a component on/off.

## The Network Model and its Elements

As the system's main potential is in handling different types of network nodes and making the investigation of a heterogeneous energy producing and distribution system possible, the elements of the network models and their properties have a huge role. The network nodes can be classified as follows.

### Energy Sources

The system considers renewable energy sources (water, bio, wind, solar, and geo), non-renewable energy sources (natural gas, petrol, coal, nuclear), and quick

Figure 2: Edit power source properties (Név: name or location, Bekapcsolási költség: cost of starting up, Indítási idő: start-up time, Üzemköltség: operational cost, Környezeti szorzó: environmental factor, Optimális sorrend: optimal order)

Figure 3: Edit station properties (Név: name or location, Teljesítmény: power)

start-up energy sources (gas turbines) when the energy provided by power plants is insufficient for consumers.

Each energy source has a unique name and a maximum output, which defines an upper limit for the source (Fig.2). A minimum output is defined as a lower limit, below that the operation is not profitable. Start-up cost is the cost needed to switch on the source, and start-time is the time required to start producing energy. The operational cost is a financial value which is needed for one hour of operation. Power sources have an environmental multiplier. This multiplier is 1 for renewable sources, 0.2 for non-renewable ones and 0.1 for quick start-up sources by default, but it can be edited any time during the modelling. Larger values are better, the maximum is 1 but the value cannot be 0. The system calculates an order between sources from their start-up cost, operational cost and environmental multiplier. This order can be modified by the user before starting the simulation.

### Distributing Elements

Distributing elements for the system are power plant stations that distribute the energy to multiple network stations that further distribute the energy to retail stations directly transmit the energy to consumers.

Distributing stations have only two properties (Fig.3). They have a unique name to identify them and a maximum throughput, which is the maximum power that the station can distribute to lower stations or consumers. If that limit is reached the station will not pick up more power even if the consumers need more.

Név:	C1
Fogyasztás:	100
Prioritás:	0
eventSw:	1
current:	46

Figure 4: Edit consumer properties (Név: name or location, Fogyasztás: consumption, Prioritás: priority)

### Consumers

The residential consumers are linked to the model through homes, while corporate consumers include factories, public institutions, etc.

Consumers have a rate of consumption that describes their maximum required power. Current consumption is estimated during the daytime in the simulation. Consumers also have an order of priority that can be modified by the user but corporate consumers always have priority over residential consumers (Fig.4).

### Connections

Connections have a length property, which will be used for calculating the loss, dissipated by the cables resistance. Networks can be built up by the previously introduced network nodes by connecting them appropriately. The order of connectivity is as follows:

- power sources,
- power plant distribution station,
- network distribution station,
- retail distribution station, and
- consumer.

Connections can be established only in this order regardless of the performance of individual components.

### Database and Implementation Details

Properties of the network model elements and the network formed are stored in an associative array that can be used directly by the system. At each time it is saved, this array is stored in JavaScript Object Notation (JSON) format in a text file for each project separately.

The database array contains an entry for all components of the model. Every component has an ID, a name, a type and position on the modelled field. Energy sources also have a fuel type, start-up time, start-up cost, running cost, environmental factor, and minimum and maximum performance level attributes. Stations have a defined maximum tolerance. For consumers, there is a stored average consumption rate, which dynamically changes over time. Each object has a sub-array, which stores the ID of any other components that are connected to the current one.

Consumer objects have priority numbers that define the relevance of the consumer. If the power source cannot produce enough energy to satisfy all needs, then the consumer that has the highest priority number will be switched off from the network. The priority order equals the order of creation of components, but the corporate consumers always have preference. The order can be changed by the user any time in modelling mode and during the simulation.

### Implementation Details

The program is implemented in JavaScript language with plug-ins like jQuery and jsPlumb. The plug-in jQuery is the most popular extension of the JavaScript language. It makes it easier to select, move, remove or modify the elements on the interface by selecting the element by its ID and modifying its properties. The system uses an in-house jQuery plug-in, windows.js. This plug-in creates free movable small windows on the interface and fills them with appropriate content defined by the programmer. The jsPlumb plug-in is an open-source plug-in for JavaScript, created to visually connect elements on the interface with straight lines or Bezier curves. The database is stored in JSON format text files, created and edited by Hypertext Preprocessor (PHP) functions and called asynchronously by JavaScript's Asynchronous JavaScript And XML (AJAX) protocol. PHP is a server-side scripting language, but in our case its only function is to properly save and load database files to the server computer. The whole software can be started in a browser on the user's computer and it connects to the server only while loading or saving the project. The interface is fully interactive, in modelling mode the objects can be moved or removed, in simulating mode switched on and off.

### Simulation Possibilities

The system was created for simulating immediate events during the operation of a modelled energy distribution network. After forming the network, the software makes it possible to cause different immediate events. These sever a connection or switch on/off sources, stations and/or consumers. All of these events can be carried out on the graphical interface of the software (Fig.5).

The simulation is daytime-based. It starts at 6:00 am. Users can set the step time from 1 min or sec to 60 min or sec. At the beginning the system distributes the energy produced by the power plant(s) to all consumers in a user defined order. If a power plant does not produce enough power then the last consumer will be switched off and so on. The electricity-related behaviour will be implemented in the future into the software. A possible solution is to build an ideal flow model as a cooperative game over a graph with the sources and consumers located at the nodes, each described by a maximum supply or desired demand and the power lines

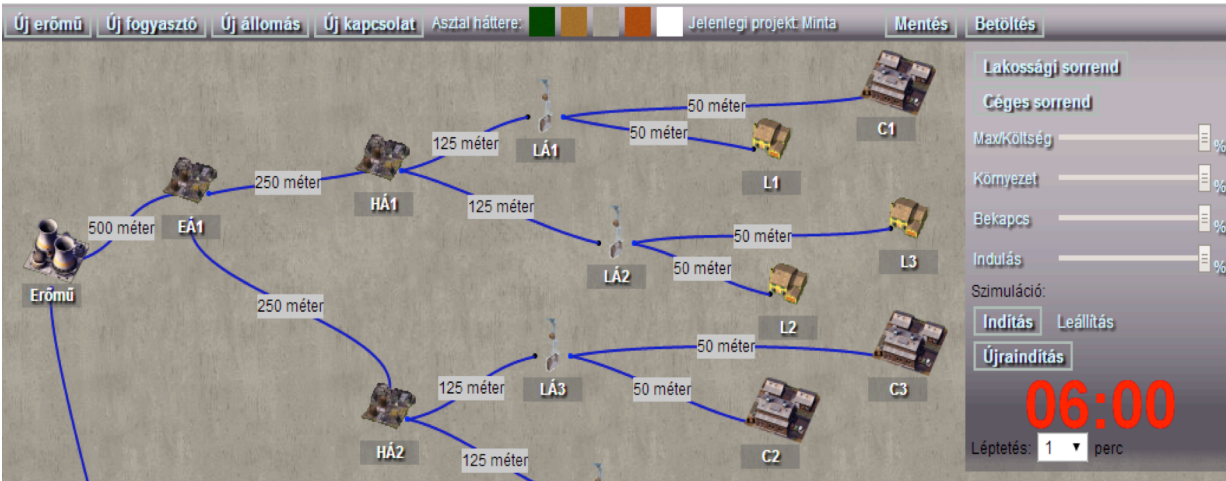


Figure 5: The graphical interface of the software (Új erőmű: new powerplant, Új fogyasztó: new consumer, Új állomás: new station, Új kapcsolat: new connection, Mentés: Save, Betöltés: Load, Lakossági sorrend: order of households, Céges sorrend: order of companies, MaxKöltség: maximum cost, Környezet: environment, Bekapcs: start-up, Indulás: begin, Indítás: start, Leállítás: stop, Újrindítás: restart)

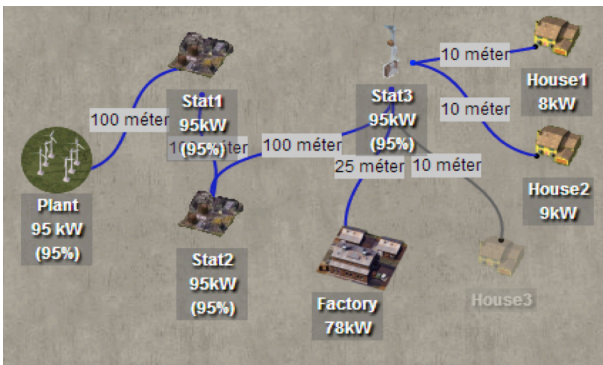


Figure 6: The model of our example (méter: distance in m)

represented by the edges, each with a given power transmission capacity and admittance value describing their ability to transmit electricity. [4] The user is able to initiate immediate events and the system reacts to them in real-time and recalculates the distribution. Calculation of the consumption rate is based on the Hungarian average with a small random factor.

### An Example for a Simulation

Let us assume that we have a power plant with a maximum power of 100 kW. The model has one of each type of stations, three households (10-10 kW maximum) and a factory (80 kW maximum) (Fig.6). Normally, all of the consumers are satisfied, but in the peak times, when the factory and the houses also approach their maximum consumption, the power will not be enough for every consumer, so the system switches off the retail consumer that is last in the priority order. There will not be a consumption reduction, but a complete shutdown. Subsequently, the plant will have to produce 95% of the maximum power. In this example all of the stations can transfer the maximum of 100 kW, but if a station cannot transfer this, then the consumer with the largest priority number connected to this station will be switched off, regardless

of the current level of the power source. If the consumption is too high, it is possible that complete distribution stations are switched off.

### Further Developments

The current system can model and simulate a fictional power network with components and connections, but the main goal of the project is to create a simulating software that can model and simulate a real electrical network. It is important to emphasize that the unit of the power of the sources and the consumption are now only kW. We need to include that the voltage of connection cables depends on the length of the connection and the diameter of the cable that are required to calculate the amperage from the resistance of the cable.

International connections transmit 750 kV, and the main network in Hungary transmits 400 kV starting from the power plants (Fig.7). The distribution stations transform and divide it to lower values until the voltage reaches the necessary 250 V for retail and 360 V (or more) for corporate consumers. During the transformations, the system needs to use Kirchhoff's current law that states that at any node in an electrical circuit, the sum of currents flowing into that node is equal to the sum of currents flowing out of that node. That means that the system has to calculate amperages for every incoming and outgoing connection of the distribution stations based on the consumption of the consumers and the target voltage of the cables.

The biggest problem of power distribution networks in reality is to satisfy all consumers at all the time, even if the load is very low, without making large changes to the output of the power sources everyday. The current solution in Hungary is nighttime power. Households using electric water heaters have nighttime electric meters, when the consumption of corporate consumers is drastically reduced. This solution slightly optimizes the operation of power plants.

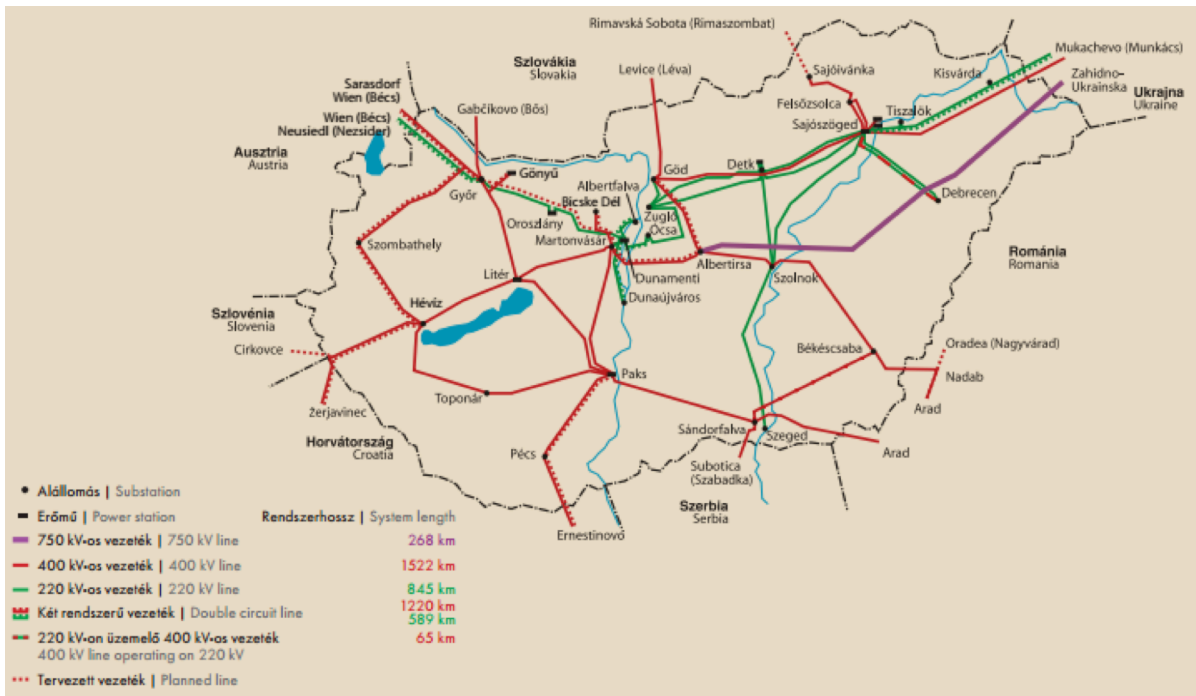


Figure 7: The Hungarian transmission network

## Conclusion

This paper presented the planning phase and implementation of a web-based system that makes it possible to construct an energy distribution network together with different types of energy sources and consumers. The simulations are carried out to determine the most effective response to different immediate events (e.g. a sudden network problem or failure of an energy source). The simulation takes into account both cost-related and time-related properties, too. The present state of the software provides a basis for further works, which intend to add deeper electricity-related properties and behaviour to the system.

## ACKNOWLEDGEMENT

The authors are thankful for scientific guidance by Prof. KATALIN M. HANGOS from the Computer and Automation Research Institute. We acknowledge the

financial support of the Hungarian State and the European Union under the TAMOP-4.2.2.A-11/1/KONV-2012-0072 project.

## REFERENCES

- [1] BREITNER M.H.: Modeling the transformation of the German energy system until 2050: A multi-criteria, long term optimization problem with many constraints, *Operations Res. Proc.* 2012, 369-374
- [2] GEYSEN D., BOOIJ P., WARMER C.: A framework for simulation and control of hybrid energy networks, *Proc. EnergyCon 2014*, Dubrovnik, Croatia, 2014
- [3] PADULLES J., AULT G.W., McDONALD J.R.: An integrated SOFC plant dynamic model for power systems simulation, *Int. J. Power Sources* 2000, 86, 495-500
- [4] CSERCSIK D., KÓCZY L.Á.: Externalities in the games over electrical power transmission networks, *IEHAS Discussion Papers*, 2011, No 1125



HUNGARIAN JOURNAL OF INDUSTRY AND CHEMISTRY

HJIC

Advertise upcoming meetings,

conferences, workshops,

new products or services;

make public announcements,

introduce your research laboratory

on the pages of the

**Hungarian Journal of Industry and Chemistry**

Please contact us if interested!

---

EDITORIAL OFFICE: UNIVERSITY OF PANNONIA

P.O. BOX 158, VESZPRÉM H-8201 (HUNGARY)

Tel.: +36 (88) 624-746, E-mail: [hjic@almos.uni-pannon.hu](mailto:hjic@almos.uni-pannon.hu);

web: [hjic.mk.uni-pannon.hu](http://hjic.mk.uni-pannon.hu)

Felelős szerkesztő: Szilágyi Róbert Károly, PhD

Kiadja: Pannon Egyetem, 8200 Veszprém, Egyetem u. 10.

Levél cím: H-8201 Veszprém, Postafiók 158, Tel.: (88) 624-000

Felelős kiadó: a Pannon Egyetem, Mérnöki Kar dékánja

## ON THE PARAMETRIC UNCERTAINTY OF WEAKLY REVERSIBLE REALIZATIONS OF KINETIC SYSTEMS

GYÖRGY LIPTÁK <sup>✉1</sup>, GÁBOR SZEDERKÉNYI<sup>1,2</sup> AND KATALIN M. HANGOS<sup>1,3</sup>

<sup>1</sup>Process Control Research Group, MTA SZTAKI, Kende u. 13-17, Budapest, 1111, HUNGARY

<sup>2</sup>Faculty of Information Technology, Péter Pázmány Catholic University, Práter u. 50/a, Budapest, 1083, HUNGARY

<sup>3</sup>Department of Electrical Engineering and Information Systems, University of Pannonia, Egyetem u. 10,  
Veszprém, 8200, HUNGARY

<sup>✉</sup>E-mail: lipgyorgy@gmail.com

The existence of weakly reversible realizations within a given convex domain is investigated. It is shown that the domain of weakly reversible realizations is convex in the parameter space. A LP-based method of testing if every element of a convex domain admits weakly reversible realizations is proposed. A linear programming method is also presented to compute a stabilizing kinetic feedback controller for polynomial systems with parametric uncertainty. The proposed methods are illustrated using simple examples.

**Keywords:** parametric uncertainty; computational methods; optimization; kinetic systems

### Introduction

The notion of parametric robustness is well-known and central in linear and nonlinear systems and control theory [1]. It is used for ensuring a desirable property, such as stability, in a given domain in the parameter space around a nominal realization having the desired property.

The aim of the paper is to extend the notions and tools of parametric robustness for a class of positive polynomial systems, namely a class of kinetic systems. Only the very first steps are reported here that offer a computationally efficient method for checking one of the many important properties of kinetic systems, their weak reversibility.

### Basic Notions and Methods

The basic notions and tools related to reaction kinetic systems and their realizations are briefly summarized in this section.

#### *Kinetic Systems, their Dynamics and Structure*

Deterministic kinetic systems with mass action kinetics or simply chemical reaction networks (CRNs) form a wide class of non-negative polynomial systems, that are able to produce all the important qualitative phenomena (e.g. stable/unstable equilibria, oscillations, limit cycles, multiplicity of equilibrium points and even chaotic behaviour) present in the dynamics of nonlinear processes [2].

The general form of dynamic models studied in this paper is the following

$$\dot{x} = M \cdot \psi(x), \quad (1)$$

where  $x \in \mathbb{R}^n$  is the state variable and  $M \in \mathbb{R}^{n \times m}$ . The monomial vector function  $\psi : \mathbb{R}^n \rightarrow \mathbb{R}^m$  is defined as

$$\psi_j(x) = \prod_{i=1}^n x_i^{Y_{ij}}, \quad j = 1, \dots, m \quad (2)$$

where  $Y \in \mathbb{N}_0^{n \times m}$ . The system Eq.(1) is kinetic if and only if the matrix  $M$  has a factorization

$$M = Y \cdot A_k. \quad (3)$$

The Kirchhoff-matrix  $A_k$  has non-positive diagonal and non-negative off-diagonal elements and zero column sums. The matrix pair  $(Y, A_k)$  is called the realization of the system Eq.(1).

*The chemically originated notions:* The chemically originated notions of kinetic systems are as follows: the *species* of the system are denoted by  $X_1, \dots, X_n$ , and the concentrations of the species are the state variables of Eq.(1), i.e.  $x_i = [X_i] \geq 0$  for  $i = 1, \dots, n$ . The structure of kinetic systems is given in terms of its *complexes*  $C_i$ ,  $i = 1, \dots, m$  that are non-negative linear combinations of the species i.e.  $C_i = \sum_{j=1}^n [Y]_{ji} X_j$  for  $i = 1, \dots, m$ , and therefore  $Y$  is also called the *complex composition matrix*.

*The reaction graph:* The weighted directed graph (or reaction graph) of kinetic systems is  $G = (V, E)$ , where

$V = \{C_1, C_2, \dots, C_m\}$  and  $E$  denote the set of vertices and directed edges, respectively. The directed edge  $(C_i, C_j)$  (also denoted by  $C_i \rightarrow C_j$ ) belongs to the reaction graph if and only if  $[A_k]_{j,i} > 0$ . In this case, the weight assigned to the directed edge is  $C_i \rightarrow C_j$  is  $[A_k]_{j,i}$ .

*Stoichiometric subspace:* Stoichiometric subspace  $S$  is given by the span of the reaction vectors

$$S = \{[Y]_{\cdot i} - [Y]_{\cdot j} \mid [A_k]_{ij} > 0\}. \quad (4)$$

The stoichiometric compatibility classes of a kinetic system are the affine translations of the stoichiometric subspace:  $(x_0 + S) \cap \mathbb{R}_{\geq 0}^n$ .

### Structural Properties and Dynamical Behaviour

It is possible to utilize certain structural properties of kinetic systems that enable us to effectively analyze the stability of the system.

*Deficiency:* There are several equivalent ways to define deficiency. We will use the following definition

$$\delta = \dim(\ker(Y) \cap \text{Im}(B_G)), \quad (5)$$

where  $B_G$  is the incidence matrix of the reaction graph. It is easy to see that deficiency is zero if  $\ker(Y) = \{0\}$  or equivalently  $\text{rank}(Y) = m$ .

*Weak reversibility:* A CRN is called *weakly reversible* if whenever there exists a directed path from  $C_i$  to  $C_j$  in its reaction graph, then there exists a directed path from  $C_j$  to  $C_i$ . In graph theoretic terms, this means that all components of the reaction graph are strongly connected components.

*Deficiency zero theorem:* A weakly reversible kinetic system with zero deficiency has precisely one equilibrium point in each positive stoichiometric compatibility class that is locally asymptotically stable (conjecture: globally asymptotically stable).

### Computing Weakly Reversible Realizations Formulated as an Optimization Problem

In this section, first a method for computing weakly reversible realization based on Ref.[3] is briefly presented. We assume that we have a kinetic polynomial system of the form Eq.(1).

We use the fact known from the literature that a realization of a CRN is weakly reversible if and only if there exists a vector with strictly positive elements in the kernel of  $A_k$ , i.e. there exists  $b \in \mathbb{R}_+^n$  such that  $A_k \cdot b = 0$  [4]. Since  $b$  is unknown, too, this condition in this form is not linear. Therefore, we introduce a scaled matrix  $\tilde{A}_k$

$$\tilde{A}_k = A_k \cdot \text{diag}(b) \quad (6)$$

where  $\text{diag}(b)$  is a diagonal matrix with elements of  $b$ . It is clear from Eq.(6) that  $\tilde{A}_k$  is also a Kirchhoff matrix

and that  $\mathbf{1} \in \mathbb{R}^m$  (the  $m$ -dimensional vector containing only ones) lies in kernel of  $\tilde{A}_k$ . Moreover, it is easy to see that  $\tilde{A}_k$  defines a weakly reversible network if and only if  $A_k$  corresponds to a weakly reversible network. Then, the weak reversibility and the Kirchhoff property of  $\tilde{A}_k$  can be expressed using the following linear constraints

$$\begin{aligned} \sum_{i=1}^m [\tilde{A}_k]_{ij} &= 0, \quad j = 1, \dots, m \\ \sum_{i=1}^m [\tilde{A}_k]_{ji} &= 0, \quad j = 1, \dots, m \\ [\tilde{A}_k]_{ij} &\geq 0, \quad i, j = 1, \dots, m, \quad i \neq j \\ [\tilde{A}_k]_{ii} &\leq 0, \quad i = 1, \dots, m. \end{aligned} \quad (7)$$

Moreover, the equation Eq.(3) is transformed by  $\text{diag}(b)$  (we can do this, because  $\text{diag}(b)$  is invertible):

$$M \cdot \text{diag}(b) = Y \cdot \underbrace{A_k}_{\tilde{A}_k} \cdot \text{diag}(b) \quad (8)$$

Finally, by choosing an arbitrary linear objective function of the decision variables  $\tilde{A}_k$  and  $b$ , weakly reversible realizations of the studied kinetic system can be computed (if any exist) in a LP framework using the linear constraints Eq.(7) and (8).

### Weakly Reversible CRN Realizations

In this section, first the convexity of the weakly reversible Kirchhoff matrix will be shown. After that the practical benefits of this property will be demonstrated in the field of system analysis and robust feedback design.

#### Convexity of the Weak Reversibility in the Parameter Space

**Theorem 1.** Let  $A_k^{(1)}$  and  $A_k^{(2)}$  be  $m \times m$  weakly reversible Kirchhoff matrices. Then the convex combination of the two matrices remains weakly reversible.

*Proof.* The idea behind the proof is based on Ref.[5]. A Kirchhoff matrix is weakly reversible if and only if there is a strictly positive vector in its kernel. Therefore strictly positive vectors  $p_1, p_2$  exist such as  $A_k^{(1)} \cdot p_1 = 0$  and  $A_k^{(2)} \cdot p_2 = 0$ . Let us define the following scaled Kirchhoff matrix:  $\hat{A}_k^{(1)} = A_k^{(1)} \cdot \text{diag}(p_1)$  and  $\hat{A}_k^{(2)} = A_k^{(2)} \cdot \text{diag}(p_2)$ . These scaled matrices have identical structures to the original ones. Moreover,  $\hat{A}_k^{(1)} \cdot \mathbf{1}^{(m)} = 0$  and  $\hat{A}_k^{(2)} \cdot \mathbf{1}^{(m)} = 0$  where the vector  $\mathbf{1}^{(m)}$  denotes the  $m$  dimensional column vector composed of ones. For that

$$(\lambda \hat{A}_k^{(1)} + (1 - \lambda) \hat{A}_k^{(2)}) \cdot \mathbf{1}^{(m)} = 0. \quad (9)$$

for any  $\lambda \in [0, 1]$ . Therefore the convex combination of the original two realizations has to be weakly reversible.  $\square$

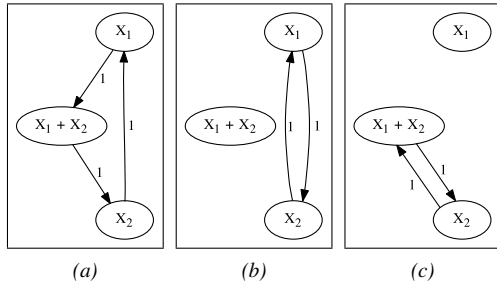


Figure 1: A weakly reversible reaction graphs of the three realizations  $(Y, A_k^{(1)})$ ,  $(Y, A_k^{(2)})$  and  $(Y, A_k^{(3)})$

### Weak Reversibility of CRN Realizations with Parametric Uncertainty

We assume that a CRN with parametric uncertainty is given as

$$\dot{x} = M \cdot \psi(x), \quad (10)$$

where  $x \in \mathbb{R}^n$  is the state variable,  $\psi \in \mathbb{R}^n \rightarrow \mathbb{R}^m$  contains the monomials and the matrix  $M \in \mathbb{R}^{n \times m}$  is an element of the following set

$$\mathcal{M} = \left\{ \sum_{i=1}^l \alpha_i M_i \mid (\forall i : \alpha_i \geq 0) \wedge \sum_{i=1}^l \alpha_i = 1 \right\}. \quad (11)$$

The goal is to find a method for checking the weak reversibility of the system Eq.(10) for all matrices  $M \in \mathcal{M}$ .

When all vertices  $M_i$  have a weakly reversible realization  $(Y, A_k^{(i)})$  then any element of the set  $\mathcal{M}$  has a realization  $(Y, A_k)$  such that  $A_k$  is the convex combination of the Kirchhoff matrices  $A_k^{(i)}$ . The obtained realization  $A_k$  will be weakly reversible due to Theorem 1. Therefore, it is enough to compute a weakly reversible realization for each matrix  $M_i$  by using the previously presented LP-based method.

### A Simple Example

Let us consider the following polynomial system

$$\begin{bmatrix} \dot{x}_1 \\ \dot{x}_2 \end{bmatrix} = M \cdot \begin{bmatrix} x_1 \\ x_2 \\ x_1 x_2 \end{bmatrix}, \quad (12)$$

where  $M$  is an arbitrary convex combination of the following three matrices

$$M_1 = \begin{bmatrix} 0 & 1 & -1 \\ 1 & -1 & 0 \end{bmatrix},$$

$$M_2 = \begin{bmatrix} -1 & 1 & 0 \\ 1 & -1 & 0 \end{bmatrix}, \text{ and}$$

$$M_3 = \begin{bmatrix} 0 & 1 & -1 \\ 0 & 0 & 0 \end{bmatrix}.$$

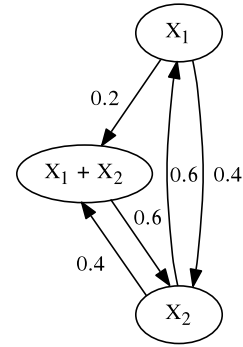


Figure 2: A weakly reversible realization of the convex combination  $M = 0.2M_1 + 0.4M_2 + 0.4M_3$

In order to show weak reversibility for all possible convex combinations, we have to find a weakly reversible realization for each matrix  $M_1$ ,  $M_2$  and  $M_3$ . The resulting weakly reversible reaction graphs are depicted in Fig.1, while Fig.2 illustrates an inner point realization which is weakly reversible too.

### Computing Kinetic Feedback for a Polynomial System with Parametric Uncertainty

Besides the possible application of the above described LP-based method for robust stability analysis, it can also be used for stabilizing feedback controller design. For this purpose, a generalized version of our preliminary work on kinetic feedback computation for polynomial systems to achieve weak reversibility and minimal deficiency [6] is used here.

### The Feedback Design Problem

We assume that the equation of the open-loop polynomial system with linear constant parameter input structure is given as

$$\dot{x} = M \cdot \psi(x) + Bu, \quad (13)$$

where  $x \in \mathbb{R}^n$  is the state vector,  $u \in \mathbb{R}^p$  is the input and  $\psi \in \mathbb{R}^n \rightarrow \mathbb{R}^m$  contains the monomials of the open-loop system. The input matrix is  $B \in \mathbb{R}^{n \times p}$ , the corresponding complex composition matrix is  $Y$  with rank  $m$ , and  $M \in \mathbb{R}^{n \times m}$  is an element of the following set

$$\mathcal{M} = \left\{ \sum_{i=1}^l \alpha_i M_i \mid (\forall i : \alpha_i \geq 0) \wedge \sum_{i=1}^l \alpha_i = 1 \right\}. \quad (14)$$

Moreover, a positive vector  $\bar{x} \in \mathbb{R}_{>0}^n$  being the desired equilibrium point is given as a design parameter. Note that the above polynomial system is not necessarily kinetic, i.e. not necessarily positive, and may not have a positive equilibrium point at all.

The aim of the feedback is to set a region in the state space  $R \subseteq \mathbb{R}_{\geq 0}^n$  where  $\bar{x}$  is (at least) a locally asymptotically stable equilibrium point of the closed-loop system for all  $M \in \mathcal{M}$ .

For this purpose we are looking for a feedback in the form

$$u = K\psi(x) \quad (15)$$

which transforms the open-loop system into a weakly reversible kinetic system with zero deficiency for all  $M \in \mathcal{M}$  with the given equilibrium point  $\bar{x}$ .

### Feedback Computation

Similarly to the realization computation, the matrix  $K$  will be determined by solving an LP problem. The convexity result shows that it is enough to compute one weakly reversible realization  $(Y, A_k^{(r)})$  in each vertex  $M_r$  to ensure weak reversibility for all possible closed-loop systems. All realizations will have zero deficiency, because of the rank condition  $\text{rank}(Y) = m$  [7].

First we note, that the realization  $(Y, A_k^{(r)})$  that corresponds to the closed-loop system is

$$M_r + B \cdot K = Y \cdot A_k^{(r)}. \quad (16)$$

where the matrix  $A_k^{(r)}$  should be Kirchhoff

$$\begin{aligned} \sum_{i=1}^m [\tilde{A}_k]_{ij} &= 0, \quad j = 1, \dots, m \\ [\tilde{A}_k]_{ij} &\geq 0, \quad i, j = 1, \dots, m, \quad i \neq j \\ [\tilde{A}_k]_{ii} &\leq 0, \quad i = 1, \dots, m. \end{aligned} \quad (17)$$

In order to obtain a weakly reversible closed-loop system with an equilibrium point  $\bar{x}$ , the matrix  $A_k^{(r)}$  should be weakly reversible and has to have the vector  $\psi(\bar{x})$  in its right kernel, i.e.

$$A_k^{(r)} \cdot \psi(\bar{x}) = 0. \quad (18)$$

Finally, by choosing an arbitrary linear objective function of the decision variables  $A_k^{(1)}, \dots, A_k^{(l)}$  and  $K$ , the feedback gain  $K$  can be computed (if it exists) in a LP framework using the linear constraints Eqs.(16-18).

With the resulting feedback gain  $K$ , the point  $\bar{x}$  will be an equilibrium point of all possible closed-loop systems, and  $\bar{x}$  will be locally asymptotically stable in the region  $\mathcal{S} = (\bar{x} + S) \cap \mathbb{R}_{\geq 0}^n$ , where  $S$  is the stoichiometric subspace of the closed-loop system.

### Example

Let the open-loop system be given as

$$\dot{x} = M \begin{bmatrix} x_1 x_2 \\ x_2 x_3 \\ x_1 \end{bmatrix} + \begin{bmatrix} 0 \\ 1 \\ 0 \end{bmatrix} u \quad (19)$$

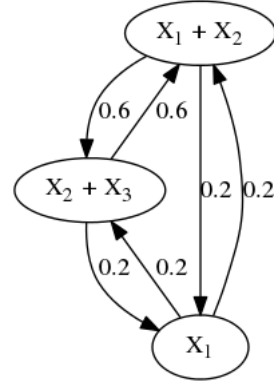


Figure 3: Weakly reversible realization of the closed-loop system, where

$$M = 0.6M_1 + 0.2M_2 + 0.2M_3$$

where  $M$  is an arbitrary convex combination of the following three matrices:

$$\begin{aligned} M_1 &= \begin{bmatrix} -1 & 1 & 0 \\ 2 & 1 & 2 \\ 1 & -1 & 0 \end{bmatrix}, \\ M_2 &= \begin{bmatrix} 0 & 0 & 0 \\ 1 & 1 & 3 \\ 0 & 0 & 0 \end{bmatrix}, \text{ and} \\ M_3 &= \begin{bmatrix} 0 & 1 & -1 \\ 2 & 0 & 3 \\ 0 & -1 & 1 \end{bmatrix}. \end{aligned}$$

The desired equilibrium point  $\bar{x} = [1 \ 1 \ 1]^T$ .

We are looking for a feedback law with gain  $K$  which transforms the matrices  $M_i$  into weakly reversible kinetic systems with the given equilibrium point.

By solving the feedback design LP optimization problem using the linear constraints Eqs.(16-18), the computed feedback is in the following form:

$$u = [ \ 2 \ 1 \ 2 \ ] \psi(x). \quad (20)$$

Fig.3 depicts a weakly reversible realization of the closed-loop system. The obtained closed-loop system in an inner point of the convex set  $\mathcal{M}$  has the following stoichiometric subspace:

$$S = \text{span} \left( \left( \begin{bmatrix} 1 \\ 1 \\ 0 \end{bmatrix} - \begin{bmatrix} 0 \\ 1 \\ 1 \end{bmatrix}, \begin{bmatrix} 1 \\ 1 \\ 0 \end{bmatrix} - \begin{bmatrix} 1 \\ 0 \\ 0 \end{bmatrix} \right) \right). \quad (21)$$

Therefore, the equilibrium point  $\bar{x}$  will be asymptotically stable with the region  $\mathcal{S} = (\bar{x} + S) \cap \mathbb{R}_{\geq 0}^n$ . Note, that one should choose the initial value of the state variables from  $\mathcal{S}$ .

Fig.4 shows the time dependent behaviour of the closed-loop solutions started from different initial points in  $\mathcal{S}$ .

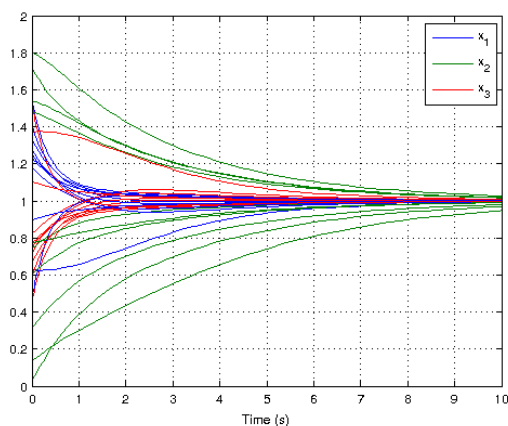


Figure 4: Time-domain simulation of the closed-loop system

### Conclusion

It is shown in this paper that the domain of weakly reversible realizations is convex in the parameter space. This property is utilized for developing methods in system analysis and robust control design. An LP-based optimization method is proposed for testing if every element of a convex domain given by its extremal matrices admits a weakly reversible realization. An LP-based feedback design method is also proposed that guarantees stability with a desired equilibrium point. The proposed methods are illustrated with simple examples.

### REFERENCES

- [1] SILJAK D.: Parameter space methods for robust control design: a guided tour, *Aut. Contr., IEEE Transactions on*, 1989, 34(7), 674–688
- [2] ANGELI D.: A tutorial on chemical network dynamics, *Eur. J. Contr.*, 2009, 15, 398–406
- [3] SZEDERKÉNYI G., HANGOS K. M., TUZA Z.: Finding weakly reversible realizations of chemical reaction networks using optimization, *MATCH Commun. Math. Comp. Chem.*, 2012, 67, 193–212
- [4] FEINBERG M., HORN F.: Chemical mechanism structure and the coincidence of the stoichiometric and kinetic subspaces, *Arch. Rational Mechanics and Analysis*, 1977, 66(1), 83–97
- [5] RUDAN J., SZEDERKÉNYI G., HANGOS K.M., PÉNI T.: Polynomial time algorithms to determine weakly reversible realizations of chemical reaction networks, *J. Math. Chem.*, 2014, 52(5), 1386–1404
- [6] LIPTÁK G., SZEDERKÉNYI G., HANGOS K.M.: Kinetic feedback computation for polynomial systems to achieve weak reversibility and minimal deficiency, 13th Eur. Control Conf. ECC, Strasbourg, France, 2014, 2691–2696
- [7] ANGELI D., LENHEE, P.D., SONTAG E.D.: On the structural monotonicity of chemical reaction networks, *Proc. 45th IEEE Conf. Decision and Control*, 2006, 7–12



HUNGARIAN JOURNAL OF INDUSTRY AND CHEMISTRY

HJIC

Advertise upcoming meetings,

conferences, workshops,

new products or services;

make public announcements,

introduce your research laboratory

on the pages of the

**Hungarian Journal of Industry and Chemistry**

Please contact us if interested!

---

EDITORIAL OFFICE: UNIVERSITY OF PANNONIA

P.O. BOX 158, VESZPRÉM H-8201 (HUNGARY)

Tel.: +36 (88) 624-746, E-mail: [hjic@almos.uni-pannon.hu](mailto:hjic@almos.uni-pannon.hu);

web: [hjic.mk.uni-pannon.hu](http://hjic.mk.uni-pannon.hu)

Felelős szerkesztő: Szilágyi Róbert Károly, PhD

Kiadja: Pannon Egyetem, 8200 Veszprém, Egyetem u. 10.

Levél cím: H-8201 Veszprém, Postafiók 158, Tel.: (88) 624-000

Felelős kiadó: a Pannon Egyetem, Mérnöki Kar dékánja

## STABILITY AND PARAMETER SENSITIVITY ANALYSES OF AN INDUCTION MOTOR

ATTILA FODOR<sup>1</sup>, ROLAND BÁLINT<sup>✉1</sup>, ATTILA MAGYAR<sup>1</sup>, AND GÁBOR SZEDERKÉNYI<sup>2</sup>

<sup>1</sup>Department of Electrical Engineering and Information Systems, University of Pannonia,  
Egyetem u. 10., Veszprém, 8200, HUNGARY

<sup>2</sup>Pazmány Péter Catholic University, Práter u. 50/a, Budapest, 1083, HUNGARY

<sup>✉</sup>E-mail: balint.roland27@gmail.com

A simple dynamical model of an induction motor is derived and analyzed in this paper based on engineering principles that describe the mechanical phenomena together with the electrical model. The used state space model consists of nonlinear state equations. The model has been verified under the usual controlled operating conditions when the speed is controlled. The effect of load on the controlled induction motor has been analyzed by simulation. The sensitivity analysis of the induction motor has been applied to determine the model parameters to be estimated.

**Keywords:** induction motor, stability analysis, sensitivity analysis

### Introduction

Induction motors (IM) are the most commonly used electrical rotating machines in several industrial applications. Irrespective of size and the application area, these motors share the most important dynamical properties, and their dynamical models have a similar structure.

Because of the specialties and great practical importance of IMs in industrial applications, their modelling for control purposes is well investigated in the literature. Besides basic textbooks [1-3], there are several papers that describe the modelling and use the developed models for the design of different types of controllers: vector control [1, 4], sensorless vector control [5] and direct torque control (DTC) [6]. The aim of this paper is to build a simple dynamical model of the IM and to perform its parameter sensitivity analysis. The results of this analysis will be the basis of the next step since the final aim of our study is to estimate the parameters of the IM and design a controller that can control the speed and torque of the IM. The state space model has been implemented in the Matlab/Simulink environment which enables us to analyze the parametric sensitivity based on simulation experiments.

### Nonlinear Model of an Induction Motor

In this section a state space model of an induction motor (IM) is presented. The model development is largely based on Refs.[1, 8-10]. For constructing the IM model, the following modelling assumptions are made:

1. a symmetrical triphase stator winding system is assumed,

2. the flux density is radial in the air gap,
3. the copper loss and the slots in the machine can be neglected,
4. the spatial distribution of the stator fluxes and apertures wave are considered to be sinusoidal,
5. stator and rotor permeability are assumed to be infinite with linear magnetic properties.

According to the above modelling conditions the mathematical description of the IM is developed through the space-vector theory. If the voltage of the stator is presumed to be the input excitation of the machine, then the spatial distribution along the stator of the  $x$  phase voltage can be described by the complex vector  $v_{sx}(t)$ . We can determine the orientation of the voltage vector  $v_s$ , the direction of the respective phase axis and the voltage polarity.

$$\begin{aligned} i_s(t) &= \frac{2}{3} (a^0 \cdot i_{sa}(t) + a^1 \cdot i_{sb}(t) + a^2 \cdot i_{sc}(t)) \\ &= \sqrt{2} \cdot i_{\text{eff}}(t) \cdot e^{j\omega_0 t + \frac{\pi}{2} + \varphi_i}, \end{aligned} \quad (1)$$

where  $a$  is the  $e^{j120^\circ}$  vector and  $i_{sa}$ ,  $i_{sb}$  and  $i_{sc}$  are the following:

$$i_{sa}(t) = \text{Re}(a^0 \cdot i_s(t)) = \text{Re}(i_s(t)),$$

$$i_{sb}(t) = \text{Re}(a^2 \cdot i_s(t)), \text{ and}$$

$$i_{sc}(t) = \text{Re}(a^1 \cdot i_s(t)).$$

In Eq.(1),  $2/3$  is the normalizing factor. The flux density distribution can be obtained by integrating the current density wave along the cylinder of the stator. The flux linkage wave is a system variable, because it contains detailed information about the winding geometry.

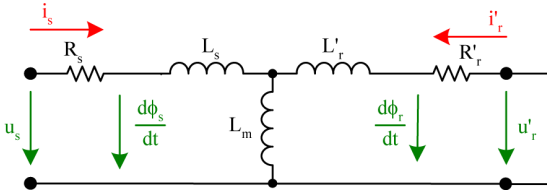


Figure 1: The equivalent circuit of the IM

The rotating flux density wave induces voltages in the individual stator windings. Thus stator voltage  $v_s(t)$  can be represented as the overall distributed voltages in all phase windings:

$$\begin{aligned} v_s(t) &= \frac{2}{3} (a^0 \cdot v_{sa}(t) + a^1 \cdot v_{sb}(t) + a^2 \cdot v_{sc}(t)) \\ &= \sqrt{2} \cdot v_{\text{eff}}(t) \cdot e^{j\omega_0 t + \frac{\pi}{2} + \varphi_u}, \end{aligned} \quad (2)$$

where  $a$  is the  $e^{j120^\circ}$  vector and  $i_{sa}$ ,  $i_{sb}$  and  $i_{sc}$  are the following:

$$v_{sa}(t) = \text{Re}(a^0 \cdot u_s(t)) = \text{Re}(u_s(t)),$$

$$v_{sb}(t) = \text{Re}(a^2 \cdot u_s(t)), \text{ and}$$

$$v_{sc}(t) = \text{Re}(a^1 \cdot u_s(t)).$$

Considering the stator of the IM as the primer side of the transformer, then using Kirchoff's voltage law the following equation can be written (Fig.1):

$$v_s(t) = i_s(t) \cdot R_s + \frac{d\phi_s(t)}{dt}. \quad (3)$$

As for the secondary side of the transformer, it can be deduced that the same relationship is true for the rotor side space vectors:

$$v_r(t) = i_r(t) \cdot R_r + \frac{d\phi_r(t)}{dt} = 0. \quad (4)$$

Eqs.(3) and (4) describe the electromagnetic interaction as the connection of first order dynamical subsystems:

$$\phi_s(t) = i_s(t) \cdot L_s + i_r(t) \cdot L_m, \text{ and} \quad (5)$$

$$\phi_r(t) = i_s(t) \cdot L_m + i_r(t) \cdot L_r. \quad (6)$$

Since four complex variables ( $i_s(t)$ ,  $i_r(t)$ ,  $\phi_s(t)$ , and  $\phi_r(t)$ ) are presented in Eqs.(5) and (6), flux equations are needed to complete the relationship between them.

The mechanical power ( $P_{\text{mech}}(t)$ ) of the IM can be defined as:

$$P_{\text{mech}}(t) = \frac{W_{\text{mech}}(t)}{dt}, \quad (7)$$

where the mechanical energy ( $P_{\text{mech}}(t)$ ) in the rotating system can be given by the following expression:

$$P_{\text{mech}}(t) = \frac{W_{\text{mech}}(t)}{dt} = T_{\text{mech}}(t) \cdot \omega_r, \quad (8)$$

where  $T_e(t)$  is the torque and  $\omega_r$  is the angular velocity of the IM. Afterwards the energy balance of the IM is as follows:

$$W_e = W_{\text{mech}} + W_R + W_{\text{Field}}, \quad (9)$$

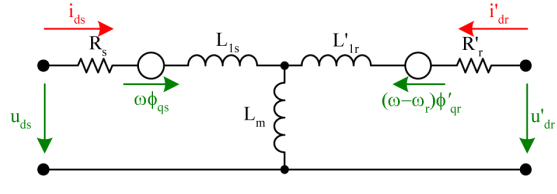


Figure 2: The equivalent circuit of the d-axis of the IM

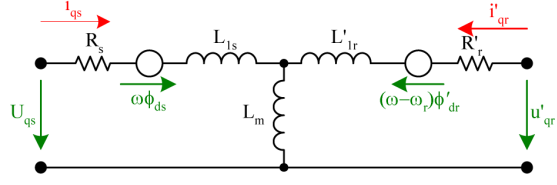


Figure 3: The equivalent circuit of the q-axis of the IM

where

$$P_e = \frac{W_e(t)}{dt} = \frac{3}{2} \text{Re}(u_s \cdot i_s + u_r \cdot i_r) \quad (10)$$

is the input electrical power,

$$P_R = \frac{W_R(t)}{dt} = \frac{3}{2} \text{Re}(R_s \cdot |i_s|^2 + R_r \cdot |i_r|^2) \quad (11)$$

represents the resistive power losses and

$$P_{\text{Field}} = \frac{W_{\text{Field}}(t)}{dt} = \frac{3}{2} \text{Re} \left( \frac{d\phi_s}{dt} i_s + \frac{d\phi_r}{dt} i_r \right) \quad (12)$$

is the air gap power. Using Eqs.(8-12),

$$P_{\text{mech}}(t) = T_{\text{mech}}(t) \cdot \omega_r = \frac{3}{2} \cdot \frac{L_m}{L_r} \cdot \phi_s(t) \times i_s(t), \text{ and} \quad (13)$$

$$T_e = 1.5p \cdot (\phi_{ds} i_{qs} - \phi_{qs} i_{ds}). \quad (14)$$

The equivalent circuit of the IM can be decomposed to direct axis and quadratic axis components by Park's transformation as shown in Figs.2 and 3.

The actual terminal voltage  $v$  of the windings can be written in the form

$$v = \pm \sum_{j=1}^J (R_j i_j) \pm \sum_{j=1}^J \left( \frac{d\phi_j}{dt} \right), \quad (15)$$

where  $i_j$  are the currents,  $R_j$  are the winding resistances, and  $\phi_j$  are the flux linkages. The positive directions of the stator currents point out of the IM terminals.

By composing the d and q axes of the IM the following equations can be written:

$$v_{qs} = R_s \cdot i_{qs} + \frac{d\phi_{qs}}{dt} + \omega \cdot \phi_{ds}, \quad (16)$$

$$v_{ds} = R_s \cdot i_{ds} + \frac{d\phi_{ds}}{dt} - \omega \cdot \phi_{qs}, \quad (17)$$

$$v_{qr} = R'_r \cdot i'_{dr} + \frac{d\phi'_{dr}}{dt} + (\omega - \omega_r) \cdot \phi'_{dr}, \text{ and} \quad (18)$$

$$v_{dr} = R'_r \cdot i'_{dr} + \frac{d\phi'_{dr}}{dt} - (\omega - \omega_r) \cdot \phi'_{qr}. \quad (19)$$

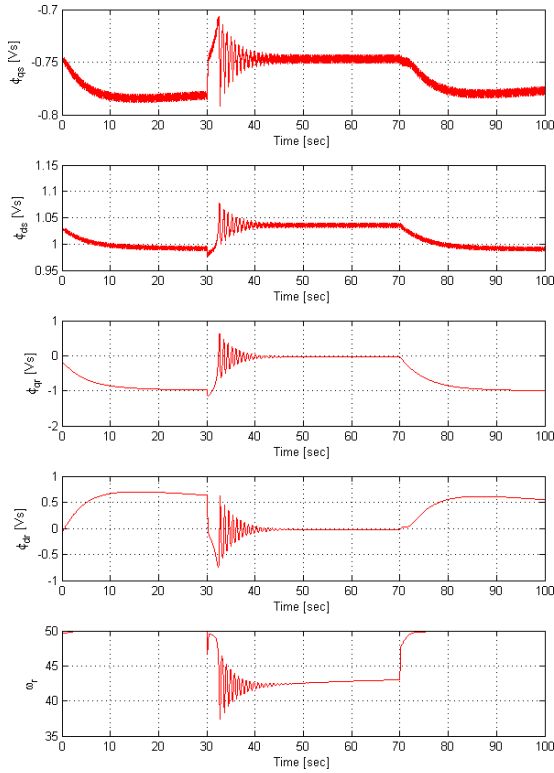


Figure 4: Response to the step change of the speed-controlled IM

$$\frac{d\omega_m}{dt} = \frac{1}{2H} (T_e - F \cdot \omega_m - T_{mech}) \quad (20)$$

where  $\omega$  is the reference frame angular velocity,  $\omega_r$  is the electrical angular velocity,

$$\phi_{qs} = L_s \cdot i_{qs} + L_m i'_{qr}, \quad (21)$$

$$\phi_{ds} = L_s \cdot i_{ds} + L_m i'_{dr}, \quad (22)$$

$$\phi_{qr} = L_r \cdot i'_{qr} + L_m i'_{qs}, \text{ and} \quad (23)$$

$$\phi_{dr} = L_r \cdot i'_{dr} + L_m i'_{ds}. \quad (24)$$

The above model can be written in state space form by expressing the time derivative of the fluxes and  $\omega$  from the voltage and swing equations Eqs.(21-24). The nonlinear state space model of the IM is given by Eqs.(25-29):

$$\begin{aligned} \frac{d\phi_{qs}}{dt} &= \frac{-R_s}{L_s - \frac{L_m^2}{L_r}} \cdot \phi_{qs} - \frac{R_s \cdot L_m}{L_r (L_s - \frac{L_m^2}{L_r})} \cdot \phi'_{qr} \\ &- \omega \cdot \phi_{ds} + v_{qs}, \end{aligned} \quad (25)$$

$$\begin{aligned} \frac{d\phi_{ds}}{dt} &= \frac{-R_s}{L_s - \frac{L_m^2}{L_r}} \cdot \phi_{ds} + \frac{R_s \cdot L_m}{L_r (L_s - \frac{L_m^2}{L_r})} \cdot \phi'_{dr} \\ &- \omega \cdot \phi_{qs} + v_{ds}, \end{aligned} \quad (26)$$

$$\begin{aligned} \frac{d\phi'_{qr}}{dt} &= \frac{-R'_r}{L_m - \frac{L'_r \cdot L_s}{L_m}} \cdot \phi_{qs} \\ &+ \frac{-R'_r \cdot L_s}{L_m \cdot (L_m - \frac{L'_r \cdot L_s}{L_m})} \cdot \phi'_{qr} \\ &- \omega \cdot \phi'_{dr} + \omega_r \cdot \phi'_{dr} + v_{qr}, \end{aligned} \quad (27)$$

$$\begin{aligned} \frac{d\phi'_{dr}}{dt} &= \frac{-R'_r}{L_m - \frac{L'_r \cdot L_s}{L_m}} \cdot \phi_{ds} \\ &+ \frac{-R'_r \cdot L_s}{L_m \cdot (L_m - \frac{L'_r \cdot L_s}{L_m})} \cdot \phi'_{dr} \\ &+ \omega \cdot \phi'_{qr} - \omega_r \cdot \phi'_{qr} + v_{dr}, \text{ and} \end{aligned} \quad (28)$$

$$\begin{aligned} \frac{d\omega_r}{dt} &= \frac{1}{2H} \cdot \frac{1.5 \cdot p \cdot L_m}{L_m \cdot (L_s - \frac{L_m^2}{L_r})} \cdot \phi'_{dr} \cdot \phi_{qs} \\ &- \frac{1}{2H} \cdot \frac{1.5 \cdot p \cdot L_m}{L_m \cdot (L_s - \frac{L_m^2}{L_r})} \cdot \phi'_{qr} \cdot \phi_{ds} \\ &- \frac{F}{2H} \cdot \omega_r - \frac{T_m}{2H}. \end{aligned} \quad (29)$$

The state vector of the above model is  $\mathbf{x} = [\phi_{qs}, \phi_{ds}, \phi'_{qr}, \phi'_{dr}, \omega_r]^T \in \mathbb{R}^5$ , and the input variables are organized in terms of the the input vector  $\mathbf{u} = [v_{qr}, v_{dr}, -T_{mech}]^T \in \mathbb{R}^3$ . It is assumed that all the state variables can be measured i.e.  $\mathbf{y} = \mathbf{x}$ .

### Model Validation

The dynamical properties of the IM have been investigated. The response of the speed-controlled motor has been tested under step-like changes. The simulation results are shown in Fig.4, where the fluxes ( $\phi_{qs}$ ,  $\phi_{ds}$ ,  $\phi'_{qr}$ , and  $\phi'_{dr}$ ) and the angular velocity ( $\omega$ ) are shown.

### Model Analysis

The above model Eqs.(21-24) has been verified by simulation against engineering intuition.

### Local Stability Analysis

As the final aim of our research is to estimate the parameters of a particular Grundfos IM, first of all the resistances ( $R_s$  and  $R_r$ ) of the IM were measured. Afterwards the values of the inductances ( $L_{ls}$ ,  $L_{lr}$  and  $L_m$ ) and the mechanical parameters ( $H$  and  $F$ ) of a similar IM with similar  $R_s$  and  $R_r$  found in the literature have been used. The parameters used during the model and the sensitivity analyses are the following:

$$\begin{aligned} R_s &= 0.196 \text{ Ohm} \\ R_r &= 0.0191 \text{ Ohm} \\ L_{ls} &= 0.0397 \text{ H} \\ L_{lr} &= 0.0397 \text{ H} \\ L_m &= 1.354 \text{ H} \\ H &= 0.095 \\ F &= 0.0548 \\ p &= 1 \end{aligned} \quad (30)$$

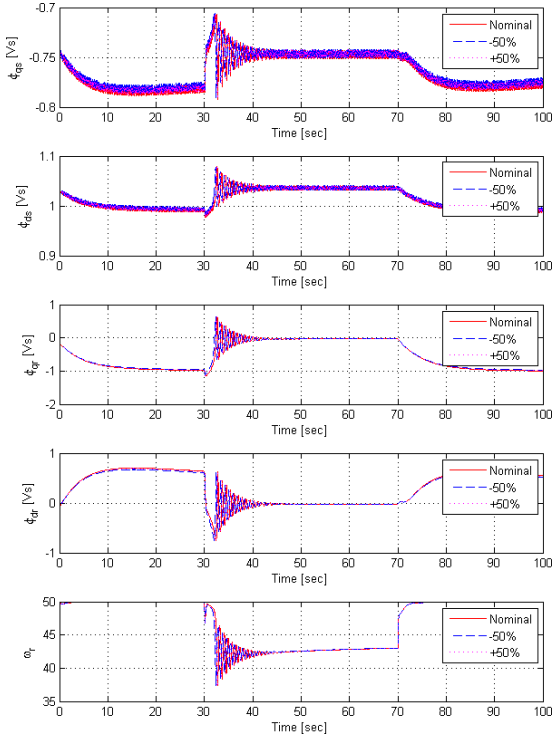


Figure 5: The model state variables for a  $\pm 50\%$  change of  $L_m$

It can easily be seen that the IM model is nonlinear since there are products of two state variables in the following equations:

- Eq.(27):  $\phi'_{dr}$  is multiplied by  $\omega_r$
- Eq.(28):  $\phi'_{qr}$  is multiplied by  $\omega_r$
- Eq.(29):  $\phi'_{dr}$  is multiplied by  $\phi_{qs}$
- Eq.(29):  $\phi'_{qr}$  is multiplied by  $\phi'_{ds}$

For the local stability analysis we have to calculate the eigenvalues of the system. The examined equilibrium point is

$$\begin{aligned}
 \phi_{qs} &= -0.744 \text{ Vs} \\
 \phi_{ds} &= 1.0287 \text{ Vs} \\
 \phi'_{qr} &= -0.174 \text{ Vs} \\
 \phi'_{dr} &= -0.087 \text{ Vs} \\
 \omega_r &= 48.477 \text{ s}^{-1}
 \end{aligned} \tag{31}$$

The numerical value of the Jacobian of the nonlinear model (i.e. the state matrix of the locally linearized model) is as follows:

$$\begin{bmatrix}
 -2.504 & -50 & 2.4328 & 0 & 0 \\
 50 & -2.504 & 0 & 2.4328 & 0 \\
 0.2370 & 0 & -0.244 & -1.522 & 0 \\
 0 & 0.2370 & 1.5222 & -0.244 & 0 \\
 -8.617 & 17.077 & 0 & 0 & -0.288
 \end{bmatrix}. \tag{32}$$

The eigenvalues of the state matrix of the linearized systems are:

$$\begin{aligned}
 \lambda_{1,2} &= -2.504 \pm j49.98, \\
 \lambda_{3,4} &= -0.243 \pm j1.534, \text{ and} \\
 \lambda_5 &= -0.288
 \end{aligned} \tag{33}$$

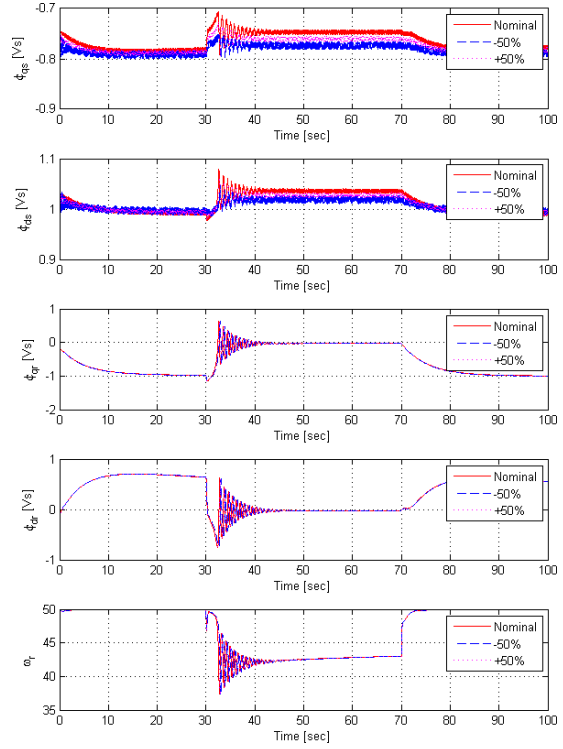


Figure 6: The model state variables for a  $\pm 50\%$  change in  $R_s$

It is apparent that the real parts of the eigenvalues are negative with small magnitudes.

#### Parameter Sensitivity Analysis

the sensitivity of the nonlinear model to the mutual inductance has been investigated. The steady state value of the system variables does not change (as is apparent in Fig.5) even for a considerably large change in  $L_m$ . Sensitivity analysis of the inductances  $L_{lr}$ ,  $L_{ls}$  of the stator and rotor, resistances of the stator  $R_s$  and the damping constant  $F$  has also been investigated. In this investigation it can be seen that the values of the state variables were changed a bit, as shown in Fig.6.

The analysis of the resistances of the rotor  $R'_r$  and the inertia  $H$  of the rotor showed that every value of the state variables changed significantly, as shown in Fig.7.

As a final result of the sensitivity analysis, we can define the following groups of parameters:

- *Not sensitive:* Mutual inductance  $L_m$ . Since the state space model of interest is insensitive in this respect, the values of this parameter cannot be reliably determined from measurement data using any parameter estimation method.
- *Sensitive:* These sensitive parameters are candidates for parameter estimation.
  - Less: inductances  $L_{lr}$  and  $L_{ls}$ , resistance of the stator  $R_s$  and the damping constant  $F$ .
  - More: resistances of the rotor  $R'_r$  and the inertia  $H$  of the rotor.
- *Critically sensitive:* none.

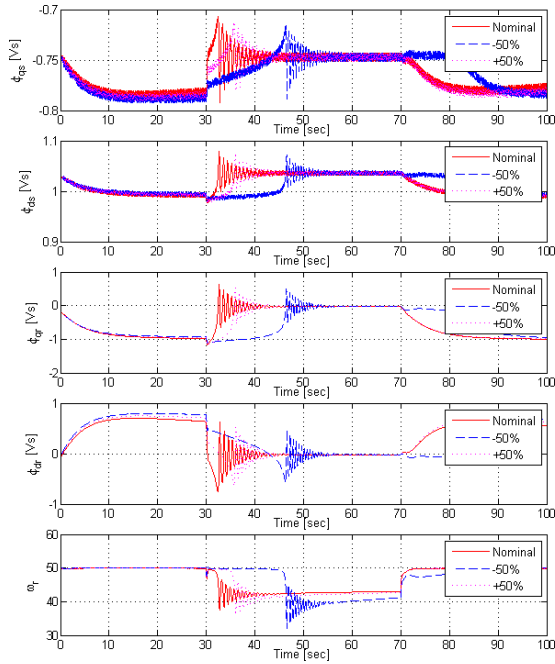


Figure 7: The model state variables for a  $\pm 50\%$  change in  $H$

### Conclusion

The simple nonlinear dynamical model of an IM has been investigated in this paper. It has been shown that the model is locally asymptotically stable with regards to a physically meaningful equilibrium state. The effect of the controlled generator has been analyzed by simulation using a traditional PI controller. It has been found that the controlled system is stable and can follow the set-point changes. Seven parameters of the model were selected for sensitivity analysis, and the sensitivity of the state variables has been investigated. As a result, the parameters were partitioned into three groups. Based on the results presented here, a future aim is to estimate the parameters of the model for a real system from measurements. The sensitivity analysis enables us to select the candidates for estimation that are inductances  $L_{lr}$  and  $L_{ls}$ , resistances  $R_s$  and  $R_r$ , the damping constant  $F$  and the inertia  $H$ . An additional future aim is to develop a model for control purposes and investigate different controllers before applying them on real systems.

### ACKNOWLEDGEMENT

We acknowledge the financial support of this work by the Hungarian State and the European Union under the TAMOP-4.2.2.A-11/1/KONV-2012-0072 project. We acknowledge also the investigated IM of Grundfos Hungary Producer Ltd.

### SYMBOLS

$C_1, C_2, C_3$	constant
$F$	damping constant
$\phi_{qs}$ and $\phi_{ds}$	$q$ and $d$ components of the stator flux
$\phi'_{qr}$ and $\phi'_{dr}$	$q$ and $d$ components of the reduced rotor flux
$H$	inertia constant
$i_{qs}$ and $i_{ds}$	$q$ and $d$ components of the stator current
$i'_{qr}$ and $i'_{dr}$	$q$ and $d$ components of the reduced rotor current
$L_m$	mutual inductance
$p$	number of pole pairs
$R_r$ and $L_r$	rotor resistance and inductance
$R'_r$ and $L'_r$	reduced value of rotor resistance and inductance
$R_s$ and $L_s$	stator resistance and inductance
$v_d$ and $v_q$	$q$ and $d$ components of the stator voltage
$\omega$	angular velocity of the magnetic field
$\omega_r$	angular velocity of the rotor
$T_{mech}$	mechanical torque

### REFERENCES

- [1] VAS P.: Artificial-intelligence-Based Electrical Machines and Drives, Oxford University Press, 1999
- [2] VAS P.: Sensorless Vector and Direct Torque Control. Oxford University Press, 1998.
- [3] ZHENG L., FLETCHER J.E., WILLIAMS B.W. HE X.: Dual-Plane Vector Control of a Five-Phase Induction Machine for an Improved Flux Pattern, IEEE Transac. Ind. Elec., 2008, 55(5), 1996–2005
- [4] LEVI E.: Impact of Iron Loss on Behavior of Vector Controlled Induction Machines, IEEE Transac. Ind. Appl., 1995, 31(6), 1287–1296
- [5] HASEGAWA M., MATSUI K.: Robust Adaptive Full-Order Observer Design with Novel Adaptive Scheme for Speed Sensorless Vector Controlled Induction Motors, Proc. 28th Annual Conf. Industrial Electronics Society, IEEE 2002, 2002, 1, 83–88
- [6] GEYER T., PAPAFOTIU G., MORARI M.: Model Predictive Direct Torque Control-Part I: Concept, Algorithm, and Analysis, IEEE Transac. Ind. Elec., 2009, 56(6), 1894–1905
- [7] KRAUSE P.C., WASYN CZUK O., SUDHOFF S.D.: Analysis of Electric Machinery, IEEE Press, New York, 1995
- [8] MOHAN N., UNDELAND T.M., ROBBINS W.P.: Power Electronics: Converters, Applications, and Design, John Wiley & Sons Inc., New York, 1995
- [9] HATOS P., FODOR, A., MAGYAR A.: Parameter sensitivity analysis of an induction motor, Hung. J. Ind. Chem., 2011, 39(1), 157–161



HUNGARIAN JOURNAL OF INDUSTRY AND CHEMISTRY

HJIC

Advertise upcoming meetings,

conferences, workshops,

new products or services;

make public announcements,

introduce your research laboratory

on the pages of the

**Hungarian Journal of Industry and Chemistry**

Please contact us if interested!

---

EDITORIAL OFFICE: UNIVERSITY OF PANNONIA

P.O. BOX 158, VESZPRÉM H-8201 (HUNGARY)

Tel.: +36 (88) 624-746, E-mail: [hjic@almos.uni-pannon.hu](mailto:hjic@almos.uni-pannon.hu);

web: [hjic.mk.uni-pannon.hu](http://hjic.mk.uni-pannon.hu)

Felelős szerkesztő: Szilágyi Róbert Károly, PhD

Kiadja: Pannon Egyetem, 8200 Veszprém, Egyetem u. 10.

Levél cím: H-8201 Veszprém, Postafiók 158, Tel.: (88) 624-000

Felelős kiadó: a Pannon Egyetem, Mérnöki Kar dékánja